Localization microscopy of constrained fluorescent molecules
Pushing towards Ångström-scale resolution through cryogenics

Hulleman, C.N.

DOI
10.4233/uuid:bb197cfd-b5a4-4b6c-933c-52f7d1d2732f

Publication date
2021

Document Version
Final published version

Citation (APA)
Hulleman, C. N. (2021). *Localization microscopy of constrained fluorescent molecules: Pushing towards Ångström-scale resolution through cryogenics*. [Dissertation (TU Delft), Delft University of Technology]. https://doi.org/10.4233/uuid:bb197cfd-b5a4-4b6c-933c-52f7d1d2732f

Localization microscopy of constrained fluorescent molecules

Pushing towards Ångström-scale resolution through cryogenics

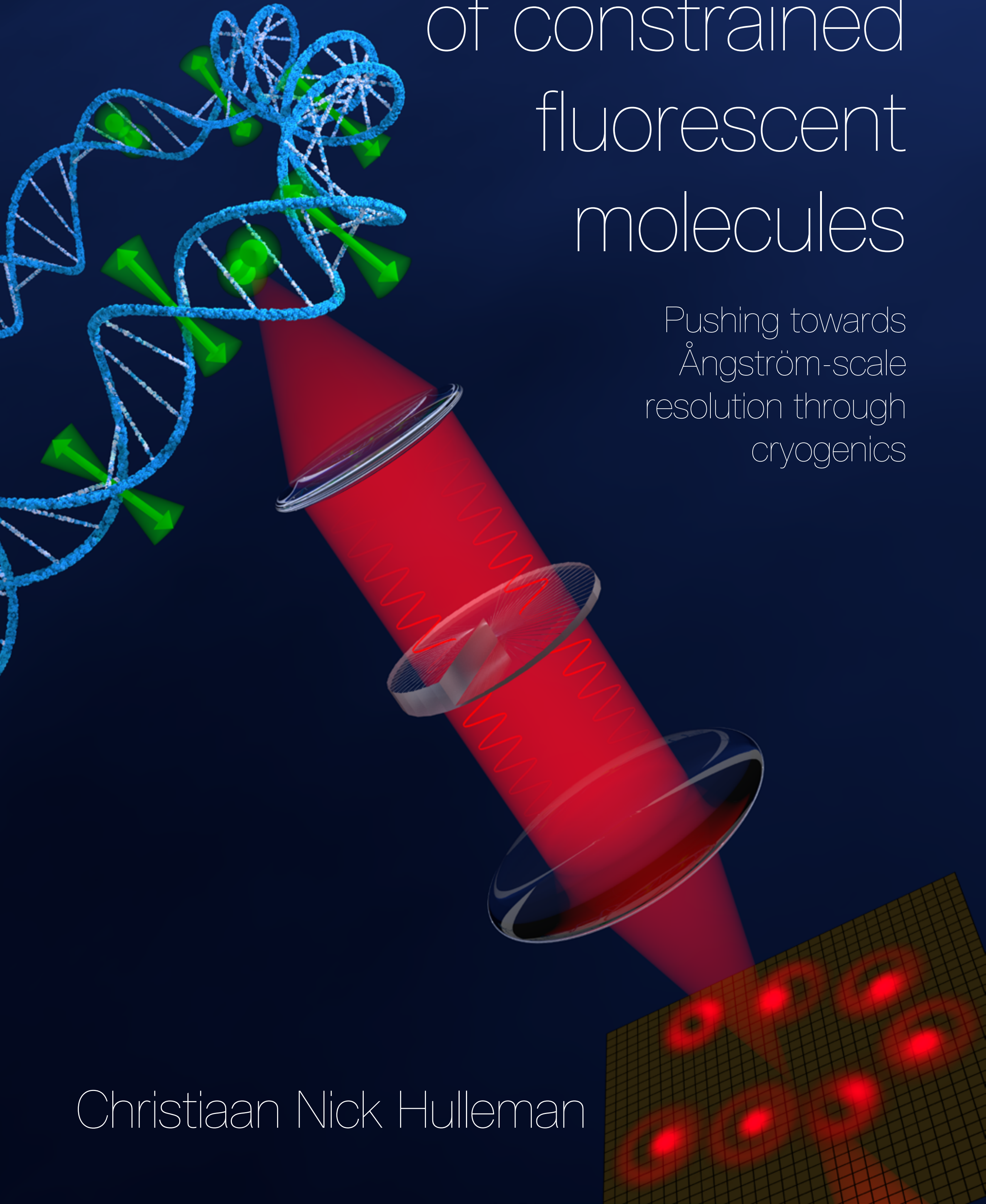

Christiaan Nick Hulleman

Localization microscopy of constrained fluorescent molecules

Pushing towards Ångström-scale resolution through cryogenics

Localization microscopy of constrained fluorescent molecules

Pushing towards Ångström-scale resolution through cryogenics

Proefschrift

ter verkrijging van de graad van doctor
aan de Technische Universiteit Delft,
op gezag van de Rector Magnificus Prof.dr.ir. T.H.J.J. van der Hagen,
voorzitter van het College voor Promoties,
in het openbaar te verdedigen op donderdag 23 december 2021 om 15:00 uur

door

Christiaan Nick HULLEMAN

Natuurkundig ingenieur, Technische Universiteit Delft, Nederland,
geboren te Spijkenisse, Nederland.

Dit proefschrift is goedgekeurd door de

promotor: Prof.dr. B. Rieger
promotor: Prof.dr. S. Stallinga

Samenstelling promotiecommissie:

Rector Magnificus,	voorzitter
Prof.dr. B. Rieger,	Technische Universiteit Delft, promotor
Prof.dr. S. Stallinga,	Technische Universiteit Delft, promotor
Onafhankelijke leden:	
Prof.dr. J. Bewersdorf	Yale University, Verenigde Staten
Prof.dr. V. Sandoghdar	Max Planck Institute for the Science of Light, Duitsland
Prof.dr.ir. E.J.G. Peterman	Vrije Universiteit Amsterdam
Prof.dr. G.H. Koenderink	Technische Universiteit Delft
Dr.ir. J.P. Hoogenboom	Technische Universiteit Delft
Prof.dr. W.M.J.M. Coene	Technische Universiteit Delft, reservelid

TU Delft Delft University of Technology

erc
European Research Council
Established by the European Commission

Keywords: super-resolution, single-molecule localization microscopy, cryogenic temperatures, stimulated emission depletion, fluorescence, optical aberrations and polarization.

Printed by: Ridderprint | www.ridderprint.nl.

Front & Back: Artistic impression of the Vortex PSF (front) and cryogenic polarization control (back) made by C.N. Hulleman.

ISBN 978-94-6384-278-5

If you know the enemy and know yourself, you need not fear the result of a hundred battles. If you know yourself but not the enemy, for every victory gained you will also suffer a defeat. If you know neither the enemy nor yourself, you will succumb in every battle.

Sun Tzu

Contents

Summary

Localization microscopy has circumvented the diffraction limit by sequentially imaging individual light emitting molecules at a time. The position of these individual molecules can be determined and a super-resolution reconstruction is made with improved resolution. Normally freely rotating emitters are used such that the point spread function (PSF) is rotationally symmetric and only minor errors in the localization process are made by approximating the PSF with a Gaussian. The precision with which the individual emitters can be localized scales with the $1/\sqrt{N}$, N the number of detected photons so that more detected photons leads to a better localization precision. However, the emission of fluorescent molecules is limited by photobleaching, a light induced chemical reaction to a permanent non-fluorescent state.

In this thesis we investigate the effect of cooling the sample to cryogenic temperatures with liquid nitrogen. This reduces the chemical reaction rates and improves photostability more than 100 fold. To use localization microscopy it is necessary to switch the fluorescent molecules between an on-state and off-state, this turns out to be difficult at cryogenic temperatures. Standard methods used at room temperature in aqueous media do not work. As the molecules are frozen in place at cryogenic temperatures we use polarized light to selectively image molecules with certain orientations at a time. To realize this it is necessary to generate pure linear polarization with an arbitrary orientation in the sample plane. By calibrating the phase difference induced by the dichroic mirrors this can be achieved, effectively modulating the fluorescence of fixed dipole emitters at cryogenic temperatures. The addition of an orthogonal linearly polarized stimulated emission depletion (STED) beam narrows the orientational distribution of fluorescing molecules. This method does induce some degree of sparsity, however, it is not enough for localization microscopy of dense biological samples. Furthermore, the STED process reduces the photon yield of single molecules. This is presumably caused by the long dark-state recovery measured on fluorescent molecules in vacuum and at cryogenic temperatures.

Localization microscopy of fixed or orientationally constrained emitters has long been avoided as the orientation of individual molecules leads to bias in the localizations. There are various ways to eliminate this bias but they reduce the amount of information that can be extracted from the sample. By fixing the orientation of fluorescent emitters to biomolecules of interest they become reporters for the orientation of the biomolecules. We have devised the so-called Vortex PSF with which the orientation, 3D position and degree of rotational constraint can be extracted from a single image. Alternatively the orientation of single-molecules can be probed with varying polarization states over multiple frames achieving a better precision with less photons.

Samenvatting

Lokalisatie microscopie omzeilt de diffractie-limiet door individuele oplichtende moleculen sequentieel af te beelden. De positie van deze individuele moleculen kan heel precies gemeten worden en zo wordt een super-resolutie reconstructie gemaakt met verbeterde resolutie. Normaal gesproken worden vrij roterende fluorescerende moleculen gebruikt zodat de puntspreidingsfunctie (PSF) rotatie-symmetrisch is en alleen kleine fouten worden gemaakt in het lokalisatie procédé met Gaussische functies. De precisie waarmee moleculen gelokaliseerd kunnen worden schaalt met $1/\sqrt{N}$, met N het aantal gedetecteerde fotonen waardoor meer gedetecteerde fotonen leidt tot een betere lokalisatieprecisie. De emissie van fluorescerende moleculen is gelimiteerd door bleking, een door licht geinduceerde chemische reactie naar een permanente niet-fluorescente toestand.

In dit proefschrift onderzoeken we het effect van het afkoelen van het sample naar cryogene temperatuur met vloeibaar stikstof. Dit reduceert de chemische reactiesnelheid en verbeterd de fotostabiliteit meer dan 100 keer. Om lokalisatie microscopie te gebruiken is het essentieel om de moleculen te kunnen schakelen tussen een aan en uit-toestand, echter blijkt dit moeilijk te zijn bij cryogene temperaturen. Standaard methoden die op kamertemperatuur gebruikt worden in waterige media werken niet. Omdat de moleculen vastgevroren zijn bij cryogene temperatuur gebruiken we gepolariseerd licht om selectief moleculen af te beelden met verschillende orientaties. Om dit te bewerkstelligen is het nodig om puur lineair gepolariseerd licht te generen met een willekeurig te kiezen orientatie in de voorwerpruimte. Door het faseverschil geïnduceerd door de dichroische spiegels te kalibreren kunnen we dit verwezenlijken en effectief de fluorescentie van vaste dipolen bij cryogene temperatuur moduleren. De toevoeging van een orthogonaal lineair gepolariseerd gestimuleerde-emissie depletie (STED) bundel versmalt de orientationale verdeling van fluorescerende moleculen. Deze methode resulteert in een kleine mate van schaarste maar niet voldoende voor lokalisatie microscopie van biologische monsters die dicht gelabeld zijn door fluorescente moleculen. Verder reduceert het STED procédé de licht opbrengst van enkele moleculen. Dit is waarschijnlijk te wijten aan de lange tijdsduur van herstel van fluorescentie uit een donkere toestand, gemeten aan fluorescerende moleculen in vacuüm en bij cryogene temperatuur.

Lokalisatie microscopie van moleculen met een vaste orientatie of een beperkt bereik van orientaties is lang vermeden omdat effecten van de orientatie van individuele moleculen aanleiding geeft tot onnauwkeurige lokalisaties. Er zijn verschillende manieren om deze onnauwkeurigheid te vermijden maar die reduceren de hoeveelheid informatie dat uit een monster gehaald kan worden. Door de orientatie van fluorescerende moleculen vast te maken aan interessante biomoleculen kunnen zij de orientatie van deze biomoleculen overnemen. We hebben de Vortex PSF bedacht, waarmee de orientatie, 3D positie en mate van rotatiebeperking bepaald kan worden

uit een enkele afbeelding. Een alternatief is om met verschillende polarisatietoestanden over meerdere opnames van de camera de orientatie te bepalen waarmee een betere precisie met minder fotonen behaald kan worden.

1

Introduction

1.1. Optical microscopy

Optical microscopy techniques still depend on the same basic microscope imaging system as 140 years ago, despite many developments such as super-resolution. The microscope hardware typically consists of two lenses, an objective lens near the object and a tube lens near the camera. This imaging system is usually a 4f system where there are four focal distances between the object and image as illustrated in figure 1.1(a). In a 4f system the Fourier transform of the image plane can be found in the Back Focal Plane (BFP). In the BFP, light rays originating from a specific spatial coordinate in the sample plane correspond to a specific angle. The ratio between the focal distance of the tube lens and the objective lens determines the magnification $M = f_2/f_1$.

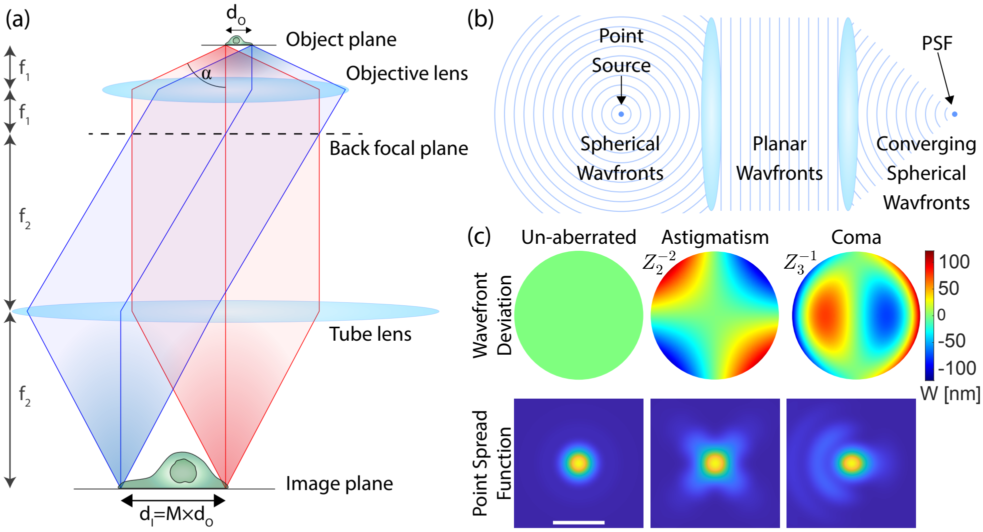

Figure 1.1: Principles of optical microscopy. **(a)** Diagram of a 4f microscope system which creates a magnified image of an object. This ray diagram illustrates that one location in the object plane corresponds to one angle in the Back Focal Plane (BFP) and conversely one position in the BFP corresponds to a unique angle in the object plane. **(b)** From a wavefront point of view, a point source emits spherical wavefronts of equal phase and a lens converts this to planar wavefronts. Upon refocusing, these wavefronts create an interference pattern that is called the point spread function. **(c)** Wavefront aberrations are deviations from the planar wavefronts in the Fourier plane. The wavefront deviations of common first order aberrations like astigmatism (Z_2^{-2}) and coma (Z_3^{-1}) are described by Zernike polynomials resulting in the corresponding PSFs. Scale bar is 500 nm.

Another way to look at this concept is to imagine a point source emitting light in all directions and look at surfaces of equal phase of the electric field. These surfaces are called wavefronts and in the ideal case a spherical wavefront originating from a point source is converted to a planar wavefront by the lens as illustrated in figure 1.1(b). After another lens, converging spherical wavefronts create an interference pattern in the image plane called the Point Spread Function (PSF). This interference pattern is due to the wave-nature of light and the in-focus size is limited by diffraction as described by E. Abbe in 1873 [1]

$$d = \frac{\lambda}{2n\sin(\alpha)}. \tag{1.1}$$

This equation describes the limit of resolution in optical microscopy, where λ is the wavelength, n the refractive index, α the angle of the marginal ray and d is the smallest discernable period of a spatially periodic object. To satisfy the Nyquist sampling theorem the camera pixel size should be smaller than half the diffraction limit, a higher magnification or finer sampling will not improve the resolution.

With ideal lenses the PSF is perfectly symmetric. However, in practice the wavefronts in the Fourier plane are not planar and any deviation from this flat wavefront is called a wavefront aberration. The most convenient way to describe these wavefront aberrations is with Zernike polynomials which form an orthogonal basis on the unit disk [2]. The Zernike polynomials describe commonly occurring aberrations in optics. For example Z_2^{-2} is a primary astigmatism mode and Z_3^{-1} a primary coma mode with their wavefront deviation and PSF illustrated in figure 1.1(c). If we want to induce aberrations or correct the wavefronts, the ideal location to do this is in the BFP as here all light passes through the same place independent of the emitters' location in the object plane.

1.2. Fluorescence microscopy

In fluorescence microscopy, fluorescent molecules also known as fluorophores are used to spectrally separate excitation and emitted light. This leads to a very high contrast between fluorescently labelled and non-labelled biomolecules. The specific labelling of biomolecules can be very useful for example in locating proteins and probing their function [3]. The spectral separation can be explained by the relationship between energy and wavelength of a photon $E = hc/\lambda$ [4]. A fluorescent molecule looses energy due to vibrational relaxation after absorbing an excitation photon. A photon with lower energy and longer wavelength is emitted when transitioning from the excited state to the ground state, this process is called fluorescence. This change in wavelength can be seen from the shift between the absorption and emission spectrum of a typical fluorophore in figure 1.2(a). With a bandpass emission filter the reflected excitation laser light is blocked and only the fluorescence signal is transmitted. The resolution of reconstructed images can be smaller than the diffraction limit by using spatially varying excitation patterns like in SIM [5, 6], MINFLUX [7, 8] and SIMFLUX [9].

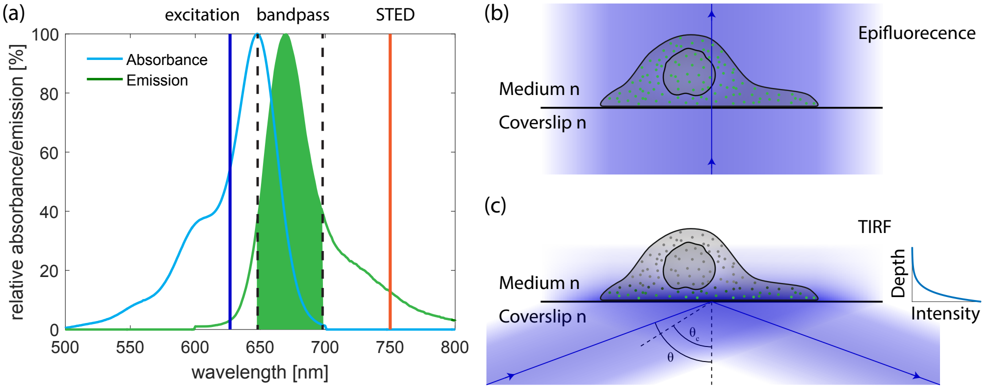

Figure 1.2: Principles of fluorescence and Total Internal Reflection Fluorescence microscopy (TIRF). **(a)** Absorption and emission spectrum of a typical fluorophore, with the excitation and STED laser wavelengths indicated in dark blue and orange respectively. The region between the dashed black lines is transmitted by the bandpass filter. **(b)** In epifluorescence the excitation laser passes straight from bottom to top exciting all the fluorophores. **(c)** In TIRF the excitation is limited by the decaying evanescent field near the coverslip-medium interface. Therefore out-of-focus fluorophores deeper in the sample do not fluoresce and the background fluorescence is decreased.

The fluorescence of a molecule can be ”turned off” by stimulating the emission at a different wavelength before the molecule spontaneously emits fluorescence. The Stimulated Emission Depletion (STED) laser stimulates the fluorescent molecule to emit a photon that is identical to the incoming photon from the laser [10, 11]. Though the molecule still emits light it is considered a virtual off-state as it is blocked by the bandpass filter. This suppression of the fluorescence can be used to control when and where fluorescent molecules emit light.

In normal epifluorescence microscopes the excitation laser passes straight through the sample and illuminates all fluorophores, therefore emission comes from a wide range of depths in the sample as illustrated in figure 1.2(b). Emitted fluorescence that does not originate from the focal plane of the microscope deteriorates the contrast of the image. By inclining the incident excitation beam beyond the critical angle, $\theta_c = \arcsin\left(n_{\mathrm{medium}}/n_{\mathrm{coverslip}}\right)$, on a glass-medium interface the excitation beam is totally internally reflected. In Total Internal Reflection Fluorescence microscopy (TIRF) there is a non-propagating evanescent electric field in the medium that can excite fluorophores near the interface as the intensity of this field decreases exponentially with depth [12]. By doing so only the fluorophores near the interface emit light and out-of-focus background is reduced as illustrated in figure 1.2(c).

1.3. Localization microscopy

Imaging single-molecules allows images of individual emitters to be fitted with a model, for example a 2D Gaussian, to determine the position with a precision beyond the diffraction limit [13]. In 1995 Betzig proposed an expansion of this idea to localize each individual molecule and combine them to build a super-resolution reconstruction of the underlying structure [14]. This concept is depicted in figure 1.3(a), where the estimated mean position of the photon distribution is marked by the blue cross. This is illustrated in more detail with a 1D cross-section in figure 1.3(b). The underlying point spread function distributes light over the camera pixels, resulting in a noisy image signal governed by the Poisson distribution. This noisy image is then fitted with a Gaussian function to determine the mean molecule position with a precision smaller than the size of the PSF. A Gaussian function is not the most accurate model for the PSF but it is quick and sufficient to approximate the central peak of a freely rotating fluorophore's PSF. However rotationally constrained fluorophores no longer have a rotationally symmetric PSF due to the dipole emission pattern further elaborated in section 1.5, making the Gaussian model inaccurate for fixed dipole emission [15].

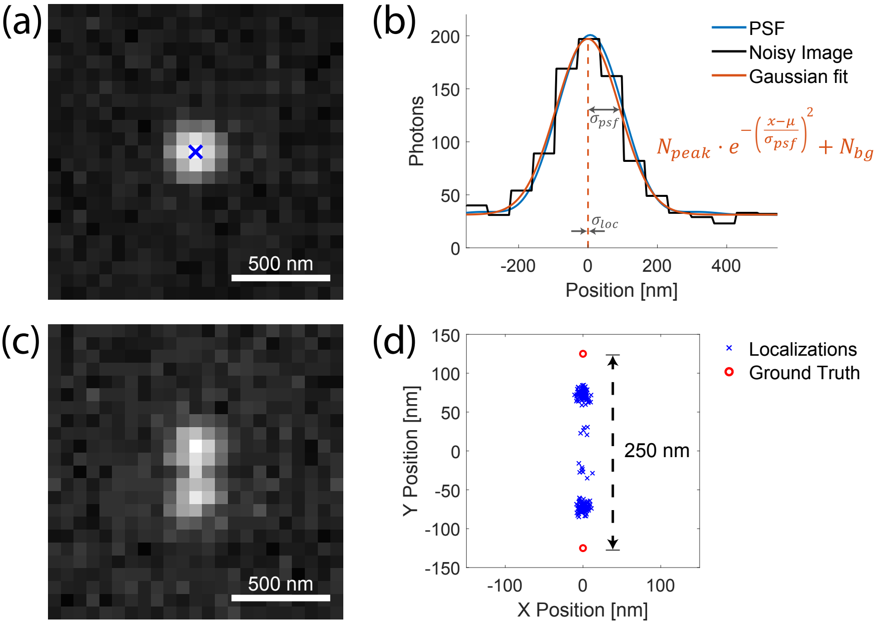

Figure 1.3: The concept and limits of localization microscopy. **(a)** Simulated individual emitter fitted with a 2D Gaussian model resulting in the estimated position marked with the blue cross. **(b)** 1D cross-section illustrating the pixelated and noisy image of the PSF and a Gaussian fit to the noisy image. The localization precision (σ_{loc}) can be much smaller than the standard deviation of the PSF (σ_{psf}). In a region around the centre, a Gaussian function approximates the PSF reasonably well but it does not account for the diffraction rings seen around ± 300 nm or additional aberrations. **(c)** Simulated image of two emitters separated by 250 nm. **(d)** Localizations from 100 simulated images of barely separated emitters show a large bias in the localizations.

Problems arise when individual emitters are not well separated, for instance two emitters 250 nm apart yield overlapping PSFs as seen in figure 1.3(c). The localizations of each individual emitter is biased towards the other emitter as the photons from the other emitter are contributing to one side of the PSF as shown in figure 1.3(d). This leads to reconstruction artefacts where "bridges" are created between fluorophores by inaccurate localizations [16, 17]. Therefore to successfully localize the position of each emitter in a densely labelled sample it is necessary to separate their emission, for example in time, to get a sparse set of emitters in each camera frame. The controlled switching of fluorophores is the key element in localization microscopy. The switching can be done in a variety of ways, for example: using an activation laser to convert fluorophores from a dark state to a fluorescent state (F)PALM [18, 19], or by stochastic switching between dark and bright states at high excitation laser intensities (d)STORM [20, 21] or by fluorophores that bind and unbind over time (DNA)-PAINT [22, 23]. To optimize the imaging conditions, buffers with diffusing molecules are used to promote or inhibit stochastic switching between dark and bright states.

Figure 1.3(b) indicated a localization precision better than the diffraction limit. This improvement is because the precision of localization is not ultimately limited by the size of the PSF but by the precision of fitting the PSF. The precision of localization is described by the following equation [24],

$$\sigma_{loc} = \frac{\sigma_{psf}}{\sqrt{N}}, \tag{1.2}$$

where more elaborate equations take pixel size and background photons into account [25, 26]. Here in equation 1.2 the standard deviation of the PSF (σ_{psf}) is limited to a typical value of ~ 100 nm by the wavelength of light and the refractive index of the immersion medium. Therefore the most direct way to improve the localization precision is to increase the number of photons (N) captured from each individual emitter.

Besides localizing the position in 2D it is also of interest to determine the emitters axial location. An unaberrated PSF is symmetric around the focal plane, thereby making estimation of the z position difficult. By engineering the PSF in the BFP this symmetry can be broken creating a unique PSF shape as a function of the axial position. For example the addition of astigmatism [27, 28] or an optimized combination of aberrations could be used [29, 30] or more complicated phase profiles like the Double-Helix [31, 32]. Alternatively, the light could be split into two different focal planes where the size difference of the PSF in the two images determines the z position [33]. An even more complex approach to extract the z position is called 4Pi and uses two opposing objectives and the interference of fluorescence emission at the detector [34, 35].

1.4. Fluorescence microscopy at cryogenic temperatures

From equation 1.2 it is clear that increasing the number of photons will improve the localization precision. The limiting factor for photon yield is photobleaching, this is when a fluorophore converts to a permanent non-fluorescent state. There are many pathways by which photobleaching occurs but reaction with oxygen is the most common [36]. By using an oxygen scavenging system the photon yield can be increased slightly but this also changes the blinking behaviour, the intermittent emission of fluorescence [37–39]. At cryogenic temperatures reactive molecules like oxygen can no longer freely diffuse through the sample as they are frozen, this significantly reduces the photobleaching rate [40]. Additionally, at lower temperatures it is harder to overcome the activation barrier for chemical reactions like photobleaching, which further reduces the photobleaching rate [41]. By cooling single-molecule emitters to cryogenic temperatures, typically liquid nitrogen ($77\ \mathrm{K}$) or liquid helium ($4.2\ \mathrm{K}$), the photon yield can be increased by more than 10-100 times [42–44].

To attain such low temperatures requires vast modifications or custom-built microscopes, as large temperature gradients need to be maintained between the sample and the environment. This is typically done by placing the sample in vacuum to eliminate convection and conduction. Alternatively long working distance objectives can be used to keep a bigger space between the cold sample and the objective. To prevent condensation and ice formation in this configuration, the cold areas are flushed with pure nitrogen gas. Therefore most samples at cryogenic temperatures are in an oxygen deprived environment, either in vacuum or saturated with nitrogen gas.

1.4.1. Blinking, photoactivation and photoswitching characteristics

This oxygen deprived environment changes the blinking characteristics of fluorophores similarly to using oxygen scavengers in liquid buffers. However at cryogenic temperatures the sample is in a frozen state. Therefore typical imaging buffers based on the diffusion of stabilizing and catalyzing molecules as used in conventional localization microscopy will not work effectively. Even fluorescent proteins embedded in a resin polymer have different blinking behaviours depending on the environment surrounding the sample; be it vacuum, partial pressure of oxygen, nitrogen or water vapour [45–47].

The inability to use typical localization microscopy buffers makes controllably switching standard organic dyes at cryogenic temperatures difficult. This limits the amount of sparsity that can be induced at cryogenic temperatures which is essential for imaging densely labelled biological samples with localization microscopy. When there are only a few emitters per diffraction limited spot however, standard organic dyes can still be used for localization microscopy at cryogenic temperatures. This is illustrated by imaging DNA rulers [43, 48], or imaging fluorophore binding sites on proteins with Ångström resolution [49].

The activation barrier that reduces photobleaching can also limit the photochemical reactions needed for photoswitchable dyes [50]. Large scale conformational changes typically required for photoactivation of fluorescent proteins are inhibited at cryogenic temperatures [51]. Therefore most commonly used photo activatable fluorescent proteins do not activate efficiently at cryogenic temperatures [52]. A few fluorescent proteins like Padron only require small scale local changes to activate, which is plausible at cryogenic temperatures [53]. An increasing amount of fluorescent proteins that can be activated at cryogenic temperatures are being found [51–58]. However the common drawbacks of fluorescent proteins over organic dyes remain, the large size and significantly lower photon yield [50, 59]. At cryogenic temperatures successfully activated fluorescent proteins only emit $\sim 1000-2000$ photons per protein [54], with one promising exception PAmKate with $\sim 10,000$ photons [60, 61]. This relatively low photon count results in a typical localization precision of $10-20$ nm which is easily surpassed with organic dyes at room temperature.

Without a method to control the switching between fluorescent and non-fluorescent states of organic dyes at cryogenic temperatures, it is worth looking at other super-resolution techniques than localization microscopy. Fluctuation based reconstructions like SOFI [62] are useful in this respect as they do not require fully separated emitters to achieve a resolution beyond the diffraction limit. After correction for drift that is typically worse due to the temperature differences in cryogenic microscopy cryo-SOFI can be used to enhance the resolution of cryo-fluorescence microscopy by 2-3 times [63]. Similarly, a two times resolution improvement can be realized with cryo-SIM without the need for blinking [64]. These methods are useful if a high resolution is not required or for quickly selecting regions of interest as illustrated in [58].

1.4.2. Numerical Aperture

Most cryogenic fluorescence microscopes use long working distance objectives with a relatively low numerical aperture $\mathrm{NA} < 0.8$ $(\mathrm{NA} = n\sin(\alpha))$. This is necessitated by the temperature gradient or vacuum window between the sample and the objective. This limits the size of the PSF and consequently the localization precision. With a material of refractive index n between the objective and the emitter, the NA can be increased up to $\mathrm{NA} = n$ to capture the maximal 2π solid angle with one objective. The larger the solid angle the more photons are detected from each emitter.

Increasing the captured solid angle can be done by using a reflective objective lens [65, 66] with an NA of 0.99 in liquid helium ($n \simeq 1.02$ [67]). This high NA lens comes with a very limited field of view (FOV) of ~ 1.5 μm, reducing the NA to 0.93 can improve the FOV to a still limited value of 36 μm [68]. To facilitate an $\mathrm{NA} > 1$ at cryogenic temperatures an immersion medium with a refractive index $n > 1$ is needed that does not freeze. Liquid propane could be used as such an immersion medium to get an $\mathrm{NA} \sim 1.3$ [69]. However, the refractive index of liquid propane is higher than that of water leading to spherical aberrations with water-immersion objectives. A variety of cryogenic liquids have been found with a refractive index closer to water making them useful to be combined with water-immersion objectives [70]. By thermally isolating the first lens of a water-immersion objective from the rest a sufficiently high temperature gradient can be maintained to image at cryogenic temperatures with an NA of 1.15 [71]. To further maximize the NA, samples can be mounted directly on the first lens, on a so called solid immersion lens. Using a high refractive index for the solid immersion lens a high NA of 2.17 can be realized at cryogenic temperatures [48]. Similar to the reflective objective lenses this comes with a reduced FOV, however in this case with a solid immersion lens there is only a single usable region approximately 60 μm wide per sample.

1.4.3. Correlative cryogenic fluorescence microscopy and electron microscopy

Research into fluorescence microscopy at cryogenic temperatures is commonly driven by the desire to combine the specific labelling of biomolecules in fluorescence microscopy with Ångström scale resolution of cryogenic Electron Microscopy (cryo-EM) [72]. Ideally this is all integrated into a single workflow at cryogenic temperatures [73–76]. For cryo-EM it is essential to rapidly freeze the sample to form amorphous ice that does not damage the sample [77]. This is typically done by immersing a thin sample in liquid ethane or propane. Sample holders can be engineered so that live cells can be observed with light microscopy and cooled rapidly enough to avoid crystallization, selecting the moment of freezing on a ms timescale [78, 79]. If thereafter the sample reaches a temperature above the glass transition temperature ($T \simeq 140$ K) the molecules become flexible and can rearrange into a crystalline structure, this process is called devitrification. This is detrimental to contrast in electron microscopy as the crystal structure diffracts the electrons. This highlights a serious limitation to the integration of the two, as high laser powers commonly used in STORM and STED microscopy cause devitrification in the samples on EM grids [56]. This is due to the relatively high absorption and low heat conduction of the carbon grid, making the combination of fluorescence super-resolution and cryo-EM experimentally challenging.

Besides the influence on devitrification and conformational changes of proteins it is important to realize that cooling to cryogenic temperatures also fixes the orientation of fluorescent molecules and thereby the fluorescent dipole. As of yet this is usually not taken into account in cryogenic localization microscopy but can induce errors up to 40 nm [80].

1.5. Dipole emission and polarized light

Fluorescent molecules can be considered to lowest order as electric dipoles, meaning that they emit a dipole radiation pattern and are sensitive to the polarization of excitation light. In typical localization microscopy experiments this is not observed as the fluorescent molecules are attached with a flexible linker allowing the molecule to emit many photons under different orientations of the emission dipole moment during a single camera frame. This averages out on the camera and appears as an isotropic emitter. However, when the fluorophore's orientation is constrained the dipole emission pattern can be observed [81, 82]. Figure 1.4(a) illustrates a fluorescent dipole with the black arrow representing the molecular dipole moment, red curves the electric field and the red arrows the phase of the electric field. With the dipole moment aligned perpendicular to the optical axis the observed electric field is largely in-phase leading to an image with constructive interference in the centre as seen in figure 1.4(b). A dipole moment aligned along the optical axis results in observed electric fields that are out of phase and lead to destructive interference and consequently a ring shaped PSF as seen in figure 1.4(c). As the dipole moment transitions from perpendicular to parallel to the optical axis the photon distribution shifts such that it is no longer centred around the position of the emitter. This leads to position biases of 40 nm or more in localization microscopy of fixed emitters [15, 80, 83].

Besides influence on the emitted fluorescence, a fixed dipole moment also influences the excitation efficiency. The probability of exciting a fixed dipole scales with the inner product between the excitation polarization $\vec{E}$ and the excitation transition dipole moment $\vec{\mu}$ of the fluorescent molecule $I \sim |\vec{\mu} \cdot \vec{E}|^2 = |\vec{\mu}|^2|\vec{E}|^2 \cos(\alpha)^2$, where α is the angle between the two. By rotating the polarization of the excitation laser around the optical axis the in-plane angle of the excitation transition dipole moment can be determined [84–86]. The full absorption dipole orientation of single-molecules can be probed by scanning a focused laser spot with a spatially varying polarization [87, 88]. Altering the excitation polarization is of interest at cryogenic temperatures to vary which fluorophores are effectively excited and imaged.

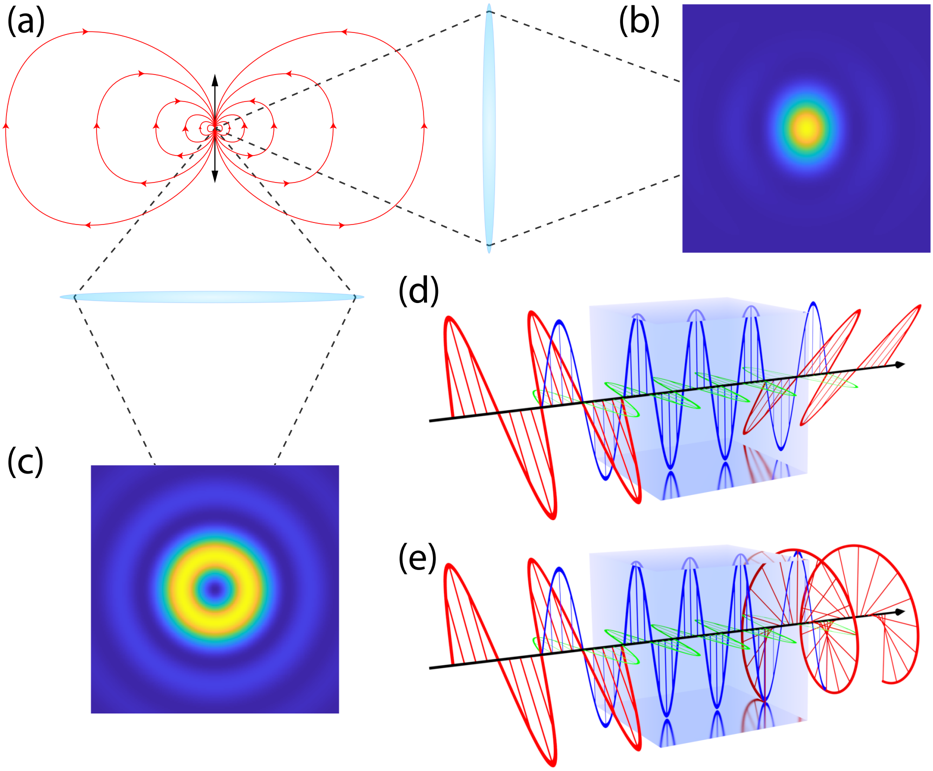

Figure 1.4: Dipole emission and polarization change. **(a)** Fluorophores are radiating dipoles, the molecular dipole moment is represented by the black arrow and the red curves represent the electric field with arrows indicating the phase. **(b)** Image of a fluorescent dipole oriented perpendicular to the optical axis. **(c)** Image of a fluorescent dipole oriented along the optical axis. **(d)** Polarization change with a $\lambda/2$ wave plate (transparent blue block). The green and blue waves represent the horizontal and vertical component of the incoming red electromagnetic wave. **(e)** Polarization change with a $\lambda/4$ wave plate.

To maximize the excitation efficiency of a fluorophore, linearly polarized excitation light needs to be aligned parallel to the excitation transition dipole moment. The polarization state of the excitation light can be changed using birefringent materials that have different refractive indices depending on the oscillation direction of the electromagnetic wave. The incoming electromagnetic wave can be split into two components, one aligned with the fast axis of the birefringent material and one aligned with the slow axis. The component aligned with the fast axis travels faster through the material and the phase difference between the two components changes. The wave plate in figure 1.4(d) has the fast axis aligned vertically, there the blue wave only has 2.5 periods within the birefringent material compared to 3 periods for the green component, resulting in a $\lambda/2$ phase shift which rotates linearly polarized light. A phase shift of $\lambda/4$ can convert linear to circularly polarized light as illustrated in figure 1.4(e). Using materials where the birefringence depends on an externally applied electric field the phase delay can be actively controlled.

1.6. Motivation

The goal of this thesis is to push the resolution limit of fluorescence microscopy towards 1 nm. In particular using localization microscopy where the localization precision and ultimately the resolution scales with the number of detected photons. The pursued way to increase the number of photons is by cooling the sample to cryogenic temperatures. Cooling the sample to these temperatures brings a lot of engineering challenges but also makes inducing the sparsity required for localization microscopy difficult. This is the main obstacle to achieving high resolution localization microscopy images at cryogenic temperatures.

Of course achieving a 1 nm resolution is not a goal in and of itself. The purpose of research in this direction is to develop tools with which biologists can visualize biological structures with fluorescently labelled biomolecules at the scale of the molecules that build up the cells, for example, to image the 3D conformation of DNA in its native state. To achieve this it is vital to avoid localization bias, as commonly seen in localization microscopy of fixed emitters like those at cryogenic temperatures. Besides only avoiding localization bias, when the fluorophores are rotationally constrained to biomolecules of interest they can reveal the orientation of those biomolecules. This can be used to visualize the organization of structures that cannot be determined by 3D localization alone. Examples are the visualization of structures that twist around their own axis, or small deformations in the surface of lipid membranes, or tracking the orientation of motor proteins.

1.7. Outline

Photon Yield Enhancement of Red Fluorophores at Cryogenic Temperatures

In **chapter 2** the photon yield of red organic dyes is investigated at cryogenic temperatures. The particular interest in red fluorophores is the low autofluorescence of biological samples in this part of the spectrum. Additionally, the red/near-infrared fluorophores can be switched off with STED using a high power Titanium-sapphire laser as described in the next chapter. The photon yield of all investigated fluorophores is shown to increase by at least 100 times at ($89\ \mathrm{K}$) compared to room temperature. This implies that the localization precision can be improved 10 fold, corresponding to a theoretical localization precision of $\sim 0.1\ nm$. In practice the experimental localization precision is slightly worse due to residual drift. Furthermore, the photoactivatable dye PA-JF 646 was investigated but showed no photoactivation at cryogenic temperatures.

Fluorescence Polarization Control for On–Off Switching of Single Molecules at Cryogenic Temperatures

Inducing sparsity to perform localization microscopy at cryogenic temperatures is the focus of **chapter 3**. To achieve this, we propose to perform polarization controlled STED on fixed fluorescent dipoles at cryogenic temperatures. The desired orientation of fluorescent dipoles that we want to image is not suppressed by the STED laser as it is aligned perpendicular to the molecular dipole moment and thus the inner product between the two is zero. Molecules that are not aligned perpendicular to the polarization of the STED laser will be depleted. If the polarization of the STED laser in the sample is not perfectly linear then the fluorescence of the fluorophores with the desired orientation also reduces. Even though the input polarization from the laser is linear the polarization in the sample plane can be elliptical. To avoid this we have measured the polarization change throughout the microscope and supply a polarization state that pre-compensates for the phase difference induced by the dichroic mirror, resulting in linearly polarized light in the sample plane. To verify the polarization quality we measured the modulation on single-molecule emitters where the intensity can be reduced to the background level, which is not the case for diagonally oriented molecules without our compensation method. Lastly we show an improved design for a liquid nitrogen cryostat for imaging fluorescent samples with reduced vibrations.

Polarized Stimulated-Emission Depletion and Dark-State Lifetime at Cryogenic Temperatures

The method to induce sparsity at cryogenic temperatures as proposed in the previous chapter could work perfectly if fluorophores never transition to temporary or permanent dark states. In **chapter 4** we show the experimentally achieved angle narrowing on single-molecules with polarized STED at cryogenic temperatures. Higher STED laser powers lead to a narrower set of molecules in the ”on” state and thus a better sparsity but also a reduced survival time and consequently less emitted photons. A common pathway for bleaching in STED microscopy is via the triplet state [89]. To investigate if this was limiting the photon yield in our experiments, we probed the dark state lifetime of bulk fluorophores in vacuum and found a lifetime $30 - 10000$ times longer than the typical triplet state lifetime in atmospheric conditions. Performing pulsed STED at cryogenic temperatures with a period between each pulse for the dark state to relax back to the ground state would be far too slow for any practical application.

Simultaneous orientation and 3D localization microscopy with a Vortex point spread function

Inspired by the desire to determine the orientation of fixed dipole emitters at cryogenic temperatures, we have developed a PSF-engineering approach to determine the orientation of fixed dipole emitters from a single in-focus image in **chapter 5**. The relatively low NA used in our cryogenic microscope does not collect much light from molecules aligned along the optical axis, therefore we implemented this on a standard microscope with an oil immersion objective. With this method the orientation of constrained molecules can easily be visualized. The PSF fitter developed along with the Vortex PSF can successfully determine the 3D location and both orientation angles of constrained emitters, along with the degree of orientational constraint. With this method we have visualized re-orienting single-molecules and the binding landscape of Sytox Orange intercalators in λ-DNA on a coverslip.

Photon efficient orientation estimation using polarization modulation in single-molecule localization microscopy

In **chapter 6** we take the concept of polarization control from the previous chapters and expand it to 3D polarization control in high-NA and TIRF microscopes. The waveplates used before are replaced with an electronically controlled Pockels cell to quickly change the polarization state. With the polarization state continuously switching, fluorescence of fixed emitters is modulated as the excitation efficiency varies. Utilizing this polarization control we have developed schemes to probe the fluorescent dipole's in-plane orientation or it's full 3D orientation. The advantage of this method is that the orientation can successfully be determined at lower photon counts.

Conclusion and outlook

This last chapter summarizes the main results and discusses their implications. Furthermore, suggestions are made to continue pushing cryogenic localization microscopy towards 1 nm resolution.

References

[1] E. Abbe, *Beiträge zur Theorie des Mikroskops und der mikroskopischen Wahrnehmung,* Archiv für Mikroskopische Anatomie **9**, 413 (1873).

[2] F. Zernike, *Beugungstheorie des schneidenver-fahrens und seiner verbesserten form, der phasenkontrastmethode,* Physica **1**, 689 (1934).

[3] B. N. Giepmans, S. R. Adams, M. H. Ellisman, and R. Y. Tsien, *The fluorescent toolbox for assessing protein location and function,* Science **312**, 217 (2006).

[4] M. Planck, *Ueber das Gesetz der Energieverteilung im Normalspectrum,* Annalen der Physik **309**, 553 (1901).

[5] R. Heintzmann and C. G. Cremer, *Laterally modulated excitation microscopy: improvement of resolution by using a diffraction grating,* in *Optical Biopsies and Microscopic Techniques III*, Vol. 3568 (SPIE, 1999) pp. 185–196.

[6] M. G. Gustafsson, *Surpassing the lateral resolution limit by a factor of two using structured illumination microscopy,* Journal of Microscopy **198**, 82 (2000).

[7] F. Balzarotti, Y. Eilers, K. C. Gwosch, A. H. Gynnå, V. Westphal, F. D. Stefani, J. Elf, and S. W. Hell, *Nanometer resolution imaging and tracking of fluorescent molecules with minimal photon fluxes,* Science **355**, 606 (2017).

[8] K. C. Gwosch, J. K. Pape, F. Balzarotti, P. Hoess, J. Ellenberg, J. Ries, and S. W. Hell, *MINFLUX nanoscopy delivers 3D multicolor nanometer resolution in cells,* Nature Methods **17**, 217 (2020).

[9] J. Cnossen, T. Hinsdale, R. Ø. Thorsen, M. Siemons, F. Schueder, R. Jungmann, C. S. Smith, B. Rieger, and S. Stallinga, *Localization microscopy at doubled precision with patterned illumination,* Nature Methods **17**, 59 (2020).

[10] S. W. Hell and J. Wichmann, *Breaking the diffraction resolution limit by stimulated emission: stimulated-emission-depletion fluorescence microscopy,* Optics Letters **19**, 780 (1994).

[11] T. A. Klar, S. Jakobs, M. Dyba, A. Egner, and S. W. Hell, *Fluorescence microscopy with diffraction resolution barrier broken by stimulated emission,* Proceedings of the National Academy of Sciences of the United States of America **97**, 8206 (2000).

[12] D. Axelrod, *Cell-substrate contacts illuminated by total internal reflection fluorescence.* Journal of Cell Biology **89**, 141 (1981).

[13] F. Güttler, T. Irngartinger, T. Plakhotnik, A. Renn, and U. P. Wild, *Fluorescence microscopy of single molecules,* Chemical Physics Letters **217**, 393 (1994).

[14] E. Betzig, *Proposed method for molecular optical imaging,* Optics Letters **20**, 237 (1995).

[15] J. Enderlein, E. Toprak, and P. R. Selvin, *Polarization effect on position accuracy of fluorophore localization,* Optics Express **14**, 8111 (2006).

[16] J. Sinkó, R. Kákonyi, E. Rees, D. Metcalf, A. E. Knight, C. F. Kaminski, G. Szabó, and M. Erdélyi, *TestSTORM: Simulator for optimizing sample labeling and image acquisition in localization based super-resolution microscopy,* Biomedical Optics Express **5**, 778 (2014).

[17] P. Fox-Roberts, R. Marsh, K. Pfisterer, A. Jayo, M. Parsons, and S. Cox, *Local dimensionality determines imaging speed in localization microscopy,* Nature Communications **8**, 13558 (2017).

[18] E. Betzig, G. H. Patterson, R. Sougrat, O. W. Lindwasser, S. Olenych, J. S. Bonifacino, M. W. Davidson, J. Lippincott-Schwartz, and H. F. Hess, *Imaging intracellular fluorescent proteins at nanometer resolution,* Science **313**, 1642 (2006).

[19] S. T. Hess, T. P. Girirajan, and M. D. Mason, *Ultra-high resolution imaging by fluorescence photoactivation localization microscopy,* Biophysical Journal **91**, 4258 (2006).

[20] M. J. Rust, M. Bates, and X. Zhuang, *Sub-diffraction-limit imaging by stochastic optical reconstruction microscopy (STORM),* Nature Methods **3**, 793 (2006).

[21] M. Heilemann, S. Van De Linde, M. Schüttpelz, R. Kasper, B. Seefeldt, A. Mukherjee, P. Tinnefeld, and M. Sauer, *Subdiffraction-resolution fluorescence imaging with conventional fluorescent probes,* Angewandte Chemie - International Edition **47**, 6172 (2008).

[22] A. Sharonov and R. M. Hochstrasser, *Wide-field subdiffraction imaging by accumulated binding of diffusing probes,* Proceedings of the National Academy of Sciences of the United States of America **103**, 18911 (2006).

[23] R. Jungmann, C. Steinhauer, M. Scheible, A. Kuzyk, P. Tinnefeld, and F. C. Simmel, *Single-molecule kinetics and super-resolution microscopy by fluorescence imaging of transient binding on DNA origami,* Nano Letters **10**, 4756 (2010).

[24] R. E. Thompson, D. R. Larson, and W. W. Webb, *Precise nanometer localization analysis for individual fluorescent probes,* Biophysical Journal **82**, 2775 (2002).

[25] K. I. Mortensen, L. S. Churchman, J. A. Spudich, and H. Flyvbjerg, *Optimized localization analysis for single-molecule tracking and super-resolution microscopy,* Nature Methods **7**, 377 (2010).

[26] B. Rieger and S. Stallinga, *The lateral and axial localization uncertainty in super-resolution light microscopy,* ChemPhysChem **15**, 664 (2014).

[27] L. Holtzer, T. Meckel, and T. Schmidt, *Nanometric three-dimensional tracking of individual quantum dots in cells,* Applied Physics Letters **90**, 053902 (2007).

[28] B. Huang, W. Wang, M. Bates, and X. Zhuang, *Three-Dimensional Super-Resolution Reconstruction Microscopy,* Science **319**, 810 (2008).

[29] Y. Shechtman, S. J. Sahl, A. S. Backer, and W. E. Moerner, *Optimal Point Spread Function Design for 3D Imaging,* Physical Review Letters **113**, 133902 (2014).

[30] Y. Shechtman, L. E. Weiss, A. S. Backer, S. J. Sahl, and W. E. Moerner, *Precise Three-Dimensional Scan-Free Multiple-Particle Tracking over Large Axial Ranges with Tetrapod Point Spread Functions,* Nano Letters **15**, 4194 (2015).

[31] S. R. P. Pavani, M. A. Thompson, J. S. Biteen, S. J. Lord, N. Liu, R. J. Twieg, R. Piestun, and W. E. Moerner, *Three-dimensional, single-molecule fluorescence imaging beyond the diffraction limit by using a double-helix point spread function,* Proceedings of the National Academy of Sciences of the United States of America **106**, 2995 (2009).

[32] H.-l. D. Lee, S. J. Sahl, M. D. Lew, and W. E. Moerner, *The double-helix microscope super-resolves extended biological structures by localizing single blinking molecules in three dimensions with nanoscale precision,* Applied Physics Letters **100**, 153701 (2012).

[33] M. F. Juette, T. J. Gould, M. D. Lessard, M. J. Mlodzianoski, B. S. Nagpure, B. T. Bennett, S. T. Hess, and J. Bewersdorf, *Three-dimensional sub-100 nm resolution fluorescence microscopy of thick samples,* Nature Methods **5**, 527 (2008).

[34] S. Hell and E. H. K. Stelzer, *Properties of a 4Pi confocal fluorescence microscope,* Journal of the Optical Society of America A **9**, 2159 (1992).

[35] S. W. Hell, S. Lindek, C. Cremer, and E. H. Stelzer, *Measurement of the 4Pi-confocal point spread function proves 75 nm axial resolution,* Applied Physics Letters **64**, 1335 (1994).

[36] B. Kozankiewicz and M. Orrit, *Single-molecule photophysics, from cryogenic to ambient conditions,* Chemical Society Reviews **43**, 1029 (2014).

[37] Y. Harada, K. Sakurada, T. Aoki, D. D. Thomas, and T. Yanagida, *Mechanochemical coupling in actomyosin energy transduction studied by in vitro movement assay,* Journal of Molecular Biology **216**, 49 (1990).

[38] S. Weiss, *Fluorescence spectroscopy of single biomolecules,* Science **283**, 1676 (1999).

[39] A. Yildiz, J. N. Forkey, S. A. McKinney, T. Ha, Y. E. Goldman, and P. R. Selvin, *Myosin V walks hand-over-hand: Single fluorophore imaging with 1.5-nm localization,* Science **300**, 2061 (2003).

[40] W. E. Moerner and M. Orrit, *Illuminating single molecules in condensed matter,* Science **283**, 1670 (1999).

[41] R. Zondervan, F. Kulzer, M. A. Kol'chenko, and M. Orrit, *Photobleaching of Rhodamine 6G in Poly(vinyl alcohol) at the Ensemble and Single-Molecule Levels,* Journal of Physical Chemistry A **108**, 1657 (2004).

[42] S. Weisenburger, B. Jing, A. Renn, and V. Sandoghdar, *Cryogenic localization of single molecules with angstrom precision,* Nanoimaging and Nanospectroscopy **8815**, 88150D (2013).

[43] S. Weisenburger, B. Jing, D. Hänni, L. Reymond, B. Schuler, A. Renn, and V. Sandoghdar, *Cryogenic colocalization microscopy for nanometer-distance measurements,* ChemPhysChem **15**, 763 (2014).

[44] W. Li, S. C. Stein, I. Gregor, and J. Enderlein, *Ultra-stable and versatile widefield cryo-fluorescence microscope for single-molecule localization with subnanometer accuracy,* Optics Express **23**, 3770 (2015).

[45] E. Brama, C. J. Peddie, M. L. Jones, M. C. Domart, X. Snetkov, M. Way, B. Larijani, and L. M. Collinson, *Standard fluorescent proteins as dual-modality probes for correlative experiments in an integrated light and electron microscope,* Journal of Chemical Biology **8**, 179 (2015).

[46] C. J. Peddie, K. Blight, E. Wilson, C. Melia, J. Marrison, R. Carzaniga, M.-C. Domart, P. O'Toole, B. Larijani, and L. M. Collinson, *Correlative and integrated light and electron microscopy of in-resin GFP fluorescence, used to localise diacylglycerol in mammalian cells,* Ultramicroscopy **143**, 3 (2014).

[47] C. J. Peddie, M. C. Domart, X. Snetkov, P. O'Toole, B. Larijani, M. Way, S. Cox, and L. M. Collinson, *Correlative super-resolution fluorescence and electron microscopy using conventional fluorescent proteins in vacuo,* Journal of Structural Biology **199**, 120 (2017).

[48] L. Wang, B. Bateman, L. C. Zanetti-Domingues, A. N. Moores, S. Astbury, C. Spindloe, M. C. Darrow, M. Romano, S. R. Needham, K. Beis, D. J. Rolfe, D. T. Clarke, and M. L. Martin-Fernandez, *Solid immersion microscopy images cells under cryogenic conditions with 12 nm resolution,* Communications Biology **2**, 74 (2019).

[49] S. Weisenburger, D. Boening, B. Schomburg, K. Giller, S. Becker, C. Griesinger, and V. Sandoghdar, *Cryogenic optical localization provides 3D protein structure data with Angstrom resolution,* Nature Methods **14**, 141 (2017).

[50] H. Li and J. C. Vaughan, *Switchable Fluorophores for Single-Molecule Localization Microscopy,* Chemical Reviews **118**, 9412 (2018).

[51] A. R. Faro, V. Adam, P. Carpentier, C. Darnault, D. Bourgeois, and E. De Rosny, *Low-temperature switching by photoinduced protonation in photochromic fluorescent proteins,* Photochemical and Photobiological Sciences **9**, 254 (2010).

[52] Y. W. Chang, S. Chen, E. I. Tocheva, A. Treuner-Lange, S. Löbach, L. Søgaard-Andersen, and G. J. Jensen, *Correlated cryogenic photoactivated localization microscopy and cryo-electron tomography,* Nature Methods **11**, 737 (2014).

[53] A. Regis Faro, P. Carpentier, G. Jonasson, G. Pompidor, D. Arcizet, I. Demachy, and D. Bourgeois, *Low-temperature chromophore isomerization reveals the photoswitching mechanism of the fluorescent protein Padron,* Journal of the American Chemical Society **133**, 16362 (2011).

[54] B. Liu, Y. Xue, W. Zhao, Y. Chen, C. Fan, L. Gu, Y. Zhang, X. Zhang, L. Sun, X. Huang, W. Ding, F. Sun, W. Ji, and T. Xu, *Three-dimensional super-resolution protein localization correlated with vitrified cellular context,* Scientific Reports **5**, 13017 (2015).

[55] S. Wang, S. Li, G. Ji, X. Huang, and F. Sun, *Using integrated correlative cryo-light and electron microscopy to directly observe syntaphilin-immobilized neuronal mitochondria in situ,* Biophysics Reports **3**, 8 (2017).

[56] M. W. Tuijtel, A. J. Koster, S. Jakobs, F. G. A. Faas, and T. H. Sharp, *Correlative cryo super-resolution light and electron microscopy on mammalian cells using fluorescent proteins,* Scientific Reports **9**, 1369 (2019).

[57] M. W. Tuijtel, A. J. Koster, F. G. A. Faas, and T. H. Sharp, *Correlated Cryo Super-Resolution Light and Cryo-Electron Microscopy on Mammalian Cells Expressing the Fluorescent Protein rsEGFP2,* Small Methods **3**, 1900425 (2019).

[58] D. P. Hoffman, G. Shtengel, C. S. Xu, K. R. Campbell, M. Freeman, L. Wang, D. E. Milkie, H. A. Pasolli, N. Iyer, J. A. Bogovic, D. R. Stabley, A. Shirinifard, S. Pang, D. Peale, K. Schaefer, W. Pomp, C. L. Chang, J. Lippincott-Schwartz, T. Kirchhausen, D. J. Solecki, E. Betzig, and H. F. Hess, *Correlative three-dimensional super-resolution and block-face electron microscopy of whole vitreously frozen cells,* Science **367**, 265 (2020).

[59] R. Kaufmann, P. Schellenberger, E. Seiradake, I. M. Dobbie, E. Y. Jones, I. Davis, C. Hagen, and K. Grünewald, *Super-resolution microscopy using standard fluorescent proteins in intact cells under cryo-conditions,* Nano Letters **14**, 4171 (2014).

[60] P. D. Dahlberg, A. M. Sartor, J. Wang, S. Saurabh, L. Shapiro, and W. E. Moerner, *Identification of PAmKate as a Red Photoactivatable Fluorescent Protein for Cryogenic Super-Resolution Imaging,* Journal of the American Chemical Society **140**, 12310 (2018).

[61] P. D. Dahlberg, S. Saurabh, A. M. Sartor, J. Wang, J. Wang, P. G. Mitchell, W. Chiu, W. Chiu, L. Shapiro, and W. E. Moerner, *Cryogenic single-molecule fluorescence annotations for electron tomography reveal in situ organization of key proteins in Caulobacter,* Proceedings of the National Academy of Sciences of the United States of America **117**, 13937 (2020).

[62] T. Dertinger, R. Colyer, G. Iyer, S. Weiss, and J. Enderlein, *Fast, background-free, 3D super-resolution optical fluctuation imaging (SOFI),* Proceedings of the National Academy of Sciences **106**, 22287 (2009).

[63] F. Moser, V. Prazák, V. Mordhorst, D. M. Andrade, L. A. Baker, C. Hagen, K. Grünewald, and R. Kaufmann, *Cryo-SOFI enabling low-dose super-resolution correlative light and electron cryo-microscopy,* Proceedings of the National Academy of Sciences of the United States of America **116**, 4804 (2019).

[64] M. A. Phillips, M. Harkiolaki, D. M. Susano Pinto, R. M. Parton, A. Palanca, M. Garcia-Moreno, I. Kounatidis, J. W. Sedat, D. I. Stuart, A. Castello, M. J. Booth, I. Davis, and I. M. Dobbie, *CryoSIM: super-resolution 3D structured illumination cryogenic fluorescence microscopy for correlated ultrastructural imaging,* Optica **7**, 802 (2020).

[65] H. Inagawa, Y. Toratani, K. Motohashi, I. Nakamura, M. Matsushita, and S. Fujiyoshi, *Reflecting microscope system with a 0.99 numerical aperture designed for three-dimensional fluorescence imaging of individual molecules at cryogenic temperatures,* Scientific Reports **5**, 12833 (2015).

[66] T. Furubayashi, K. Motohashi, K. Wakao, T. Matsuda, I. Kii, T. Hosoya, N. Hayashi, M. Sadaie, F. Ishikawa, M. Matsushita, and S. Fujiyoshi, *Three-Dimensional Localization of an Individual Fluorescent Molecule with Angstrom Precision,* Journal of the American Chemical Society **139**, 8990 (2017).

[67] E. F. Burton, *Refractive Indexes of Helium I and II,* Nature **140**, 1015 (1937).

[68] M. Fujiwara, T. Ishii, K. Ishida, Y. Toratani, T. Furubayashi, M. Matsushita, and S. Fujiyoshi, *Aberration-corrected cryogenic objective mirror with a 0.93 numerical aperture,* Applied Physics Letters **115**, 033701 (2019).

[69] M. Le Gros, G. McDermott, M. Uchida, C. Knoechel, and C. Larabell, *High-aperture cryogenic light microscopy,* Journal of Microscopy **235**, 1 (2009).

[70] R. Faoro, M. Bassu, and T. P. Burg, *Determination of the refractive index of liquids at cryogenic temperature,* Applied Physics Letters **113**, 081903 (2018).

[71] R. Faoro, M. Bassu, Y. X. Mejia, T. Stephan, N. Dudani, C. Boeker, S. Jakobs, and T. P. Burg, *Aberration-corrected cryoimmersion light microscopy,* Proceedings of the National Academy of Sciences of the United States of America **115**, 1204 (2018).

[72] A. Sartori, R. Gatz, F. Beck, A. Rigort, W. Baumeister, and J. M. Plitzko, *Correlative microscopy: Bridging the gap between fluorescence light microscopy and cryo-electron tomography,* Journal of Structural Biology **160**, 135 (2007).

[73] C. L. Schwartz, V. I. Sarbash, F. I. Ataullakhanov, J. R. Mcintosh, and D. Nicastro, *Cryo-fluorescence microscopy facilitates correlations between light and cryo-electron microscopy and reduces the rate of photobleaching,* Journal of Microscopy **227**, 98 (2007).

[74] L. F. van Driel, J. A. Valentijn, K. M. Valentijn, R. I. Koning, and A. J. Koster, *Tools for correlative cryo-fluorescence microscopy and cryo-electron tomography applied to whole mitochondria in human endothelial cells,* European Journal of Cell Biology **88**, 669 (2009).

[75] S. Li, G. Ji, Y. Shi, L. H. Klausen, T. Niu, S. Wang, X. Huang, W. Ding, X. Zhang, M. Dong, W. Xu, and F. Sun, *High-vacuum optical platform for cryo-CLEM (HOPE): A new solution for non-integrated multiscale correlative light and electron microscopy,* Journal of Structural Biology **201**, 63 (2018).

[76] X. Xu, Y. Xue, B. Tian, F. Feng, L. Gu, W. Li, W. Ji, and T. Xu, *Ultra-stable super-resolution fluorescence cryo-microscopy for correlative light and electron cryo-microscopy,* Science China Life Sciences **61**, 1312 (2018).

[77] M. Adrian, J. Dubochet, J. Lepault, and A. W. McDowall, *Cryo-electron microscopy of viruses,* Nature **308**, 32 (1984).

[78] M. Fuest, G. M. Nocera, M. M. Modena, D. Riedel, Y. X. Mejia, and T. P. Burg, *Cryofixation during live-imaging enables millisecond time-correlated light and electron microscopy,* Journal of Microscopy **272**, 87 (2018).

[79] M. Fuest, M. Schaffer, G. M. Nocera, R. I. Galilea-Kleinsteuber, J.-E. Messling, M. Heymann, J. M. Plitzko, and T. P. Burg, *In situ Microfluidic Cryofixation for Cryo Focused Ion Beam Milling and Cryo Electron Tomography,* Scientific Reports **9**, 19133 (2019).

[80] S. Stallinga and B. Rieger, *Accuracy of the Gaussian Point Spread Function model in 2D localization microscopy,* Optics Express **18**, 24461 (2010).

[81] A. P. Bartko and R. M. Dickson, *Three-dimensional orientations of polymer-bound single molecules,* Journal of Physical Chemistry B **103**, 3055 (1999).

[82] M. Böhmer and J. Enderlein, *Orientation imaging of single molecules by wide-field epifluorescence microscopy,* Journal of the Optical Society of America B **20**, 554 (2003).

[83] J. Engelhardt, J. Keller, P. Hoyer, M. Reuss, T. Staudt, and S. W. Hell, *Molecular orientation affects localization accuracy in superresolution far-field fluorescence microscopy,* Nano Letters **11**, 209 (2011).

[84] T. Ha, T. A. Laurence, D. S. Chemla, and S. Weiss, *Polarization spectroscopy of single fluorescent molecules,* Journal of Physical Chemistry B **103**, 6839 (1999).

[85] E. J. Peterman, H. Sosa, L. S. Goldstein, and W. E. Moerner, *Polarized fluorescence microscopy of individual and many kinesin motors bound to axonemal microtubules,* Biophysical Journal **81**, 2851 (2001).

[86] A. S. Backer, M. Y. Lee, and W. E. Moerner, *Enhanced DNA imaging using super-resolution microscopy and simultaneous single-molecule orientation measurements,* Optica **3**, 659 (2016).

[87] A. I. Chizhik, A. M. Chizhik, A. Huss, R. Jäger, and A. J. Meixner, *Nanoscale probing of dielectric interfaces with single-molecule excitation patterns and radially polarized illumination,* Journal of Physical Chemistry Letters **2**, 2152 (2011).

[88] N. Karedla, S. C. Stein, D. Hähnel, I. Gregor, A. Chizhik, and J. Enderlein, *Simultaneous Measurement of the Three-Dimensional Orientation of Excitation and Emission Dipoles,* Physical Review Letters **115**, 173002 (2015).

[89] G. Donnert, J. Keller, R. Medda, M. A. Andrei, S. O. Rizzoli, R. Lührmann, R. Jahn, C. Eggeling, and S. W. Hell, *Macromolecular-scale resolution in biological fluorescence microscopy,* Proceedings of the National Academy of Sciences of the United States of America **103**, 11440 (2006).

2

Photon yield enhancement of red fluorophores at cryogenic temperatures

Single Molecule Localization Microscopy has become one of the most successful and widely applied methods of Super-resolution Fluorescence Microscopy. Its achievable resolution strongly depends on the number of detectable photons from a single molecule until photobleaching. By cooling a sample from room temperature down to liquid nitrogen temperatures, the photostability of dyes can be enhanced by more than 100 *fold, which results in an improvement in localization precision greater than* 10 *times. Here, we investigate a variety of fluorescent dyes in the red spectral region, and we find an average photon yield between* $3.5\cdot10^6$ *to* $11\cdot10^6$ *photons before bleaching at liquid nitrogen temperatures, corresponding to a theoretical localization precision around* 0.1 *nm.*

Parts of this chapter have been published as: **C.N. Hulleman**, W. Li, I. Gregor, B. Rieger, and J. Enderlein, *Photon Yield Enhancement of Red Fluorophores at Cryogenic Temperatures*, ChemPhysChem **19**, 1774-1780 (2018).

2.1. Introduction

The last 25 years have seen a revolution in optical far field microscopy, in particular due to the invention of super-resolution methods such as STED, PALM and STORM [1]. Especially the two latter methods, which are methods of the class of Single-Molecule Localization Microscopy (SMLM), now routinely achieve image resolutions of 10-20 nm [2, 3]. The attainable localization precision of SMLM is ultimately limited by the amount of detected photons until bleaching (or photoswitching), and follows the generic law

$$\sigma_{loc} = \frac{\sigma_{psf}}{\sqrt{N}} \approx \frac{0.25\lambda}{\mathrm{NA}\sqrt{N}}, \tag{2.1}$$

where λ is the emission wavelength, NA the numerical aperture of the objective, and N is the number of detected photons [4]. More complex equations have been developed taking background and camera pixelation into account [5], but equation 2.1 represents the most favorable scenario and thus a lower limit for the attainable resolution.

As can be seen, one way to increase the achievable localization precision and thus image resolution is to increase the NA by using an oil immersion objective for example. However, another way is to increase the number of detected photons N. Thus, cooling a sample and thereby increasing the photostability of the fluorescent dye molecules can have a tremendous impact on resolution in SMLM. Cooling reduces all photochemical reaction rates and thus inhibits bleaching, thereby enabling significantly more photons to be detected from a molecule, resulting in a localization precision in the Ångström range [6, 7]. Weisenburger et al. compared the performance of dyes with an emission peak of 552-576 nm at liquid helium temperatures (4.4 K), finding an increase of one to two orders of magnitude in the number of detected photons [6]. Li et al. built a cryo-fluorescence microscope with samples contained in a liquid nitrogen cryostat and analyzed the performance of ATTO 647N, finding an increase of more than two orders of magnitude in photon yield [7]. One more advantage of cryo-fluorescence microscopy is that it offers the possibility for correlative light and electron microscopy (cryo-CLEM), adding the specificity of fluorescent labelling to the superior structural resolution of electron microscopy (cryo-EM) [8, 9].

The resolution in a super-resolution image is not solely determined by the localization precision but equally by the density of emitters [10]. In cases where one can image many instances of a biological structure, the synthesis of many of these images into one final super-super-resolution image (particle averaging) can tremendously increase the effective label density and signal-to-noise ratio. In this case, the achievable resolution is finally only determined by the single-molecule localization precision σ_{loc} [11, 12]. Here, we see the biggest possible impact that improved localization precision at cryogenic temperatures can have on resolving molecular details with Ångström resolution.

For imaging of biological samples, red fluorescent dyes are particularly interesting due to the reduced auto-fluorescence and lower scattering intensity in the red spectral region [13]. Wurm et al. investigated the performance of red fluorophores at room temperature, comparing ATTO 647N and various Abberior STAR dyes [14]. ATTO 647N and Abberior STAR635 yielded the highest brightness, though the phosphorylated dye Abberior STAR635P had the best signal-to-noise ratio (SNR) due to reduced unspecific background staining. The high brightness of ATTO 647N and contrast of Abberior STAR635P makes them also excellent candidates for cryo-fluorescence microscopy.

We present, in this chapter, experimental results for the photon yield of various red dyes at liquid nitrogen temperatures. In particular, we tested the dyes Abberior STAR635P, ATTO 647N, Alexa Fluor 647, ATTO 655, Cy5, and two Silicon-Rhodamine dyes, SiR and (Janelia Farm) JF 646. The intention is to find red dyes that offer the highest localization precision due to their increased photon yield at cryogenic temperatures.

2.2. Results and discussion

For estimating the photostability of a dye, we immobilized a sparse concentration of the dye on a quartz surface and determined how many molecules could be localized in an image over the course of time. This number exponentially decayed with increasing time due to photobleaching, and typically fits well with a bi-exponential function. Thus, at room temperature we determined values of the half life, the time required to reduce the fluorescing molecules by 50%, ranging from $t_{1/2}$ = 36 seconds for Abberior STAR635P to $t_{1/2}$ = 173 seconds for ATTO 655 (Figure 2.1a). The excitation intensity for the room temperature measurement was 240 W/cm^2. At cryogenic temperatures of ~89 K, each dye was measured at 3 different intensities, 100 W/cm^2, 240 W/cm^2, and 360 W/cm^2 (Figure 2.1b-h). The half life was 128 times longer at cryogenic temperatures for ATTO 647N at an excitation intensity of 240 W/cm^2 ($t_{1/2}$ = 111 minutes compared to $t_{1/2}$ = 52 seconds). The other dyes have a half life at cryogenic temperatures of $t_{1/2}$ = 310 minutes for JF 646, $t_{1/2}$ = 44 minutes for Alexa Fluor 647, $t_{1/2}$ = 43 minutes for Cy5, $t_{1/2}$ = 18 minutes for SiR, $t_{1/2}$ = 12 minutes for Abberior STAR635P, and $t_{1/2}$ = 10 minutes for ATTO 655, at the same excitation intensity of 240 W/cm^2. Making a direct comparison of the half life at an equal absorption rate between cryogenic and room temperature is difficult as the absorption efficiency can vary as a function of temperature. Higher excitation intensities lead to faster bleaching of the fluorescent molecules; reducing the intensity to 100 W/cm^2 decreases the bleaching rate whilst retaining a good signal-to-noise ratio in the images. The slow bleaching of JF 646, ATTO 647N, and Abberior STAR635P implies that they would be best for long-lasting cryogenic experiments.

In each image the number of detected photons from a given molecule is calculated, when summed over all the frames, the total photon yield per molecule till photobleaching is obtained (see Experimental Section for details). The photon yield distribution of ATTO 647N at room temperature at 240 W/cm^2 excitation intensity shows an exponential distribution (Figure 2.2a). Thus, we fitted these photon yield histograms with a single exponential decay function, $f(N) = A \cdot \exp(-N/\gamma)$ (a bi-exponential function only shows a marginal improvement in fit quality). Before fitting, we excluded the first bin because it can contain falsely identified weakly fluorescent signals. For ATTO 647N at room temperature, the mean photon yield from the exponential fit is $\gamma = 2.1 \pm 0.1 \cdot 10^4$ photons, the uncertainty here is the 95% confidence interval of the fit. At cryogenic temperatures of ~ 89 K, the mean photon yield increases by a factor of 240 to $\gamma = 5.1 \pm 0.5 \cdot 10^6$ photons for ATTO 647N at 240 W/cm^2 excitation intensity. The mean photon yields for all the tested dyes at cryogenic temperatures range from $\gamma = 2.9 \pm 0.8 \cdot 10^6$ for SiR to $\gamma = 6.5 \pm 0.3 \cdot 10^6$ for JF 646 at 100 W/cm^2 excitation intensity. This implies a mean theoretical localization precision of around 0.1 nm using equation 2.1 with a wavelength of $\lambda = 685$ nm and NA $= 0.7$.

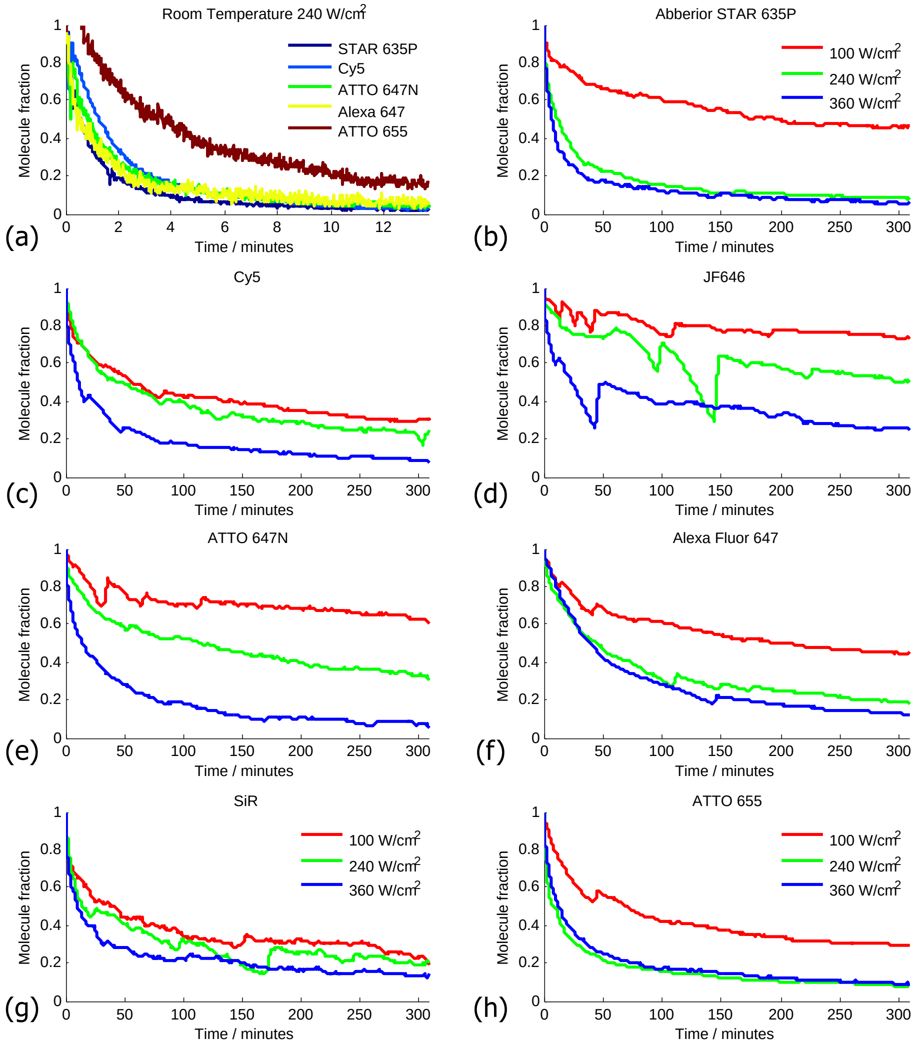

Figure 2.1: Photobleaching curves at room and cryogenic temperatures, as determined by the number of still fluorescing molecules per frame. **(a)** Room temperature measurement of Abberior STAR635P, Cy5, ATTO 647N, Alexa Fluor 647 and ATTO 655 at 240 W/cm^2 excitation intensity in the sample plane over 13 minutes. **(b)**-**(h)** Decay curves at ~89 K and 3 different intensities of 100 W/cm^2 (red), 240 W/cm^2 (green) and 360 W/cm^2 (blue) for: **(b)** Abberior STAR635P, **(c)** Cy5, **(d)** JF 646, **(e)** ATTO 647N, **(f)** Alexa Fluor 647, **(g)** SiR and **(h)** ATTO 655. Curves are smoothed with a moving average filter with a span of 200 seconds. The large jumps in the curves are due to axial drift/defocusing, which required manual refocusing while imaging over several hours. Legends for (b)-(h) are identical.

It is also possible to determine the experimental localization precision by calculating the standard deviation of the localizations over a small subset of frames and scaling this by the amount of photons captured. For Abberior star 635P at 100 W/cm^2

excitation intensity, we found an average standard deviation of 12 nm over 10 frames for 9 different molecules with an average total photon yield of $7\cdot10^6$ photons. Scaling with the ratio $\sqrt{N_{10\text{ frames}}/N_{\text{total}}}$ gives a mean localization precision of 0.3 nm, which is slightly larger than the theoretical localization precision due to mechanical drift.

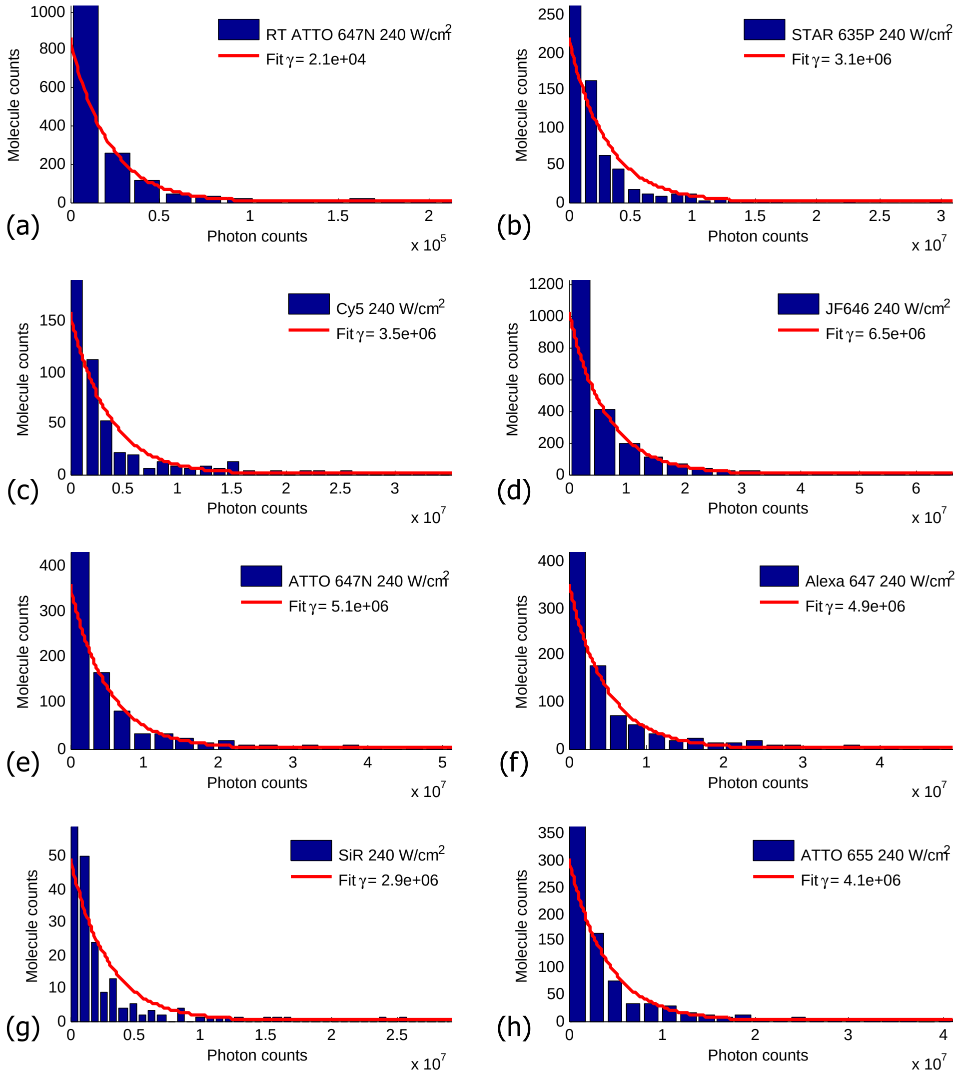

Figure 2.2: Histogram of photon counts fitted with an exponential decay. **(a)** Room temperature measurement of ATTO 647N at 240 W/cm² excitation intensity. Cryogenic measurements (~89 K) at 240 W/cm² excitation intensity for **(b)** Abberior STAR635P, **(c)** Cy5, **(d)** JF 646, **(e)** ATTO 647N, **(f)** Alexa Fluor 647, **(g)** SiR and **(h)** ATTO 655.

This implies that all tested dyes are suitable for high resolution cryogenic super-resolution microscopy, as this is already smaller than the linker length used to attach fluorescent dyes to biomolecules [15].

To better compare the results between different dyes, we corrected the measured photon yield numbers by taking into account the different overlap between a dye's emission spectrum and the transmission spectrum of the optical emission filters used in our experiment. Thus, we calculated the photon yield that one would observe if the emission filter would perfectly match the emission spectrum of a given dye. Again, we find that in most cases the photon yield γ is larger for lower excitation intensities (Figure 2.3a). The highest determined mean photon yield is $\gamma = 11.1 \pm 0.9 \cdot 10^6$ photons for the dye Abberior STAR635P at 100 W/cm^2 excitation intensity. The maximum absolute photon yield that we observed (over all detected molecules for a given dye) ranged between $7.9 \cdot 10^7$ photons for a SiR dye molecule and $3.6 \cdot 10^8$ photons for a JF 646 dye molecule.

A cumulative histogram of detected photons per molecule at 100 W/cm^2 excitation intensity shows the distribution of detectable photons till photobleaching at cryogenic conditions (Figure 2.3b). These histograms were normalized to the total molecule count (first left-hand columns in the figure) which is the sum of all molecules that were fluorescent for at least one minute after the start of the measurement.

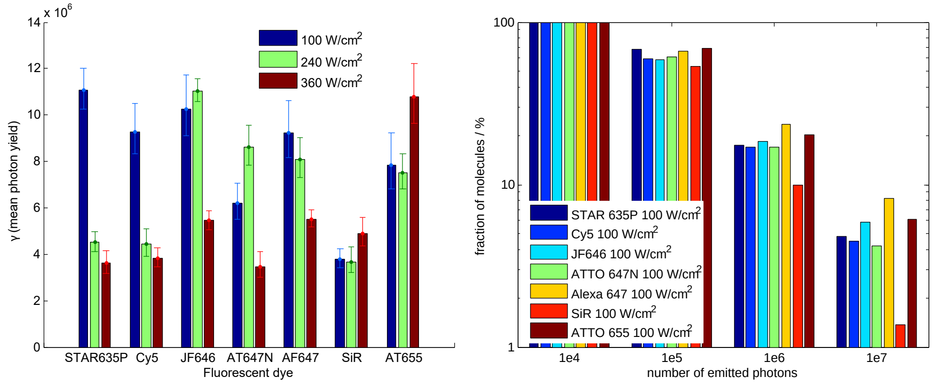

(a) (b)

Figure 2.3: **(a)** Mean photon yield γ and 95% confidence interval from the exponential fits of the photostability decay curves of 7 dyes for 3 different intensities at cryogenic temperatures (~89 K). **(b)** Cumulative histogram of the number of detected photons per molecule at 100 W/cm^2 excitation intensity and ~89 K. All molecule numbers were referenced against the number of molecules that survived the first minute of measurement time (100%, left columns in bar plot).

Finally, we can use equation 2.1 to calculate the minimal required photon yield per molecule to achieve a localisation precision of 1 nm, which is $6 \cdot 10^4$ photons for our system. Typically, for 80% of all molecules at cryogenic temperatures there were at least $6 \cdot 10^4$ detected photons for all tested dyes and different excitation intensities. The chance of finding a molecule with a localisation precision equal to or better than 0.1 nm ($\geq 6 \cdot 10^6$ photons) was found to be higher for a lower excitation intensity (100 W/cm^2) for all dyes except ATTO 655. The dyes with the highest probability of achieving ≤0.1 nm localisation precision are Alexa Fluor 647 (11.1%), ATTO 655 (14.4%), and JF 646 (8.7%). The molecules emitting these amounts of photons were fluorescing during almost the entire experiment suggesting that the photon count from these molecules could be further increased by extending the measurement time.

2.3. Conclusion

The mean photon yield of ATTO 647N (uncorrected for spectra) of $5 \cdot 10^6$ photons at 240 W/cm^2 and $3 \cdot 10^6$ photons at 360 W/cm^2 agrees well with the result found by Li et al. ($3.5 \cdot 10^6$ photons at 300 W/cm^2) [7]. The maximal photon yield at liquid nitrogen temperatures is lower than at liquid helium temperatures, with only $\sim 5\%$ of molecules with 10^7 detected photons or more compared to $> 20\%$ at liquid helium temperatures as found by Weisenburger et al. [16]. Although the photon yield is lower, liquid nitrogen is more easily suited for fluorescence microscopy as phonons are frozen out at liquid helium temperatures leading to a significant narrowing of the absorption and emission spectra [17], making efficient excitation of a fluorophore more challenging with standard laser lines.

All tested dyes show good performance for cryogenic localization, achieving an average theoretical localization precision around 0.1 nm from $3.5 \cdot 10^6$ to $11 \cdot 10^6$ photons. This is a more than hundred-fold increase in photon yield over room temperature, leading to a 10 fold increase in localization precision. An additional enhancement in localisation precision could be attained by combining cryogenic sample conditions with high NA objectives. For example with a fluid immersion lens [18, 19], or solid immersion lens [20, 21].

From this study it seems that JF 646, Alexa Fluor 647, and ATTO 655 give the highest photon yields resulting in the best localization precision. It is assumed that due to the low density, most identified molecules are indeed single-molecules, which is also corroborated by the observed single-step bleaching of almost all identified molecules.

At ~89 K we found that the mean photon yield of the best dye was 3.1 times higher than the dye with the lowest mean photon yield. This means that there is a difference factor of 1.8 ($= \sqrt{3.1}$) between the localization precision of the tested dyes. However, photon yield at cryogenic temperatures is not the only factor to be taken into consideration for dye selection. Other important factors are ease of biological labelling, solubility, cell permeability, net charge, extinction coefficient, stability, and non-specific staining.

The enhanced localisation precision at cryogenic temperatures can push SMLM towards high resolution imaging of nanoscale structures such as: synapses [22], genomic substructures, DNA/RNA interactions, protein complex conformations [23], and other small-medium sized biomolecules [15]. Cryogenic SMLM can not only bridge the resolution gap between electron microscopy and fluorescence microscopy but also allow for seamless imaging workflow between first LM and then EM while persevering the sample cryogenic state. In particular LM can add specificity to the

”gray” EM images and can help to easier guide and interpret the molecular composition of larger complexes.

This study has only addressed photon yield and its impact on localization of single molecules. To perform super-resolution measurements on biological samples, it is still necessary to induce sparsity so that individual molecules can be localized. One obvious way to do that would be to use PALM or dSTORM. All the dyes that were studied here did not show significant photoswitching which could be used for dSTORM (ATTO 647N, Alexa 647 and Cy5 have previously been shown to have a 10 times slower blinking rate at cryogenic conditions [24]). Also, we did not see any photoactivation of PA-JF 646 [25] at cryogenic conditions, although this dye shows excellent photoactivation at room temperature. Photoswitching could be possible at cryogenic temperatures as some dyes stochastically switch between on and off states under certain conditions. For example Weisenburger et al. [15] was able to distinguish 4/16 intensity levels from 2/4 ATTO 647N molecules respectively. Also ATTO 488 and Alexa Fluor 488 do show stochastic photoswitching in vacuum at cryogenic temperatures [24].

Thus, besides for maximum photon yield, future work has also to screen for photoswitching ability at cryogenic temperatures. Besides organic dyes, promising candidates might be fluorescent proteins. For example, it is known that the fluorescent protein PA-GFP can be activated under cryogenic conditions [9], indicating that cryo-PALM may be feasible using this protein. Another method could be to induce sparsity by using polarization-dependent excitation and stimulated emission depletion [23, 26], although this will require a much more demanding experimental setup.

2.4. Experimental section

2.4.1. Cryostat

The microscope used in this study is built solely for cryogenic Liquid Nitrogen (LN2) temperature measurements and has already been extensively described earlier [7]. Samples coated on 200 μm thick quartz cover slips are mounted in the cryostat and are imaged through a 0.5 mm thick quartz window to maintain vacuum. Quartz is used instead of glass due to its reduced autofluorescence. The sample chamber is pumped to a pressure $\leq 1.6 \cdot 10^{-5}$ mbar. The cryostat is filled with LN2 and the temperature is left to stabilize for one hour. Once stabilized, it is possible to measure for more than 5 hours with a temperature between 89-93 K and a typical temperature change of 0.1 K/hour.

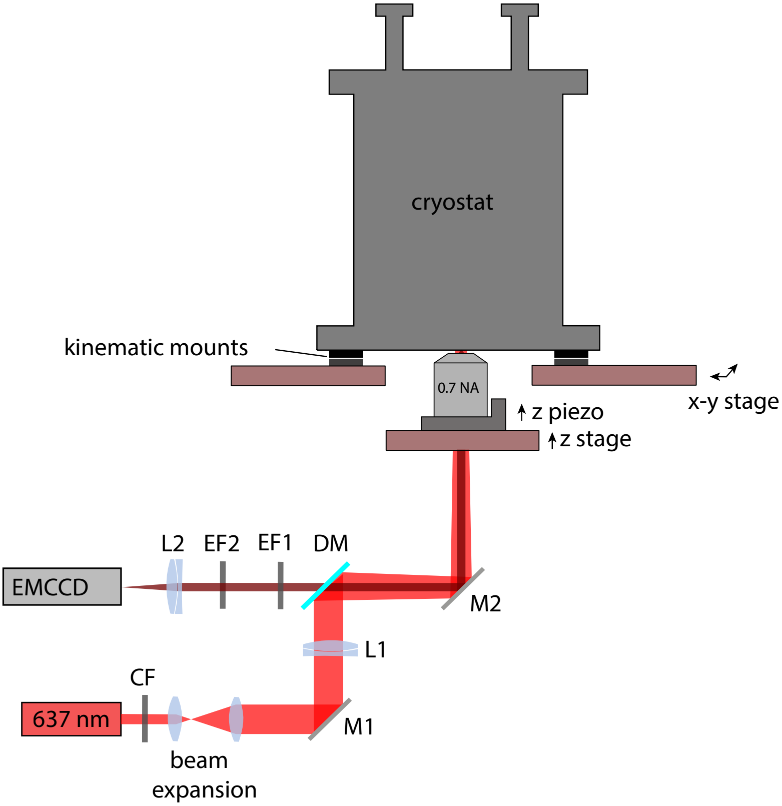

Figure 2.4: Cryo-fluorescence microscope with the sample mounted in the vacuum environment of the cryostat. Imaging is done with a long working distance 0.7NA objective onto an EMCCD camera. The excitation laser is focused onto the back focal plane of the objective and illuminates the field of view of the camera.

2.4.2. Fluorescence microscope

The whole cryostat is mounted on a motorized x-y stage, and the objective (LUCPLFLN 60x/0.7NA, Olympus) is mounted on both a motorized z stage and a piezo z-stage (PIFOC, PI). The excitation and emission path is that of a typical epi-fluorescence microscope (Figure 2.4). The red 637 nm continuous wave excitation laser (OEM-SD-637-500, CNI) is filtered by a clean-up filter CF (HC 640/14, Semrock), expanded by a telescope (Plano convex f=30 mm, f=100 mm, Thorlabs), and focused onto the back focal plane of the objective by lens L1. The dichroic mirror DM (Di01-R405/488/532/635, Semrock) reflects the excitation laser and transmits the fluorescence from the sample. The fluorescence is filtered by two emission filters EF1 (FF01-446/510/581/703, Semrock) and EF2 (ET 685/50, Chroma) and focused by lens L2 (AC508-180-A-ML, Thorlabs) onto an EMCCD camera (Ixon Ultra 897, Andor). Excitation intensities are estimated by measuring the power of the parallel beam after the objective with a power meter and dividing it by the illuminated area in the sample plane.

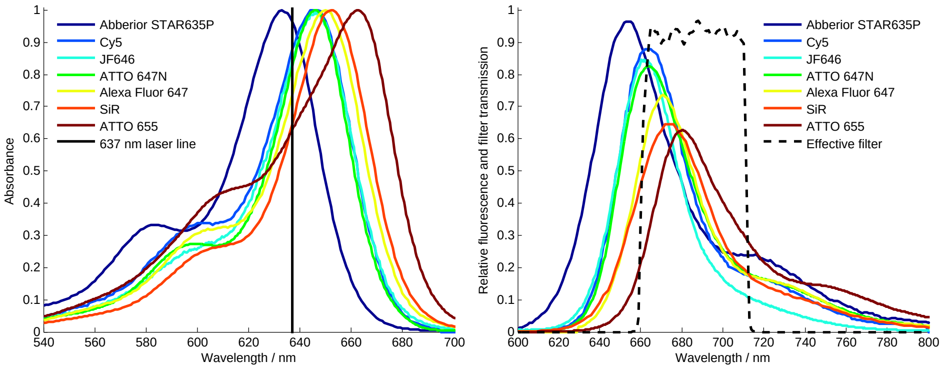

(a) Absorption spectra

(b) Effective emission spectra

Figure 2.5: Absorption and emission spectra of Abberior STAR635P, Cy5, JF 646, ATTO 647N, Alexa Fluor 647, SiR and ATTO 655. The emission spectra are normalized with excitation at 637 nm. The effective filter is the combined action of the dichroic mirror, quad-band filter and ET685/50 bandpass filter.

We investigated the dyes; Abberior STAR635P, Cy5, JF 646 (spectrum from [27]), ATTO 647N, Alexa Fluor 647, SiR and ATTO 655, which have very similar excitation and emission spectra (figure 2.5). The emission spectra are scaled to their values at 637 nm excitation, and they are plotted along with the transmission curve of the emission filter combination used in our experiment (figure 2.5b). To correct for the effect of the emission filter and imperfect excitation wavelength, we up-scaled photon count numbers by the scaling factor

$$\text{scaling factor} = \frac{\int_{\text{abs}_{\text{peak}}+10\text{ nm}}^{800\text{ nm}} (\text{em. spectrum}) d\lambda}{\int_{600\text{ nm}}^{800\text{ nm}} (\text{em. spectrum}) \cdot (\text{em. filter function}) d\lambda}. \qquad (2.2)$$

In the denominator, we start the integration only 10 nm after the absorption peak to model the gradual transition between reflection and transmission of a dichroic mirror. In order to obtain the compensated photon counts, the raw photon count number is multiplied by this scaling factor for each dye. The scaling factor ranges from 1.7 for JF 646 to 2.5 for Abberior STAR635P.

2.4.3. Sample preparation

Initially, each organic dye is diluted with distilled, de-ionized and filtered water to a 100 pM concentration. 5 μL of this dilution is deposited on a quartz slide and spin-coated at 3000 RPM for 45 seconds. The quartz slide is imaged at room temperature to determine the density of molecules in the 136.5 μm × 136.5 μm field of view. We aimed at having ~400 single molecules in the field of view to balance sparsity whilst retaining enough molecules after extensive bleaching. Dye concentrations were adjusted between 25 pM and 500 pM to achieve the desired number of initial molecules. At cryogenic temperatures, the initial amount of single molecules was found to be higher, 400-1200 instead, because at room temperature many molecules would have already been bleached during focusing, thus lowering the amount of molecules. Concentrations were not compensated for this effect but kept at 200-400 localizations at room temperature to maintain consistency between measurements.

2.4.4. Image acquisition

To maximize the total amount of captured photons for each cryogenic photon yield measurement, the full time duration over which the cryostat is stable is used. In total, 18,000 frames with 1 second exposure time are recorded, resulting in 130-220 photons per molecule per frame. Each frame has a readout time of 25 ms, resulting in a total measurement of ~5 hours. All data is acquired with an EM gain of 100, and an EMCCD sensor temperature of -45 °C. Although the system is very stable, there is still a typical axial drift of 3 μm over 5 hours causing defocusing. To compensate for this, it is necessary to manually refocus the system periodically. We found that refocusing every 10 minutes during the first hour and then after every hour thereafter is sufficient.

2.4.5. Image analysis

The Analog-Digital Units (ADU) of the camera images can be converted into photons when knowing the bias b, EM gain G, and specific sensitivity s of the camera, by using the equation

$$N = (A - b)\frac{s}{G}. \tag{2.3}$$

The amplitude of the Gaussian fit to a single molecule image was used to calculate the total number of detected photons from a molecule in each frame. Recently, it has been shown that 2D Gaussian fitting can lead to a 10-30% underestimation of the photon counts [28], but we did not take this into account here. After tracking each molecule over the course of the whole measurement, the total number of detected photons per molecule was determined.

Molecule tracking was done using TrackNTrace, an open-source MATLAB framework for localizing and tracking molecules [29]. TrackNTrace identifies molecules in two steps. We used a cross-correlation for the candidate detection step, and a 2D Gaussian fitting for the refinement step. The localized molecules were tracked using a nearest neighbour approach.

The tracking procedure was applied twice, where the initial tracking is done with no frame gaps, meaning that blinking leads to new tracks. This results in reliable data to calculate the average drift from frame to frame. The data is then adjusted for this average drift and tracked again, but now frame gaps are allowed (up to the total measurement duration). This allows molecules to blink but still be identified as one and the same molecule. This method reduces the chance of identifying distinct molecules as a single molecule. Combined with the low density of molecules, we assume that almost all identified molecules are single.

References

[1] S. Hell, *Microscopy and its focal switch,* Nature Methods **6**, 24 (2009).

[2] E. Betzig, G. Patterson, R. Sougrat, O. Lindwasser, S. Olenych, J. Bonifacino, M. Davidson, J. Lippincott-Schwartz, and H. Hess, *Imaging intracellular fluorescent proteins at nanometer resolution.* Science **313**, 1642 (2006).

[3] M. Rust, M. Bates, and X. Zhuang, *Sub-diffraction-limit imaging by stochastic optical reconstruction microscopy (STORM),* Nature Methods **3**, 793 (2006).

[4] S. Stallinga and B. Rieger, *Accuracy of the Gaussian Point Spread Function model in 2D localization microscopy.* Optics Express **18**, 24461 (2010).

[5] B. Rieger and S. Stallinga, *The lateral and axial localization uncertainty in super-resolution light microscopy,* ChemPhysChem **15**, 664 (2014).

[6] S. Weisenburger, B. Jing, A. Renn, and V. Sandoghdar, *Cryogenic localization of single molecules with Angstrom precision,* SPIE NanoScience + Engineering **8815**, 88150D (2013).

[7] W. Li, S. Stein, I. Gregor, and J. Enderlein, *Ultra-stable and versatile wide-field cryo-fluorescence microscope for single-molecule localization with sub-nanometer accuracy.* Optics Express **23**, 3770 (2015).

[8] R. Kaufmann, C. Hagen, and K. Grünewald, *Fluorescence cryo-microscopy: Current challenges and prospects,* Current Opinion in Chemical Biology **20**, 86 (2014).

[9] Y.-W. Chang, S. Chen, E. Tocheva, A. Treuner-Lange, S. Löbach, L. Søgaard-Andersen, and G. Jensen, *Correlated cryogenic photoactivated localization microscopy and cryo-electron tomography,* Nature Methods **11**, 737 (2014).

[10] R. Nieuwenhuizen, K. Lidke, M. Bates, D. Puig, D. Grünwald, S. Stallinga, and B. Rieger, *Measuring image resolution in optical nanoscopy,* Nature Methods **10**, 557 (2013).

[11] A. Löschberger, S. van de Linde, M.-C. Dabauvalle, B. Rieger, M. Heilemann, G. Krohne, and M. Sauer, *Super-resolution imaging visualizes the eightfold symmetry of gp210 proteins around the nuclear pore complex and resolves the central channel with nanometer resolution,* Journal of Cell Science **125**, 570 (2012).

[12] J. Broeken, H. Johnson, D. S. Lidke, S. Liu, R. P. J. Nieuwenhuizen, S. Stallinga, K. A. Lidke, and B. Rieger, *Resolution improvement by 3d particle averaging in localization microscopy,* Methods and Applications in Fluorescence **3**, 014003 (2015).

[13] J. Berlier, A. Rothe, G. Buller, and J. Bradford, *Quantitative comparison of long-wavelength Alexa Fluor dyes to Cy dyes: fluorescence of the dyes and their bioconjugates,* The Journal of Histochemistry & Cytochemistry **51**, 1699 (2003).

[14] C. Wurm, K. Kolmakov, F. Göttfert, H. Ta, M. Bossi, H. Schill, S. Berning, S. Jakobs, G. Donnert, V. Belov, and S. Hell, *Novel red fluorophores with superior performance in STED microscopy,* Optical Nanoscopy **1**, 7 (2012).

[15] S. Weisenburger, D. Boening, B. Schomburg, K. Giller, S. Becker, C. Griesinger, and V. Sandoghdar, *Cryogenic optical localization provides 3D protein structure data with Angstrom resolution,* Nature Methods **14**, 141 (2017).

[16] S. Weisenburger, B. Jing, D. Hänni, L. Reymond, B. Schuler, A. Renn, and V. Sandoghdar, *Cryogenic colocalization microscopy for nanometer-distance measurements,* ChemPhysChem **15**, 763 (2014).

[17] W. E. Moerner and M. Orrit, *Illuminating single molecules in condensed matter,* Science **283**, 1670 (1999).

[18] M. Le Gros, G. Mcdermott, M. Uchida, C. Knoechel, and C. Larabell, *High-aperture cryogenic light microscopy,* Journal of Microscopy **235**, 1 (2009).

[19] M. Metzger, A. Konrad, S. Skandary, I. Ashraf, A. J. Meixner, and M. Brecht, *Resolution enhancement for low-temperature scanning microscopy by cryo-immersion,* Opt. Express **24**, 13023 (2016).

[20] L. Wang, M. C. Pitter, and M. G. Somekh, *Wide-field high-resolution solid immersion fluorescence microscopy applying an aplanatic solid immersion lens,* Appl. Opt. **49**, 6160 (2010).

[21] D. Wildanger, B. R. Patton, H. Schill, L. Marseglia, J. P. Hadden, S. Knauer, A. Schönle, J. G. Rarity, J. L. O'Brien, S. W. Hell, and J. M. Smith, *Solid immersion facilitates fluorescence microscopy with nanometer resolution and sub-Ångström emitter localization,* Advanced Materials **24**, OP309 (2012).

[22] M. Sauer and M. Heilemann, *Single-molecule localization microscopy in eukaryotes,* Chemical Reviews **117**, 7478 (2017).

[23] C. N. Hulleman, M. Huisman, R. J. Moerland, D. Grünwald, S. Stallinga, and B. Rieger, *Fluorescence polarization control for on–off switching of single molecules at cryogenic temperatures,* Small Methods **2**, 1700323 (2018).

[24] W. Li, *Single Molecule Cryo-Fluorescence Microscopy*, Ph.D. thesis, Georg-August-Universität Göttingen (2016).

[25] J. Grimm, B. English, H. Choi, A. Muthusamy, B. Mehl, P. Dong, T. Brown, J. Lippincott-Schwartz, Z. Liu, T. Lionnet, and L. Lavis, *Bright photoactivatable fluorophores for single-molecule imaging,* Nature Methods **13**, 985 (2016).

[26] N. Hafi, M. Grunwald, L. van den Heuvel, T. Aspelmeier, J.-H. Chen, M. Zagrebelsky, O. Schütte, C. Steinem, M. Korte, A. Munk, and P. Walla, *Fluorescence nanoscopy by polarization modulation and polarization angle narrowing,* Nature Methods **11**, 579 (2014).

[27] J. Grimm, A. Muthusamy, Y. Liang, T. Brown, W. Lemon, R. Patel, R. Lu, J. Macklin, P. Keller, N. Ji, and L. Lavis, *A general method to fine-tune fluorophores for live-cell and in vivo imaging,* Nature Methods **14**, 987 (2017).

[28] R. Ø. Thorsen, C. N. Hulleman, S. Stallinga, and B. Rieger, *Signal photon count estimation in single molecule localization microscopy,* in *Quantitative BioImaging Conference (QBI)* (Göttingen, Germany, January 4-6, 2018).

[29] S. Stein and J. Thiart, *TrackNTrace: A simple and extendable open-source framework for developing single-molecule localization and tracking algorithms,* Scientific Reports **6**, 37947 (2016).

3

Fluorescence polarization control for on–off switching of single molecules at cryogenic temperatures

Light microscopy, allowing sub-diffraction-limited resolution, has been among the fastest developing techniques at the interface of biology, chemistry, and physics. Intriguingly no theoretical limit exists on how far the underlying measurement uncertainty can be lowered. In particular data fusion of large amounts of images can reduce the measurement error to match the resolution of structural methods like cryo-electron microscopy. Fluorescence, although reliant on a reporter molecule and therefore not the first choice to obtain ultraresolution structures, brings highly specific labeling of molecules in a large assembly to the table and inherently allows the detection of multiple colors, which enables the interrogation of multiple molecular species at the same time in the same sample. In this chapter we describe what polarization depletion of fluorescence at cryogenic temperatures can contribute for high-resolution fluorescence imaging of biological samples, like whole cells. A method to generate linearly polarized light in an epifluorescence microscope is presented and verified to generate very low ellipticity in the polarized light. This is a necessity to perform polarization dependent depletion of fluorescence. Furthermore a design of a cryostat with a larger volume of liquid nitrogen is presented, enabling longer imaging times at cryogenic temperatures.

Parts of this chapter have been published as: **C.N. Hulleman**, M. Huisman, R.J. Moerland, D. Grünwald, S. Stallinga, and B. Rieger, *Fluorescence Polarization Control for On–Off Switching of Single Molecules at Cryogenic Temperatures*, Small Methods **2**, 1700323 (2018).

3.1. Introduction

Over the last decade, new microscopy methods, frequently referred to as "super-resolution microscopy" or "nanoscopy," have achieved much higher resolution (∼10–50 nm) than conventional light microscopy (∼250 nm). The resolution of conventional microscopy is limited by diffraction to a length scale $\lambda/2\text{NA}$, where λ is the emission wavelength, and $\text{NA} = n\sin(\alpha)$ is the so-called numerical aperture of the objective, where n is the refractive index of the immersion medium and α is the marginal ray angle of the light beam collected by the objective. With the introduction of different nanoscopy techniques [1–4] the diffraction limit has been circumvented, giving a resolution that starts to close the resolution gap between light and electron microscopy. Where electron microscopy can reveal details below the order of a nanometer, it does not offer efficient specific labeling or multicolor imaging the way light microscopy does.

A group of techniques termed single-molecule localization microscopy (SMLM), e.g., photoactivated localization microscopy (PALM), (direct) stochastic optical reconstruction microscopy ((d)STORM), and many other flavors [2–5], has found the most widespread use, as it is relatively undemanding on the experimental setup and the subsequent image analysis. The key idea is to image and localize isolated single fluorescent molecules over many acquisitions. The ability of switching the fluorescent labels between a bright emitting "on" state and a dark nonemitting "off" state, resulting in blinking, is essential. This leads to a sparse subset of all labels in the sample being in their "on" state at any time point, which can be localized with a much higher precision than the diffraction limit [6]. This localization uncertainty is on the order of $\lambda/\left(\text{NA}\sqrt{N_{\text{ph}}}\right)$, implying that already a moderate photon count of 100–1000 results in a ten times smaller uncertainty compared to the diffraction limit. The required ratio of on/off times to image only single emitters in a region of size λ/NA is typically smaller than 1/100 to 1/1000 depending on the labeling density, exposure time, and additional parameters [7].

The image resolution, defined as the size of the smallest detail that can be reliably discerned in an image, is determined by the localization precision and the density of fluorescent labels. Previously we have introduced the concept of Fourier ring correlation (FRC) into super-resolution microscopy for taking all resolution factors into account [8]. The FRC quantifies the available image information as a function of spatial frequency, i.e., across all length scales, and points to a resolution limit via a threshold criterion. The FRC resolution in SMLM can be a value of 2π times the localization uncertainty, depending on an adequate labeling density [8], providing a resolution of down to ∼30 nm for high-photon-yield fluorophores like Alexa647 (several thousand photons, localization precision of ∼5 nm).

There are a number of emerging developments that address the limitations of labeling technologies. Advances in biophotochemistry have resulted in the development of labels that make a direct covalent bond to the target molecule, such as click-chemistry [9, 10], effectively giving a small (<1 nm) label size. Improvements of known dyes like Rhodamines have led to much brighter, more stable, and cell-permeable labels with tunable emission properties [11, 12]. Also, techniques for high labeling density [13] and the use of data-fusion techniques [14, 15] ameliorate the labeling limitations. Based upon these developments, it may be anticipated that the localization imprecision will soon become the limiting factor for resolution.

Very recently, a new breakthrough technique to further push localization imprecision was proposed, called MINFLUX [16]. In this technique a single fluorophore is illuminated by a doughnut beam a number of times (typically four times), where the position of the doughnut beam is changed from illumination to illumination across a region of size L. The number of photons per illumination is collected at a photodiode and the set of photon counts is used in a triangulation procedure to estimate the position of the molecule. Surprisingly, the localization precision scales as $L/\sqrt{N_{\mathrm{ph}}}$, independent of the diffraction length λ/NA. By choosing L on the order of 50 nm, an order of magnitude in precision can be gained compared to standard SMLM. The big drawback of this technique, however, is that the position of the molecule must be established to be within the tiny region of interest of size $L \sim 50$ nm by a prior experiment. A development road to application of MINFLUX across the full field of view of the objective does not appear to be in sight, and seems less than straightforward to devise.

The localization precision can be reduced to well below 1 nm if more than 10^6 photons are recorded. Collection of these amounts of photons is possible for uncaging dyes [17], which today have been used infrequently, in DNA PAINT approaches where an effectively endless reservoir of dyes is imaged [18], or through imaging at cryogenic temperatures [19–21]. At cryogenic temperatures, dyes have a very low rate of photobleaching and localization precisions below 1 nm are typical. For fluorescent proteins, however, freezing only offers a moderate increase in total photon count before bleaching [22]. The increased localization precision is especially beneficial for data-fusion techniques that rely on localizations to register or align different identical particles to obtain a super-super-resolved particle [15].

A challenge for data-fusion methods lies in the need for the sample to be immobilized during acquisition of individual images, but working with cells at cryogenic temperatures has the inherent advantage of fixation, while the method of vitrification by plunge freezing is considered a very fast and mild fixation technique, compared to chemical fixation at room temperature [23]. With vitrification being used for cryo-electron-microscopy (cryo-EM) sample preparation, it also allows easier integration into correlative studies [23–25].

On the downside, the traditional switching mechanism for photon emission of dyes does not work for frozen samples. Photoswitching either requires a conformational change of the fluorophore itself, such as in PALM [2], or a liquid buffer solution for chemical interaction with the fluorophores, such as in dSTORM [4]. Very inefficient photoconversion at cryogenic temperatures has been reported and used for correlative studies in transmission electron microscopy [22], but imaging of a densely labeled sample would not have been possible at such photoswitching rates. For a very small number of dyes, spontaneous blinking has successfully been used to reconstruct a 3D structure from 2D projections [20].

3.2. Fluorescence polarization control

Here, we propose the use of polarization control to establish on/off switching of fluorophores at cryogenic temperatures. At cryogenic temperatures, already in the range of liquid nitrogen, the absorption dipole axis of an individual fluorophore has a fixed orientation making it possible to tune the excitation of the fluorophores by rotating the state of polarization of the excitation beam (see Figure 3.1). The excitation efficiency scales as $\cos^2(\theta)$ with θ being the angle between the (linear) excitation polarization and the dipole axis [26]. This effect alone gives rise to an on/off ratio of one to one, which, however, is far from what is needed for producing the sparsity that is typically used in SMLM. The level of sparsity can be improved by making use of fluorescence depletion by stimulated emission, similar to stimulated emission depletion (STED) [1]. A second beam, redshifted compared to the excitation beam, and with a polarization orthogonal to the excitation beam, is used to illuminate the sample (see Figure 3.1). As a result most excited molecules are driven back to the ground state with the exception of molecules with an absorption dipole that is close to the orientation perpendicular to the polarization of the depletion beam. As a consequence, the fluorescence emission will no longer follow the original $\cos^2(\theta)$ distribution, but a much more sharply peaked distribution instead.

We can make an estimate of the improvement in sparsity by employing the analogy of the proposed method with STED. Hell [27] stated that the resolution of STED scales as

$$\frac{\lambda}{2\mathrm{NA}\sqrt{1+I_{\mathrm{dep}}/I_0}} \tag{3.1}$$

where I_{dep} is the intensity of the depletion beam and $I_0 \sim \hbar\omega/\sigma\tau$ (with $\hbar\omega$ being the photon energy, σ the cross-section, and τ the lifetime) at constant intensity. Similarly, we conjecture that the angular emission profile after depletion has a full width at half maximum (FWHM) that may be described by

$$\mathrm{FWHM} \approx \frac{\pi}{2\sqrt{1+I_{\mathrm{dep}}/I_0}} \tag{3.2}$$

resulting in a sparsity factor π/FWHM that can be much larger than 1, in principle achieving the same type of FWHM narrowing as in standard STED.

So far, we have only considered excitation and depletion polarizations and dipole orientations in the plane of the sample. This matches with the relatively low NA of objective lenses that can be used in cryogenic setups (typically up to NA = 0.7) [19, 21]. Under these conditions the polarization of the excitation and depletion beams is necessarily close to being in-plane polarized, and fluorophores with dipole orientations that are substantially tilted with respect to the sample plane are not excited and remain invisible. Possible extensions to high-NA excitation, depletion, and imaging using immersion technology, in particular a solid immersion lens, would open up possibilities for polarization control over the full 4π solid angle of polarization and dipole orientations.

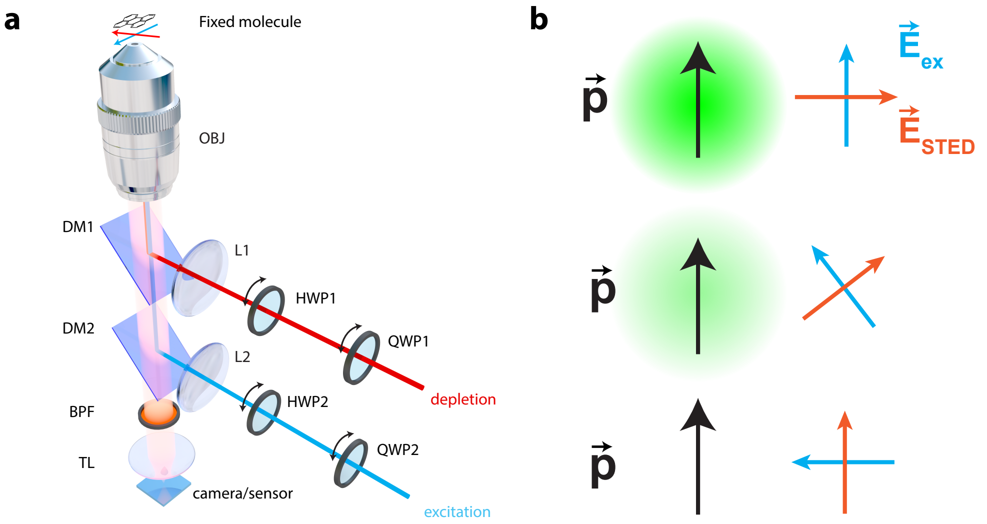

Figure 3.1: **(a)** Schematic drawing of the setup. A custom-built microscope is composed of an objective OBJ and tube lens TL. Dichroic mirrors DM1 and DM2 are used to reflect excitation and depletion laser light toward the objective, and let the fluorescence from the sample pass to the camera. A bandpass filter BPF is used to further suppress the potential leaked through laser light. Lenses L1 and L2 are used to focus the lasers on the back focal plane of the objective for epi-illumination. Full control over the polarizations of both lasers in the sample plane is obtained through the use of half-lambda (HWP1 and HWP2) and quarter-lambda wave plates (QWP1 and QWP2) for each laser path, respectively. **(b)** With the excitation laser $\vec{E}_{\text{ex}}$ parallel to the molecular transition dipole $\vec{p}$ and the depletion laser $\vec{E}_{\text{STED}}$ perpendicular, the molecule fluoresces at maximum intensity. The excitation efficiency is reduced when $\vec{p}$ is at an angle with $\vec{E}_{\text{ex}}$. Moreover, the increased inner product with $\vec{E}_{\text{STED}}$ leads to efficient depletion of the molecule and a sparsity in the sample based on angular selection of transition dipoles, compared to a case where only $\vec{E}_{\text{ex}}$ is present.

Hafi et al. already put forward the idea to use polarization as an effective way to introduce sparsity in combination with STED, similar to our setup in Figure 3.1 [28]. Later Frahm and Keller showed however that their results were, in fact, due to post-processing of the data by a sparsity-enhancing deconvolution algorithm and not based on polarization control [29]. Closer inspection of the data of Hafi et al. reveals that they reported very poor modulation depths when changing the polarization (their Figure 2) [28]. Two experimental factors might have caused these poor modulation depths, thereby impairing their results, while the conceptual idea is working, as we demonstrate below. To do so we first improved the effective polarization in the sample plane (the first experimental factor), by carefully calibrating the different optical elements in the microscope such that full modulation over the background can be seen. Second, we used fluorescent molecules fixed by spincoating in a polymer solution to have stable molecular transition dipoles (the second experimental factor).

3.3. Optimizing light polarization at the sample

We developed a method to control the polarization of excitation and STED beam at the sample plane. To this end, we calibrate the optical system to know how polarization is changed by the different components in the setup as depicted in Figure 3.1, and, in particular, we measured the effect of the retarders (half wave plate (HWP) and quarter wave plate (QWP)) instead of assuming their nominal action. In the following, we briefly introduce the concept of the Stokes vector and the Mueller matrix, which allows the description (and manipulation) of the polarization state of light. We describe the electric field of a monochromatic plane wave, traveling along the z-axis, by

$$E_x(t) = E_{0x} \cos\left(\omega t + \delta_x\right) \tag{3.3}$$

$$E_y(t) = E_{0y} \cos\left(\omega t + \delta_y\right) \tag{3.4}$$

Here, we have taken $z = 0$ for convenience, and E_{0x} and E_{0y} represent the amplitude of the electric field in the x- and y-directions, respectively. The angular frequency is given by ω, and δ_x and δ_y are the phase factors for the respective electric field components. In general, the tip of the electric field vector traces an ellipse in space for arbitrary amplitudes and phases, the polarization ellipse. It can be shown that the Stokes 4-vector $\vec{S}$ and the electric fields are related as [30]

$$\begin{pmatrix} S_0 \\ S_1 \\ S_2 \\ S_3 \end{pmatrix} = \begin{pmatrix} E_{0x}^2 + E_{0y}^2 \\ E_{0x}^2 - E_{0y}^2 \\ 2E_{0x}E_{0y}\cos\delta \\ 2E_{0x}E_{0y}\sin\delta \end{pmatrix} \tag{3.5}$$

with $\delta = \delta_y - \delta_x$. The first stokes parameter S_0 describes the total intensity of the light. Of the remaining parameters, S_1 describes the amount of horizontally or vertically polarized light, S_2 the amount of diagonally polarized light (±45°), and S_3 the amount of left/right-handed circularly polarized light. The 4×4 Mueller matrix M transforms two Stokes vectors $\vec{S}_{out} = \mathrm{M}\vec{S}_{in}$ and describes how the polarization state is changed by an optical system. Once the Mueller matrix of a system has been determined, the required input polarization state in order to get a desired output polarization state can be retrieved via M^{-1}. Here, we have used a dual rotating retarder polarimeter [31], which consists of a polarizer, a QWP, the system under test, a second QWP, and an analyzer. The two QWPs are rotated simultaneously but with a 5:1 ratio, which gives the 16 elements of M after Fourier analysis of the resulting intensity signal for different angles. With the free-space requirement that M is the identity matrix we can calibrate the polarimeter [32] and the orientation and retardance of the retarders. In our implementation, the QWPs (AQWP05M-600, Thorlabs) are rotated with computer-controlled rotation stages (8MPR16-1, Standa). The polarizers are of the GL10 type (Thorlabs) with an anti-reflection coating suitable for the wavelength used.

In order to measure $\vec{S}_{\mathrm{in}}$ and $\vec{S}_{\mathrm{out}}$, we use a Stokes polarimeter [30] composed of a rotating QWP (AQWP05M-600, Thorlabs) and a polarizer (GL10, Thorlabs). Here, the retarding wave plate is rotated with a computer-controlled stage (8MPR16-1, Standa) as well. The laser light running through the system is modulated with the aid of an optical chopper wheel (MC2000-EC, Thorlabs) and detected with a silicon photodiode (DET10A, Thorlabs), after focusing with an additional lens (LB1901-B, Thorlabs). A lock-in amplifier (SR830, Stanford Research Systems) is used to demodulate the detector signal. Both types of setup are computer-controlled from within MATLAB (The MathWorks). Thus, with the combination of a Stokes and a Mueller polarimeter, we can fully determine the polarization transfer function of our microscope (see Figure 3.1a) and the polarization state of the light itself in the sample plane.

3.4. Results of polarization control

In order to evaluate our calibration procedure over naive usage of the nominal action of the retarders, we measured Stokes vectors for both setups (see Figure 3.2a–c). Without DM1 and QWP2 present (see Figure 3.1a), we insert 638 nm linearly polarized laser light into the excitation path (LDH-D-C-640, PicoQuant), where the initial linear polarization is generated with a Glan- Laser calcite polarizer (GL10, Thorlabs). First, we naively try to rotate the polarization by rotating an achromatic half-wave retarder (AHWP05M-600, Thorlabs) in steps of 5° and measure the polarization state at the sample plane with Stokes vector polarimetry (compare the red solid lines in Figure 3.2a–c). In the coordinate system of the microscope, a horizontal polarization, corresponding to $\vec{S} = (1{,}1{,}0{,}0)$, is identical to s-polarized light hitting the dichroic mirror DM2 (FF652-Di01, Semrock). This corresponds to $\alpha = 0°$ in Figure 3.2. Vertically polarized light is identical to $\vec{S} = (1, -1, 0, 0)$ and corresponds to $\alpha = 90°$. From Figure 3.2a–c we see that these two linear polarizations are well defined with normalized $\vec{S} = (1, 0.981, 0.013, 0.023) \pm (0, 2, 1, 1) \times 10^{-3}$ (1σ) at $\alpha = 0°$ and $\vec{S} = (1, -0.995, -0.093, -0.005) \pm (0, 0.3, 2, 2) \times 10^{-3}$ at $\alpha = 90°$. However, for the diagonal polarizations at $\alpha = 45°$ and $\alpha = 135°$, corresponding to $\vec{S} = (1, 0, \pm 1, 0)$, it is obvious that S_2 is far from (minus) unity, and in fact S_3 is near (minus) unity. Therefore, in the straightforward implementation, polarizations deviating from horizontal and vertical are increasingly elliptically polarized, even approaching circularity.

Next, we calibrate our Mueller polarimeter and measure the Mueller matrix of the excitation path by the method described elsewhere [32]. In this case, we do not insert HWP2 and QWP2 into the path. Therefore, we obtain the Mueller matrix of the combination of the dichroic mirror DM2, lens L2 (LA1433-633, Thorlabs) and the objective (Plan Apo VC 100×/1.40, Nikon), as well as a measurement of the retardances of the used QWPs. Here, we used QWP2 as part of the Mueller polarimeter, thus obtaining the actual retardance. Furthermore, we determine the retardance of HWP2 by the method described by Goldstein [30]. The total polarization transfer function of the excitation light is then $\mathrm{M}_{\mathrm{tot}} = \mathrm{M}_{\mathrm{mic}}\mathrm{M}_{\mathrm{HWP2}}\mathrm{M}_{\mathrm{QWP2}}$, where $\mathrm{M}_{\mathrm{QWP2}}$ and $\mathrm{M}_{\mathrm{HWP2}}$ are the Mueller matrices of the wave plates, and $\mathrm{M}_{\mathrm{mic}}$ is the Mueller matrix of DM2 with the objective. By this procedure we are able to predict the Stokes vector, and hence the polarization, of the light moving through the excitation branch including HWP2 and QWP2. Moreover, we can predict the angles of the retarders that are necessary to obtain any required polarization state in the sample plane. We use this possibility to compensate the error in polarization, induced by DM2 and the objective, in order to obtain linearly polarized light in the sample plane (compare the blue solid lines in

Figure 3.2a–c). From visual inspection, it is clear that over the whole range of linear polarizations, the ellipticity is strongly reduced (compare the blue and red lines in Figure 3.2c).

We focus our attention on the diagonal polarizations, which are problematic without correction. For $\alpha = 45°$, $\vec{S} = (1, 0.015, -0.976, -0.015) \pm (0, 2, 2, 2) \times 10^{-3}$ and for $\alpha = 135°$, $\vec{S} = (1, 0.025, 0.989, -0.029) \pm (0, 2, 3, 1) \times 10^{-3}$, after calibration. The linearity of the polarization at these angles therefore is vastly improved. We see in Figure 3.2c that there is still some residual ellipticity with the Mueller-matrix-based compensation method. We therefore add a numerical optimization algorithm, which searches for the optimal wave plate angles to minimize S_3. The cost function returns the error between the ideal and the measured Stokes vector components

$$\text{err} = |S_1 - S_{1m}| + |S_2 - S_{2m}| + 10\,|S_3 - S_{3m}| \tag{3.6}$$

where we emphasize the error in S_3, the component which leads to ellipticity. For each angle α, the optimization is run (compare the green solid lines in Figure 3.2a–c). Ideally, in all cases S_3 is identical to zero. Visibly, S_3 is closer to zero throughout the range of α after optimization. The root-meansquare error for the different schemes in Figure 3.2c shows a substantial improvement from 0.66 (naive rotation of HWP2: red), 0.04 (Mueller matrix: blue), and 0.01 (optimized: green).

Figure 3.2d shows the S_3 component of a Stokes vector measurement of just an HWP (AHWP05M-980, Thorlabs, dashed red line) with the depletion laser (Mai Tai HP 750 nm, Spectra-Physics). When compared to the case that the DM1 (FF697-SDi01, Semrock) is installed in the depletion path (red solid line), the dramatic effect of the dichroic mirror (DM) on the ellipticity of the polarization is clearly visible. We obtained an optimized DM for the depletion path from Chroma, not only for a high reflectivity of the laser, but also for a minimal phase difference between the s and p-components, which indeed has nearly no influence on the ellipticity of the beam (cf. the measured blue curve), and merely changes the circular component, induced by the HWP, in handedness. An additional optimization step as described above essentially eliminates this part (green curve).

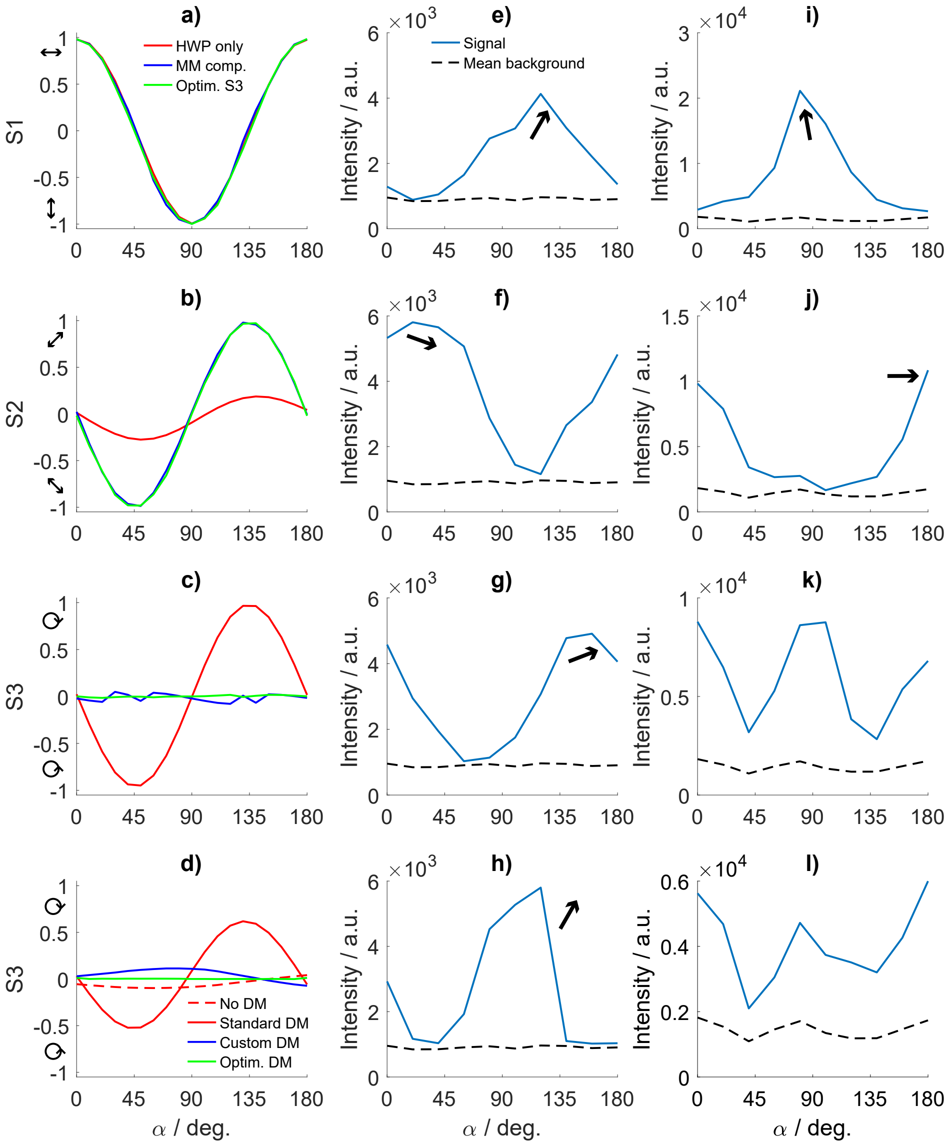

Figure 3.2: **(a)**-**(c)** Normalized Stokes vector components S1, S2, and S3 for the dichroic mirror used for excitation as a function of α, the desired polarization orientation angle. Rotating only an HWP yields the red curve. Using calculated orientations of the QWP and HWP based on the measured Mueller matrix yields the blue curve. Optimizing the orientation of the wave plates based on the resulting Stokes vector yields the green curve. **(d)** Normalized S3 Stokes vector component for the standard and custom dichroic mirror for the depletion path. The dashed red curve is a direct measurement of a rotating HWP only. **(e)**-**(h)** Mean intensity of single molecule emitters using the optimized QWP and HWP orientations, the black arrows depict the estimated molecule's transition orientation. **(i)**-**(l)** Mean intensity fluctuation of single-molecule emitters during rotation of only an HWP; again the black arrows indicate estimated molecular transition dipole orientations.

We now turn to single-molecule fluorescence measurements of fixed dyes (at room temperature) as a function of polarization to investigate the performance of our calibration above. We apply and compare the naive polarization rotation scheme and the calibrated, optimized scheme. For each angle α, we obtain a fluorescence image with the aid of an EMCCD camera (Ixon Ultra 888, Andor), with an exposure time of 1 s, an EM gain of 25, and a sensor temperature of −60 °C. In order to prepare the samples, a stock solution of ATTO 647N (ATTO-TEC) was diluted to a final concentration of 2.8×10^{-10} M in demineralized water, mixed with 0.5 wt% of poly(vinyl alcohol) (PVA). Spin-coating this solution at 3000 rpm for 1 min onto cleaned cover slips resulted in samples of single molecules with a randomly fixed dipole transition moment. Figure 3.2e–h shows the mean fluorescence intensity of a selection of four molecules for the optimized polarization rotation scheme (blue solid lines). The background (black dashed lines) has been determined as the average of five locations without any molecules. The black arrows serve as an illustration of the in-plane dipole moment of each molecule, based on the phase of the intensity modulation. Figure 3.2i–l shows the results for the naive implementation on four other molecules. Here, we clearly see the improvement of our calibration procedure. For (near) horizontal and vertical dipole orientations, the modulation depth is comparable in both cases (nearly 100%), as for these polarizations, the DM hardly alters the polarization. However, for diagonal transition dipole moments, the calibration approach remains near a 100% modulation depth, highlighting the superiority of our scheme, in contrast to the naive implementation where the near-circular quality of the polarization at the relevant angles α results in a strong electric field component along the dipole transition moment.

3.5. Cryostat design

Among the various methods to boost the number of available photons, cooling of the sample to cryogenic temperatures, which also fixes the dipole moments of all emitters in the sample, is ideally suited for the use of polarization STED to enable high-density labeling while maintaining emitter sparsity. However, the use of an STED beam adds a heat load not typically present in imaging at cryogenic temperatures. A very powerful cryostat design, enabling fluorescence cryo-microscopy (cryoFM) on practically any microscope platform, was presented by Li et al. [21] Adding an additional heat source to cryoFM raises the question as to what can be done to improve the cooling capacity of such a cryostat, both with respect to transferring heat from the sample and maintaining imaging duration upward of 5 h.

Different methods have been suggested to increase the cooling capacity to the sample. The modularity of the Li cryostat is of high practical value as it demands a minimum of modifications to the microscope platform, arguing to focus on increasing the tank volume, raising questions as to how to best scale the size of the heat exchange interface in the cryostat (see Figure 1 in Li et al. [21]) while maintaining the structural stability of the original design. We used finite-element simulations to optimize the cooling capacity and mechanical stability. Simulations were done in Solidworks Simulation (Premium package, Dassault Systems) using a curvature-based solid mesh with four Jacobian points and element sizes between 1 and 20 mm.

For thermal simulations about 433 000 nodes, forming roughly 270 000 elements, with a maximum aspect ratio of ~200 (>90% of elements had a ratio of <3 and less than 0.5% of elements had a ratio of >10) were used. For frequency simulations, finding the first five natural frequencies and their amplitude at resonance, about 170 000 nodes, forming >100 000 elements, with a maximum aspect ratio of ~48 (>89% of elements had a ratio of <3 and less than 0.6% of elements had a ratio of >10) were used. The goals for a cryostat with an increased cooling capacity (see Figure 3.3) are to better tolerate the use of additional external heat sources, like a STED beam, possibly increase the duration of the cooling cycle to allow for longer observation times, and maintain cooling temperatures suitable for cryoFM using liquid nitrogen while maintaining maximum vibration damping.

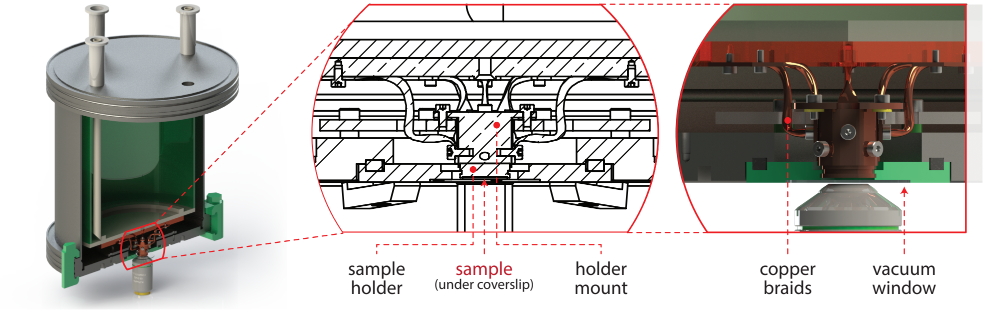

Figure 3.3: Improved cryostat design for cryo-fluorescence microscopy. The model depicted here features three main improvements over the design by Li et al.: [21] (1) a 2 × larger liquid nitrogen tank for long-term super-resolution imaging, (2) four additional copper braids between the holder mount and the heat dissipater to allow more heat flux and increase cooling capacity, and (3) vibrational-mode optimization to maximize damping and minimize drift while maintaining thermal insulation. These improvements make the new design more suitable for cryo-polarization STED imaging.

By increasing the number of vibrationally decoupling thermal conductivity braids between the holder mount and the heat dissipater at the bottom of the nitrogen tank (Figure 3.3), the maximum heat flux is effectively doubled. We increased the size of the tank by a factor of two, allowing approximately double the original cold measurement time at traditional operation. The sample holder can still be dismounted from its magnetic base through a replaceable vacuum window, and the sample is mounted to the sample holder with a magnet and stainless steel ring. The dimensions of the parts that suspend the holder mount in vacuum were optimized to increase thermal insulation and effectively dampen low-frequency oscillations, pushing the predicted resonance modes well into the kilohertz range. Specifically, we analyzed the impact of additional mounting points for the holder mount. We found that, depending on the number of spacer rings, an increase of mounting holes from 4 to 8 will result in a 2 K temperature increase at the sample holder, while causing 32 K higher temperatures at the cooling disk. As to be expected, a higher number of mounting points yield higher resonance frequencies. Differences in the first three modes (along the x, y, and z-directions) were <30% with resonance frequencies in the range of 1900 Hz (x, y) and 2600 Hz (z) if eight mounting points were used, and 1400 Hz (x, y) and 1900

Hz (z) if four mounting points were used. The fourth and fifth modes showed differences below 1% and were in the range of 2500 Hz. Interestingly, the shape of the spacers used (strips vs rings) was shown to be in favor of rings (yielding >20% differences in heat conductivity, roughly scaling with surface-area differences). Taken together, optimization of the cooling capacity of a closed cryostat as described by Li et al. [21] should use fewer mounting holes as the stability improvements lie in a frequency range well above 1 kHz, but increased numbers of mounting holes increase heat flow substantially. While the effective heat load on the cryostat introduced by an STED beam is currently unknown, our simulations indicate no downside to increasing the thermal coupling of the sample holder by increasing the number of copper braids between the holder mount and the heat dissipater.

While cooling performance and the resulting imaging time remain to be assessed for STED experiments (investigated on a further improved cryostat design in chapter 4). The design presented here should be capable of dissipating a substantial part, if not all, of the heat added by a depletion beam. Sensors that accurately register the temperature cooling stages within the cryostat can be used to examine the performance during experiments, as well as to provide an estimate of the amount of energy deposited into the sample by an external source.

3.6. Outlook and conclusion

Minimizing the localization uncertainty and reducing the overall measurement error could lead to FRC resolution values below or in the range of the size of an individual emitter. While new measurement modalities like MINFLUX show the way to improve localization uncertainty at low photon count, increasing the photon budget by means of improved labels or cooling of the sample is already possible today. The power of data fusion to reduce the measurement error has been demonstrated by resolving structural details of nuclear pore complexes in cells using SMLM style imaging [14]. We showed that by using Stokes and Mueller polarimetry, we were able to measure and improve the effective polarization in the sample plane. We considered design limitations to increase heat flow and cooling capacity of a modular cryostat to account for the additional heat load of an STED beam in cryoFM and argue that our measurements of the effective polarization depletion in the sample plane are the missing element to achieve nanometer-ranged FRC resolution in SMLM.

Combining single-emitter-resolution localization microscopy with biological tools (i.e., CRISPR and its derivatives) to unequivocally label specific proteins inside cells would allow the visualization of structures that have never been directly seen before such as genomic substructures, DNA/RNA interactions, and protein complex conformations.

References

[1] S. W. Hell and J. Wichmann, *Breaking the diffraction resolution limit by stimulated emission: stimulated-emission-depletion fluorescence microscopy,* Optics Letters **19**, 780 (1994).

[2] E. Betzig, G. H. Patterson, R. Sougrat, O. W. Lindwasser, S. Olenych, J. S. Bonifacino, M. W. Davidson, J. Lippincott-Schwartz, and H. F. Hess, *Imaging intracellular fluorescent proteins at nanometer resolution,* Science **313**, 1642 (2006).

[3] M. J. Rust, M. Bates, and X. Zhuang, *Sub-diffraction-limit imaging by stochastic optical reconstruction microscopy (STORM),* Nature Methods **3**, 793 (2006).

[4] M. Heilemann, S. Van De Linde, M. Schüttpelz, R. Kasper, B. Seefeldt, A. Mukherjee, P. Tinnefeld, and M. Sauer, *Subdiffraction-resolution fluorescence imaging with conventional fluorescent probes,* Angewandte Chemie - International Edition **47**, 6172 (2008).

[5] T. Klein, S. Proppert, and M. Sauer, *Eight years of single-molecule localization microscopy,* Histochemistry and Cell Biology **141**, 561 (2014).

[6] R. J. Ober, S. Ram, and E. S. Ward, *Localization Accuracy in Single-Molecule Microscopy,* Biophysical Journal **86**, 1185 (2004).

[7] A. R. Small, *Theoretical Limits on Errors and Acquisition Rates in Localizing Switchable Fluorophores,* Biophysical Journal **96**, L16 (2009).

[8] R. P. J. Nieuwenhuizen, K. A. Lidke, M. Bates, D. L. Puig, D. Grünwald, S. Stallinga, and B. Rieger, *Measuring image resolution in optical nanoscopy,* Nature Methods **10**, 557 (2013).

[9] P. J. M. Zessin, K. Finan, and M. Heilemann, *Super-resolution fluorescence imaging of chromosomal DNA,* Journal of Structural Biology **177**, 344 (2012).

[10] A. Raulf, C. K. Spahn, P. J. M. Zessin, K. Finan, S. Bernhardt, A. Heckel, and M. Heilemann, *Click chemistry facilitates direct labelling and super-resolution imaging of nucleic acids and proteins,* RSC Advances **4**, 30462 (2014).

[11] J. B. Grimm, B. P. English, J. Chen, J. P. Slaughter, Z. Zhang, A. Revyakin, R. Patel, J. J. Macklin, D. Normanno, R. H. Singer, T. Lionnet, and L. D. Lavis, *A general method to improve fluorophores for live-cell and single-molecule microscopy,* Nature Methods **12**, 244 (2015).

[12] J. B. Grimm, T. A. Brown, A. N. Tkachuk, and L. D. Lavis, *General Synthetic Method for Si-Fluoresceins and Si-Rhodamines,* ACS Central Science **3**, 975 (2017).

[13] W. R. Legant, L. Shao, J. B. Grimm, T. A. Brown, D. E. Milkie, B. B. Avants, L. D. Lavis, and E. Betzig, *High-density three-dimensional localization microscopy across large volumes,* Nature Methods **13**, 359 (2016).

[14] A. Löschberger, S. van de Linde, M.-C. Dabauvalle, B. Rieger, M. Heilemann, G. Krohne, and M. Sauer, *Super-resolution imaging visualizes the eightfold symmetry of gp210 proteins around the nuclear pore complex and resolves the central channel with nanometer resolution,* Journal of Cell Science **125**, 570 (2012).

[15] J. Broeken, H. Johnson, D. S. Lidke, S. Liu, R. P. J. Nieuwenhuizen, S. Stallinga, K. A. Lidke, and B. Rieger, *Resolution improvement by 3D particle averaging in localization microscopy,* Methods and Applications in Fluorescence **3**, 14003 (2015).

[16] F. Balzarotti, Y. Eilers, K. C. Gwosch, A. H. Gynnå, V. Westphal, F. D. Stefani, J. Elf, and S. W. Hell, *Nanometer resolution imaging and tracking of fluorescent molecules with minimal photon fluxes,* Science **355**, 606 (2017).

[17] J. C. Vaughan, S. Jia, and X. Zhuang, *Ultrabright photoactivatable fluorophores created by reductive caging,* Nature Methods **9**, 1181 (2012).

[18] R. Jungmann, C. Steinhauer, M. Scheible, A. Kuzyk, P. Tinnefeld, and F. C. Simmel, *Single-molecule kinetics and super-resolution microscopy by fluorescence imaging of transient binding on DNA origami,* Nano Letters **10**, 4756 (2010).

[19] S. Weisenburger, B. Jing, D. Hänni, L. Reymond, B. Schuler, A. Renn, and V. Sandoghdar, *Cryogenic Colocalization Microscopy for Nanometer-Distance Measurements,* ChemPhysChem **15**, 763 (2014).

[20] S. Weisenburger, D. Boening, B. Schomburg, K. Giller, S. Becker, C. Griesinger, and V. Sandoghdar, *Cryogenic optical localization provides 3D protein structure data with Angstrom resolution,* Nature Methods **14**, 141 (2017).

[21] W. Li, S. C. Stein, I. Gregor, and J. Enderlein, *Ultra-stable and versatile widefield cryo-fluorescence microscope for single-molecule localization with subnanometer accuracy,* Optics Express **23**, 3770 (2015).

[22] Y.-W. Chang, S. Chen, E. I. Tocheva, A. Treuner-Lange, S. Löbach, L. Søgaard-Andersen, and G. J. Jensen, *Correlated cryogenic photoactivated localization microscopy and cryo-electron tomography,* Nature Methods **11**, 737 (2014).

[23] L. F. van Driel, J. A. Valentijn, K. M. Valentijn, R. I. Koning, and A. J. Koster, *Tools for correlative cryo-fluorescence microscopy and cryo-electron tomography applied to whole mitochondria in human endothelial cells,* European Journal of Cell Biology **88**, 669 (2009).

[24] A. Briegel, S. Chen, A. J. Koster, J. M. Plitzko, C. L. Schwartz, and G. J. Jensen, *Chapter Thirteen - Correlated Light and Electron Cryo-Microscopy,* in *Cryo-EM Part A Sample Preparation and Data Collection*, Methods in Enzymology, Vol. 481, edited by G. J. Jensen (Academic Press, 2010) pp. 317–341.

[25] B. G. Kopek, G. Shtengel, C. S. Xu, D. A. Clayton, and H. F. Hess, *Correlative 3D superresolution fluorescence and electron microscopy reveal the relationship of mitochondrial nucleoids to membranes,* Proceedings of the National Academy of Sciences of the United States of America **109**, 6136 (2012).

[26] T. Ha, T. Enderle, D. S. Chemla, P. R. Selvin, and S. Weiss, *Single Molecule Dynamics Studied by Polarization Modulation,* Physical Review Letters **77**, 3979 (1996).

[27] S. W. Hell, *Far-Field Optical Nanoscopy,* Science **316**, 1153 (2007).

[28] N. Hafi, M. Grunwald, L. S. van den Heuvel, T. Aspelmeier, J.-H. Chen, M. Zagrebelsky, O. M. Schütte, C. Steinem, M. Korte, A. Munk, and P. J. Walla, *Fluorescence nanoscopy by polarization modulation and polarization angle narrowing,* Nature Methods **11**, 579 (2014).

[29] L. Frahm and J. Keller, *Polarization modulation adds little additional information to super-resolution fluorescence microscopy,* Nature Methods **13**, 7 (2016).

[30] D. H. Goldstein, *Polarized Light*, 3rd ed. (CRC Press, Boca Raton, FL, USA, 2010).

[31] R. M. A. Azzam, *Photopolarimetric measurement of the Mueller matrix by Fourier analysis of a single detected signal,* Optics Letters **2**, 148 (1978).

[32] P. S. Hauge, *Mueller matrix ellipsometry with imperfect compensators,* Journal of the Optical Society of America **68**, 1519 (1978).

4

Polarized Stimulated-Emission Depletion and dark-state lifetime in vacuum and at cryogenic temperatures

With the growing popularity of cryogenic correlative light and electron microscopy it is becoming increasingly important to bridge the resolution gap between these two modalities. At cryogenic temperatures the photon yield of fluorophores is a few orders of magnitude higher than at room temperature enabling localization precisions on the Ångström scale. The current challenge is to induce sparsity at cryogenic temperatures such that individual fluorescent molecules can be localized. In this chapter we demonstrate the progress of using polarized Stimulated-Emission Depletion (STED) to induce sparsity at cryogenic temperatures. We generate linear polarization of arbitrary in-plane orientations to achieve polarized STED with a sparsity of 3.3:1. Furthermore, we have probed the dark-state lifetime of ATTO 647N at cryogenic temperatures and in vacuum at room temperature. This dark state in vacuum is long-lived (τ = 38 ms) and could be the cause for reduced photostability of fluorophores under STED illumination in vacuum. The experiments were done on an in-house designed and built liquid nitrogen cryostat, enabling 30 hours of stable cryogenic fluorescence microscopy.

Parts of this chapter have been accepted for publication in Physical Review A as: **C.N. Hulleman**, R.J. Moerland, S. Stallinga, and B. Rieger, *Polarized Stimulated-Emission Depletion and Dark-State Lifetime at Vacuum and Cryogenic Temperature Conditions*.

4.1. Introduction

The diffraction limited resolution in fluorescence microscopy can be circumvented with localization microscopy [1–3]. The localization precision primarily scales with wavelength λ, Numerical Aperture NA and number of captured photons N as $\lambda/\left(\mathrm{NA}\sqrt{N}\right)$ [1]. Performing localization microscopy at cryogenic temperatures has numerous advantages with this in mind. Firstly, the sample can be fixed in a near-native state without the need for chemical fixation, thereby eliminating fixation artefacts [4]. Secondly, the photobleaching rate of fluorophores is reduced at cryogenic temperatures [5]. Therefore more photons can be extracted from each fluorophore, resulting in a better possible localization precision. The engineering challenge to maintain temperature gradients and minimize drift has been solved to some degree [6–11]. There is, however, still one major drawback to performing localization microscopy at cryogenic temperatures, which is the ability to induce sparsity. Sparsity is usually achieved by turning individual organic dyes on and off with either an active or stochastic process such that fluorophores can be localized individually.

Some success has been achieved with fluorescent proteins, which can switch on an off at cryogenic temperatures with a photon yield of $\sim 10,000$ photons [12]. This is, however, a small fraction of the photon yield of organic dyes at cryogenic temperatures, where more than $1,000,000$ photons are routinely achieved in sparse samples [7, 13, 14]. This hundredfold difference in photon yield translates to a 10 times difference in localization precision [15]. An effective way to induce sparsity with organic dyes at cryogenic temperatures has not been reported so far, which implies that the high photon yield and associated localization precision cannot be fully utilized yet. The strength of cryogenic localization microscopy with organic dyes is, however, evident when using a limited and known number of dyes per biomolecule, and has been used to reveal the structure of proteins with Ångström resolution [16].

To induce sparsity at cryogenic temperatures we have proposed the use of polarized Stimulated-Emission Depletion (STED) in chapter 3 [9]. This idea is based on work of Hafi et al. where they use mutually orthogonal linearly polarized excitation and depletion beams to modulate the fluorescence to achieve super-resolution [17]. Their implementation, however, was later shown to owe its resolution enhancement primarily to the sparsity enhancing deconvolution and not only the polarization modulation [18]. Their reported fluorescence modulation contrast before deconvolution was very low, presumably because both laser beams were rotated by a single $\lambda/2$ retarder and any phase difference between polarizations induced in the other parts of the microscope were not accounted for. In chapter 3 we have solved this issue of low fluorescence modulation contrast through optimization of the polarization states for arbitrary polarization orientation angles [9]. Polarization STED with this improved modulation contrast can be used to induce sparsity on samples with fixed dipole emitters, like those frozen in place at cryogenic temperatures. The induced sparsity can subsequently be used for localizing single molecules to assemble a localization microscopy image. In this way a genuine resolution enhancement can be achieved through localization microscopy at cryogenic temperatures, avoiding any deconvolution steps.

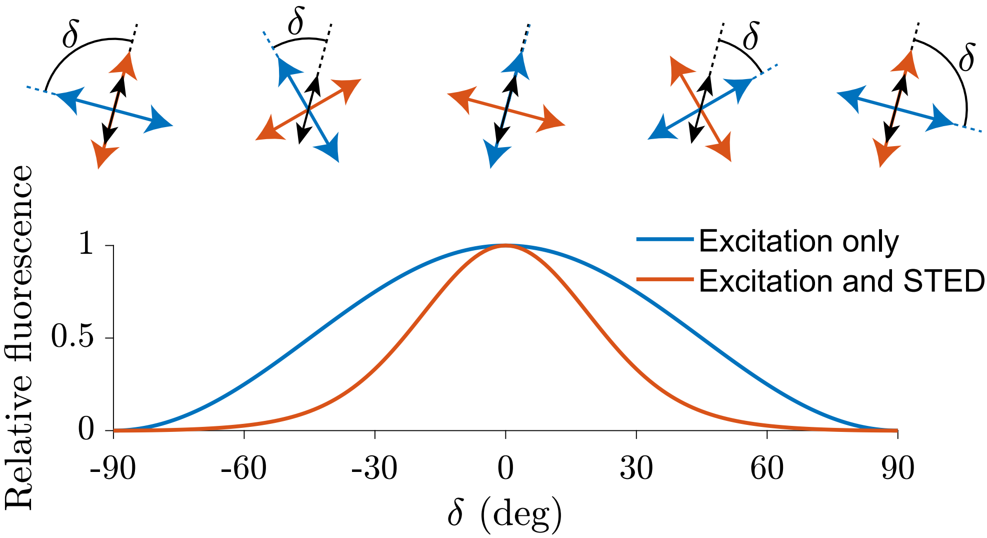

Figure 4.1: Fluorophores with their fluorescent molecular dipole moment's in-plane projection illustrated in black can be excited by a linearly polarized excitation laser beam (blue). The relative emitted fluorescence scales with the inner product between them, proportional to $\cos^2\delta$ where δ is the angle between the two in-plane orientations. With a linearly polarized STED laser beam (orange) the relative fluorescence is suppressed for non-zero inner-products between the dipole moment and the electric field vector of the STED beam. Arranging the in-plane excitation and depletion polarization perpendicular to each other the angular subset of fluorescing molecules is reduced without reducing the fluorescence of fluorophores oriented in the desired direction.

In this thesis chapter we investigate the sparsity induced at cryogenic temperatures with polarized STED. We also assess the drawbacks of this method for single-molecule localization microscopy at cryogenic temperatures. In particular we have focused on longer lived triple-states [19] that limit the achievable photon yield. We probed this dark state for ATTO 647N molecules and its recovery through ensemble level measurements at cryogenic and room temperatures in vacuum and through pulsed excitation with variable off-times.

4.2. Polarized Stimulated-Emission Depletion

4.2.1. Polarized STED theory and optical setup

The fluorescence of fixed dipoles can be modulated using in-plane linearly polarized light as illustrated in Fig. 4.1. If the fixed fluorescent dipole moment and excitation electric field are parallel the excitation is most efficient and the relative fluorescence maximal. The relative fluorescence decreases as the angle (δ) between the fluorescent dipole moment and excitation electric field changes ($\sim \cos^2\delta$). The addition of an in-plane linearly polarized depletion beam with a perpendicular polarization to the excitation beam narrows the set of fixed emitters that have significant fluorescence [17]. The relative fluorescence is decreased as the depletion beam stimulates the emission of a photon identical to the incident depletion photon which is not

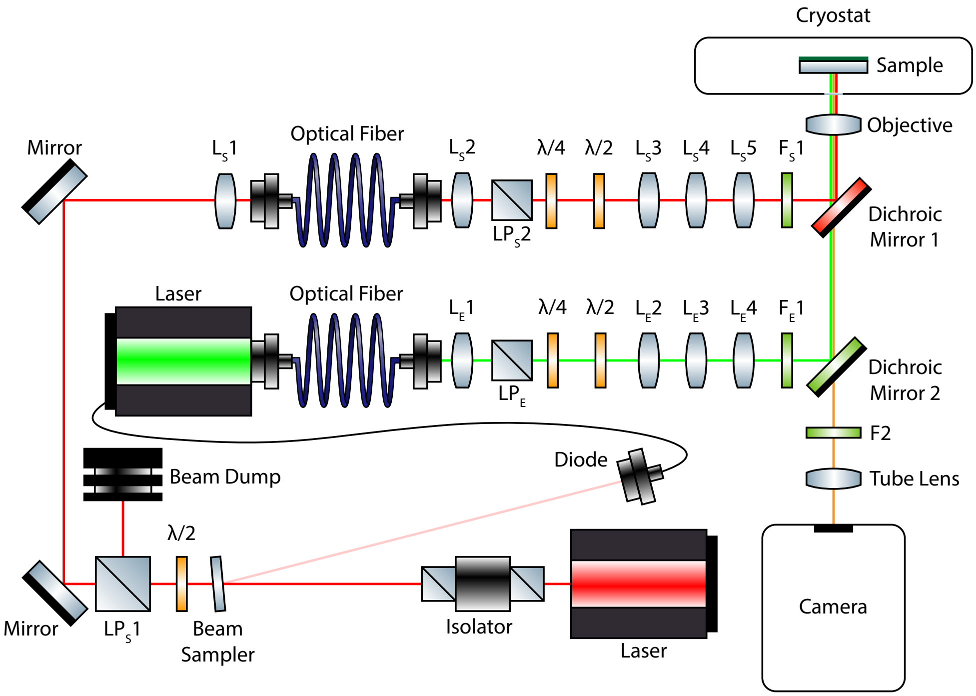

Figure 4.2: Optical setup for polarized STED at cryogenic temperatures.

detected on the camera as it is blocked by the fluorescence filters [20]. With the additional perpendicular depletion beam the relative fluorescence scales with $\sim \cos^n \delta$, where $n \geq 2$ increases with increasing STED laser power. In this way the set of orientations of effectively fluorescing dipoles is reduced with more STED laser power. For fluorescent dipole moments not aligned in-plane (perpendicular to the optical axis) the maximal excitation efficiency will be reduced, however, molecules aligned along the desired in-plane projection ($\delta = 0°$) will still not be depleted as the fluorescent dipole moment is perpendicular to the depletion polarization. To ensure that the fluorescent molecules oriented in the desired direction are not depleted, the STED beam needs to be linearly polarized. Any ellipticity in the polarization leads to a non-zero inner product between the depletion polarization and the fluorescent molecular dipole and consequently a non-zero chance of depletion.

The essential parts of the optical system as illustrated in Fig. 4.2 are the polarization control, pulse stretching of the depletion beam and synchronization with the excitation pulses. The depletion beam path illustrated in red comes from a femtosecond tunable Ti:Sapphire laser (Mai Tai HP, SpectraPhysics) that goes through an optical isolator (IO-5-780-HP, Thorlabs) to prevent back reflections into the laser cavity. A beam sampler (10B20-01NC.2, Newport) reflects $\sim 3\%$ to a photodetector (DET025A/M, Thorlabs) to synchronize the excitation pulses. The depletion beam power is modulated by a $\lambda/2$ waveplate (10RP52-2, Newport) and Glan-laser polarizer LP_S1 (10GL08AR.16, Newport) which is reflected into a beamdump (PL15, Newport). Components with a subscript S are in the STED beam-path. The beam is then focused by a aspheric lens (C430TME-B, Thorlabs) into a 50 m long polarization maintaining fibre (PM630-HP, Thorlabs) mounted on an actively controlled stage (NanoMax 300, Thorlabs). The feedback for this stage comes from an additional beam sampler (BSF10-B, Thorlabs) and photodiode (FDS1010, Thorlabs) placed between L_S2 and the $\lambda/4$ waveplate. The beam is collimated by an aspheric lens L_S2 (C280TMD-B, Thorlabs) and polarized by the linear polarizer LP_S2 (GL10-B, Thorlabs). The $\lambda/4$ (AQWP05M-980, Thorlabs) and $\lambda/2$ (AHWP05M-980, Thorlabs) waveplates are mounted in rotation stages (8MPR16-1, Standa). L_S3 (LA1229-B, Thorlabs) and L_S4 (LC1715-B, Thorlabs) reduce the beam size and L_S5 (LA1708-B, Thorlabs) focuses on the back focal plane of the objective lens (CFI S Plan Fluor ELWD 60XC, Nikon). The depletion beam spectrum is filtered by F_S1 (FF01-775/46, Semrock) and reflected off dichroic mirror 1 (A custom shortpass filter with an edge wavelength of ~ 700 nm and reduced phase shift between s and p-polarized light between 700-800 nm, Chroma).

Coloured in green is the excitation beam path, with components denoted with a subscript E, which originates from a fiber coupled picosecond pulsed laser source (LDH-D-C-640, Picoquant). Timing of the pulses is synchronized from the beam pickoff from the depletion beam which is mounted on rails (RLA300/M, Thorlabs) allowing for fine-tuning of the timing between the two pulses. For coarse timing adjustments a coaxial delay box (DB64, SRS) is used. The beam is collimated by an aspheric lens L_E1 (A397TM-A, Thorlabs). After a linear polarizer LP_E (GL10-A, Thorlabs) the polarization state is altered by a $\lambda/4$ (AQWP05M-600, Thorlabs) and $\lambda/2$ (AHWP05M-600, Thorlabs) waveplate mounted in rotation stages (8MPR16-1, Standa). The beam is demagnified by L_E2 (LA1229-B, Thorlabs) and L_E3 (LC1715-B, Thorlabs). L_E4 (LA1461-B, Thorlabs) focuses on the back focal plane of the objective lens. The excitation beam is filtered by F_E1 (FF01-637/7, Semrock) and reflected off dichroic mirror 2 (FF652-DI01, Semrock). The fluorescence indicated with an orange beam passes through the two dichroic mirrors and is filtered by F2 which consists of two (FF01-676/29, Semrock) filters and is then focused on the camera by a tube lens (ITL200, Thorlabs). For the polarized STED experiments an EMCCD camera (iXon Ultra 888, Andor) was used and for probing the dark-state lifetime an sCMOS camera (Zyla 4.2 PLUS, Andor) was used.

4.2.2. Cryostat

The sample is contained in a cryostat that is a modified version of the one designed by Li et al. [7]. In chapter 3 we doubled the liquid nitrogen capacity to 3 liters allowing for a full day of imaging at cryogenic temperatures and increased the heat conduction between the liquid nitrogen and the sample holder [9]. A drawback of their system is that for sample loading the heavy (~ 30 kg) cryostat needs to be lifted, which becomes more problematic with the increased 3 liter volume and associated weight. To alleviate this problem in our cryostat the sample is loaded and imaged horizontally (Fig. 4.3) as opposed to the original vertical layouts [7, 9]. This horizontal layout also eases the development of the microscope as optical components are

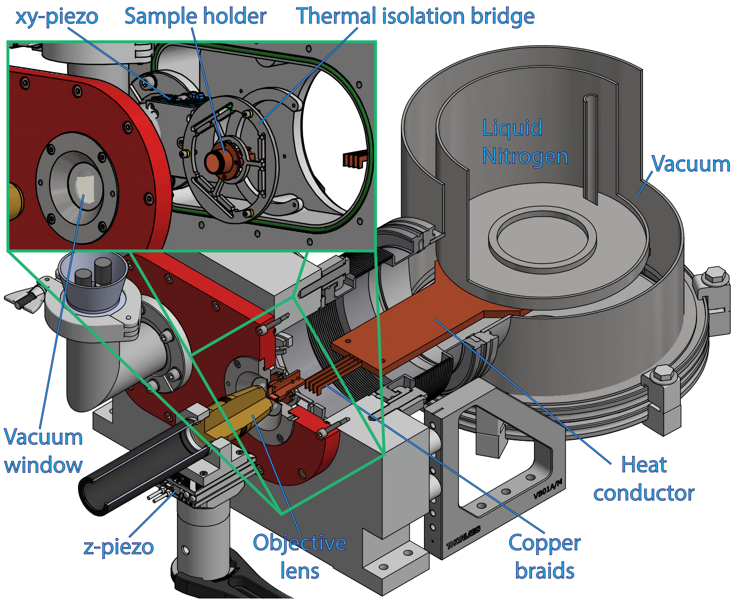

Figure 4.3: Illustration of the liquid nitrogen cryostat with horizontal loading and xy piezo stage in vacuum.

easily accessible. Instead of translating the entire cryostat on large motorized stages, only the sample holder and thermal isolation bridge are translated with xy piezo stages (Q-545.140, PI) inside the vacuum chamber. This allows for easy and accurate translation of the sample and the possibility for active drift correction. To minimize the heat transfer through radiation, the cold surfaces (heat conductor and liquid nitrogen tank) are encased with a 10-layer insulation foil (SCBnrc03, Cryoandmore). The connection from the sample holder to the thermal isolation bridge and to the piezo stage bracket is through polyetheretherketone (PEEK) spacers and screws, as PEEK has a low thermal conductivity and expansion coefficient. Furthermore, the thermal isolation bridge is redesigned to offer reduced thermal conduction between the inside and outside while retaining a good stiffness (see inset in Fig. 4.3). The objective mounted on a long-travel piezo stage (Q-545.240, PI) can be retracted and the vacuum window removed to exchange samples. A similar sample loading procedure to the one described by Li et al. [7] could potentially be used for frozen samples.

The vacuum chamber is pumped to a pressure $\leq 5\times\ 10^{-5}$ mbar with a turbomolecular pump (TMU 065, Pfeiffer) and diaphragm roughing-pump (MVP 055-3, Pfeiffer), the pressure is measured with a full-range gauge (PKR 250, Pfeiffer). After pumping, the liquid nitrogen container is filled requiring ~ 12 liters to cool and completely fill the cryostat. Once the temperature is stabilized, after about an hour, the vacuum valve is closed and the pumps can be switched off as a vacuum of $\sim 1\times10^{-5}$ mbar is maintained by the large cold-surface at liquid nitrogen temperature. With this cryostat the sample can be kept at cryogenic temperatures for 30 hours with a

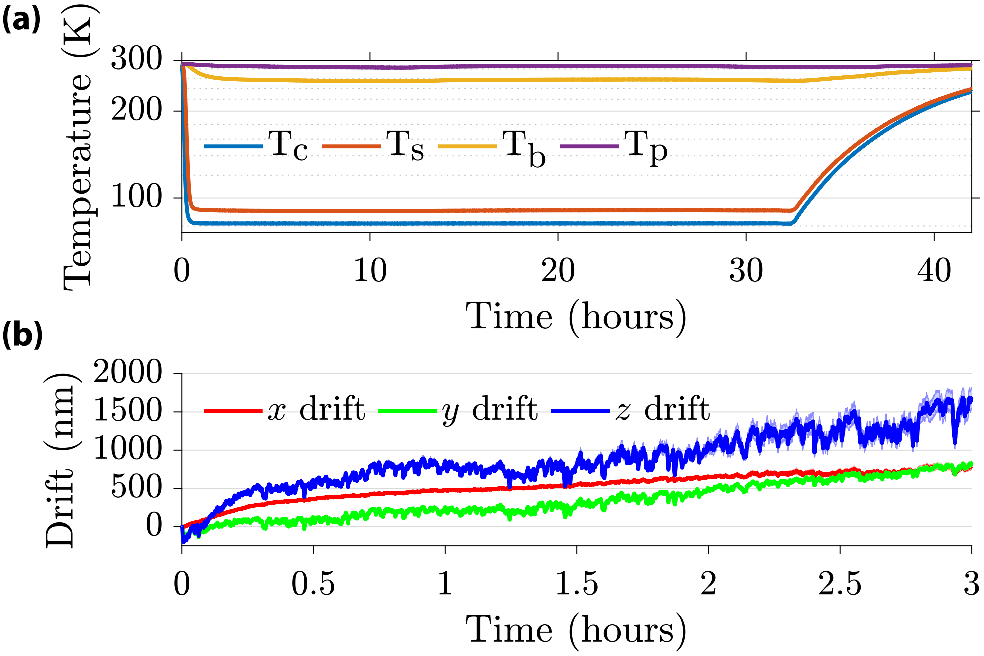

Figure 4.4: Temperature and drift of the sample in the cryostat. **(a)** Temperature of the heat conductor $\mathrm{T_c}$, sample holder $\mathrm{T_s}$, thermal isolation bridge $\mathrm{T_b}$, and piezo stage bracket $\mathrm{T_p}$ throughout an entire liquid nitrogen filled cycle. **(b)** Drift determined by 3D astigmatic localization of 5 fluorescent beads (shaded region represents ± one standard deviation).

smooth pressure increase from 1.2×10^{-5} mbar to 8.3×10^{-5} mbar. Over this 30 hour period a sample temperature of $\mathrm{T_s} = 90.48\pm0.17$ K can be realized with a very small average temperature slope of $\Delta\mathrm{T_s} = 0.04$ K/hour and maximally $\Delta\ \mathrm{T_s} = 0.13$ K/hour (Fig. 4.4(a)). The thermal isolation bridge $\mathrm{T_b} = -17 \pm 1.3\ ^\circ\mathrm{C}$ reduces the thermal energy flux from the piezo stage bracket $\mathrm{T_p} = 12.3 \pm 1.2\ ^\circ\mathrm{C}$ towards the sample. The temperature of the copper heat conduction block $\mathrm{T_c} = 81.63 \pm 0.02\ \mathrm{K}$ is higher than liquid nitrogen temperature (77 K) as the sensor is mounted closer to the copper braids. Temperatures are measured with PT1000 sensors and a 4-channel data logger (PT-104, Picotech). Cooling of the sample can be done at a rate of 850 K/hour and the rate of temperature increase after all the liquid nitrogen is evaporated is only 18.5 K/hour which illustrates the thermal isolation quality.

With the addition of a weak cylindrical lens, astigmatic localization can be used to determine the 3D drift from beads [21]. Here we used a 4 meter focal-length lens (4000 YO 25, Comar Optics) and a vectorial PSF model [22] to estimate the optical aberrations ($Z_2^{-2} = -133\ m\lambda$ and $Z_2^2 = 55\ m\lambda$) from a z-stack and thereafter the 3D position of multiple beads. The xy drift is only ~ 800 nm over 3 hours measured by localizing 5 fluorescent beads over 6320 frames (Fig. 4.4(b)). The z-drift is slightly worse, up to ~ 1600 nm over 3 hours. The majority of drift occurs during the first 20 minutes after onset of laser illumination. The drift is relatively smooth such that it can be corrected for in post-processing or, alternatively, an active drift correction method could be implemented.

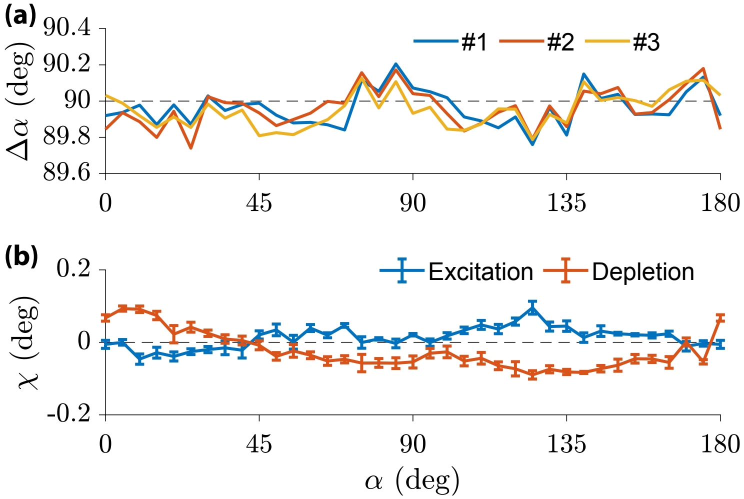

Figure 4.5: Polarization orientation and ellipticity. **(a)** Relative angle between excitation and STED polarization $\Delta\alpha = \alpha_{\text{exc}} - \alpha_{\text{dep}}$ for 3 repeated measurements. **(b)** Ellipticity angle (χ) for the excitation and depletion polarization, error bars are ± one standard deviation.

4.2.3. Linear polarization in fluorescence microscopes

To successfully perform polarized STED it is essential that the depletion beam is linearly polarized, such that molecules oriented perpendicular to the STED polarization orientation angle are not depleted. Generating linearly polarized excitation light with an arbitrary orientation in the sample plane of a fluorescence microscope is not trivial as primarily the dichroic mirror can introduce a large phase shift between s- and p-polarized light [9]. The optical setup utilizes both a $\lambda/4$ and $\lambda/2$ waveplate for each beam-path to rotate the polarization and compensate for any phase differences induced by the dichroic mirrors. To measure and optimize the polarization we have used a dual rotating retarder polarimeter as described in chapter 3 [9]. Both the excitation beam and orthogonal depletion beam are co-rotated in 5° steps. The angle difference between the two linearly polarized beams is $\Delta\alpha = \alpha_{\text{exc}} - \alpha_{\text{dep}} = 89.96^\circ \pm 0.1^\circ$ with 3 repeated measurements shown in Fig. 4.5(a). The ellipticity angle for the excitation beam was $\chi = 0.013^\circ \pm 0.03^\circ$ and for the depletion beam $\chi = -0.024^\circ \pm 0.05^\circ$ (Fig. 4.5(b)).

The effectiveness of the polarization optimization can be seen from the excitation only modulation of single ATTO 647N molecules at cryogenic temperatures, irrespective of their orientation (blue curves in Fig. 4.6). Using only a $\lambda/2$ waveplate it is not possible to generate diagonal linear polarization states at the sample due to the phase shift of the dichroic mirror. Instead the polarization is elliptical and almost circular as evident from the poor modulation of diagonally oriented molecules (red curve Fig. 4.6(b)).

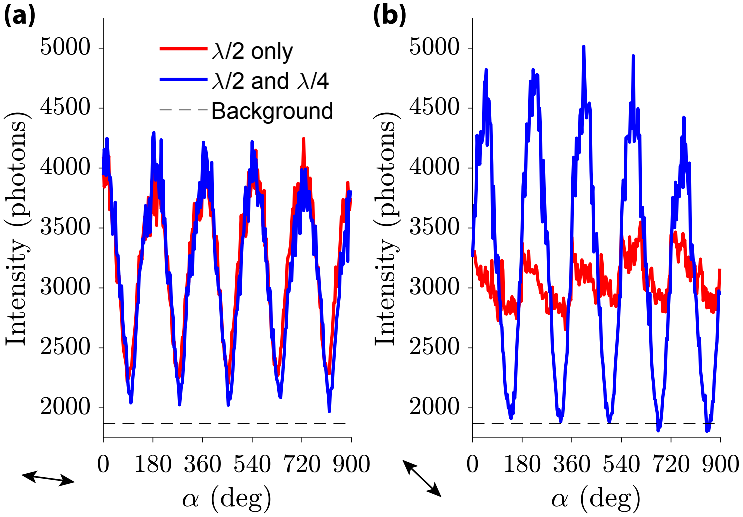

Figure 4.6: Influence of polarization extinction ratio on the modulation contrast of single-molecule fluorescence. **(a)** Fluorescence modulation of an almost horizontally oriented single ATTO 647N molecule ($\phi = 7.7^\circ \pm 1.6^\circ$). The red curve only utilizes a $\lambda/2$ waveplate to rotate the polarization, the blue curve utilizes both a $\lambda/2$ and $\lambda/4$ waveplate to compensate for depolarization induced by the dichroic mirror. **(b)** Fluorescence modulation of an almost diagonally oriented molecule ($\phi = 43.7^\circ \pm 1.1^\circ$). The modulation contrast using only a $\lambda/2$ waveplate is very low as diagonal input polarization becomes elliptical after the dichroic mirror. The data is acquired with 2000 ms camera exposure and 1 kW/cm^2 excitation intensity.

4.2.4. Polarized STED at cryogenic temperatures

A depletion laser beam perpendicularly polarized to the excitation beam reduces the fluorescence of fluorophores that do not have their molecular dipole moment oriented parallel to the excitation polarization. This is termed angle narrowing as the set of effectively fluorescing molecule orientations is reduced. Angle narrowing using polarized STED can lead to some degree of sparsity at cryogenic temperatures. To illustrate this we measured the fluorescence modulation of individual fluorophores with varying STED laser powers. The excitation and depletion efficiencies scale with the polar angle (angle with the optical axis) of individual fluorophores, therefore a single stable molecule is selected to make a fair comparison of the angle narrowing as a function of STED laser power. At each STED laser power, two periods of polarization rotation are applied and the average normalized fluorescence intensities for selected STED laser powers are shown in Fig. 4.7(a). Here pulsed STED was utilized where ~ 100 ps excitation pulses are synchronized to $100 - 500$ ps STED pulses. The STED laser pulses are longer for higher incident laser powers due to self-phase modulation, consequently the peak STED laser power does not scale linearly with incident power (Appendix 4.5.1). The fluorescence intensity at different STED laser powers is fitted with the function $I = |a\cos(\delta + b)|^n + c$ to estimate the FWHM (Fig. 4.7(b)). The uncertainty at $65\ \mathrm{MW/cm^2}$ is larger as the molecule was in a dark state during one of the periods. The smallest FWHM of 54° occurred at $81\ \mathrm{MW/cm^2}$. With a FWHM of 54° a sparsity of 180:54 or 3.3:1 can be realized as 180 degrees covers all unique in-plane orientations. With continuous-wave polarized STED this can be improved somewhat towards 6:1, which is still far from hundreds or thousands to one required for dense biological samples [23].

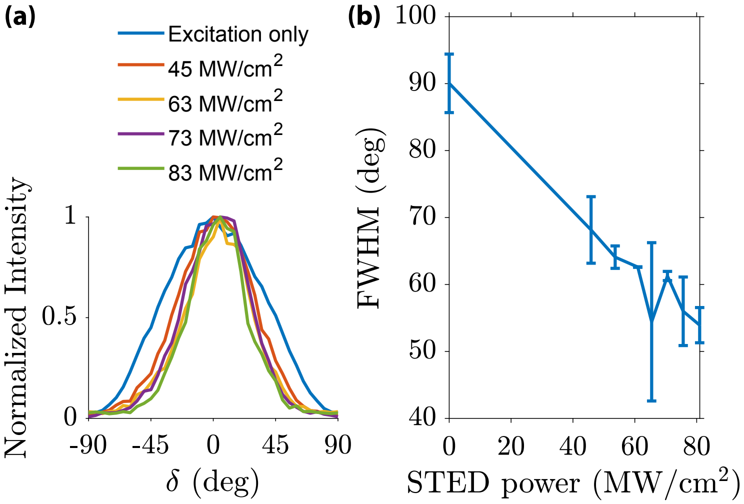

Figure 4.7: FWHM reduction with increasing STED laser power. **(a)** Relative fluorescence intensity averaged over 2 periods of a single ATTO 647N molecule illuminated with polarized STED with varying peak STED laser powers. The relative angle is the difference between the excitation polarization orientation angle and the in-plane orientation of the fluorescent molecular dipole moment ($\delta = \alpha_{\text{exc}} - \phi$). **(b)** Angular FWHM at varying STED laser peak powers estimated from the fitted function. Error bars are ± one standard deviation.

In principle the STED laser power could be increased a further 5 fold with the available power from the laser, however, this leads to an unfeasible high intensity at the pulse-stretching fiber facet. The temperature increase of the sample by addition of the STED laser is only $\Delta T \approx 9$ K with 1 W average STED laser power (still well below the glass transition temperature of ice, and no dipole moment re-orientation of the emitter is observed). The survivability of single-molecules at cryogenic temperatures under polarized STED does decrease with increasing laser power. To illustrate this as well as the fact that the modulation is largely determined by the STED laser we have imaged single ATTO 647N molecules at cryogenic temperatures where the excitation polarization is circularly polarized and only the polarization angle of the linearly polarized STED beam is rotated (Fig. 4.8). In this case continuous-wave STED was used and the intensity is time-averaged and therefore lower. The intensity per unit of time in Fig. 4.8 is similar to Fig. 4.6, but the exposure is 85% shorter to capture as many modulation periods as possible. The total number of photons captured from these individual molecules is 37,675 photons at 75 kW/cm^2, 98,242 photons at 360 kW/cm^2, 16,491 photons at 780 kW/cm^2 and 21,851 photons at 1090 kW/cm^2.

This amount of photons is 1-2 orders of magnitude below reported average photon yields of sparse single-molecules at cryogenic temperatures [7, 13–15]. One of

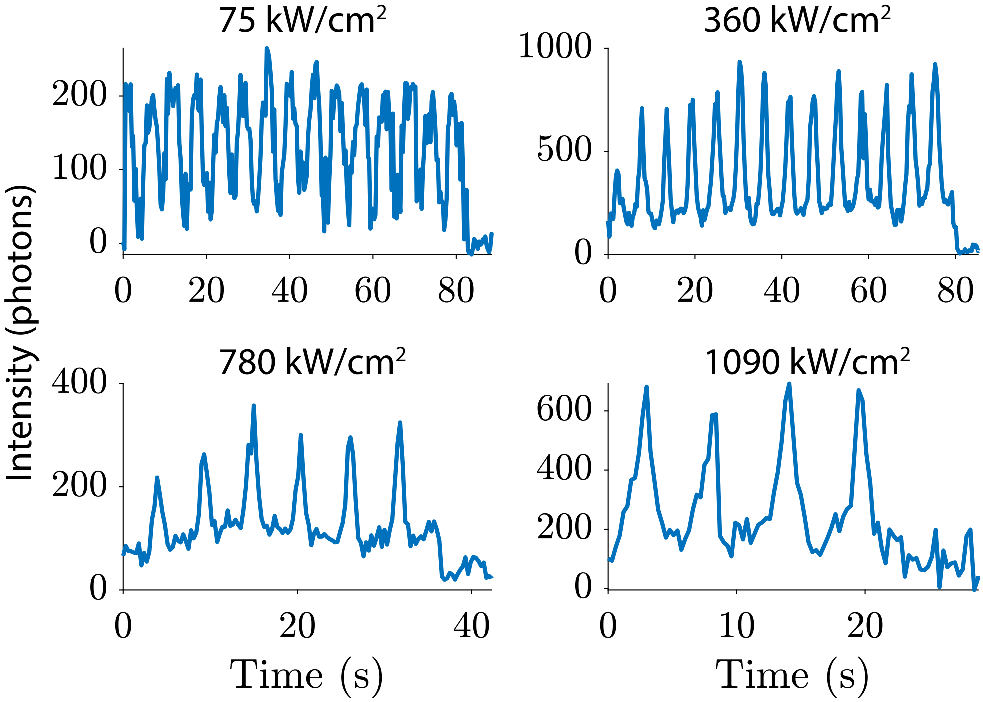

Figure 4.8: Modulation of individual ATTO 647N molecules at cryogenic temperatures from rotating linearly polarized STED and stationary circularly polarized excitation until bleaching. At higher STED laser powers the survival time and photon yield is reduced. The data is acquired with 300 ms camera exposure and 1 kW/cm² excitation intensity

the main bleaching pathways in STED microscopy is through the triplet state [24]. The STED process, however, also has a protective property as it rapidly depletes the singlet excited state thereby reducing the transition rate to a triplet state in the first place [24]. Whether this protective property still plays an important roll at cryogenic temperatures and in vacuum is unclear as many of the underlying state-transition rates may be different. Typical cryogenic fluorescence microscopes have the sample contained in either vacuum or an environment saturated with nitrogen gas, which could increase the triplet-state lifetime significantly. To determine if this could be a reason for the reduced photon yield with polarized STED we investigated dark states that occur in vacuum and at cryogenic temperatures in the following section.

4.3. Dark-state lifetime

It is clear that the triplet state plays a key role in the photophysics of single-molecules [25]. Most typically, fluorophores have a triplet-state lifetime in the microsecond range [19, 24, 26]. In oxygen deprived samples, for example those with oxygen scavengers, the triplet-state lifetime is orders of magnitudes longer [27, 28].

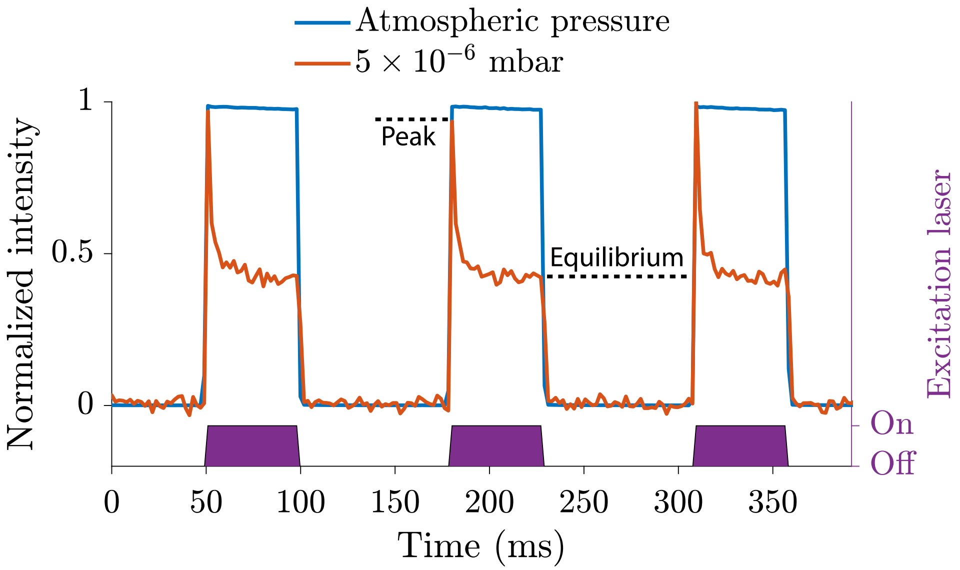

Figure 4.9: Ensemble-level fluorescence emission of ATTO 647N under periodic illumination, with excitation laser on-time of 50 ms and off-time of 80 ms. In vacuum there is a rapid dark state buildup, evident from the decrease in fluorescence intensity after onset of excitation illumination.

This is because oxygen plays a key role in quenching the fluorophore's triplet state through energy transfer from the fluorophore in a triplet state to oxygen in a triplet state [19]. If this prolonged triplet state is also present in vacuum and cryogenic systems, this should lead to observable dark states with dark-state lifetimes on the order of $1-100$ ms. For that reason we have probed such dark states by intermittent excitation periods [29].

4.3.1. Accumulation of fluorophores in a dark state in vacuum

Periodically switching the excitation laser on and off allows the dynamics of the dark state of fluorophores to be probed on the ensemble level. The fluorescence intensity of ATTO 647N molecules at atmospheric pressure follows the intensity of excitation when switching the laser on for 50 ms and then off for 80 ms (Fig. 4.9). There is no observable build up into a dark state as the fluorescence intensity has a flat profile, which is to be expected as the triplet-state lifetime is on the order of a few microseconds [19, 24, 26]. Pumping the same sample to a vacuum of 5×10^{-6} mbar a non-stable fluorescence intensity is observed under periodic illumination as a dark state builds up. After onset of illumination there is a sharp exponential decrease in fluorescence intensity that reaches an equilibrium level. Fitting a biexponential function to the buildup time reveals a characteristic timescale of 2.2 ± 0.5 ms. The dark-state buildup time could actually be faster as this measured value is on the same timescale as the frame time (1.97 ms). Not illuminating the sample for a sufficient amount of time allows the fluorophores to recover to the ground-state. Thereafter a peak in the fluorescence intensity will be observed when the excitation laser is turned on again.

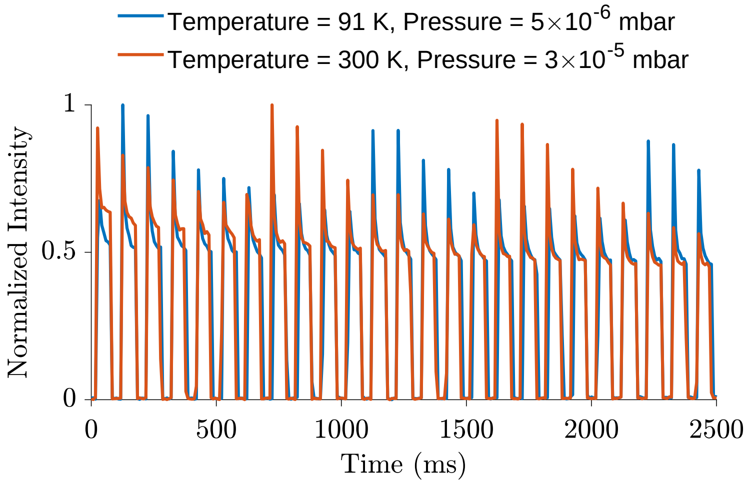

Figure 4.10: Fluorescence modulation and dark-state buildup of ATTO 647N in vacuum at room temperature and cryogenic temperatures. The excitation laser is modulated with 50 ms on-time and 50 ms off-time.

The accumulation of this dark state is present at both room and cryogenic temperatures in vacuum (Fig. 4.10). From this figure it can be seen that dark-state buildup and recovery times are similar as is the ratio between the peak level and equilibrium level. There is also a clear problem with aliasing as seen from the distinct time-varying peak intensity. This stems from the fact that the dark-state buildup is fast compared to the camera frame rate and that no photons are collected during frame readouts. The data in Fig. 4.10 is acquired with the EMCCD camera using 5 ms exposure and a frame rate of 120 fps. To reduce the frame readout time an sCMOS camera was used for the following experiments along with Fig. 4.9, as this enables the use of 1 ms exposure and 508 fps frame rate. As the difference between the dynamics of the dark state at cryogenic and room temperature is so small, the following experiments were performed at room temperature.

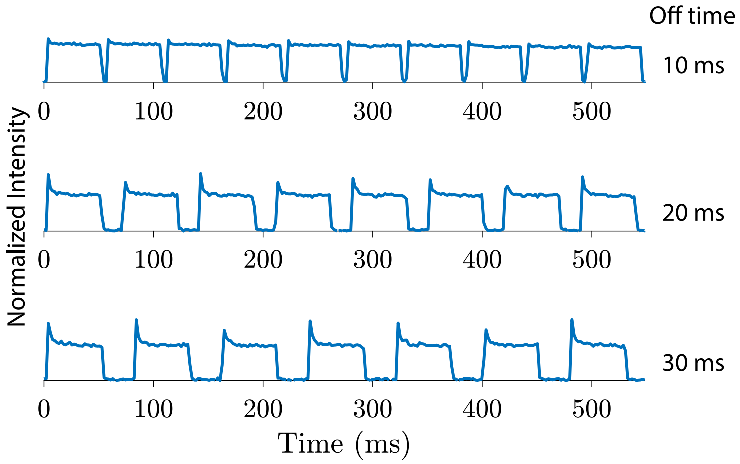

Figure 4.11: During the off-time of excitation illumination there is a recovery from the dark state. The amount of dark-state recovery scales with the off-time duration, as seen from the increasing peaks at the onset of illumination.

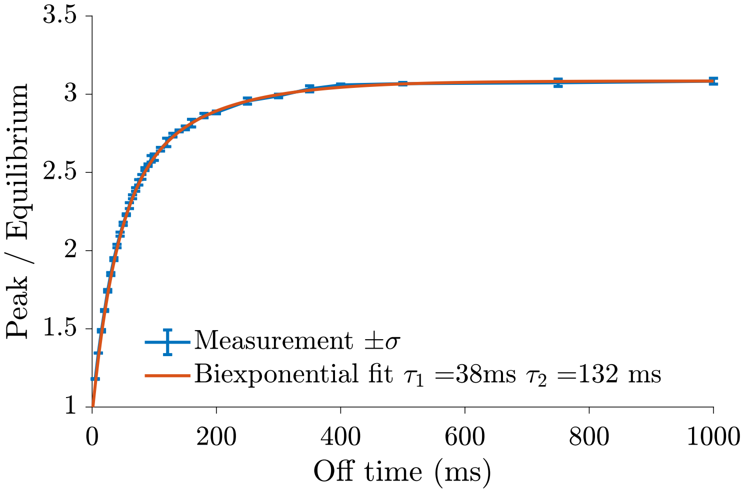

Figure 4.12: To probe the dark-state lifetime, the peak / equilibrium ratio was measured for varying off-times. The change in this ratio is well fitted with a bi-exponential function (RMSE=0.006).

4.3.2. Probing dark-state recovery

To probe the dark-state recovery time the off-time between excitation pulses is varied. Longer off-times allow more fluorophores to recover back to the ground state and consequently a higher peak fluorescence signal at the onset of the next excitation pulse. The influence of varying the off-time can be seen from the time traces in Fig. 4.11 with 10 ms, 20 ms and 30 ms off-times. By comparing the ratio of peak level to equilibrium level for varying off-times the dark-state lifetime can be measured.

To reduce the influence of aliasing each off-time is measured for 40 periods and the highest 5 peak values are analyzed. The peak / equilibrium ratio shown in Fig. 4.12 varies smoothly as a function of the off-time and the standard deviation of the 5 analyzed ratios is small ($\tilde{\sigma} = 0.013$). The change of the peak / equilibrium ratio as a function of off-time is well fitted by a double exponential function $c - ae^{-t_{\mathrm{off}}/\tau_1} + be^{-t_{\mathrm{off}}/\tau_2}$. For ensemble level ATTO 647N the recovery times at 4×10^{-5} mbar are $\tau_1 = 38$ ms and $\tau_2 = 132$ ms. The found τ_1 dark-state lifetime is similar to the triplet-state lifetime found in oxygen depleted aqueous solutions (28 ± 7 ms [27] and 29 ± 5 ms [28]). Analyzing more measurements lowers the peak / equilibrium ratio but has almost no influence on the calculated dark-state recovery time τ_1.

4.3.3. Dark-state lifetime reduction with Trolox

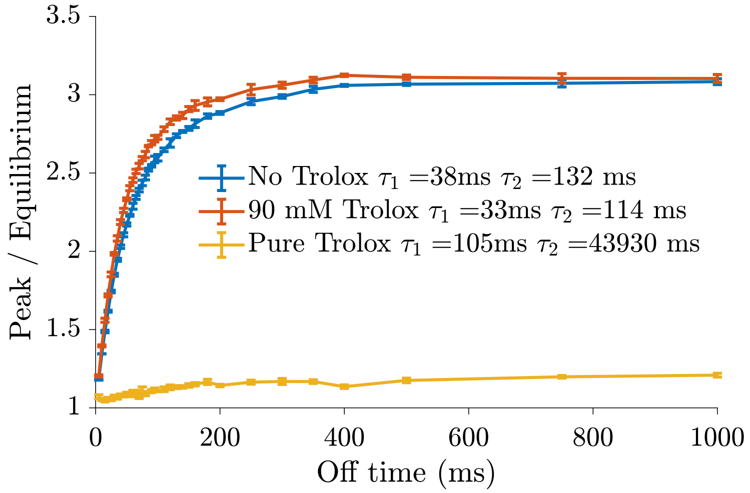

Figure 4.13: Rapid dark-state recovery with the addition of Trolox. 90 mM of Trolox in a thin layer of single molecules slightly reduces the dark-state lifetime. In a thick layer of pure Trolox the dark-state buildup is largely eliminated.

In an attempt to reduce the dark-state lifetime in vacuum we investigated the addition of Trolox. Trolox is known to function as an antiblinking and antibleaching agent by quenching the triplet state [30]. Comparing an ensemble level of spin-coated ATTO 647N with and without 90 mM of Trolox the dark-state lifetime is reduced from $\tau_1 = 38$ ms to $\tau_1 = 33$ ms, which can also be seen from the faster increase in the peak / equilibrium ratio in Fig. 4.13.

Instead of spin-coating the 90 mM concentration of Trolox which creates a flat and essentially 2D layer, it is also possible to create a sample by letting the dye and Trolox solution evaporate. In this way a solid droplet of higher concentration Trolox is realized which we termed 'pure' Trolox. At this high concentration of Trolox the peak / equilibrium curve becomes flat around a value of 1. This is because there is almost no observable build up of the triplet state and the time traces look similar to the case of atmospheric pressure in Fig. 4.9. The initial dark-state lifetime around ~ 30 ms of spin-coated ensemble level ATTO 647N has disappeared, instead the slower decay time $\tau_1 = 105$ ms is still present which is comparable to the $\tau_2 \approx 120$ ms value from the spin-coated sample.

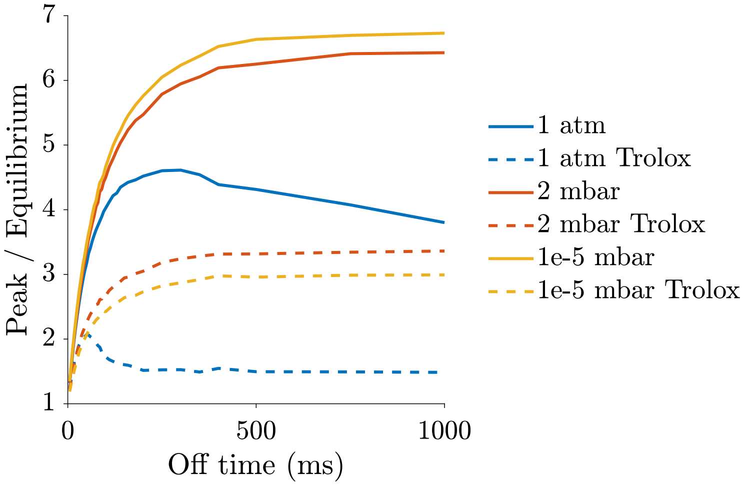

Figure 4.14: Peak / equilibrium ratio of a 100 nM concentration of ATTO 647N embedded in PVA with 4 mM of Trolox and without at varying pressures. The standard deviation of the measurements is comparable to those in Fig. 4.12 & 4.13 and error bars are left out for clarity.

To mimic a thin biological sample we have embedded ATTO 647N and Trolox in a spin-coated layer of Polyvinyl alcohol (PVA). This reduces the average distance between fluorophores and Trolox as the molecules are not only spread in a single 2D layer but are distributed in 3D. In this thicker layer a reduction in the peak / equilibrium ratio can be achieved at lower Trolox concentrations. Figure 4.14 compares the peak / equilibrium ratio of PVA samples with Trolox (dashed curve) and without Trolox (solid curve) at various pressures. At each pressure the sample with Trolox has a significantly lower buildup of the dark state and therefore a lower peak / equilibrium ratio. The difference between atmospheric pressure and ~ 2 mbar is large for both the sample with and without Trolox. At atmospheric pressure there appears to be an initial peak in the peak / equilibrium ratio which then reduces again and does not match the expected exponential behaviour. This could possibly be caused by molecules diffusing into the PVA sample. Interestingly, further reducing the pressure from ~ 2 mbar to $\leq 10^{-5}$ mbar makes a relatively small difference in peak / equilibrium ratio.

4.4. Conclusions

Polarized STED can be used to narrow the set of fixed fluorescing molecules at cryogenic temperatures. Unfortunately the FWHM achieved with significant STED powers does not induce enough sparsity to perform localization microscopy on dense biological samples. The level of sparsity achieved could be improved by varying the polarization states also towards the optical axis instead of only rotating the mutually perpendicular polarization states around the optical axis. This would approximately square the amount of sparsity but would be excessively complicated to realize in a low NA cryogenic microscope. An additional 27% better FWHM could be achieved using 2-photon excitation as the basic excitation dependence is enhanced quadratically yielding a $\cos^4 \delta$ dependence [31], before inclusion of additional polarized STED. Next to the limited improvement in sparsity the use of STED also has a negative impact on the photon yield of fluorophores at cryogenic temperatures. With the STED process fluorophores are still going through the photo-cycle whilst they are in the 'off' state, thereby increasing the chance of photobleaching.

In our cryostat the sample is contained in vacuum which causes a prolonged dark-state lifetime. The dark-state lifetime of ATTO 647N in vacuum was found to be $\tau = 38$ ms. Unfortunately this dark-state lifetime is not significantly longer than the typical fluorescence on-state lifetime. If this was the case, it could be utilized to directly induce sparsity in samples in vacuum and at cryogenic temperatures. This prolonged dark-state lifetime, a few orders of magnitude longer than in ambient conditions, increases the chances of irreversible photobleaching of the fluorophores.

The average dark-state lifetime in vacuum can be decreased by the addition of Trolox. For a significant decrease of the dark-state lifetime a very high concentration of Trolox needs to be added to fixed and non-diffusing samples. A standard sample in a liquid buffer can suffice with a lower concentration of Trolox as these molecules diffuse. This increases the chance of a Trolox molecule being in the proximity of a fluorophore in the triplet state. For fixed and frozen samples it would be ideal to constrain stabilizing molecules like Trolox to the proximity of the fluorophore. A conjugate of covalently bound NPA (a photostabilizer) and ATTO 647N that stabilizes fluorescence emission and significantly reduces triplet-state lifetime [28] can be very useful to further increase the photon yield of frozen fluorophores at cryogenic temperatures. With such a conjugation of dye and stabilizing molecule the fluorescence emission is more robust without the need for excess amounts of chemicals in the imaging buffer.

Instead of localizing molecules it is possible to use fluctuation based algorithms like SOFI [10, 32] in combination with the additional modulation from polarized STED, though this will not fully utilize the high photon yield available at cryogenic temperatures. Another potential approach would be an expansion along the lines of Cryogenic Optical Localization in 3D (COLD) [16], where a small known number of fluorophores are only localized when it is certain from the fluorescence time-trace that a single molecule is fluorescing during that frame. It should be possible to make an accurate estimation of a larger though still limited amount of molecules present in each time-frame until all fluorophores are bleached, by utilizing the slow bleaching and high photon count at cryogenic temperatures along with polarization modulation. This information can then be combined with a multi-emitter fitting procedure [33, 34]. This eliminates the typical problem of multi-emitter fitting where the number of emitters is unknown. The algorithm would then work in reverse chronological order starting with the frames with only one emitter per diffraction limited spot and sequentially fit frames with more emitters utilizing the previous localizations and varying contributions depending on the polarized modulation. Similar to using polarized excitation or detection to separate and assign emitted photons when it is known there are two individual fluorophores within a diffraction limited spot [35], but expanded to determine the number of emitters from the data and combined with a complex fitting procedure. Such a multi-emitter and multi-frame fitting procedure would be computationally intensive but beneficial to extract more information from the long imaging times of fixed dipole emitters at cryogenic temperatures.

4.5. Appendices

4.5.1. Appendix A: Self-phase modulation

Pulsed STED requires well synchronized and accurate timing of pulses for an effective depletion of the fluorescence. There is also an optimal depletion pulse length typically on the order of 100 ps, depending on the fluorophore and experimental parameters [36]. To attain these pulse lengths the femtosecond laser pulses need to be stretched, here this is done by propagation through a polarization maintaining fiber. With the dispersion in the fiber, different wavelengths from the narrow spectrum of the depletion beam travel at different speeds and thus the pulse is stretched. At high instantaneous powers, however, non-linear effects play a role where the local intensity changes the local refractive index. This is called self-phase modulation and leads to longer pulses [37]. Figure 4.15(a) shows the non-constant pulse length as a function of the incident laser power.

These measurements are performed with a 12.5 GHz diode (818-BB-45, Newport) and a 13 GHz oscilloscope (WaveMaster 8 Zi-B, Teledyne Lecroy). Each data-point is the average of at least 1000 measurements. To maintain a good signal-to-noise ratio and avoid clipping, the signal after the pulse stretching fiber is measured after two additional linear polarizers (GL10-B, Thorlabs). The first eliminates the undesired polarization and the second optimizes the intensity on the diode. The relative arrival times can be calculated by correlating the arrival times of the stretched pulse to the source pulse from the beam sampler and diode that are usually used to trigger the excitation pulses. Figure 4.15(b) shows that the onset of the stretched pulse arrives earlier as the power is increased and the tail of the pulse is delayed.

The increased pulse duration due to self-phase modulation comes along with spectral broadening [37]. Standard dichroic mirrors have a phase difference between s and p-polarized light that can vary rapidly as a function of wavelength. In this case the spectral broadening could lead to a significant increase in the polarization ellipticity angle. Fortunately, with the phase optimized dichroic mirror there is only

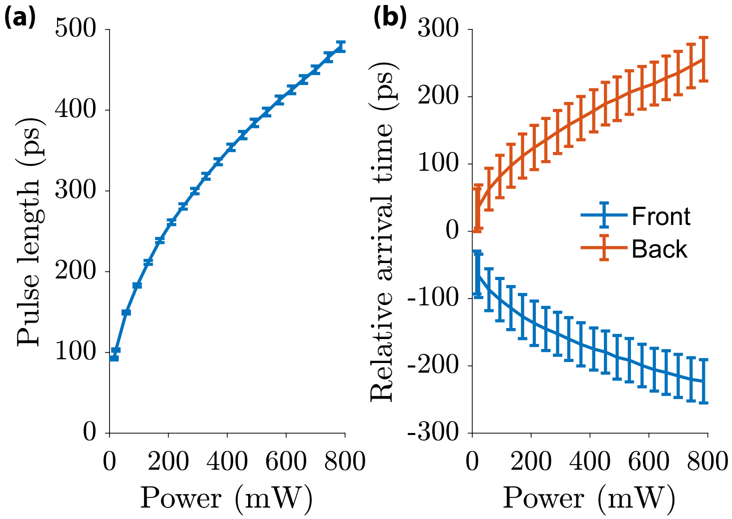

Figure 4.15: Self-phase modulation in the pulse-stretching fiber at a wavelength of 780 nm. **(a)** Pulse length (FWHM) as a function of incident laser power. **(b)** Relative arrival time of the beginning and end of the laser pulse as a function of laser power.

$\sim 4\%$ phase difference from 700 nm to 800 nm. Therefore the spectral broadening does not directly decrease the polarization extinction ratio, though it could decrease the depletion efficiency.

4.5.2. Appendix B: Sample preparation and image analysis

The sparse single-molecule level ATTO 647N samples for excitation modulation and polarized STED are prepared by spin-coating. ATTO 647N (ATTO-TEC) is diluted in Milli-Q (MQ) water to a concentration of 100 pM. 10 μL of this solution is placed on a 12 mm diameter quartz coverslip (amcoss) in the spin-coater (SPIN150i, POLOS). The coverslips are pre-cleaned by sonication for 1 hour sequentially in ethanol (Honeywell), acetone (Honeywell) and ethanol again. As the quartz coverslips are heat resistant, they can also be recycled through an additional step by burning with a Bunsen burner [7]. The spin-coater accelerates at a rate of 100 RPM/s to a rotation speed of 3000 RPM after 3.5 minutes the solution is evaporated and the sample decelerates and can be mounted in the cryostat.

For the dark-state lifetime measurements an ensemble level sample is made. From the sparse single-molecule samples an estimate of the fluorophore density is made ($0.04/\mu m^2$). The concentration of ATTO 647N is then scaled up to 1 μM to achieve a fluorohore density $\sim 400/\mu m^2$ such that each fluorophore is typically separated by 50 nm. This is to avoid the influence of Förster resonance energy transfer, which becomes relevant at fluorophore separation distances < 10 nm [38].

A 100 mM Trolox solution is made by combining 100 mg of Trolox (6-Hydroxy-2,5,7,8-tetramethylchromane-2-carboxylic acid, Sigma-Aldrich), 430 μL of methanol (Sigma-Aldrich), 345 μL NaOH (Sigma-Aldrich) and 3.2 mL of MQ water [39]. Thereafter 90 μL of this solution is mixed with 10 μL of a 10 μM solution of ATTO 647N, resulting in a final solution with 90 mM Trolox and 1 μM of ATTO 647N. For the two different samples this is either applied to a quartz coverslip with the same spin-coating protocol mentioned above or by letting a 20 μL droplet evaporate directly on the coverslip.

For ensemble level ATTO 647N in PVA, 1 gram of PVA (Mowiol 4-88, Sigma-Aldrich) is dissolved in 200 mL MQ water to create a 0.5 w% PVA solution. Thereafter 475 μL of the PVA solution is mixed with 20 μL of the 100 mM Trolox solution and 5 μL of a 10 μM ATTO 647N solution. This is then applied to a quartz coverslip with the same spin-coating protocol mentioned above.

For localization microscopy an accurate PSF model should be used that accounts for the dipole emission of fixed fluorophores. To analyze the modulation of individual fluorescent molecules it is sufficient to simply count the amount of photons in a region of interest (7×7) around the fluorophore [40]. A gain calibration (gain $0.017e^-/\mathrm{ADU}$ and offset 500.7 ADU with an EM gain setting of 100) is performed to convert analog-to-digital units to photon counts [41]. For the ensemble level measurements the fluorescence intensity is summed from the inner region of the excitation spot.

References

[1] E. Betzig, G. H. Patterson, R. Sougrat, O. W. Lindwasser, S. Olenych, J. S. Bonifacino, M. W. Davidson, J. Lippincott-Schwartz, and H. F. Hess, *Imaging intracellular fluorescent proteins at nanometer resolution,* Science **313**, 1642 (2006).

[2] S. T. Hess, T. P. Girirajan, and M. D. Mason, *Ultra-high resolution imaging by fluorescence photoactivation localization microscopy,* Biophysical Journal **91**, 4258 (2006).

[3] M. J. Rust, M. Bates, and X. Zhuang, *Sub-diffraction-limit imaging by stochastic optical reconstruction microscopy (STORM),* Nature Methods **3**, 793 (2006).

[4] M. Adrian, J. Dubochet, J. Lepault, and A. W. McDowall, *Cryo-electron microscopy of viruses,* Nature **308**, 32 (1984).

[5] W. E. Moerner and M. Orrit, *Illuminating single molecules in condensed matter,* Science **283**, 1670 (1999).

[6] R. Kaufmann, P. Schellenberger, E. Seiradake, I. M. Dobbie, E. Y. Jones, I. Davis, C. Hagen, and K. Grünewald, *Super-resolution microscopy using standard fluorescent proteins in intact cells under cryo-conditions,* Nano Letters **14**, 4171 (2014).

[7] W. Li, S. C. Stein, I. Gregor, and J. Enderlein, *Ultra-stable and versatile widefield cryo-fluorescence microscope for single-molecule localization with subnanometer accuracy,* Optics Express **23**, 3770 (2015).

[8] R. Faoro, M. Bassu, Y. X. Mejia, T. Stephan, N. Dudani, C. Boeker, S. Jakobs, and T. P. Burg, *Aberration-corrected cryoimmersion light microscopy,* Proceedings of the National Academy of Sciences of the United States of America **115**, 1204 (2018).

[9] C. N. Hulleman, M. Huisman, R. J. Moerland, D. Grünwald, S. Stallinga, and B. Rieger, *Fluorescence Polarization Control for On-Off Switching of Single Molecules at Cryogenic Temperatures,* Small Methods **2**, 1700323 (2018).

[10] F. Moser, V. Prazák, V. Mordhorst, D. M. Andrade, L. A. Baker, C. Hagen, K. Grünewald, and R. Kaufmann, *Cryo-SOFI enabling low-dose super-resolution correlative light and electron cryo-microscopy,* Proceedings of the National Academy of Sciences of the United States of America **116**, 4804 (2019).

[11] D. P. Hoffman, G. Shtengel, C. S. Xu, K. R. Campbell, M. Freeman, L. Wang, D. E. Milkie, H. A. Pasolli, N. Iyer, J. A. Bogovic, D. R. Stabley, A. Shirinifard, S. Pang, D. Peale, K. Schaefer, W. Pomp, C. L. Chang, J. Lippincott-Schwartz, T. Kirchhausen, D. J. Solecki, E. Betzig, and H. F. Hess, *Correlative three-dimensional super-resolution and block-face electron microscopy of whole vitreously frozen cells,* Science **367**, 265 (2020).

[12] P. D. Dahlberg, A. M. Sartor, J. Wang, S. Saurabh, L. Shapiro, and W. E. Moerner, *Identification of PAmKate as a Red Photoactivatable Fluorescent Protein for Cryogenic Super-Resolution Imaging,* Journal of the American Chemical Society **140**, 12310 (2018).

[13] S. Weisenburger, B. Jing, A. Renn, and V. Sandoghdar, *Cryogenic localization of single molecules with angstrom precision,* Nanoimaging and Nanospectroscopy **8815**, 88150D (2013).

[14] S. Weisenburger, B. Jing, D. Hänni, L. Reymond, B. Schuler, A. Renn, and V. Sandoghdar, *Cryogenic colocalization microscopy for nanometer-distance measurements,* ChemPhysChem **15**, 763 (2014).

[15] C. N. Hulleman, W. Li, I. Gregor, B. Rieger, and J. Enderlein, *Photon Yield Enhancement of Red Fluorophores at Cryogenic Temperatures,* ChemPhysChem **19**, 1774 (2018).

[16] S. Weisenburger, D. Boening, B. Schomburg, K. Giller, S. Becker, C. Griesinger, and V. Sandoghdar, *Cryogenic optical localization provides 3D protein structure data with Angstrom resolution,* Nature Methods **14**, 141 (2017).

[17] N. Hafi, M. Grunwald, L. S. van den Heuvel, T. Aspelmeier, J.-H. Chen, M. Zagrebelsky, O. M. Schütte, C. Steinem, M. Korte, A. Munk, and P. J. Walla, *Fluorescence nanoscopy by polarization modulation and polarization angle narrowing.* Nature Methods **11**, 579 (2014).

[18] L. Frahm and J. Keller, *Polarization modulation adds little additional information to super-resolution fluorescence microscopy,* Nature Methods **13**, 7 (2016).

[19] S. Van De Linde, I. Krstić, T. Prisner, S. Doose, M. Heilemann, and M. Sauer, *Photoinduced formation of reversible dye radicals and their impact on super-resolution imaging,* Photochemical and Photobiological Sciences **10**, 499 (2011).

[20] S. W. Hell and J. Wichmann, *Breaking the diffraction resolution limit by stimulated emission: stimulated-emission-depletion fluorescence microscopy,* Optics Letters **19**, 780 (1994).

[21] B. Huang, W. Wang, M. Bates, and X. Zhuang, *Three-Dimensional Super-Resolution Reconstruction Microscopy,* Science **319**, 810 (2008).

[22] M. Siemons, C. N. Hulleman, R. Ø. Thorsen, C. S. Smith, and S. Stallinga, *High precision wavefront control in point spread function engineering for single emitter localization,* Optics Express **26**, 8397 (2018).

[23] S. van de Linde, A. Löschberger, T. Klein, M. Heidbreder, S. Wolter, M. Heilemann, and M. Sauer, *Direct stochastic optical reconstruction microscopy with standard fluorescent probes,* Nature Protocols **6**, 991 (2011).

[24] G. Donnert, J. Keller, R. Medda, M. A. Andrei, S. O. Rizzoli, R. Lührmann, R. Jahn, C. Eggeling, and S. W. Hell, *Macromolecular-scale resolution in biological fluorescence microscopy,* Proceedings of the National Academy of Sciences of the United States of America **103**, 11440 (2006).

[25] B. Kozankiewicz and M. Orrit, *Single-molecule photophysics, from cryogenic to ambient conditions,* Chemical Society Reviews **43**, 1029 (2014).

[26] J. Widengren, U. Mets, and R. Rigler, *Fluorescence correlation spectroscopy of triplet states in solution: a theoretical and experimental study,* The Journal of Physical Chemistry **99**, 13368 (1995).

[27] C. Steinhauer, C. Forthmann, J. Vogelsang, and P. Tinnefeld, *Superresolution microscopy on the basis of engineered dark states,* Journal of the American Chemical Society **130**, 16840 (2008).

[28] J. H. M. van der Velde, J. Oelerich, J. Huang, J. H. Smit, A. Aminian Jazi, S. Galiani, K. Kolmakov, G. Gouridis, C. Eggeling, A. Herrmann, G. Roelfes, and T. Cordes, *A simple and versatile design concept for fluorophore derivatives with intramolecular photostabilization,* Nature Communications **7**, 10144 (2016).

[29] A. Giske, *CryoSTED microscopy - A new spectroscopic approach for improving the resolution of STED microscopy using low temperature,* Ph.D. thesis, Ruperto-Carola University Heidelberg (2007).

[30] T. Cordes, J. Vogelsang, and P. Tinnefeld, *On the mechanism of Trolox as antiblinking and antibleaching reagent,* Journal of the American Chemical Society **131**, 5018 (2009).

[31] J. R. Lakowicz, I. Gryczynski, J. Kuśba, and E. Danielsen, *Two photon-induced fluorescence intensity and anisotropy decays of diphenylhexatriene in solvents and lipid bilayers,* Journal of Fluorescence **2**, 247 (1992).

[32] T. Dertinger, R. Colyer, G. Iyer, S. Weiss, and J. Enderlein, *Fast, background-free, 3D super-resolution optical fluctuation imaging (SOFI),* Proceedings of the National Academy of Sciences **106**, 22287 (2009).

[33] S. J. Holden, S. Uphoff, and A. N. Kapanidis, *DAOSTORM: An algorithm for high-density super-resolution microscopy,* Nature Methods **8**, 279 (2011).

[34] F. Huang, S. L. Schwartz, J. M. Byars, and K. A. Lidke, *Simultaneous multiple-emitter fitting for single molecule super-resolution imaging,* Biomedical Optics Express **2**, 1377 (2011).

[35] D. Böning, F. F. Wieser, and V. Sandoghdar, *Polarization-Encoded Colocalization Microscopy at Cryogenic Temperatures,* ACS Photonics **8**, 194 (2021).

[36] M. Leutenegger, C. Eggeling, and S. W. Hell, *Analytical description of STED microscopy performance,* Optics Express **18**, 26417 (2010).

[37] E. Auksorius, *Multidimensional fluorescence imaging and super-resolution exploiting ultrafast laser and supercontinuum technology*, Ph.D. thesis, Imperial College London (2008).

[38] I. H. Stein, V. Schüller, P. Böhm, P. Tinnefeld, and T. Liedl, *Single-molecule FRET ruler based on rigid DNA origami blocks,* ChemPhysChem **12**, 689 (2011).

[39] J. Schnitzbauer, M. T. Strauss, T. Schlichthaerle, F. Schueder, and R. Jungmann, *Super-resolution microscopy with DNA-PAINT,* Nature Protocols **12**, 1198 (2017).

[40] R. Ø. Thorsen, C. N. Hulleman, M. Hammer, D. Grünwald, S. Stallinga, and B. Rieger, *Impact of optical aberrations on axial position determination by photometry,* Nature Methods **15**, 989 (2018).

[41] L. J. van Vliet, D. Sudar, and I. T. Young, *Digital fluorescence imaging using cooled charge-coupled device array cameras,* in *Cell Biology*, Vol. III, edited by J. Celis (Academic Press, New York, 1998) 2nd ed., pp. 109–120.

5

Simultaneous orientation and 3D localization microscopy with a Vortex point spread function

We utilize a modified Point Spread Function (PSF) for single molecule emitter imaging to estimate simultaneously the 3D position, dipole orientation, and degree of rotational constraint from a single 2D image. We use an affordable and commonly available phase plate, normally used for STED microscopy in the excitation light path, to alter the PSF in the emission light path. This resulting Vortex PSF does not require typical polarization splitting in the emission path and has a compact PSF size, making it easy to implement and combine with localization microscopy techniques. In addition to a vectorial PSF fitting routine we calibrate for field-dependent aberrations which enables orientation and position estimation within 30% of the Cramér-Rao bound limit over a 66 μm field of view. We demonstrate this technique on reorienting single molecules adhered to the cover slip, λ-DNA with DNA intercalators using binding-activated localization microscopy, and we reveal periodicity on intertwined structures on supercoiled DNA.

Parts of this chapter have been published as: **C.N. Hulleman**, R.Ø. Thorsen, E. Kim, C. Dekker, S. Stallinga, and B. Rieger, *Simultaneous orientation and 3D localization microscopy with a Vortex point spread function*, Nature Communications **12**, 5934 (2021).

5.1. Introduction

Single-Molecule Localization Microscopy (SMLM), with flavors like (F)PALM [1, 2], (d)STORM [3, 4] and (DNA)-PAINT [5, 6], have made nanoscale structural information beyond the diffraction limit more easily accessible to biologists. These super-resolution techniques commonly focus on localizing single emitters in the two dimensions of the focal plane, and sometimes in the third dimension along the optical axis. The role of molecular orientation in localization can often be ignored as the fluorescent labels are flexibly attached to the biomolecule of interest and can rotate or wobble freely, thereby appearing as isotropic emitters. In case the fluorophores are more rigidly attached, emitter orientation is either a nuisance for estimating the position of the emitters accurately or can give access to the anisotropy of the underlying biological structure. Imaging the orientation of constrained fluorescent labels has been used to visualize changes of fibroblasts under treatment [7], reveal the underlying orientation of amyloid fibrils [8] and to track motor proteins [9, 10]. Besides biological applications, the orientational information can also be used to visualize nanoscale deformations in material sciences [11]. In this chapter we demonstrate an engineered Point Spread Function (PSF), which allows in a unique manner the simultaneous estimation of the x, y and z position of the emitter, as well as the polar and azimuthal angle θ and ϕ of the molecular orientation, and the degree of orientational constraint g_2, all from a single 2D image. Thereby we can effectively combine orientation estimation and localization microscopy into a single imaging protocol.

Visualization of emission patterns from fixed fluorescent emitters dates back to near-field studies [12] and studies with high-NA fluorescence microscopes, leading to the observation of ring-shaped spots originating from molecules oriented along the optical axis [13]. Localization of these rotationally fixed molecules with a standard 2D Gaussian model leads to inaccuracies due to their dipole emission patterns [14]. The localization accuracy of these fixed dipoles is significantly worse in the presence of aberrations [15], and with a small amount of defocus errors can amount to 100 nm [16]. The impact of rotational diffusion has been studied in ref. [17] in which the authors show that a localization bias on the order of 10 nm already occurs when the fluorophores are constrained to a cone half-angle of 60°. This localization bias could be avoided altogether by removing the radially polarized component [18, 19], regrettably doing so reduces the number of signal photons. Alternatively, the polarization could be split into an x and y component and the y and x position could then be fitted from each respective polarization channel [20]. This also avoids the localization bias but results in an asymmetric localization precision.

A polarized standard PSF [20, 21] can not only be used to avoid localization bias but also to identify the in-plane orientation of fixed emitters. Unfortunately, it is very difficult to determine the out-of-plane orientation from an in-focus polarized PSF as the PSF shape does not vary a lot as a function of the polar angle. When defocusing fixed emitters with a standard PSF, the observed pattern varies more as a function of orientation, opening up a way to estimate the full orientation from a single defocused image [22–24]. A defocus of up to 1 μm spreads the emitted photons over many pixels, which has the drawback of adversely affecting localization precision. By interleaving in-focus localization with defocused spot fitting, a compromise between orientation estimation and localization precision can be made [10]. For a limited set of orientations the angles can even be extracted from in focus single molecule images in case of sufficiently high Signal-to-Noise Ratio (SNR) [11, 25, 26].

An alternative way to estimate orientation and position comes from engineering the Point Spread Function (PSF). Here techniques modify the emission beam phase profile [27–30] in the pupil plane and split the polarization [31] to measure different polarization components on the camera separately. The effective size of these engineered PSFs is large, ranging from 4-16 times the Rayleigh criterion in size ($R = 0.61\lambda/\mathrm{NA}$) in each polarization channel. This splitting of photons over a large area and multiple polarization channels reduces the Signal-to-Background Ratio (SBR) [21, 32] and limits the density of emitters per frame for localization microscopy. A recently published method referred to as Coordinate and Height super-resolution Imaging with Dithering and Orientation (CHIDO) [33] overcomes this problem with a more compact PSF that encodes the orientation and position into two different polarization channels. It turns out that this method performs 2-5 times worse on simulations than predicted by theory, despite a good maximal theoretical precision in both 3D location and orientation. Furthermore the experimental precision is even 5-6 times worse than the theoretical precision, which could be explained by the mismatch between their fitting model and experimental data. This method requires many additional optical components in the emission path such as polarization splitting and a custom produced stress-engineered optic. In addition, the latter component is particularly difficult to align and calibrate.

Here we overcome these drawbacks by introducing the Vortex PSF, a PSF engineering approach to simultaneously determine molecular orientation and position in all three spatial dimensions that does not require different polarization components to be imaged separately. Furthermore the Vortex PSF enables access to the degree of rotational mobility so that the flexibility of binding of fluorophores can be probed. Both the azimuthal and polar angle precision are good with no ambiguity between $\pm 45^\circ$ azimuthal angles, and the lateral localization precision is close to that of a standard (non-engineered) PSF. This is because a single imaged spot with the Vortex PSF has a footprint of only 4-6 times the Rayleigh criterion in size, compared to a standard PSF that has a width of 2-4 times the Rayleigh criterion. Therefore, depending on the emitter's orientation, the Vortex PSF is only 1.5-2 times larger than a standard PSF. This relatively small spot footprint on the camera leads to a favorable SBR, high localization precision and a sparsity constraint for localization microscopy on the same order of magnitude as a non-engineered PSF. The use of a calibrated aberration map over the entire Field-of-View (FOV) with a fully vectorial PSF model in the parameter estimation avoids aberration induced biases and successfully reaches the Cramér–Rao Lower Bound (CRLB). This makes it possible to maintain precision and accuracy across standard FOVs of tens of μm. Implementation of the Vortex PSF into an existing setup is easy and can be realized via an affordable off-the-shelf component. We showcase the method by tracking orientational jumps of single-molecules on a cover slip and imaging λ-DNA using Binding-Activated Localization Microscopy (BALM) [34, 35]. Furthermore the Vortex PSF enables the identification of periodicity in synthetically supercoiled DNA structures.

5.2. Results

5.2.1. Vortex PSF concept

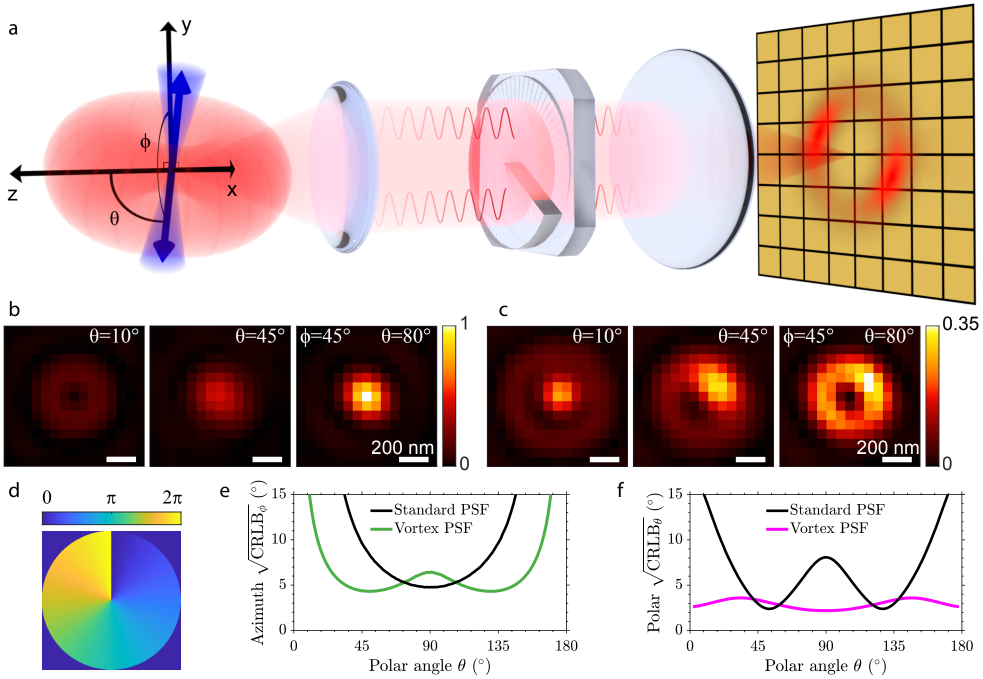

Figure 5.1: Vortex PSF concept. **(a)** A constrained dipole emitter is defined by the polar angle θ and azimuthal angle ϕ. The blue cone represents the degree of rotational constraint (g_2) of the dipole emitter and the red torus-like shape represents the dipole emission. The microscope, equipped with a vortex phase plate, induces a radial π phase difference in the Fourier plane of the emission path. This results in an asymmetric donut-like shape for fixed emitters on the camera which we call the Vortex PSF. **(b)** Simulated standard PSF of fixed emitters ($g_2 = 1$) with polar angles from left to right (10, 45, 80 degrees) and an azimuthal angle of 45 degrees. **(c)** Simulated Vortex PSF with the same angles and rotational constraint. **(d)** Phase profile of the vortex phase plate. **(e)** Azimuthal angle CRLB from simulated images as a function of the emitter polar angle (4000 signal photons, 10 background photons per pixel and $g_2 = 1$). **(f)** Polar angle CRLB as a function of the emitter polar angle with the same SBR and rotational constraint.

The orientation of a constrained dipole emitter is characterized by three numbers, the in-plane azimuthal angle ϕ, the polar angle with respect to the optical axis θ, and a parameter quantifying the degree of rotational mobility g_2 (Fig. 5.1(a)). The g_2 parameter is a weight parameter quantifying the contribution of the fixed versus free dipole component to the overall PSF, which is sufficient to quantify the impact of orientational constraint, irrespective of the form of the constraint, e.g. ”wobble-in-cone” or harmonic orientational potential well [36]. In the completely freely rotating emitter case $g_2 = 0$ and for a fully constrained emitter $g_2 = 1$. The angles ϕ and θ describing the dipole orientation lie in a hemisphere; $0^\circ \leq \theta < 180^\circ$ and $0^\circ \leq \phi < 180^\circ$.

A fixed dipole emitter that is oriented perpendicular to the optical axis ($\theta = 90^\circ$) emits fluorescence that is in-phase throughout the Fourier plane of the emission path. When imaged without the Vortex PSF, this emitter yields a Gaussian-like spot on the camera due to constructive interference in the center. The emission from a dipole oriented along the optical axis ($\theta = 0^\circ$) captured by a high-NA objective has two regions on opposite sides of the Fourier plane of the emission path that are out of phase with respect to each other. Without the Vortex PSF this emitter yields a ring-shaped PSF with a zero in the middle due to destructive interference. Figure 5.1(b) shows simulated images of standard PSFs with nearly in and out-of-plane orientations ($\theta = 80^\circ$ and $\theta = 10^\circ$). The slight asymmetry in the PSF arising from the azimuthal orientation ($\phi = 45^\circ$), however, is difficult to identify by the eye.

The Vortex PSF can be realized as an addition to any standard fluorescence microscope and only requires a single spiral phase plate in the Fourier plane of the emission path (Fig. 5.1(a)). This phase plate is commonly used in STED microscopy [37] to alter the excitation PSF, here we use it to engineer the emission PSF instead. The phase plate consists of a phase vortex of topological charge 1, thus the phase delay is a single spiral ramp from 0 to 2π, where radially opposing points always have a π phase difference between them (Fig. 5.1(d)). Adding a vortex phase plate in the Fourier plane of the emission path inverts the phase relationship described earlier for a standard PSF and creates what we call the Vortex PSF. Now out-of-plane ($\theta = 0^\circ$) orientations have constructive interference in the center, generating a central spot surrounded by a dark ring and an additional dim ring. In-plane ($\theta = 90^\circ$) orientations have destructive interference in the center resulting in a zero surrounded by a bright ring. Due to the polarization and directional emission from the fixed dipole emitter, the intensity distribution changes along this ring as a function of the azimuthal angle. When varying the polar angle from $\theta = 0^\circ$ to $\theta = 90^\circ$ the central bright spot moves outwards asymmetrically, distinctly changing the PSF shape as a function of the polar angle. Simulated Vortex PSF shapes for polar angles ($\theta = 10^\circ$, $\theta = 45^\circ$, $\theta = 80^\circ$) indicate a substantial change as a function of the polar angle, as well as a clearly recognizable impact of the azimuthal angle ($\phi = 45^\circ$) on spot shape (Fig. 5.1(c)).

Fitting molecular dipole orientations using the standard in-focus PSF is difficult because of its symmetries. The PSF is almost rotationally symmetric for all polar angles except around $\theta = 90^\circ$, where there is a slight asymmetry of the PSF as the spot is wider in one direction than the other. The azimuthal precision, quantified by the CRLB, is indeed worse for all polar angles except near $\theta = 90^\circ$ (Fig. 5.1(e)). Furthermore, the standard PSF is also symmetric around the polar angles $\theta = 0^\circ$ and $\theta = 90^\circ$ yielding an unfavorable precision in estimating the polar angle around these angles (Fig. 5.1(f)). These symmetries are broken by the Vortex PSF, resulting in a good precision over all possible orientations (Fig. 5.1(e,f)). Of course, the precision of the azimuthal angle is still expected to diverge to infinity for polar angles approaching $\theta = 0^\circ$ and $\theta = 180^\circ$ as the azimuthal angle is undefined when the dipole is aligned along the optical axis. Note that due to the symmetry of the dipole it is sufficient to use half the unit sphere to uniquely define the dipole angle.

5.2.2. Simulated precision and accuracy

We have tested the vectorial Vortex PSF model with extensive simulations to predict the experimental conditions under which the Vortex PSF can be used to correctly estimate the parameters $\Theta = (x, y, z, N, b, \phi, \theta, g_2)$ (see Supplementary Note 1 (5.5.1) for a detailed description of the model). The parameters are as follows: x, y, z are the emitter coordinates, N the number of signal photons, b the number of background photons per pixel, and orientation parameters ϕ, θ, g_2 as described earlier (Fig. 5.1(a)) . We found that all model parameters can be estimated with precision at the CRLB for all molecular orientations and degrees of orientational constraint (Supplementary Fig. 5.1), provided the signal-to-background ratio ($\mathrm{SBR} = N/b$) is sufficiently high. A practical lower limit, assuming 10 background photons per pixel (typical for SMLM), is around $\mathrm{SBR} \geq 200$ (Supplementary Fig. 5.2). At higher signal photon counts the required SBR is less stringent, for example with 4000 signal photons an $\mathrm{SBR} \geq 40$ ($b \leq 100$) is sufficient.

For dipole emitters orientated uniformly on unit sphere with $g_2 = 0.75$ and $\mathrm{SBR} = 4000/10$ the parameters can be estimated with a localization precision of $\sigma_{xy} = 5.6$ nm, $\sigma_z = 27$ nm and orientation precision of $\sigma_\phi = 5.5^\circ$, $\sigma_\theta = 3.1^\circ$ and $\sigma_{g_2} = 0.08$ (Supplementary Fig. 5.1). The polar precision appears almost constant over the unit sphere, whereas the azimuth precision performs well within polar angles ($20^\circ < \theta < 160^\circ$) after diverging for emitters oriented along the optical axis. Such polar range is notably broader than the standard PSF, as shown in Fig. 5.1(e). The amount of rotational diffusion of an emitter affects the possible orientational and axial precision while it does not affect the lateral precision. The orientation can be estimated to a precision within $\sigma_\theta < \sigma_\phi < 10^\circ$ given a rotational diffusion $g_2 > 0.4$ ($< 58^\circ$ cone half-angle). Outside this range the PSF becomes too smeared out, and the orientation information is mostly lost. The optimal axial performance is for fixed emitters $\sigma_z = 23$ nm ($g_2 = 1$), whereas it worsens for freely rotating emitters up to $\sigma_z = 49$ nm ($g_2 = 0$). In this case, when the emitters are freely rotating, the Vortex PSF has a slightly worse lateral precision compared to a non-engineered PSF ($\sigma_{xy} = 5.9$ nm versus $\sigma_{xy} = 4.5$ nm). Generally the estimation for all parameters works well over a z-range of ± 300 nm with a region of interest (ROI) of 15×15 pixels around an emitter with a pixel size of 65 nm (Supplementary Fig. 5.1). This relatively small ROI is ideal for dense single-molecule localization microscopy and attains a reliable parameter estimate for $|z| \leq 300$ nm. In Supplementary Fig. 5.3 we compare the performance to standard defocus based orientation fitting over a z-range of ± 1000 nm in simulation. The ROI size for this comparison is increased to 31×31 pixels. These simulations show that the precision with the Vortex PSF is better than with the standard PSF for z, ϕ and g_2 around focus $|z| \leq 300$ nm and the polar angle (θ) is better in an even wider region $|z| \leq 600$ nm. Outside this region the performance is equivalent. With the fluorophores in an aqueous medium ($n = 1.333$) the difference is less pronounced as the spherical aberrations from the refractive index mismatch break the symmetry around focus but the Vortex PSF still performs better for $|z| \leq 300$ nm. In these refractive index mismatched conditions the usable z-range with the Vortex PSF is about twice the range for standard defocused orientation fitting.

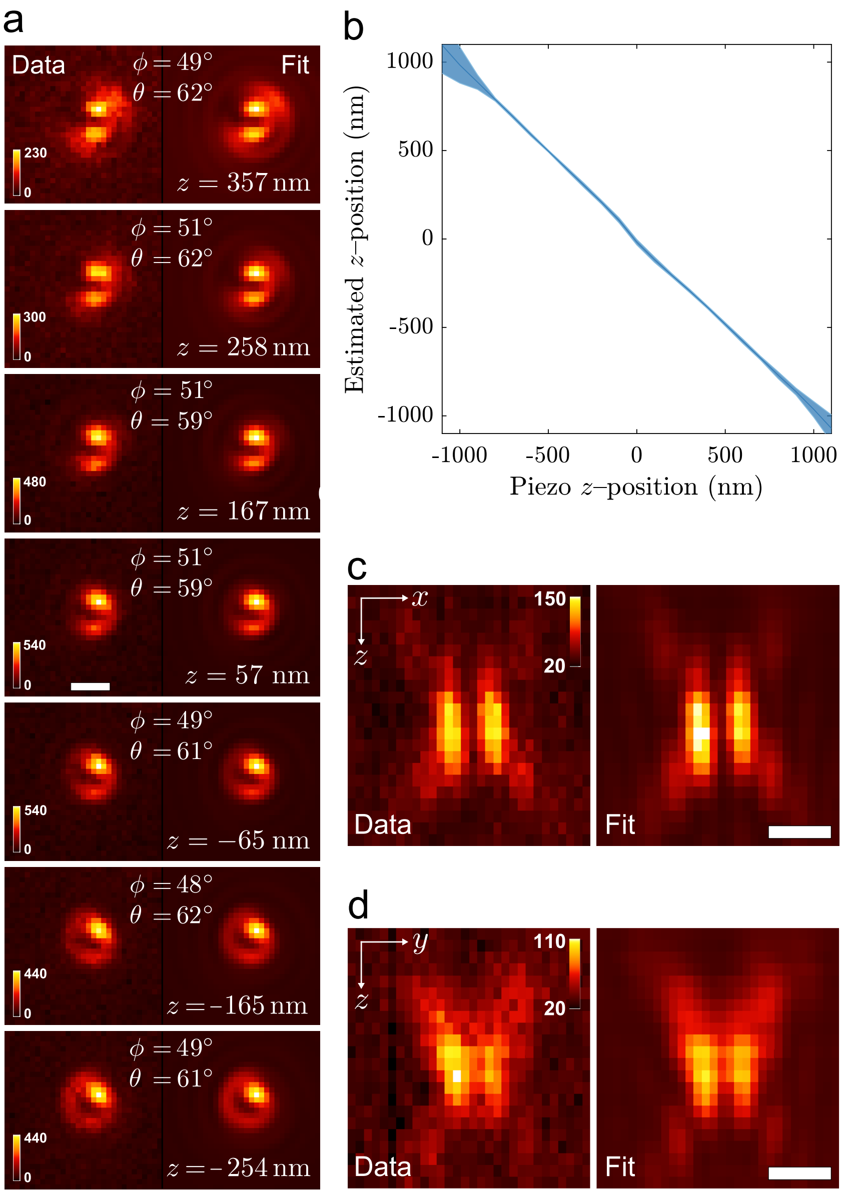

Figure 5.2: Vortex PSF validation. **(a)** Vortex PSF model fitted to an experimental z-stack of one single molecule with its estimated parameters listed in each frame. All sub-image pairs are contrast stretched with the same factor for better visibility of the PSF shape and the color bars are in units of photons per pixel. The mean signal count in the frames is 25×10^3 with a standard deviation of 4×10^3 and a mean background of 24 counts per pixel. The mean degree of orientational constraint of this molecule is $g_2 = 0.92$ with standard deviation of 0.02. **(b)** Mean estimated z position as a function of the piezo z position with the shaded region representing ± one standard deviation. The average is taken from 37 single molecules of varying orientations where the piezo z is realigned in processing to account for the in focus position not corresponding exactly with $z_{\text{piezo}} = 0$. The slope is negative due to the opposing definition of z_{piezo} and the sample z. **(c)** The cross-section in $x - z$ and **(d)** $y - z$ of a Vortex PSF, with the measurement left and fit right (pixels are stretched proportionally in z, color bar units: photons per pixel). The estimated signal photon counts were in the range $4 \times 10^3 - 50 \times 10^3$, and the estimated background photon counts were in the range $10 - 40$ photons per pixel. All scale bars are 500 nm.

Simulations show furthermore that optical aberrations must be taken into account in the fitting model. Unknown or inaccurately calibrated aberrations with values deviating from the actual values by more than 36 mλ affect the imaging model such that the estimator introduces biases and no longer reaches the CRLB (Supplementary Fig. 5.4). The aberration modes astigmatism and coma notably degrade the azimuthal precision by a factor of ~ 2, and additionally, astigmatism also degrades the localization precision by a factor of ~ 2. However, when the model is well calibrated with these aberrations, the estimator reaches the CRLB with no biases. To avoid such inadequate estimation and variation over a large field of view, we have developed an aberration map based on the Nodal Aberration Theory (NAT) [38] (See Methods (5.4) and Supplementary Note 2 (5.5.1)). Using this aberration map we obtain reliable results over a large FOV despite significant changes in aberrations throughout the FOV (Supplementary Fig. 5.5).

5.2.3. Proof-of-concept

To first verify the Vortex PSF's functionality and performance, we have imaged ATTO 565 embedded in a thin layer of PMMA (Polymethylmethacrylate) (see the methods section (5.4) for sample preparation and imaging protocol for any samples mentioned). Figure 5.2 shows the results of one of these experiments. Figure 5.2(a) shows through-focus images of a single molecule in PMMA acquired with the vortex phase plate together with the fitted PSF model and its estimated parameters. Note that a bigger region-of-interest (ROI) 31×31 is used to verify the model over a large z range compared to typical localization, where 15×15 is recommended. The same single molecule was imaged in quick succession without the vortex phase plate to verify the estimated orientations. As it is challenging to estimate orientations with the standard PSF on a single frame with high precision, the entire z-stack is used to retrieve a single estimate, which is used as a ground-truth measure. This estimate differentiates slightly from defocus imaging as described in the literature [10, 22, 23], where only a single focal slice is used. For the single molecule in Fig. 5.2(a), its orientation found for the standard PSF z-stack fit $(\phi, \theta) = (48^\circ, 60^\circ)$ agrees well with the angles found for the Vortex PSF z-slice fits $(\phi, \theta) = (49 \pm 1.5^\circ, 61 \pm 1.7^\circ)$. Here the Vortex PSF uncertainty is the standard deviation estimate of 11 focal slices, corresponding to a dynamic range of 1000 nm. Following the same procedure as for the molecule in Fig. 5.2(a), the estimated orientation of 21 different molecules is depicted in (Supplementary Fig. 5.6). The mean deviation between the orientation found with the standard PSF and Vortex PSF is $(\Delta\phi, \Delta\theta) = (-0.4 \pm 1.4^\circ, -0.2 \pm 1.2^\circ)$, indicating no bias between the two imaging modes. The Vortex PSF's mean precision is $(\sigma_\phi, \sigma_\theta) = (2.3^\circ, 1.8^\circ)$ which is respectively only 28% and 20% larger than the estimated lower limit $(\sqrt{\mathrm{CRLB}}_\phi, \sqrt{\mathrm{CRLB}}_\theta) = (1.8^\circ, 1.5^\circ)$. For the 21 molecules, the signal level varies one order of magnitude ($4.4 \times 10^3 - 45 \times 10^3$, with a mean of $17 \times 10^3 \pm 12 \times 10^3$, and a mean background of 19 photons per pixel). The mean rotational constraint parameter is $g_2 = 0.86$, with a standard deviation of 0.03. This corresponds to an average wobble cone semi-angle of $\alpha = 25.3^\circ$ which is similar to the previously found rotational constraint of single molecules in PMMA $\tilde{\gamma} = 0.85$ [39] $(\alpha = 27.8^\circ)$ and $\tilde{\gamma} \approx 0.8$ [30] $(\alpha \approx 30.7^\circ)$.

The estimated z-position shift between frames of the molecule in Fig. 5.2(a) is $\Delta\tilde{z} = 97 \pm 11$ nm, which matches the piezo shifts of 100 nm. The relationship between the estimated z-position and the piezo position averaged over 37 molecules is fitted with a linear function, resulting in a slope of -0.99 ± 0.01 and has a Root Mean Square Error (RMSE) of 16 nm over a 1200 nm range as shown in Fig. 5.2(b). To further show the quality of fit, cross-sections in the $x - z$ and $y - z$ planes are shown in Fig. 5.2(c)-(d). The agreement between the experimental data and fit with the vectorial Vortex PSF model is generally excellent. A striking detail is that even the fringe details away from focus match well. The lateral localization error, measured on individual z-slices between the two estimation modes, is 5 nm and 4 nm (RMSE) in the x and y direction. These validation experiments show that the orientation of fixed dipole emitters and their 3D position can be reliably estimated from individual focal-slice Vortex PSF images.

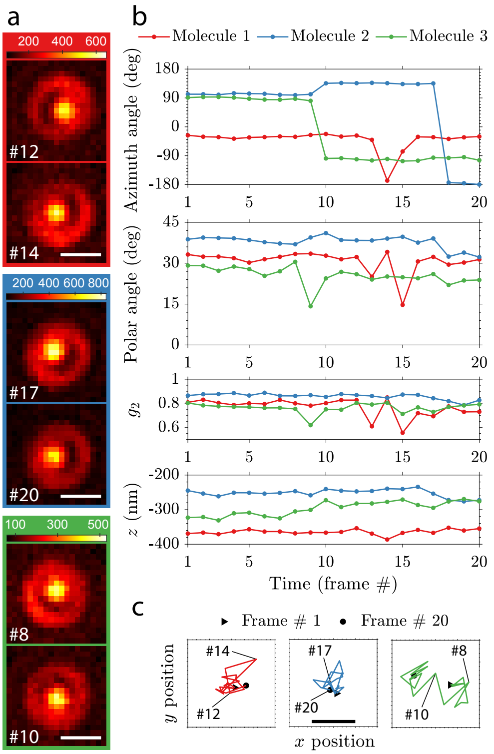

Figure 5.3: Re-orientation dynamics of single molecules imaged with the Vortex PSF. **(a)** Raw Vortex PSF images of 3 different molecules undergoing orientational transitions with frame numbers indicated in the bottom left (900ms exposure, scale bar 500 nm and color bar units: photons per pixel). **(b)** Estimated parameters over 20 frames of the three different molecules showing orientational transitions. The photon count per frame (mean ± one standard deviation) is: $N_1 = 4.7 \times 10^4 \pm 0.2 \times 10^4$ $N_2 = 5.9 \times 10^4 \pm 1.0 \times 10^4$ $N_3 = 3.3 \times 10^4 \pm 0.5 \times 10^4$ and background is: $b_1 = 91 \pm 2.0$ $b_2 = 89 \pm 1.1$ $b_3 = 80 \pm 1.7$ **(c)** Lateral localization of the emitters undergoing re-orientation with 1 nm ticks, a scale bar of 10 nm and the raw frames from (a) indicated. The localizations are drift corrected with the average trajectory of 10 stationary molecules (3.6 nm in x, 4.2 nm in y and 19 nm in z).

5.2.4. Re-orientation dynamics

The Vortex PSF can track dynamic changes in the orientation of single molecules on a cover slip. We have observed that a large portion of out-of-plane oriented ATTO 565 single molecules directly spin-coated on glass (without PMMA) show re-orientation when followed over time, indicating metastable adhesion to the glass surface (see Supplementary Movie 1). Figure 5.3(a) shows the Vortex PSF of the three highlighted molecules from Supplementary Movie 1 that re-orient over time. This can mainly be seen from the dark region that shifts location between the bright central spot and the ring around it. Additional time traces of various fitting parameters are shown in Fig. 5.3(b). The three different molecules that undergo these re-orientation events seem to primarily make jumps in the azimuthal angle. The re-orientations are also observed in the rotational constraint g_2 as it takes a lower value in the transition frames, which indicate a more freely rotating molecule or a superposition of orientations before and after the transition. These types of re-orientation would lead to large position biases in standard localization microscopy, which are avoided with the Vortex PSF (Fig. 5.3(c)). There does appear to be a marginal position shift as the molecules re-orient, however, the average standard deviation of the localizations $\sigma_{xy} = 2.7$ nm and the $\sqrt{\mathrm{CRLB}}_{xy} = 1.7$ nm show that the residual shift is small compared to the theoretical precision limit.

5.2.5. Super-resolved Lambda-DNA

A wide variety of biological structures can be labeled with rotationally constrained fluorophores [9, 10, 21, 40]. We chose to demonstrate our technique on frequently studied λ-DNA labeled with DNA intercalators [34, 35, 41] that transiently bind between the base pairs. The molecular dipole moment of the DNA intercalators is typically oriented perpendicular to the DNA axis [39, 42, 43], making this an ideal test case. We chose to use Sytox Orange which is believed to be a mono-intercalator [44] and further confirmed by elongation measurements matching that of mono-intercalators [41] (the exact chemical structure is undisclosed by the manufacturer). The sparsity required for localization microscopy is inherent from the transiently binding Sytox Orange that is essentially non-fluorescent when not intercalated [44]. In order to visualize the λ-DNA in a fluorescence microscope, molecular combing is used to align and stretch the DNA on a cover slip by a receding water-air interface [45, 46].

Figure 5.4 shows the potential of combining 3D localization microscopy and orientation estimation by imaging λ-DNA. The super-resolution reconstruction can be color-coded with one of the orientation parameters (azimuthal angle, polar angle or degree of orientational constraint) or the z-position. Figure 5.4(a) shows a subsection of the entire FOV with an azimuthal angle color-coding. The in-plane molecular orientation is clearly perpendicular to the orientation of the DNA-strands. The local orientation of the DNA strand can be determined by fitting a spline curve to the localizations on the strand. The angle difference ($\Delta\phi$) between the fluorophore and DNA axis orientation can be estimated. In other words $\Delta\phi$ describes the azimuthal angle in a coordinate frame where the DNA strand is locally pointing in the x-direction. Analyzing a single strand shows a mean azimuthal angle difference between the fluorophore and the DNA axis of $\Delta\widetilde{\phi} = 82^\circ$ with a median absolute deviation

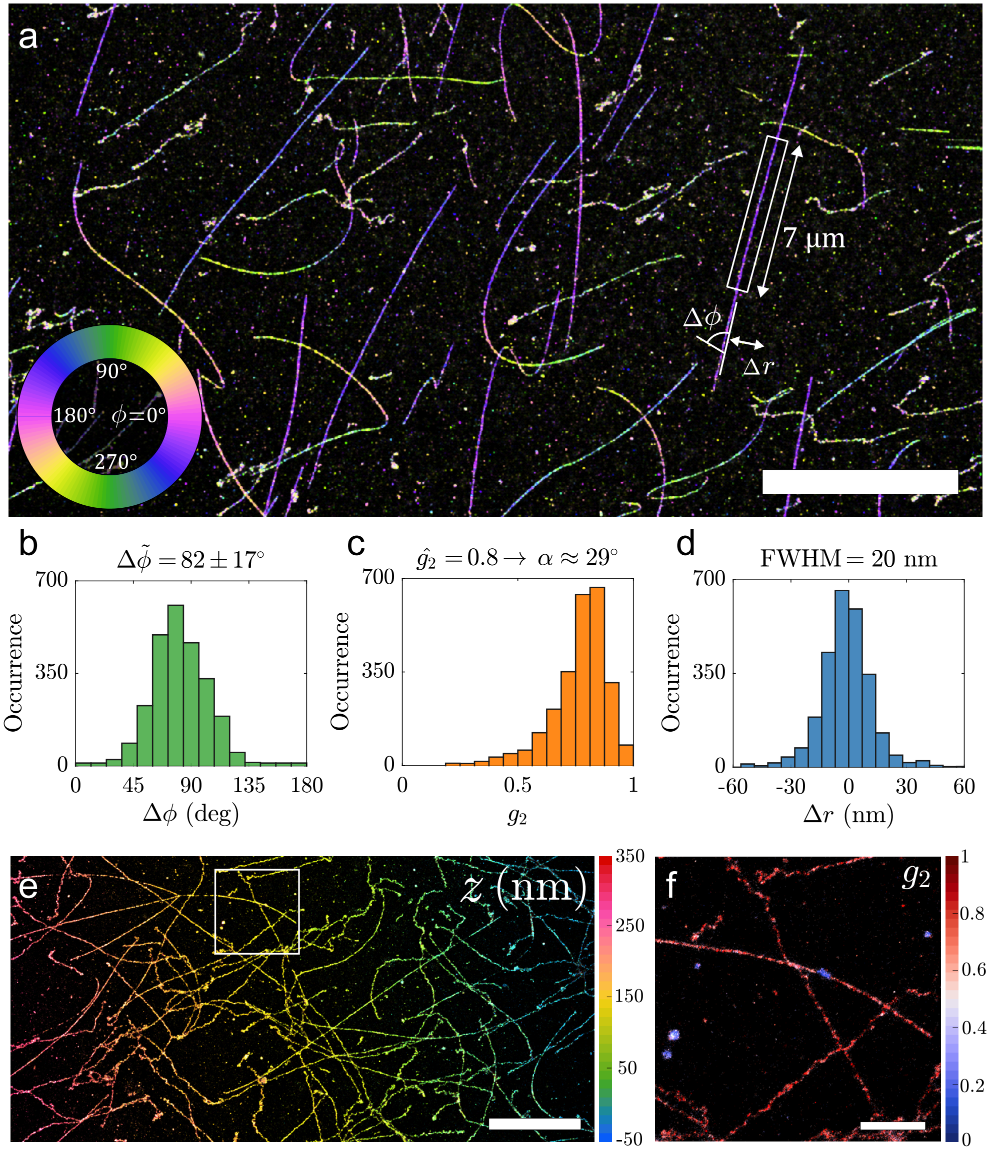

Figure 5.4: Super-resolution image of λ-DNA. **(a)** λ-DNA colorized as a function of the azimuthal angle. **(b)** Relative azimuthal angle histogram ($\Delta\phi$) with respect to the DNA axis from the strand highlighted in (a) ($\Delta\phi = 82°, \mathrm{MAD}(\Delta\phi) = 17°$). **(c)** Distribution of g_2 from the same strand, the fitted peak $g_2 = 0.8$ corresponds to a wobble cone semi-angle $\alpha = 29°$. **(d)** Position deviation from the spline fit to the DNA axis with a Full-Width Half-Maximum (FWHM) of 20 nm (Filtered to $35° \leq \theta \leq 145°$). **(e)** Tilted λ-DNA sample colorized as a function of z-position. **(f)** λ-DNA from highlighted region in (e), colorized as a function of g_2. Scale bars are (a) 10 μm, (e) 5 μm, (f) 1 μm.

(MAD) of 17° (Fig. 5.4(b)). This is essentially the same as found before ($\Delta\phi = 87^\circ$ and $\mathrm{MAD}(\Delta\phi) = 18^\circ$) [39] and similar to measurements with YOYO [42, 43]. The degree of orientational constraint g_2 along the strand is estimated with a peak at $g_2 = 0.8$, which corresponds to a maximum semi-angle $\alpha \sim 29^\circ$ in the framework of the wobble-in-cone model (Fig. 5.4(c)), slightly larger than $\sim 22^\circ$ found previously [39, 42]. All these parameters are estimated while attaining a lateral resolution (20 nm FWHM λ-DNA line-width) typical for BALM with dimeric dyes [34, 35] (Fig. 5.4(d)).

PSF fitting methods are sensitive to knowing the experimental parameters (like NA, refractive index etc.) and the Vortex PSF is no exception. The influence of variations of aberrations across the FOV has been investigated and mitigated by creating an aberration map for our microscope (see discussion in section 5.2.2 and Methods (5.4)). Spherical aberration can, however, vary easily from sample to sample depending on the refractive index, thickness of the cover slip and the setting of the correction collar. Pushing the biases of our method to levels below the precision requires caution when using catalogue values. E.g. using the catalogue value for the refractive index of the cover slip ($n = 1.523$) leads to a bias of 8.1 nm between localizations with $\theta < \pi/2$ and $\theta > \pi/2$ (Supplementary Fig. 5.7). Using an optimized cover slip refractive index of $n = 1.5209$ this bias is reduced to just 0.8 nm. Without the fine drift correction and optimized refractive index setting the FWHM of localizations of a λ-DNA strand would be 35 nm. Furthermore if the calibrated field-dependent aberrations were not taken into account in the fitting model, the localization distribution would become non-Gaussian with a λ-DNA line-width that is even twice broader (73 nm FWHM, see Supplementary Fig. 5.8).

To demonstrate the ability to resolve the lateral structure independent of defocus we use an intentionally tilted λ-DNA sample. This sample is shown in Fig. 5.4(e), where the estimated z position reveals the slope of the tilted λ-DNA sample. Comparison of the slope of the tilted and non-tilted data set (Supplementary Fig. 5.9) accurately retrieves the additional tilt of 0.42° (0.4° applied). The z localizations have a variation of 64 nm FWHM around the plane of the cover slip which is to be expected from a mean $\sqrt{\mathrm{CRLB}_z}$ of 25 nm. Figure 5.4(f) shows color-coding with the degree of orientational constraint g_2 that can be used to identify patches where binding to partially detached DNA strands and/or non-specific binding occurs. These are visible with a comparably free dipole value $g_2 \sim 0.3$, as opposed to the nearly fixed dipole value $g_2 \sim 0.8$ of the DNA strands. The achieved precision from these experiments, determined from repeated localizations of multiple on-events from the same emitter (Supplementary Fig. 5.10), is 5.4 nm and 29.7 nm in the lateral and axial dimension, and the azimuth and polar angle precision are 6.0° and 3.9° with an orientational constraint precision of 0.06. The localization and orientation precision values determined in this way are within the estimated error bars of the CRLB, with the photon distribution showing a median signal of 4600 photons and a median background of 10 photons per pixel (Supplementary Fig. 5.10).

The orientational binding landscape can be further investigated by analyzing correlations between the orientational parameters (θ, ϕ, g_2), combined with illuminating with different excitation polarizations. To that end we have imaged the same region

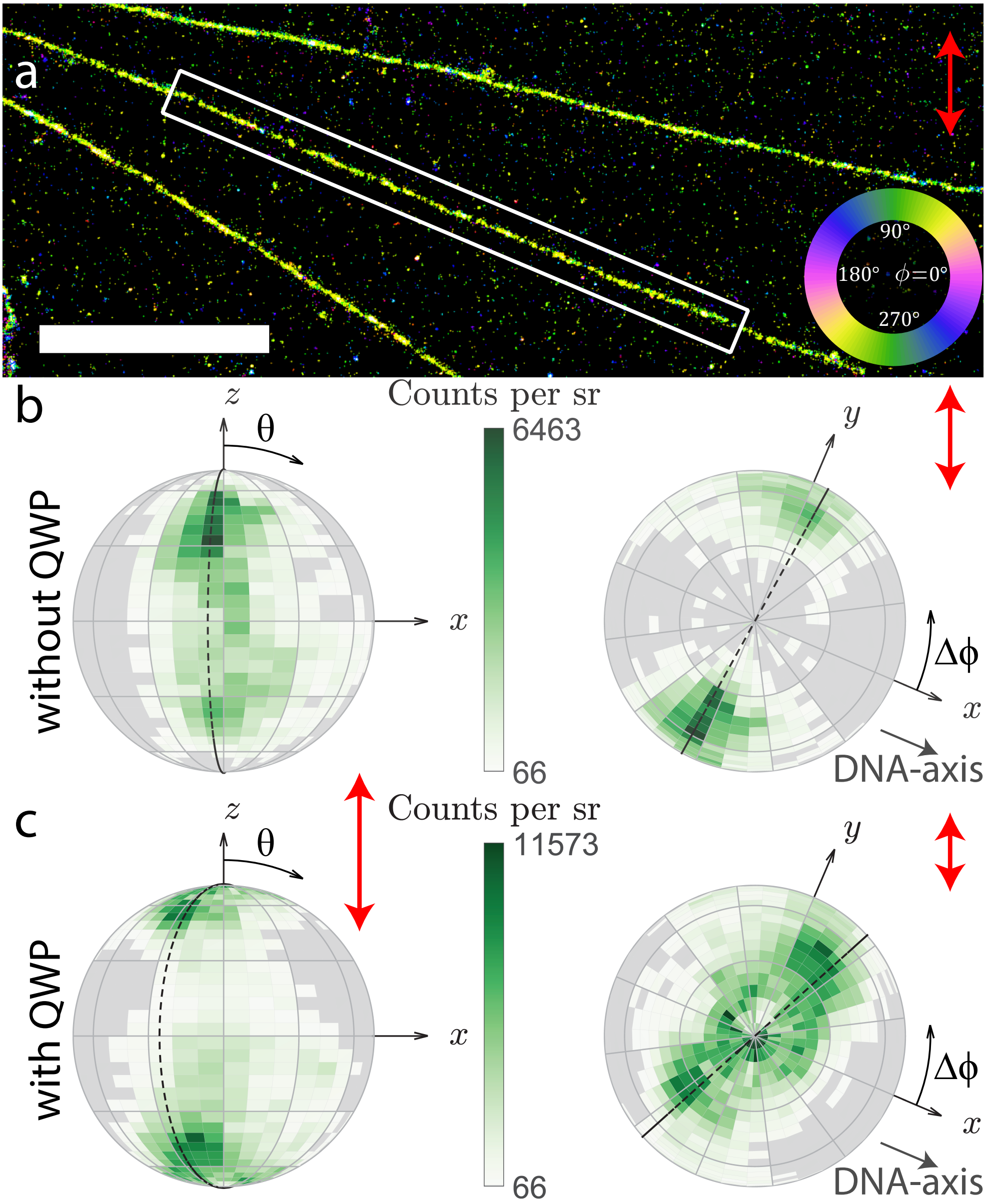

Figure 5.5: Correlation between orientation parameters of λ-DNA under different excitation polarization. **(a)** Super-resolution image of λ-DNA strands color coded with the same azimuthal map as Fig. 5.4(a) (scale bar is 3 μm). **(b)** Relative dipole orientations with respect to the DNA axis aligned along the x direction, illuminated without the QWP. On the left the view is aligned along the y axis, on the right is a top view aligned in the negative z direction. The dashed line highlights the primary population around $\Delta\phi = 84°$. **(c)** Relative dipole orientations of the same λ-DNA strand with a QWP in the illumination path. The dashed line highlights an additional population around $\Delta\phi = 65°$. Each bin spans $5°$ in the polar direction and $10°$ in the azimuthal direction, additionally there is a $30°$ coarse grid. Red arrows indicate the excitation polarization intensity.

both with and without a quarter waveplate (QWP) in the illumination laser path in Total Internal Reflection Fluorescence (TIRF) conditions (Fig. 5.5(a)). Without the QWP the excitation polarization is s-polarized (polarization extinction ratio of 240:1 and an excitation polarization orientation of $\theta = 90^\circ$ and $\phi = 90^\circ$), most effectively exciting molecules around $\theta = 90^\circ$ and $\phi = 90^\circ$ (Fig. 5.5(b)). With a QWP the polarization is less in-plane and more out-of-plane resulting in less selective excitation (polarization extinction ratio of 3:1 and a primary excitation polarization orientation of $\theta = 15^\circ$ and $\phi = 90^\circ$). This results in a polar distribution with more localizations around $\theta = \pm 40^\circ$ (Fig. 5.5(c)). Without the QWP we find the expected relative angle of $\Delta\phi = 87^\circ$ between the fluorophore and DNA axes with almost no dependence on the polar angle (Fig. 5.5(b)). With the addition of the QWP a correlation between the polar and azimuthal angle becomes visible. Next to the population of molecules with close to in-plane orientations, that still have the expected relative angle $\Delta\phi = 84^\circ$, a second population of molecules with more out of plane angles $\theta = \pm 40^\circ$ appears, that has a relative angle of $\Delta\phi = 65^\circ$ in Fig. 5.5(c)). These correlations between the orientational parameters are only found in the DNA experiments and are independent of the DNA orientation (Supplementary Fig. 5.11). Control experiments on fixed single molecules in air and PMMA show a uniform distribution over the azimuthal angles with no correlation to polar angle or degree of orientational constraint (Supplementary Fig. 5.12). Supplementary Table 5.1 summarizes the localization density of individual analyzed DNA strands for all relevant figures.

One would expect a uniform polar angle distribution for free DNA strands as Sytox Orange should intercalate in any orientation, averaging out any base pair selectivity along the strand. The proximity of the cover slip to the DNA strand could limit the physical space available for intercalators, thereby creating a non-uniform polar angle distribution and possibly shift the equilibrium azimuthal angle away from the orientation perpendicular to the DNA strand. However, this does not explain the preference for $\Delta\phi = 65^\circ$ over $\Delta\phi = 115^\circ$ for both polar angle regions. This may originate from the helical structure of the DNA and the binding potentials between the intercalator and the DNA.

A different hypothesis for the observed correlations between the orientational parameters is a change of the DNA structure to S-DNA due to overstretching. Previously it was found that overstretching results in a change of azimuthal angle to $\Delta\phi \sim 54^\circ$ [42], comparable to the value we find. The typical length of λ-DNA strands in our datasets is 17.4 μm which is 7.4% longer than its crystallographic length [47]. Although this corresponds to a relatively low percentage of overstretching it is possible that the binding affinity is not as low in the proximity of the cover slip as for free DNA strands, resulting in a relatively large population of tilted orientations compared to the DNA strand. We did not observe a correlation between the orientational parameters and the position along the DNA strand, that would correspond to domains along the strand with different orientational binding. This makes this hypothesis less likely.

5.2.6. Supercoiled DNA

With the help of the Vortex PSF we can investigate local orientation of twisted structures at the super-resolution level. Here we image supercoiled DNA, where external torsion is applied to the double stranded DNA to create a larger scale coiled structure. Such a twisted DNA can form a so-called plectoneme where two helices intertwine each other, similar to an old telephone cable, as illustrated in Figure 5.6(a). Plectonemes were generated in a 42-kbp DNA molecule that was tethered at both its ends to a cover slip, and then aligned to the surface by buffer flow application, and attached to the glass slide for imaging. While the imaging conditions, dye and buffer were the same as for the λ-DNA sample, the sample preparation method was altered significantly: To induce supercoiling, the DNA strands were initially attached to the cover slip at the both ends in the absence of Sytox Orange. Subsequently, Sytox Orange was introduced which locally unwinds DNA and generates torsional stresses in the torsionally-constrained DNA molecule, thus generating supercoils on DNA [48]. Shortly after, the flow of buffer containing a low concentration of formaldehyde aligned the supercoiled DNA in one direction and constrained the DNA to the cover slip surface (more detailed sample preparation protocol can be found in the methods (5.4)).

Orientation estimation of intercalated emitters with the Vortex PSF reveals various interesting properties of supercoiled DNA structures. Firstly the primary dipole orientation is different compared to the λ-DNA case where no additional torsion was applied. Figure 5.6(b) shows the orientation distribution of a supercoiled strand before it twists around itself. The highlighted peak around $\Delta\phi = 298^\circ$ and $\theta = 32^\circ$ (equivalent to $\Delta\phi = 118^\circ$ and $\theta = 148^\circ$) occurs on various strands. A 180° rotationally symmetric population also occurs on other DNA strands that are presumably oriented in the opposite direction with a peak around $\Delta\phi = 118^\circ$ and $\theta = 32^\circ$ (data not shown). This different azimuthal orientation found in the supercoiled DNA sample could be due to the different surface attachment protocol. This could change the physical space or electrostatic potential around the intercalator and DNA molecule.

Secondly, and more interestingly is that there appears to be a periodicity in certain orientations along the plectoneme. In Fig. 5.6(c) the azimuthal angles in the range of $90^\circ < \Delta\phi < 135^\circ$ shown in green to blue seem to occur periodically along the plectoneme. Figure 5.6(d) shows the individual localizations in different orientation subsets identified earlier along the region highlighted in Fig. 5.6(c). This periodic spacing is particularly clear in the subset of $98^\circ < \Delta\phi < 138^\circ$ and $12^\circ < \theta < 52^\circ$ shown in light blue, representing $\sim 10\%$ of all localizations. The localizations are binned in 6.5 nm intervals along the x-direction, such that an autocorrelation of the localization density can be calculated. The periodic pattern from Fig. 5.6(d) is more evident in the binned localizations in Fig. 5.6(e), compared to binned localizations from a torsionally relaxed DNA molecule (from Supplementary Fig. 5.14(b)) where no periodicity can be clearly identified. The autocorrelation along the entire plectoneme from Fig. 5.6(c) is shown in Fig. 5.6(f). The autocorrelation contains periodic peaks which is indicative of a periodic function. These periodic peaks are highlighted by equidistant black arrows and occur $\sim$ 150 nm apart. Two other plectonemes shown in Supplementary Fig. 5.13 have a periodicity of $\sim$ 122 nm and $\sim$ 130 nm. A

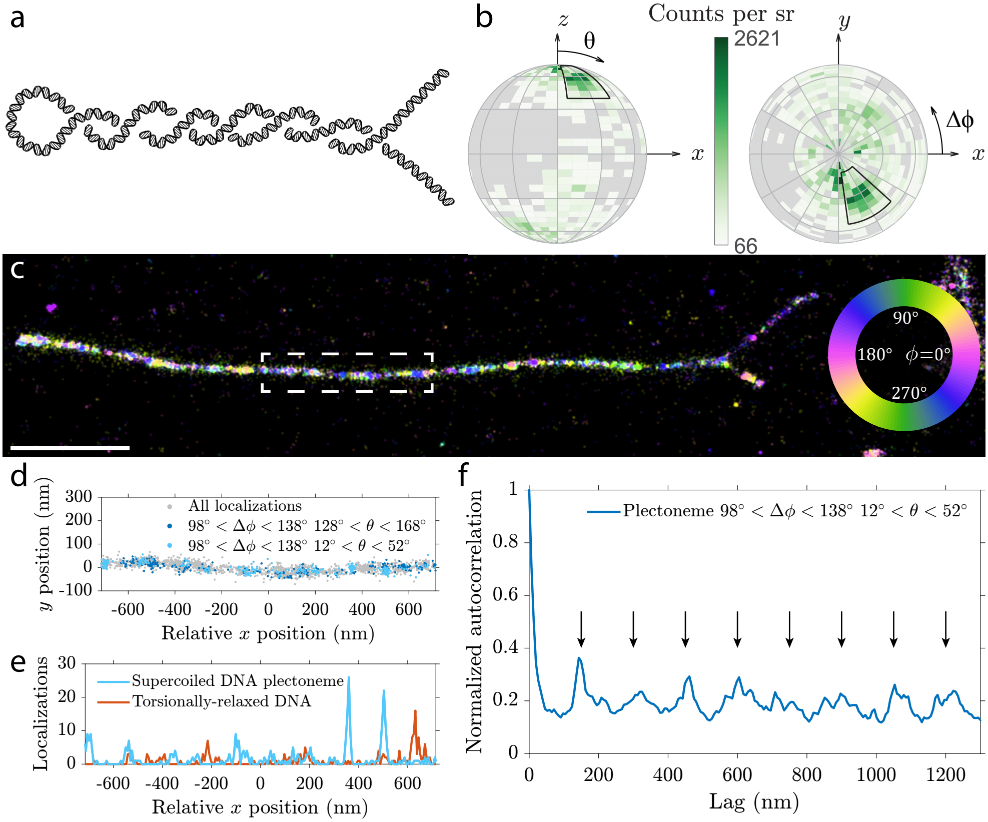

Figure 5.6: Orientation and spatial correlation in a supercoiled DNA plectoneme. **(a)** Diagram of a plectoneme formed by a single supercoiled DNA molecule where two strands are intertwined upon applied torsion. **(b)** Orientation distribution of a typical individual strand before overlap, with the DNA axis aligned in the x direction. The primary orientation analyzed in further subfigures is highlighted with the black region. Each bin spans 5° in the polar direction and 10° in the azimuthal direction, additionally there is a 30° coarse grid. **(c)** Azimuthal orientation of dipoles on a plectoneme (rotated 90 degrees clockwise to fit figure, scale bar 1 μm). **(d)** Localizations in different angular subsets from the plectoneme highlighted in (c), showing periodic clusters of localizations. **(e)** Localizations from (d) arranged in 6.5 nm bins along the x-direction compared to a torsionally relaxed DNA molecule. **(f)** Autocorrelation of localizations along the plectoneme in 6.5 nm bins. The equidistant arrows mark periodic peaks in the autocorrelation function, indicating a periodicity of ~ 150 nm.

few of the periodic peaks found in these orientational subsets can be identified in the full-data autocorrelation but cannot be directly identified as there are too many aperiodic peaks in the full-data autocorrelation. This periodicity was not found on DNA sections from the same dataset that are presumably torsionally relaxed as they are only tethered to the cover slip on one side (Supplementary Fig. 5.14). Additionally this periodicity is also not found in the λ-DNA datasets (Supplementary Fig. 5.15).

The length of the supercoiled DNA molecule estimated from localizations is 12.6 ± 0.4 μm (Supplementary Table 5.2). Compared to the crystallographic length the estimated length is 10% shorter, which may be attributed to the intertwining of the DNA molecule as the straight line projection is an underestimate of the actual DNA molecule length. The ratio between localization density on the coiled section and the individual strands before crossover is 1.94 ± 0.15 (Supplementary Table 5.2). This doubling of the localization density confirms there are two DNA strands in the coiled section. A significant change in the binding affinity in either of the sections could indicate a change in DNA conformation [42]. In future, it will be of interest to carry out a systematic study on many more plectonemes.

Lastly the orientation of supercoiled sections before and after the plectoneme appear to have opposing orientation shifts. The peak relative orientation in the region to the top right of a plectoneme is $\Delta\phi = 111^\circ$ $\theta = 36^\circ$ and to the bottom right is $\Delta\phi = -102^\circ$ $\theta = 29^\circ$, with the full distribution of all 3 section of a plectoneme shown in Supplementary Fig. 5.16. These two orientations appear shifted in opposite directions and are not 180 degree rotation symmetric which would be expected from a non-supercoiled strand.

Aside from the discernible plectoneme shape in the lateral localizations, there is further evidence of a difference between the supercoiled DNA and non-coiled λ-DNA. One difference is the change in the preferential binding orientations between the two datasets. Another is the apparent periodicity in localizations of certain orientations along the supercoiled DNA sections. Interestingly the periodicity of these localizations is on the same size scale as the expected superhelix pitch [49].

5.3. Discussion

Using the Vortex PSF we achieve accurate parameter estimation, avoiding the large position biases of several 10s of nm commonly seen with fixed dipole emitters in localization microscopy. Instead we reduce these biases to below the localization precision by matching experimental parameters like the refractive index, if one uses the nominal values for these quantities we find only a small bias of up to several nm. A key ingredient for our overall high accuracy is that we use calibrated field-dependent aberrations and supercritical angle fluorescence in the vectorial PSF model to avoid additional model mismatches. The relatively compact spot shape enables a more favorable trade-off between the precision of estimating the position and orientational parameters compared to a large PSF footprint. The vectorial PSF estimator achieves a precision close to the CRLB, and the CRLB for the Vortex PSF is relatively uniform for all possible emitter orientations. The SBR requirement of at least 200 (2000 signal photons and 10 background photons) can be met in typical SMLM experiments, and allows relatively short exposures of ~ 30 ms to be used.

To put the achievable precision of the Vortex PSF into perspective we have made a comparison to state-of-the-art PSF engineering methods for orientation estimation in Supplementary Table 5.3. Compared to the Tri-spot PSF [30], the Vortex PSF has a similar performance in the azimuthal angle, but the polar precision is significantly better. Methods focused on polarization splitting, for example a polarized PSF [21] or CHIDO [33], benefit from a better azimuthal precision as distribution of photons between the two polarization channels reveals more information about the polarization of light and consequently the orientation of the emitter dipole moment. This also appears to yield a slightly better precision in the wobble cone semi-angle α for methods with polarization splitting. Overall there is not a lot of variation in the lateral localization precision as all but the Tri-spot PSF are fairly compact PSFs. It is important to realize that currently most methods except the Vortex PSF and CHIDO cannot estimate the full 3D position along with both orientation angles and the rotational constraint. Comparing the only two methods that could estimate all these parameters simultaneously, we see that CHIDO has the advantage that the polarization splitting improves the azimuthal and axial precision. The estimator used in CHIDO, however, only gets to within 200%-500% of the theoretical CRLB limit on simulated PSFs. On experimental data this is even worse 500%-600% ($\sigma_{xy} = 13$ nm compared to $\sqrt{\mathrm{CRLB}_{xy}} = 2.3$ nm, $\sigma_z = 50$ nm compared to $\sqrt{\mathrm{CRLB}_z} = 7.5$ nm, $\sigma_\theta = 5^\circ$ compared to $\sqrt{\mathrm{CRLB}_\theta} = 0.8^\circ$, solid angle $\sigma_\Omega = 0.9$ compared to $\sqrt{\mathrm{CRLB}_\Omega} = 0.13$). This could be caused by aberrations in their system or by difficulties in characterizing the birefringence of their stress-engineered optical element. The estimation of parameters with the Vortex PSF reaches the CRLB in simulation over a wide range of signal to background ratios as shown in Supplementary Fig. 5.2. On experimental data we have shown that the Vortex PSF achieves a precision no worse than 30% above the CRLB on fixed molecules (section 5.2.3) and close to the CRLB on intercalators attached to DNA (Supplementary Fig. 5.10). Finally, the Vortex PSF has the virtue of simplicity in an optical setup compared to the Tri-spot PSF and CHIDO, which both use a custom phase-mask and polarization splitting. Summarizing, the polar precision is better with the Vortex PSF compared to other compact PSF designs, whereas the azimuthal precision is slightly worse compared to more experimentally complex polarization splitting methods. The Vortex PSF could be expanded to utilize polarization splitting and potentially improve both the azimuthal and axial precision. This would come at the cost of the simplicity of the optical setup.

We have visualized and measured orientational transitions of single molecules with metastable attachment to a glass surface. Furthermore we have applied our method to λ-DNA, corroborating previous findings that the azimuthal angle of the intercalator dipoles is almost perpendicular to the DNA axis. Our method uncovered a preferential polar orientation of intercalators attached to λ-DNA on a cover slip along with a correlation between the orientational parameters. The Vortex PSF also unveiled a periodicity along plectonemes on supercoiled DNA molecules which could be indicative of its supercoil periodicity.

We have applied the Vortex PSF to these cases to illustrate its functionality, but in principle, the Vortex PSF can be applied to any sparse sample of constrained dipole emitters. Combined with a sparsity inducing single molecule localization microscopy technique, super-resolution images can be complemented with orientation information to differentiate various sub-sets in the data, such as identifying different binding modes, different orientational configurations or local deformations. Nanoscale interactions could be investigated using chemical models on the single molecule scale.

An interesting question to address in future studies would be to compare the Vortex PSF to fundamental (quantum) limits of the estimation of orientational parameters [50, 51]. Another step to advance the Vortex PSF concept could be a speed up of the fitting algorithm by developing a GPU implementation, or by using spline interpolated models obtained from PSF calibrations [52] extended to take into account field-dependent aberrations. The feasibility of estimating the orientational confinement that is not rotationally symmetric around the preferential axis defined by the minimum of the orientational potential well in addition to the other parameters could also be investigated. Going from a uniaxially symmetric to a biaxially symmetric orientational confinement would bring the number of orientational parameters that must be estimated from three to five. Aside from the general degree or rotational constraint and the primary dipole orientation an additional parameter is needed to describe the primary direction of rotational diffusion and another for the degree of asymmetry. A reliable estimation of the then total number of 10 parameters (instead of 8) may require a more complex setup involving e.g. polarization detection in addition to the vortex phase plate. Another intriguing possibility is to study the characteristics of bis-intercalators with a double-dipole model. Finally, the analysis could be extended into the regime of slow orientational diffusion. In that regime the illumination polarization has an impact on PSF shape, implying that modulation of the illumination polarization into the method could generate useful information on the orientational constraint and diffusion of the molecule.

5.4. Methods

5.4.1. Fitting model

We use standard Maximum Likelihood Estimation (MLE) using an image formation model that describes the expected photon count across the image as a function of the molecule position $\vec{r}_0 = (x_0, y_0, z_0)$, signal photon count N of the entire PSF on the camera, background photons per pixel b, and dipole orientation $\Omega_0 = (\phi_0, \theta_0)$ with the degree of orientational constraint g_2, giving a total of 8 parameters. The underlying PSF model is the fully vectorial PSF model, as in earlier work [15, 25, 53–55], but now extended to estimate the dipole orientation along with the degree of orientational constraint. The image formation model is based on a weighted sum of the freely rotating dipole PSF and the fixed dipole PSF corresponding to the equilibrium dipole orientation [36], plus a constant background:

$$H(\vec{r}, \Omega) = N\left[\frac{(1-g_2)}{3} H_{\text{free}}(\vec{r}) + \frac{g_2}{3} H_{\text{fixed}}(\vec{r}, \Omega)\right] + \frac{b}{a^2} \tag{5.1}$$

where a is the pixel size and $0 \leq g_2 \leq 1$ represents the degree of orientational constraint, with the limiting cases of a fully free dipole $g_2 = 0$ and a fully fixed dipole $g_2 = 1$. This seems simplistic compared to more complex rotational diffusion models

[50, 56–58]. The appropriateness of the model for rotational diffusion faster than the fluorescence lifetime, however, is demonstrated in ref. [36]. An asymmetric rotational diffusion model would require 2 additional fitting parameters, raising the total amount of parameters to 10 which we expect is not realistic to fit with < 5000 photons. The vectorial PSF model takes supercritical angle fluorescence (SAF) [59, 60] into account. Without accounting for SAF, emitters in the proximity of the cover slip could have an additional position bias up to ~ 10 nm with a medium of water ($n = 1.33$) and ~ 25 nm in air ($n = 1$). Further details on the image formation model are given in Supplementary Note 1 (5.5.1).

5.4.2. Calibrated field-dependent aberrations

An important addition to the fitting model that we make is to take into account calibrated aberrations as done previously [54] and extended further to incorporate the field-dependence of aberrations [61]. We improve upon this treatment by modeling the field dependence of the aberration coefficients using the so-called Nodal Aberration Theory (NAT) instead of 2D polynomials of arbitrary order. This approach is valid for optical imaging systems with small field angles (ratio of FOV to focal length), such as telescopes or microscopes, and has been devised by Shack and Thompson [38], and later extended and used in optical design and characterization studies [62–64].

The key prediction of NAT is that the dependence of aberration coefficients on the field coordinates is well approximated by Taylor series of a low order, such that there are specific relations between the coefficients of these series for different aberrations. Such relations exist for example between the Taylor series for the two astigmatic and the two coma aberration coefficients, giving rise to zero aberration loci (two, respectively, one for astigmatism and coma), so-called ”nodes” in the FOV. The advantage of NAT in the current context is that the Taylor series fit for the different aberrations is more robust due to the predefined number of coefficients. Quantitative details on the aberration field dependence and the calibration procedure are given in Supplementary Note 2 (5.5.2). The aberration maps for 12 Zernike modes, determined from calibration measurements on 429 beads, are shown in Supplementary Fig. 5.5. The NAT predictions are in excellent agreement for astigmatism and coma, and good for the other aberration modes.

5.4.3. Simulation setup

Simulated point spread functions (PSFs) are generated according to the vectorial PSF model described in Supplementary Note 1 (5.5.1). The NA is taken to be 1.45, the wavelength 597.5 nm, the refractive index of the imaging medium 1.33, cover slip 1.523, immersion medium 1.518, a pixel size of 65 nm in object space and a region of interest (ROI) of 15x15 pixels. Unless stated otherwise, we take 4000 detected signal photons on the camera and 10 background photons per pixel, and we neglect readout noise but add Poisson noise to each image. The number of photons corresponds to the number of photons captured into the NA and thus spread over the entire FOV. The fraction of signal photons captured within the ROI compared to the entire FOV is typically 0.44 and 0.46 for the standard and Vortex PSF, respectively. The simulations are run for 10,000 randomized instances with coordinates taken from a uniform distribution over ± 1 pixel and molecular dipole orientations uniformly distributed on the unit sphere. That is, if u is a uniform random number from the distribution $U[0,1]$, the simulated angles are taken to be $\phi_0 = \pi u$ and $\theta_0 = \arccos(1-2u)$.

5.4.4. Sample preparation

Cover slips (22x22 mm No. 1.5, Marienfeld-Superior) and microscope slides (Microscope slides, Menzel Gläser Thermo Scientific) are cleaned by sonication in ethanol for 15 minutes and are then blown dry with nitrogen. All further mentions of cleaned cover slips and microscope slides are cleaned the same way except the cover slips for the λ-DNA samples. The microscope slides for the λ-DNA samples have a 5-10 mm hole drilled in them in advance to make it possible for the imaging medium to be added from above. Lambda DNA (λ-DNA) (Lambda DNA, Thermo Scientific) is aliquoted into 10 μL portions in PCR tubes and stored at -20 °C. Ascorbic acid (Ascorbic acid, Merck) is divided into ~3 mg portions in PCR tubes and the mass written on the tubes and stored at 4 °C. To make a pH 5.5 solution, 1 μL of 400 mM HCl and 600 mM Tris, is diluted in Milli-Q (MQ) water to a pH of 5.5 (approximately 90 mL). Part of a 5 mM stock solution of Sytox Orange (SYTOX Orange Nucleic Acid Stain, Invitrogen) is diluted in TE buffer (Tris-EDTA buffer solution pH 7.4, Supelco) by 4 tenfold steps to 500 nM and stored at 4 °C.

Fixed single molecule samples are made by sparsely embedding ATTO 565 in a thin layer of PMMA. 100 mg of PMMA (Poly(methyl methacrylate), Sigma-Aldrich) is dissolved in 10 grams of Toluene (Toluene, Sigma-Aldrich). ATTO 565 (ATTO 565, Sigma-Aldrich) is diluted in MQ water in 100 fold steps to ~ 5 μM. The ATTO 565 dilution is further diluted in PMMA/Toluene in 100 fold steps to a ~ 5 pM concentration. A 20 μL droplet of the mixture is placed on a clean cover slip in the spin-coater and is spun at 3000 RPM for 2 minutes. Two strips of double sided tape (Permanent Double Sided Tape, Scotch) are placed ~1.5 cm apart on a cleaned microscope slide and the cover slip is placed on top with the PMMA facing the tape side.

For single molecules without PMMA the same procedure is followed except now ATTO 565 is diluted only in MQ water to a final concentration of ~ 500 pM. After spin-coating the cover slip is placed, coated side down, on double sided tape on a microscope slide.

The λ-DNA samples are prepared by dropping a λ-DNA solution onto a rotating silanized cover slip [34, 35]. These cover slips are cleaned more extensively by sonication for 1 hour each in ethanol, acetone and then ethanol again. The cleaned cover slips are stored in ethanol. Before silanizing the surface they are removed from the ethanol and blown dry with nitrogen. An individual dry cover slip is then placed in 15 mL of Poly-L-lysine solution (Poly-L-lysine solution 0.01% sterile-filtered, Sigma-Aldrich) for 5 minutes and slightly shaken 2-3 times. Thereafter the silanized cover slip is rinsed with MQ water and left to dry overnight. A 10 μL $\lambda-$DNA aliquot is thawed and 990 μL of the pH 5.5 solution is added. For a silanized cover slip the optimal combing pH appears to be just below pH 5.5 [47]. 40 μL of this solution is applied in a drop wise fashion to the silanized cover slip on the spin-coater rotating at 2500 RPM for 30 seconds. Thereafter the speed is increased to 7000 RPM and 5 mL of MQ water is applied to rinse away non attached DNA and left spinning for

5

2 minutes to dry. A square hole is cut into a piece of double sided tape (64621, Tesa) and placed around the pre-drilled hole in the microscope slide. The cover slip is placed on the tape and pressed down with the λ-DNA side towards the tape. The ascorbic acid is hydrated with TE buffer to a concentration of 200 mM just before the experiment. 25 μL of the ascorbic acid dilution is mixed with 5 μL of 500 nM Sytox Orange and 470 μL of TE buffer. 200 μL of the imaging buffer with a final concentration of 5 nM Sytox Orange and 10mM ascorbic acid in TE buffer is added to the sample through the hole in the microscope slide while on the microscope, focusing and imaging starts as soon as possible.

To determine the aberration maps, 180 nm orange bead samples were used. A 1/100 dilution of 180 nm orange beads (PS-Speck Microscope Point Source Kit, ThermoFisher) is made by mixing 10 μL of beads with 990 μL of MQ water. Using 10 μL of this dilution, 7-10 small droplets are placed around the centre of the cleaned cover slip and allowed to dry for ~3 hours or overnight. Two strips of double sided tape (Permanent Double Sided Tape, Scotch) are placed ~1.5 cm apart on a cleaned microscope slide and the cover slip is placed on top with the beads facing the tape side. When ready to image a 20-30 μL droplet of the mounting medium (in our case immersion oil) is placed on the edge between the cover slip and microscope slide. The capillary action gradually distributes the mounting medium between the cover slip and the microscope slide. The sample is placed on the microscope when the mounting medium has reached the other side.

The plectonemic supercoiled DNA were prepared as follows. Coilable DNA constructs of 42kb in length were synthesized via cloning, PCR and DNA ligation [65]. We used linearized cosmid-I95 plasmid DNA [66] and extended both the ends of the DNA with short DNA fragments containing biotinylated dUTPs. The resulting biotin labelled DNA molecules were purified with size exclusion chromatography. The DNA was then introduced to a flow cell with a flow rate of 2 μL/min and subsequently immobilized to the surface via streptavidin-biotin linkage. After observing a reasonable density of double-tethered DNA on the surface, imaging buffer (40 mM TRIS-HCl pH 7.5, 50 mM NaCl, 2.5 mM MgCl2, 1 mM DTT, 5% (w/v) D-dextrose, 2 mM Trolox, 40 μg/mL glucose oxidase, 17 μg/mL catalase) containing 250 nM of Sytox Orange was introduced to the flow cell in order to generate positive supercoiled DNA, which can be manifested by the characteristic dynamics of plectonemic supercoiled DNA reported previously [48, 67]. To fix the plectoneme containing supercoiled DNA onto the surface, we introduce 0.2 % of formaldehyde in the same imaging buffer with 250 nM of Sytox Orange. The buffer was injected with a large flow rate of 40-50 μL/min in order to fully stretch out the plectonemes and avoid formation of DNA clumps before they adhere to the surface, providing a better alignment quality for the angle-resolved super-resolution localization imaging.

5.4.5. Imaging protocol

The main component of the optical setup is a standard microscope (Ti-E, Nikon) with a 100x 1.49 NA objective (Supplementary Fig. 5.17). A 4F relay system consisting of two 100 mm lenses (AC508-100-A-ML, Thorlabs) relays the original image plane of the microscope to the camera ((Zyla 4.2 PLUS, Andor) or (ORCA-Flash4.0 V2, Hamamatsu) for the supercoiled data) and a vortex phase plate (V-593-10-1, vortex photonics) is placed in the back focal plane between the two lenses. The vortex phase plate is mounted on a small XYZ stage (CXYZ05/M, Thorlabs) for alignment and a kinematic stage (KB75/M, Thorlabs) for quick removal and placement.

The Vortex PSF should be used with a relatively narrow emission bandwidth up to ~ 60 nm. The design wavelength of the phase plate does not need to exactly match the emission peak as long as both parameters are known and set correctly in the estimator. For fixed dipole emission PSF fitting, the fluorophore must have a single molecular dipole moment, this makes bis-intercalators like TOTO [68] and YOYO [69] unsuitable. These dimeric fluorophores have two transition dipole moments between which the excitation energy can hop [70], resulting in emission from either of the two transition dipoles almost perpendicular to one another.

In the proof-of-principle experiments ATTO 565 is embedded in PMMA, where the polymer immobilizes the fluorophores and has a refractive index of $n = 1.49$ close to that of immersion oil ($n = 1.518$). Two z-stack acquisitions with a 100 nm step-size, 600 ms exposure and $300\ \mathrm{W/cm}^2$ epi-illumination are taken in quick succession with and without the vortex phase plate to compare the Vortex PSF to defocused orientation fitting.

To create a sparse sample of individual dipole emitters that are less constrained and can reorient over time, a low concentration of ATTO 565 without PMMA is spin-coated onto a cover slip. Initially the region is imaged with epi-illumination which bleaches the in-plane molecules which showed almost no re-orientation. The remaining single molecules are excited with $3\ \mathrm{kW/cm}^2$ in TIRF conditions as the z-component of the TIRF field more effectively excites out-of-plane molecules. A relatively long exposure time of 900 ms is used to yield raw data with a very high SNR.

For the λ-DNA, after applying a fresh batch of imaging buffer and focusing, 20,000 frames are acquired with a single frame exposure time of 100 ms. The sample is illuminated with $3\ \mathrm{kW/cm}^2$ circularly polarized total internal reflection excitation. This results in an excitation profile that is approximately half in-plane and half out-of-plane, and a reduced background due to the limited penetration depth. Initially the DNA is relatively densely populated with fluorophores but after onset of laser illumination the density drops to single-molecule levels within a few hundred frames. It is not trivial to verify if this leads to a significant increase in the amount of bound and bleached molecules as the dissociation rate of Sytox Orange is also quite high [41].

5.4.6. Vortex phase plate alignment

The vortex phase plate or spiral phase plate is the same phase profile used to create high-quality donut-shaped depletion and excitation profiles from Gaussian laser beams for STED [37] and MINFLUX [71]. Coincidentally this is also the lowest order component of a Double-helix PSF [72], and a discretized version of a spiral phase plate with only 3-4 phase-steps could be used to generate a rotating PSF [73]. Here we use a vortex phase plate with a single spiral from 0 to 2π in 64 steps (V-593-10-1, vortex photonics).

A 1:1 optical relay is built on the emission path of the microscope to place the vortex phase plate in a plane conjugate to the back focal plane of the objective as illustrated in Supplementary Fig. 5.17. The phase plate is placed roughly halfway between the two relay lenses. To align the vortex phase plate, defocused images are taken of 1 μm beads (TetraSpeck Fluorescent Microspheres Size Kit, ThermoFisher) and diagonally opposing regions are recorded (Supplementary Fig. 5.18(a)). If the vortex phase plate is aligned properly, all the PSFs should have the same shape throughout the FOV as shown in Supplementary Fig. 5.18(b). When the vortex phase plate is not in the correct axial position the PSF will vary over the field of view. This is because light from different areas in the sample do not pass through the vortex phase plate in the same place as it is not conjugate to the back focal plane of the objective. The main parts of the PSF to observe for alignment is the peak in the center that does not move when the phase plate is moved and a ring that moves with the phase plate. The process of aligning the vortex phase plate involves moving the rings to be centered over the peaks over the entire FOV. The vortex phase plate should be translated along the optical axis until all the beads look the same throughout the field of view (same offset between the peak and the ring throughout the FOV) (Supplementary Fig. 5.18(c)-(d)). Thereafter the vortex phase plate can be shifted horizontally and vertically so the dark spot overlaps with the center of the bead (Supplementary Fig. 5.18(e)-(f)). Lastly the beads are translated along the optical axis and defocused in the opposite direction to verify that the rings also overlap with the center of the bead there. If the rotation direction of the vortex phase plate is unknown ($K(\vec{\rho}) = \beta/(2\pi)$ or $K(\vec{\rho}) = -\beta/(2\pi)$), then fixed single molecules can be fitted with both orientations and the correct setting will have a visually better fit (should be especially evident on molecules with $\theta = \pm 45°$).

5.4.7. Data analysis

The acquired images are offset and gain corrected to convert analog-to-digital units (ADUs) into photon numbers [74]. Then, candidate pixels with a single molecule signal are identified using an intensity threshold typically chosen as the background plus a constant of around 10 photons. These candidate pixels are segmented into ROIs of size 15×15 pixels centered at the local centroid. The local centroid gives a better first estimate of the emitter's position than the local maximum due to the Vortex PSF shape. These ROIs are fitted with a vectorial PSF model using Maximum Likelihood estimation (MLE). The vectorial PSF model incorporates emitter parameters described in Supplementary Note 1 (5.5.1) and is further tailored to take field-dependent aberrations into account described in Supplementary Note 2 (5.5.2). The optical parameters and experimental settings are set to match the experimental setup in Supplementary Fig. 5.17.

In the fitting routine potential outliers and poor localizations are filtered out as follows. The number of iterations in the MLE is terminated if the relative difference between successive log-likelihood values in the iteration drops below 10^{-6} or if the maximum number of iterations, which is set to 30, is reached. Typically fitting converges within 20 iterations, events are rejected if the maximum number is reached without convergence. Moreover, when the estimated molecule position is more than

3 pixels away from the center pixel in the ROI, it is rejected. Finally, converged localizations are tested with a normalized chi-squared (χ^2) test [54]. If a localization has a χ^2 value outside the region $0.75 \leq \chi^2 \leq 3$, it is also rejected. Additional filtering is specified where used.

The resulting localizations are corrected for sample drift following the method of Schnitzbauer et al. [75], implemented in the Picasso software (v0.2.8), available at github.com/jungmannlab/picasso. The slow timescale lateral drift for the λ-DNA experiments was on the order of 1.5 pixels (~ 100 nm) over 30 minutes. Additionally a fine drift correction is applied to this dataset, utilizing straight λ-DNA sections and minimizing the deviations from a spline fit to the DNA axis over time. Supplementary Figure 5.19 shows that these deviations of two different strands with the same orientation are correlated and can be used to improve the drift correction. For this dataset 27 strands of varying orientations are analyzed and the Δr deviations are projected into x and y deviations. These x and y deviations are then averaged with a weighting prioritizing good localization precision and a high number of localizations to generate the fine drift trajectory. This reduces the residual drift from a standard deviation of 7.6 nm (Supplementary Fig. 5.19(a)) to 3.7 nm (Supplementary Fig. 5.19(b)). Subsequently localizations of the same emitter during the emitter's on-time are linked under the condition that the position and orientation estimate between subsequent localizations is less than 3 times the largest uncertainty as shown in Supplementary Fig. 5.10.

All images are rendered with a Gaussian blurring using the scripts from the INSPR toolbox [76]. The images in Fig. 4 are rendered with a super-resolution pixel size of 6.5 nm, the image in Fig. 5 with a pixel size of 20 nm, and the image in Fig. 6 with a pixel size of 13 nm.

Estimating the axes of single DNA strands is performed by fitting a spline to the localization data. First, a DNA strand is selected from the localization data incorporating all localizations. A spline curve is fitted to the localizations using MATLAB's built-in function *fit()* employing a smoothing spline with a smoothing parameter of 10^{-1}. In order to determine the azimuthal orientations of molecules with respect to the DNA axis, the shortest distance between a given molecule and a point on the spline curve is determined, and the tangent line to the point on the spline is calculated using finite differences, giving the local DNA-strand orientation.

5.5. Appendix: Supplementary Information

5.5.1. Supplementary Note 1: Imaging PSF model

We use a full vectorial PSF model in the Vortex PSF fitting, as initially described in [25], and extend it to incorporate varying degrees of orientational constraint and orientational diffusion [36]. The expected photon count at pixel l depends on the molecule position $\vec{r}_0 = (x_0, y_0, z_0)$, the signal photon count N, background photons per pixel b, and the molecular orientation $\Omega_0 = (\phi_0, \theta_0)$ together with the degree of orientational constraint g_2, giving a total of 8 parameters. The integration of the model H gives the expected photon count:

$$\mu_l = \int_{D_l} \mathrm{d}x\mathrm{d}y\, H(\vec{r} - \vec{r}_0, \Omega) \tag{5.2}$$

where the integration is over the pixel area D_l of size $a \times a$. The image formation model is taken to be the weighted sum of the free dipole PSF and the orientation-dependent fixed dipole PSF, where the relative weights are determined by g_2, plus a constant background. There are more elaborate rotational diffusion models [50, 56–58] however this model is appropriate and sufficient for rotational diffusion with a rotational relaxation time faster than the fluorescence lifetime [36], independent of the type of rotational constraint. This model can be written as

$$H(\vec{r}, \Omega) = N\left[\frac{(1-g_2)}{3} H_{\text{free}}(\vec{r}) + \frac{g_2}{3} H_{\text{fixed}}(\vec{r}, \Omega)\right] + \frac{b}{a^2} \tag{5.3}$$

The PSF of a fixed dipole emitter is

$$H_{\text{fixed}}(\vec{r}, \Omega) = \sum_{h,j=x,y,z} A_{hj}(\vec{r}) d_h(\Omega) d_j(\Omega) \tag{5.4}$$

where $d_h(\Omega)$ are the components of the dipole unit vector

$$\vec{d}(\Omega) = (\sin\theta\cos\phi, \sin\theta\sin\phi, \cos\theta). \tag{5.5}$$

The average PSF of a freely rotating dipole emitter is

$$H_{\text{free}}(\vec{r}) = \frac{1}{3} \sum_{h=x,y,z} A_{hh}(\vec{r}) \tag{5.6}$$

with

$$A_{hj}(\vec{r}) = \sum_{k=x,y} w_{kh}(\vec{r}) w^*_{kj}(\vec{r}) \tag{5.7}$$

where the functions $w(\vec{r})$ represent the electric field component in the image plane proportional to the emission dipole component $j = x, y, z$. These functions can be expressed as integrals over the pupil plane:

$$w_{kj}(\vec{r}) = \frac{1}{\pi} \int \mathrm{d}^2\rho\, A(\vec{\rho}) \exp\left(\frac{2\pi i W(\vec{\rho})}{\lambda}\right) q_{kj}(\vec{\rho}) \exp(-i\vec{k} \cdot \vec{r}) \tag{5.8}$$

where the integration is over normalized pupil coordinates $\vec{\rho}$, $A(\vec{\rho})$ is the aplanatic amplitude correction factor, and $q_{kj}(\vec{\rho})$ are the polarization vectors given in full detail in [15]. The wavevector $\vec{k}(\vec{\rho})$ depends on the normalized pupil coordinates by

$$\vec{k}(\rho) = \frac{2\pi}{\lambda}\left(\mathrm{NA}\rho_x, \mathrm{NA}\rho_y, \sqrt{n^2 - \mathrm{NA}^2\vec{\rho}}\right) \tag{5.9}$$

with n the refractive index of the medium.

The aberration function $W(\vec{\rho}) = K(\vec{\rho}) + W_{\text{abb}}(\vec{\rho})$ includes the zone function of the vortex phase plate: $K(\vec{\rho}) = \beta/(2\pi)$ where $\beta = \arctan\left(\rho_x/\rho_y\right)$ is the azimuth pupil coordinate, and further includes field-dependent aberrations $W_{\text{abb}}(\vec{\rho})$ as described in Supplementary Note 2 (5.5.2).

The imaging model's partial derivatives with respect to the parameters are needed for the MLE optimization routine. These are easy to evaluate for the signal photon count N, background photons per pixel b, and diffusion weights g_2 as these appear linearly in the imaging model μ_k. The derivatives with respect to the fit parameters $\Theta = (x, y, z, \phi, \theta)$ are similar to [53] but now slightly more elaborate:

$$\begin{aligned}\frac{\partial \mu_l}{\partial \Theta} = N \Bigg[& \frac{1-g_2}{3} \sum_{k=x,y} \sum_{j=x,y,z} \int \mathrm{d}^2\rho \, 2\Re\left\{ w_{kj}^{*} \frac{\partial w_{kj}}{\partial \Theta} \right\} \\ & + \frac{g_2}{3} \sum_{k=x,y} \sum_{j=x,y,z} \int \mathrm{d}^2\rho \, 2\Re\left\{ w_{kj}^{*} d_j \frac{\partial \left(w_{kj} d_j \right)}{\partial \Theta} \right\} \Bigg] \end{aligned} \tag{5.10}$$

where $w_{kj} = w_{kj}(r - r_0)$ and $d_j = d_j(\Omega)$. The derivatives of w_{kj} with respect to the coordinates of the emitter are needed here:

$$\begin{aligned}\frac{\partial w_{kj}(\vec{r} - \vec{r}_0)}{\partial \vec{r}_0} = & \frac{i}{\pi} \int \mathrm{d}^2\rho \, A(\vec{\rho}) \exp\left(\frac{2\pi i W(\vec{\rho})}{\lambda} \right) q_{kj}(\vec{\rho}) \\ & \times \vec{k}(\vec{\rho}) \exp(-i\vec{k}(\vec{\rho}) \cdot (\vec{r} - \vec{r}_0)) \end{aligned} \tag{5.11}$$

as are the derivatives of the dipole vector $\vec{d}(\Omega)$ with respect to the polar and azimuthal angles:

$$\frac{\partial \vec{d}(\Omega)}{\partial \phi} = (-\sin\theta \sin\phi, \sin\theta \cos\phi, 0) \tag{5.12}$$

$$\frac{\partial \vec{d}(\Omega)}{\partial \theta} = (\cos\theta \cos\phi, \cos\theta \sin\phi, -\sin\theta). \tag{5.13}$$

5.5.2. Supplementary Note 2: Field dependent aberration coefficients

The aberrations function $W_{\text{abb}}(\vec{\rho})$ is conventionally expressed as a linear sum of the root mean square (RMS) normalized Zernike polynomials $Z_n^m(\vec{\rho})$: $W_{\text{abb}}(\vec{\rho}) = \sum_{n,m} A_n^m Z_n^m(\vec{\rho})$. In most studies the Zernike coefficients are constant parameters. In this study we follow the approach of [61] and [77] by taking the dependence on the position in the FOV into account, i.e. we take the Zernike coefficients to be functions of the field coordinates (x, y). These functions $A_n^m(x, y)$ are determined from a calibration procedure. We make a through-focus image stack of a set of beads randomly spread over the FOV, as opposed to the procedure of [77], where a single bead is positioned on a series of grid positions by the microscope stage. For each bead the Zernike coefficients are retrieved using our previous method [54]. According to Nodal Aberration Theory (NAT), the aberration coefficients $A_n^m(x, y)$ can be suitably described by low order Taylor series in x and y:

$$A_n^m(x, y) = \sum_{jk} \gamma_{nmjk} x^j y^k. \tag{5.14}$$

The set of coefficients γ_{nmjk} of these Taylor series for different positions are related [38], which we use to our advantage as this decreases the number of parameters to be determined from experiments. The NAT-model is fitted to the measured A_n^m at the beads' positions by a straightforward least-squares fit. With this calibration procedure, the estimated Zernike coefficients can effectively be interpolated over the entire imaging field.

We take into account Zernike modes with $n + |m| \leq 6$, which include primary and secondary astigmatism, coma, spherical aberration, and trefoil, and use the analysis of [78], where polynomials in the field coordinates up to order $6 - n$ are used in the NAT description of the field dependence of the contributing Zernike modes.

In the following, these expressions are summarized as implemented in our fitting using a set of perturbation coefficients $(\chi, \xi, \delta, \mu, \eta, \kappa, \nu)$. Primary astigmatism with perturbation coefficients χ is given by:

$$\begin{aligned} A_2^{-2} &= \chi_1(x^3y + xy^3) + \chi_2(x^2y + y^3) + \chi_3(x^3 + xy^2) \\ &\quad + \chi_4(x^2 + y^2) + \chi_6(xy^2 - x^3) + \chi_7 2xy^2 \\ &\quad + \chi_8 y - \chi_9 x + \chi_{10}(2xy^2) + \chi_{11} x + \chi_{12} y + \chi_{13} \end{aligned} \tag{5.15}$$

$$\begin{aligned} A_2^{2} &= \chi_1(y^4 - x^4) - \chi_2(x^3 + xy^2) + \chi_3(x^2y + y^3) \\ &\quad + \chi_5(x^2 + y^2) - \chi_6 2x^2y + \chi_7(y^3 - x^2y) \\ &\quad + \chi_8 x + \chi_9 y + \chi_{10}(y^2 - x^2) + \chi_{11} y - \chi_{12} x + \chi_{14}, \end{aligned} \tag{5.16}$$

primary coma with coefficients ξ by:

$$\begin{aligned} A_3^{-1} &= \xi_1(x^3 + xy^2) + \xi_2 x^2 + \xi_3 xy + \xi_4 x + \xi_5(x^2 + y^2) \\ &\quad + \xi_7 y + \xi_8 x + \xi_9 \end{aligned} \tag{5.17}$$

$$\begin{aligned} A_3^{1} &= \xi_1(y^3 + x^2y) + \xi_2 xy + \xi_3 y^2 + \xi_4 y + \xi_6(x^2 + y^2) \\ &\quad + \xi_7 x - \xi_8 y + \xi_{10} \end{aligned} \tag{5.18}$$

and primary spherical aberration with coefficients δ by:

$$A_4^0 = \delta_1(x^2+y^2)+\delta_2 x+\delta_3 y+\delta_4. \tag{5.19}$$

The next aberration order, trefoil with coefficients μ is given by:

$$A_3^{-3} = \mu_1(3y^2x - x^3)+\mu_2(y^2-x^2)+\mu_3 2xy+\mu_4 x+\mu_5 y+\mu_6 \tag{5.20}$$

$$A_3^{3} = \mu_1(y^3 - 3x^2y)-\mu_2 2xy+\mu_3(y^2-x^2)+\mu_4 y-\mu_5 x+\mu_7 \tag{5.21}$$

secondary astigmatism with coefficients η by:

$$A_4^{-2} = \eta_1 2xy+\eta_2 y+\eta_3 x+\eta_4 \tag{5.22}$$

$$A_4^{2} = \eta_1(y^2-x^2)-\eta_2 x+\eta_3 y+\eta_5 \tag{5.23}$$

secondary coma with coefficients κ by:

$$A_5^{-1} = \kappa_1 y+\kappa_2 \tag{5.24}$$

$$A_5^{1} = \kappa_1 x+\kappa_3 \tag{5.25}$$

and finally we include secondary spherical aberration, which is expected to be constant in the included polynomial order but here modeled to match equation (5.19), with coefficient ν:

$$A_6^0 = \nu_1(x^2+y^2)+\nu_2 x+\nu_3 y+\nu_4. \tag{5.26}$$

The independent perturbation coefficients are determined using a least-squares fit over all bead measurements to relate the perturbation coefficient to the Zernike coefficients for the field coordinates. Once the perturbation coefficients are known, the equations (5.15 – 5.26) are used as predictors based on the detected molecule position. The retrieved field-dependent Zernike aberration coefficients for our microscope are shown in Supplementary Fig. 5.5.

5.5.3. Supplementary Tables

Table 5.1: Localizations (locs) analyzed in each figure, along with the amount of localizations in an analyzed subset, estimated length and localization density.

Figure	Total # locs	# in subset	Length (μm)	Density (nm^{-1})[a]
Fig. 4(b-d)	6429	2375	7.02	0.34
Fig. 5(b)	4183	-	8.08	0.52
Fig. 5(c)	10409	-	7.93	1.31
Fig. 6(f)	9285	928	5.35	0.17
S.F. 13(b)	5646	509	3.74	0.14
S.F. 13(c)	7347	792	4.17	0.19
S.F. 14(b) $\tilde{\theta} = 148^\circ$	11485	1294	13.18	0.10
S.F. 14(b) $\tilde{\theta} = 32^\circ$	11485	1190	13.18	0.09
S.F. 14(c) $\tilde{\theta} = 148^\circ$	8737	1220	7.96	0.15
S.F. 14(c) $\tilde{\theta} = 32^\circ$	8737	921	7.96	0.12
S.F. 14(d) $\tilde{\theta} = 148^\circ$	4306	536	5.05	0.11
S.F. 14(d) $\tilde{\theta} = 32^\circ$	4306	337	5.05	0.07
S.F. 14(e) $\tilde{\theta} = 148^\circ$	7425	980	7.45	0.13
S.F. 14(e) $\tilde{\theta} = 32^\circ$	7425	538	7.45	0.07
S.F. 14(f) $\tilde{\theta} = 148^\circ$	6950	1034	6.85	0.15
S.F. 14(f) $\tilde{\theta} = 32^\circ$	6950	587	6.85	0.09
S.F. 14(g) $\tilde{\theta} = 148^\circ$	5189	543	5.61	0.10
S.F. 14(g) $\tilde{\theta} = 32^\circ$	5189	371	5.61	0.07
S.F. 15(a) $\tilde{\theta} = 148^\circ$	9153	579	7.88	0.07
S.F. 15(a) $\tilde{\theta} = 32^\circ$	9153	759	7.88	0.10
S.F. 15(b) $\tilde{\theta} = 148^\circ$	9153	1336	7.88	0.17
S.F. 15(b) $\tilde{\theta} = 32^\circ$	9153	1589	7.88	0.20

---

[a] Localization density is the ratio of localizations within the orientation subset divided by the length of the section. Unless the figure does not refer to a specific orientation subset, then it is the total number of localizations divided by the length.

Table 5.2: Localization (loc) density and length of different sections of the plectoneme construct. The two pre-coil parts are from the sections before overlap and intertwining itself.

Figure	Length (μm)[a]	Section	Loc density (nm^{-1})
Fig. 6(c)	1.00	pre-coil top	0.70
Fig. 6(c)	0.41	pre-coil bottom	1.13
Fig. 6(c)	5.81	coil	1.73
Total length (μm):	13.03	Density ratio:	1.89
S.Fig. 13(b)	1.54	pre-coil top	0.64
S. Fig. 13(b)	0.73	pre-coil bottom	1.02
S. Fig. 13(b)	5.01	coil	1.51
Total length (μm):	12.29	Density ratio:	1.82
S. Fig. 16(b)[b]	1.96	pre-coil left	0.80
S. Fig. 16(c)[b]	0.93	pre-coil right	0.87
S. Fig. 16(d)[b]	4.80	coil	1.76
Total length (μm):	12.49	Density ratio:	2.11

---

[a] The length here includes clusters at the initial DNA attachment site and where it turns around at the end of the plectoneme, this is longer than the length used for localization density analysis. For the localization density analysis, shorter uniform sections are analyzed.

[b] Same DNA molecule as Fig. 13(c).

Table 5.3: Theoretical precision limit (CRLB) comparison of various methods. The simulation parameters are set to match those from other methods, if unspecified our standard simulation parameters as described in the methods were used.

Method	N	b	σ_ϕ (°)	σ_θ (°)	σ_α (°)	σ_x (nm)	σ_y (nm)	σ_z (nm)
Tri-spot[a]	3,000	10	8	7	14	-	-	-
Vortex	3,000	10	8.4	2.2	23.4	2.7	3.1	-
xyPol[b]	380	2	4	15	19	10	10	-
Vortex	380	2	12.6	5.2	36.1	10.3	10.1	-
CHIDO[c]	10,000	0	0.4	0.5	6	0.85	0.95	3
Vortex	10,000	0	0.95	0.68	8.7	1.1	0.83	5.3
CHIDO[c]	10,000	250	1.1	1.6	13	2.8	2.6	9.2
Vortex	10,000	250	2.98	1.31	17	2.63	1.93	16.9

---

[a] Tri-spot [30], $\phi = 90^\circ$, $\theta = 90^\circ$, $g_2 = 1$, $\mathrm{NA} = 1.3$, $n_{\mathrm{medium}} = 1.518$, $\lambda = 600$ (nm), explicit values.

[b] xyPol (Polarized PSF) [21] $\phi = 135^\circ$ $\theta = 90^\circ$, $g_2 = 1$, $\mathrm{NA} = 1.4$, $n_{\mathrm{medium}} = 1.334$, $\lambda = 610$ (nm), pixelsize 58.5 (nm), values from graph.

[c] CHIDO [33], $\phi = 0^\circ$, $\theta = 90^\circ$, $g_2 = 1$, $\mathrm{NA} = 1.45$, $\lambda = 520$ (nm), pixelsize 67 (nm), ROI=21x21, values from graph.

5.5.4. Supplementary Figures

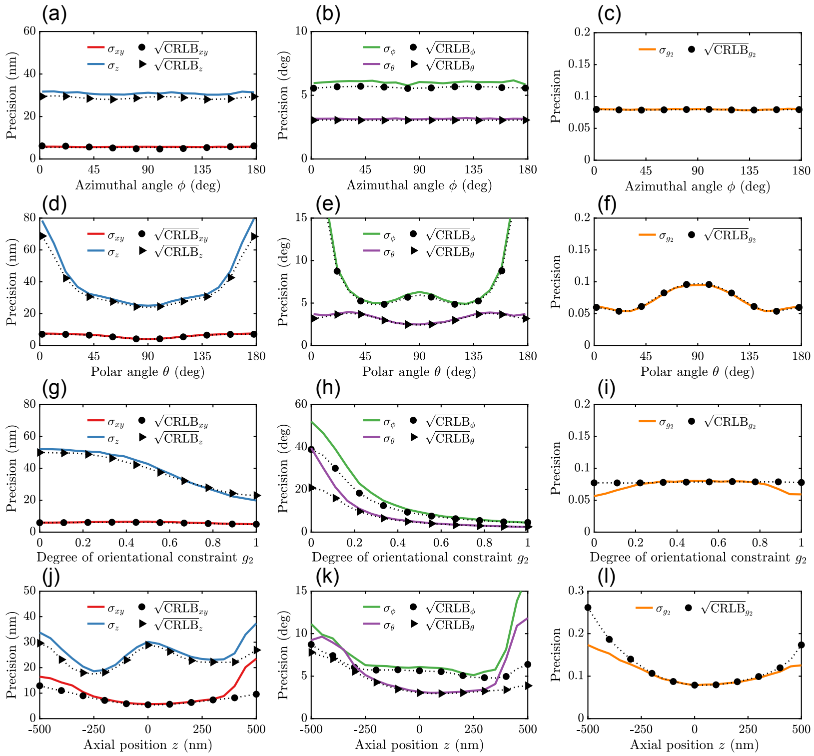

Supplementary Figure 5.1: Simulation study of the impact of molecule orientation, rotation diffusion, and axial position on the precision. **(a)** Average lateral and axial localization precision, **(b)** orientation, and **(c)** g_2 precision as a function of the molecule's azimuthal angle with its polar angle uniformly chosen on a sphere with $g_2 = 0.75$. **(d-f)** Precision as a function of the polar angle with its azimuthal angle uniformly chosen with $g_2 = 0.75$. **(g-i)** Precision as a function of degree of orientational constraint g_2 with the molecule's orientation uniformly chosen on a sphere. **(j-l)** Precision as a function of the emitter's axial position, again with the molecule's orientation uniformly chosen on a sphere ($g_2 = 0.75$). The estimator's performance (solid colorized lines) is at the CRLB (black dashed lines with symbols) for all molecule orientations, almost regardless of the rotational diffusion. There is a slight deviation in the angles at low g_2 values (close to freely rotating dipole limit). The g_2 precision drops below the CRLB in (i,l) as the estimation converges to the boundaries $[0, 1]$. The estimator achieves the CRLB for axial positions of $|z| < 300$ nm and starts to diverge outside this region as the Vortex PSF footprint becomes too large to be contained within the ROI of 15×15 pixels. The simulation parameters are as described in the Methods (5.4).

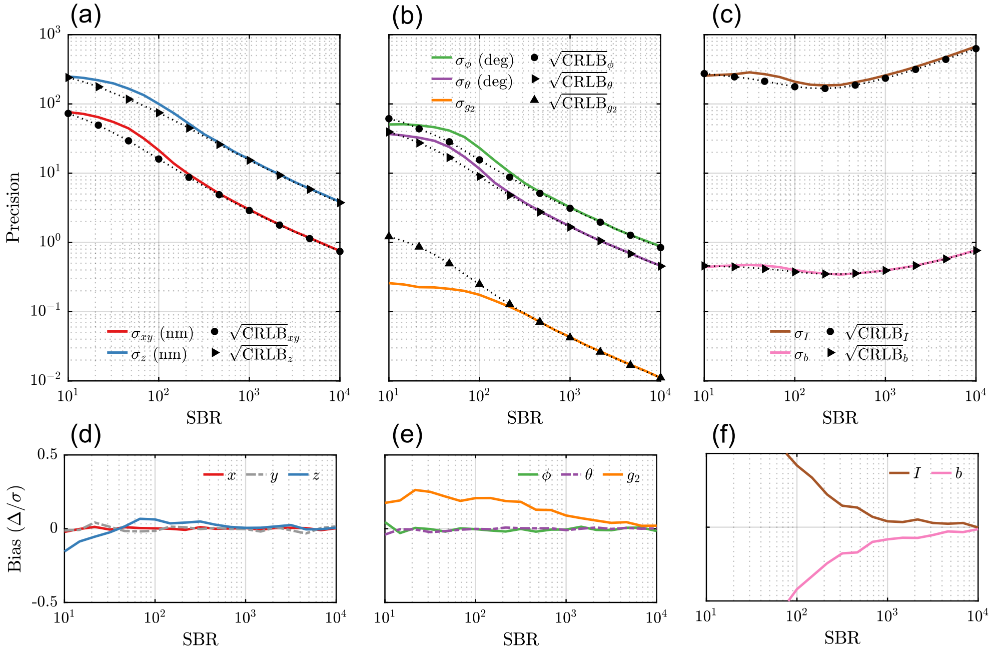

Supplementary Figure 5.2: Simulation study of the impact of signal to background ratio ($\text{SBR} = N/b$) on precision and bias of the estimated parameters. **(a)** Average lateral and axial localization precision using a Vortex PSF model on simulated emitters, simulated with the vectorial PSF (see Methods (5.4)) as a function of SBR. **(b)** The orientation precision of the azimuthal and polar angles together with the degree of orientational constraint. **(c)** The precision of the number of signal photons and of the number of background photons per pixel. The estimation performance is at the CRLB except at SBR levels below 2×10^2. **(d-f)** Similarly, the bias Δ normalized with the precision of the estimated parameters for the (d) position coordinates, (e) orientation parameters, and (f) photon count parameters. The simulation parameters are as described in the Methods (5.4). The slight bias in g_2 is primarily caused by the limited estimation range $[0, 1]$. At very low SBR, rotational diffusion estimates can be inaccurate due to shot noise [50].

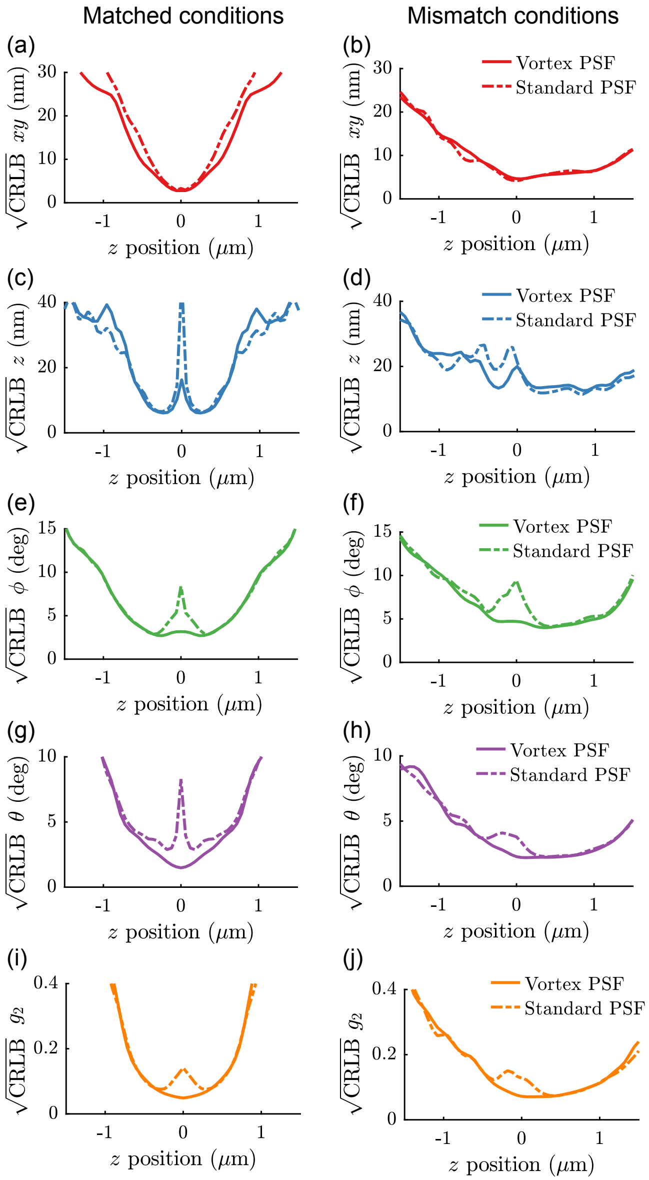

Supplementary Figure 5.3: Simulation study of the impact of axial position on the Cramér-Rao lower bound (CRLB). **(a)** The lateral (xy) CRLBs for the Vortex (solid lines) and standard PSF (dashed lines) in matched conditions ($n = 1.518$) and **(b)** mismatch conditions ($n_{\text{med}} = 1.333$, $n_{\text{cov}} = 1.523$, $n_{\text{imm}} = 1.518$). Similarly the CRLBs for the **(c-d)** axial position z, **(e-f)** azimuth angle ϕ, **(g-h)** polar angle θ, and **(i-j)** degree of orientational constraint g_2. The data points are averaged over 10,000 orientational instances sampled uniformly on the unit sphere with the same instances used to compare the Vortex and standard PSF. The PSFs are simulated in a ROI of 31×31 pixels for which the CRLB is computed.

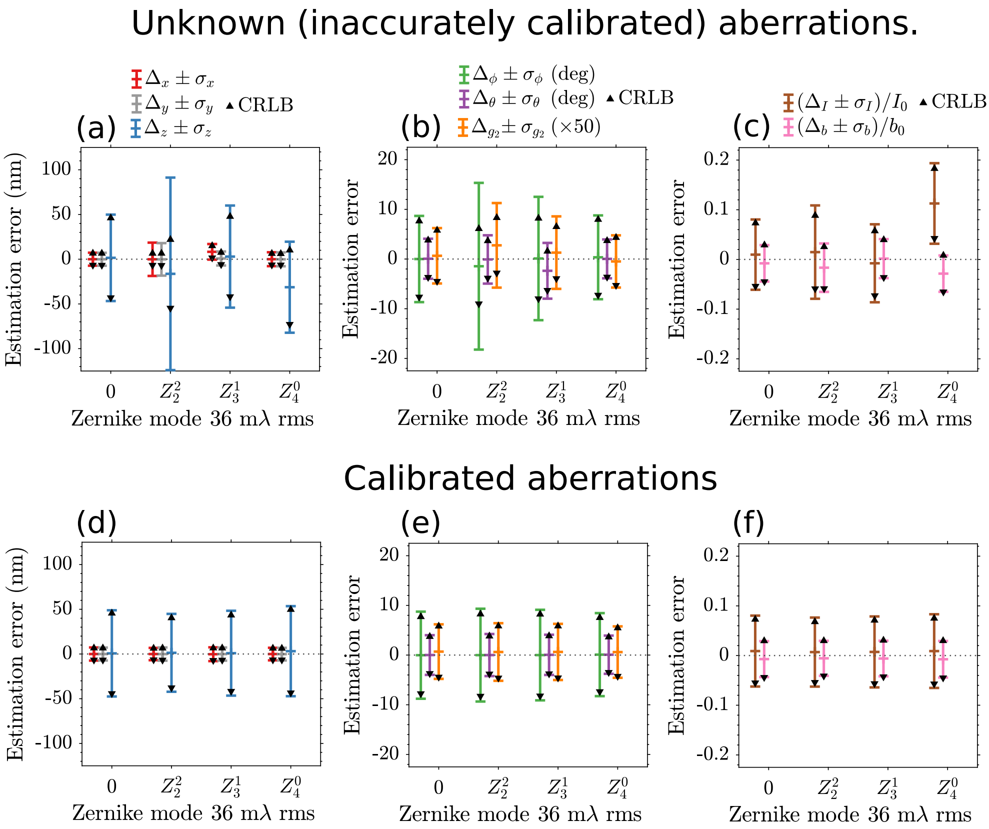

Supplementary Figure 5.4: Simulation study of the impact of unknown and known single-mode aberrations while fitting with the Vortex PSF. **(a)** Lateral and axial localization error using an unaberrated Vortex PSF model on simulated emitters with single-mode aberrations: first-order astigmatism Z_2^2, first-order coma Z_3^1, and first-order spherical Z_4^0 with RMS value of 36 mλ. The error bars indicate the mean and one standard deviation with the black marker indicating the CRLB. In the same way **(b)** shows the orientation error and **(c)** the signal and background photon error. **(d-f)** Same as (a-c) but including the aberrations in the Vortex PSF model. The performance is at the CRLB, and the bias is removed, when fitting with various known aberrations at 36 mλ level.

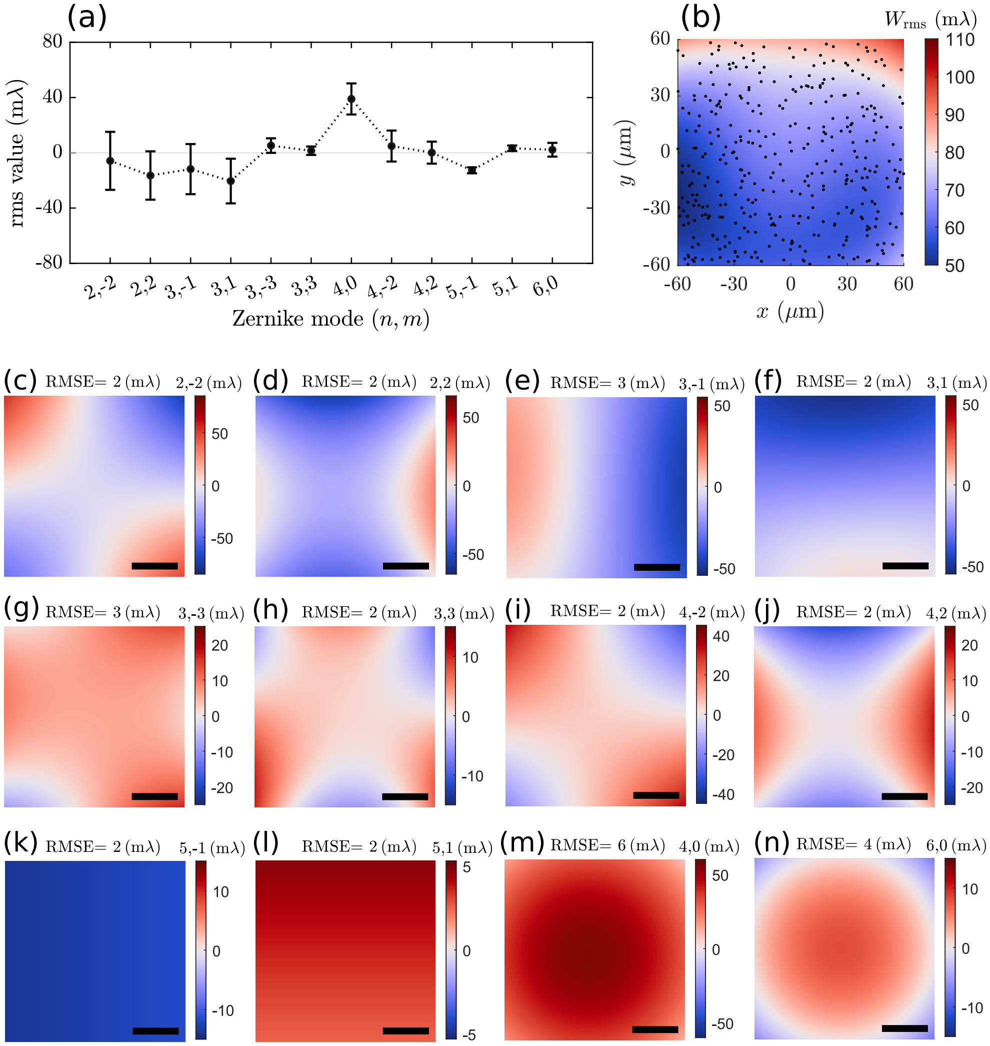

Supplementary Figure 5.5: Quantification of aberration retrieval and correction in the field of view (FOV). **(a)** Fitted Zernike modes and retrieved aberration coefficients over the entire FOV. The coefficients are averaged over 429 bead localizations with error bars indicating the mean and one standard deviation. **(b)** The total wavefront error from the field aberration surfaces in (c-n). The black dots indicate individual bead locations. **(c-n)** Fitted field aberrations from the coefficients in (a) and Zernike surfaces as explained in Supplementary Note 2 (5.5.2), with RMSE as the quality of fit. The field dependency is well-described, as the RMSE is below 6 mλ in all Zernike maps. The quality of fit is further characterized by R^2 values above 0.9 for (c, d, e, f, i, j) and above 0.5 in (g, h, m, n), and smaller when the mode appears constant in the imaged FOV (k, l). Scale bars in (c-n) are 30 μm.

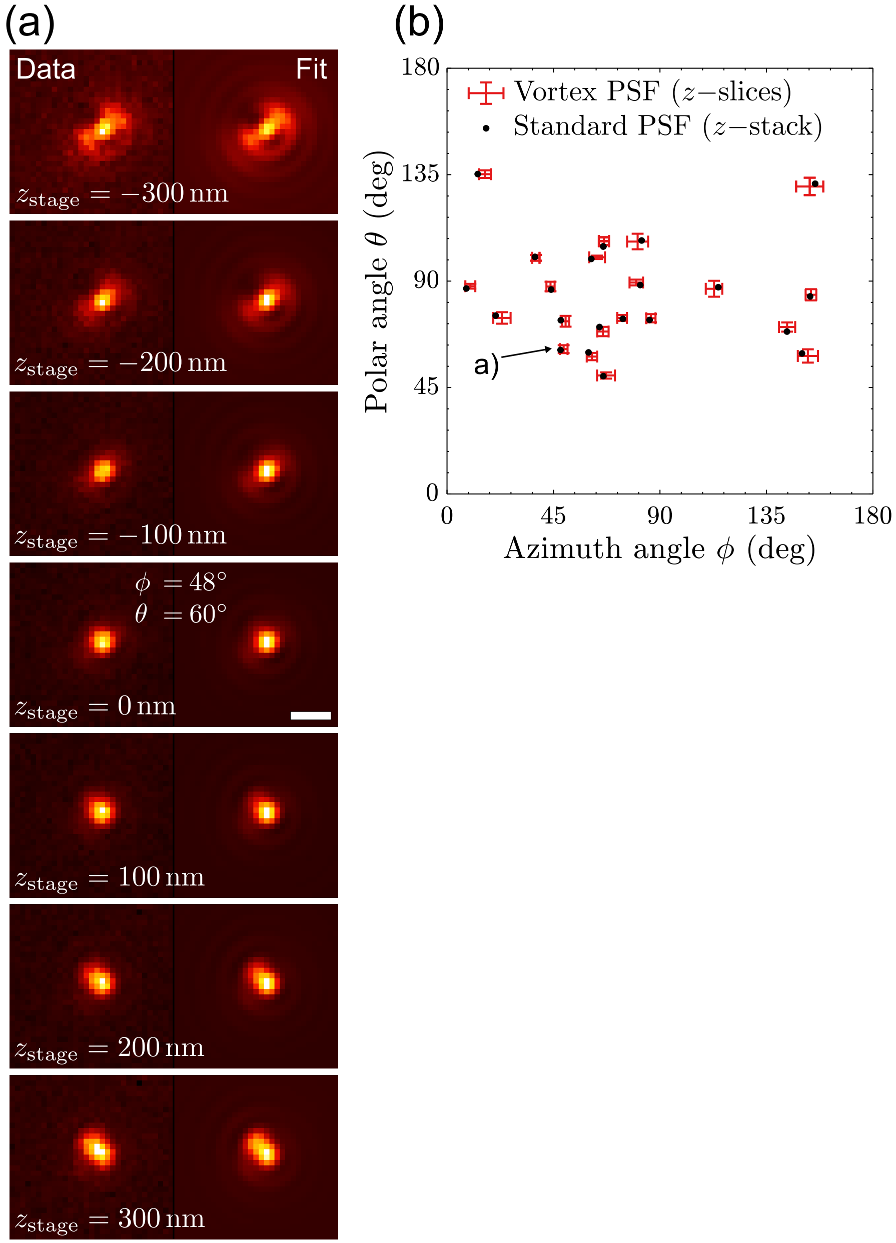

Supplementary Figure 5.6: **(a)** Standard PSF model fitted to an entire z-stack resulting in the estimated orientations of $\phi = 48°$ $\theta = 60°$. This is the same molecule from Fig. 2, where it was imaged and fitted with a Vortex PSF frame by frame. **(b)** Estimated orientations of 21 fixed molecules from a standard PSF z-stack and single-frame Vortex PSFs with error bars indicating one standard deviation. These results indicate that the single z slice estimates with the Vortex PSF and the estimate on the entire through-focus stack with the standard PSF are mutually unbiased.

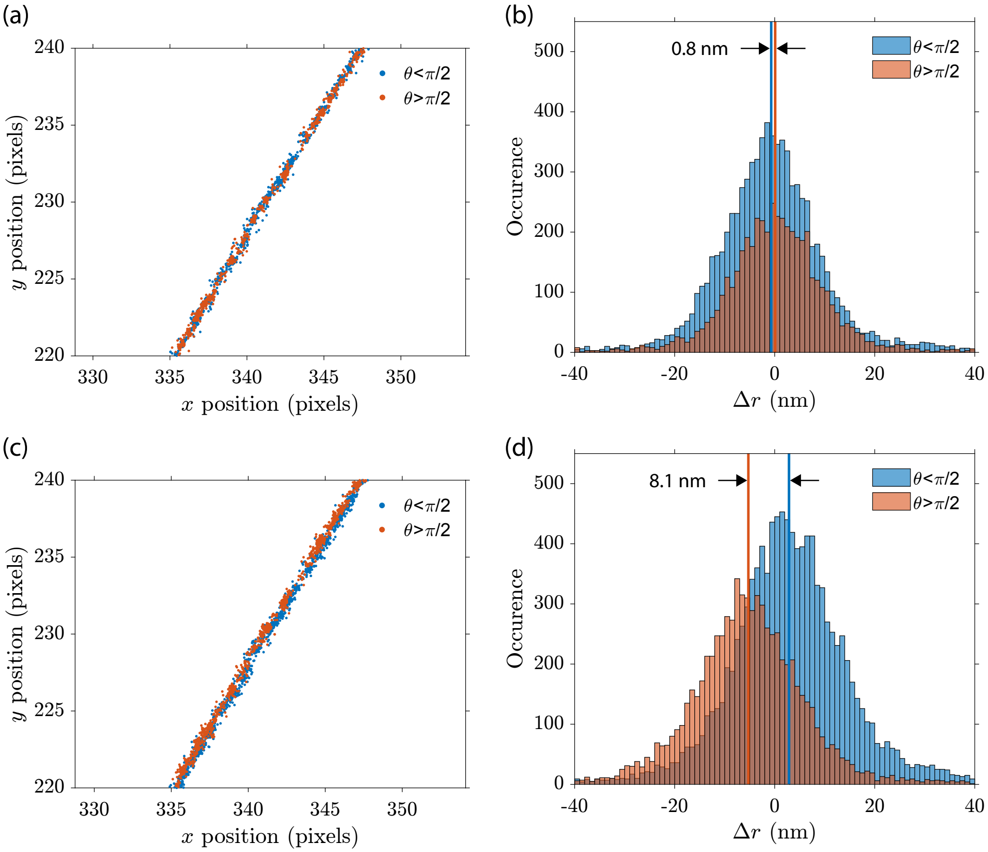

Supplementary Figure 5.7: The influence of cover slip refractive index on localization bias. **(a)** Localizations of a single λ-DNA strand with an optimized cover slip refractive index of $n_{\mathrm{cov}} = 1.5209$ split into two subsets with $\theta < \pi/2$ and $\theta > \pi/2$, showing no orientation dependent shift between the two subsets. **(b)** Histogram of the deviations from the λ-DNA strand with a distance of 0.8 nm between the mean of the two subsets. The total width of the distribution of localizations from the strand in (a) (including both subsets) is 18.6 nm FWHM. **(c)** Localizations of the same λ-DNA strand fitted with a catalogue value of the cover slip refractive index of $n_{\mathrm{cov}} = 1.523$ and the same splitting into two subsets, showing a bias between the two subsets. **(d)** The histogram of deviations from the central λ-DNA axis highlights this shift where there is 8.1 nm between the mean position of the two subsets. This slight variation in the cover slip refractive index broadens the width of the distribution of localizations on the same λ-DNA strand from (a) to 22.8 nm FWHM.

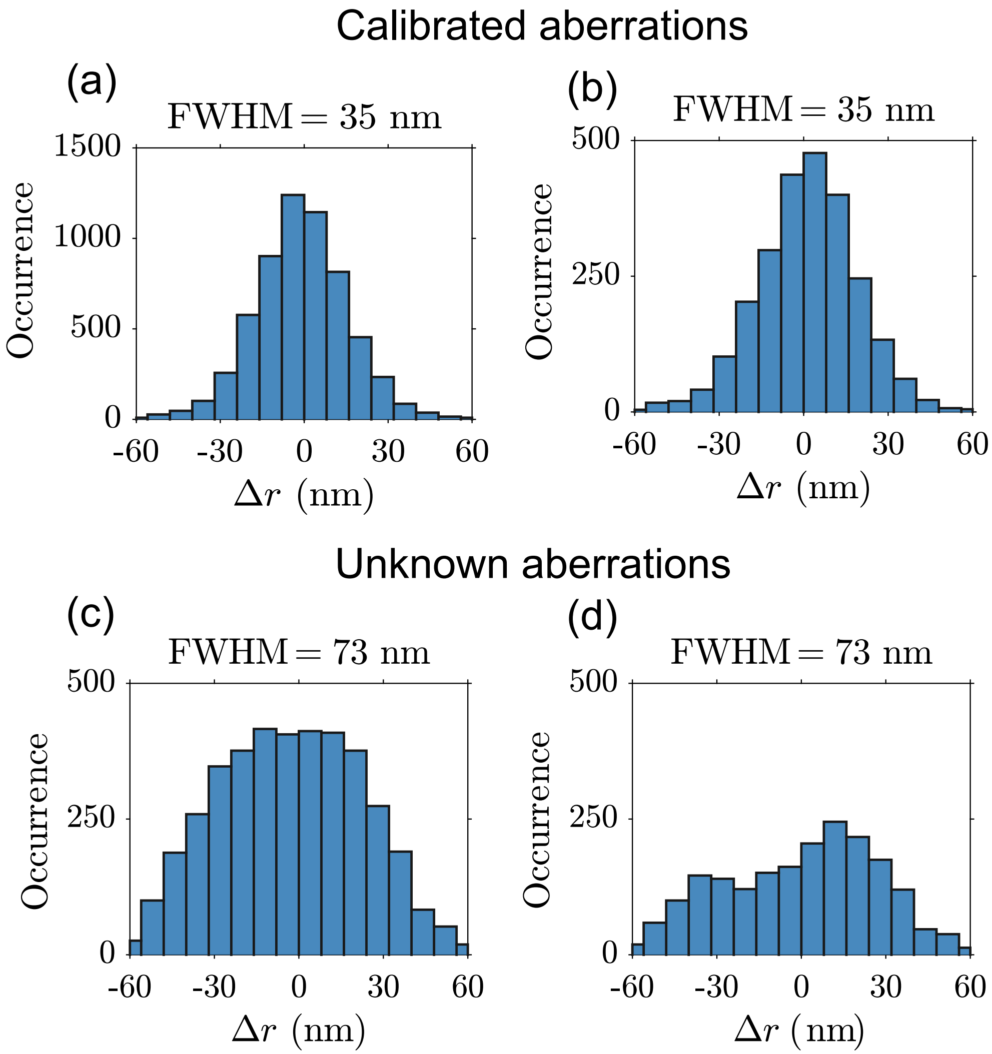

Supplementary Figure 5.8: The effect of our calibrated PSF model for the localizations of the λ−DNA in the main text (Fig. 4(a)). **(a)** Position deviation from the spline fit to the DNA axis using a calibrated PSF model results in a Gaussian-like distribution with $\mathrm{FWHM} = 35$ nm and **(b)** for polar angles $45 \leq \theta \leq 135$ results in a similar distribution with $\mathrm{FWHM} = 35$ nm. This is wider than the value in the main text as the catalogue refractive index is used and no additional fine drift correction is applied. **(c)** Using a PSF model without calibrated aberrations results in a broad distribution with $\mathrm{FWHM} = 73$ nm and **(d)** for polar angles $45 \leq \theta \leq 135$ results in a non-uniform distribution with $\mathrm{FWHM} = 73$ nm. (a-b) The FWHM is evaluated using a normal distribution fit with support $\Delta r = \pm 40$ nm and (c-d) a non-parametric fit with a normal kernel.

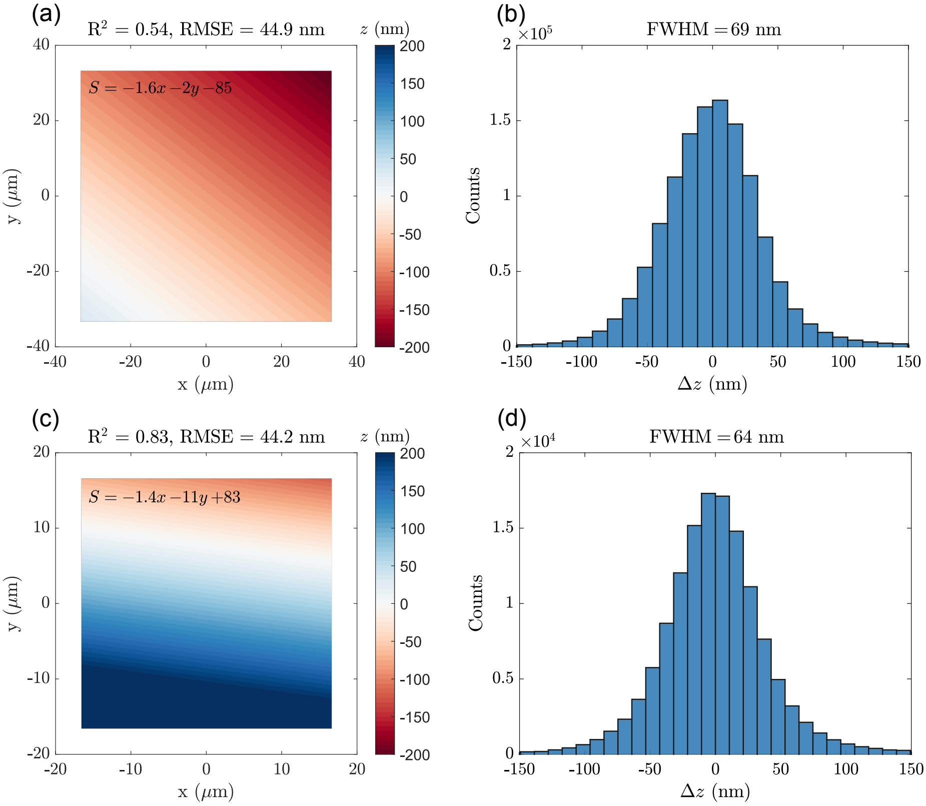

Supplementary Figure 5.9: Planar surface fit on λ-DNA localization data, with and without an additional $0.4°$ sample tilt in the y direction. **(a)** Planar surface fit to non-tilted λ-DNA sample, where S is the surface function defining the average z position in nm as a function of the x and y position in μm. **(b)** Histogram of the Δz localization deviations from the surface given in (a). **(c)** Planar surface fit to intentionally tilted λ-DNA sample, the tilt is apparent from the larger coefficient of the y-coordinate in S compared to the coefficient in the fitted plane in (a). **(d)** Histogram of the Δz localization deviations from the surface given in (c). Localizations are filtered with $g_2 \geq 0.6$ to keep the localizations that bind to the lambda-DNA, thereby ensuring a robust z-estimation of the sample plane.

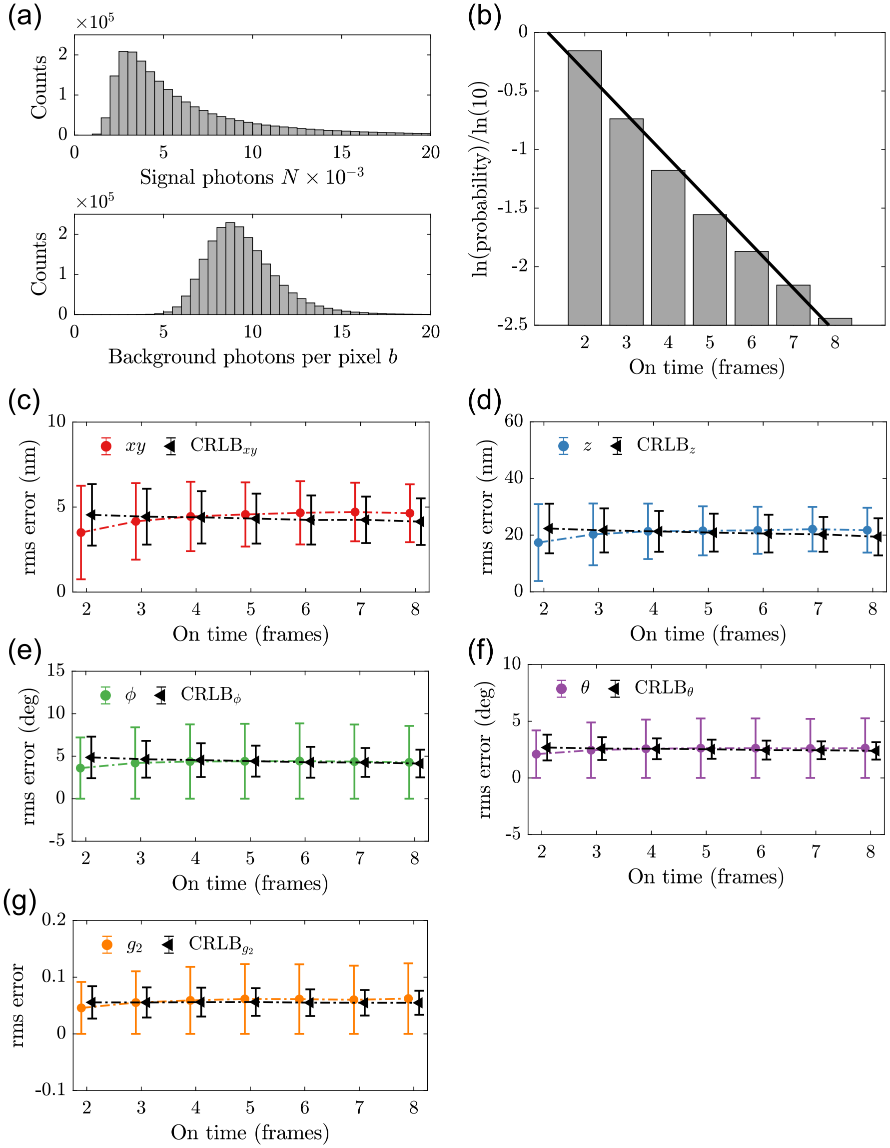

Supplementary Figure 5.10: Single-molecule run length analysis in λ-DNA experiment. **(a)** Distribution of estimated signal photon count N and background photon count per pixel b. **(b)** Natural-logarithm probability-distribution (gray bars) of subsequent on-time events up to 8 frames for the same emitter. The average on-time over all events is 1.5 frames, whereas the fitted exponential distribution gives an on-time of 1.3 frames (black line). **(c)** Lateral localization error (root-mean-square value) and CRLB (mean and s.d.) determined from repeated localizations. In the same way, **(d)** axial localization error, **(e)** azimuth angle error, **(f)** polar angle error, and **(g)** g_2 error as estimated from repeated localizations. The estimated RMS error matches well with the estimated CRLB for all parameters and the number of on-time events. The total number of linked on-events is 302,541 with experimental conditions and data analysis as further specified in the Methods (5.4).

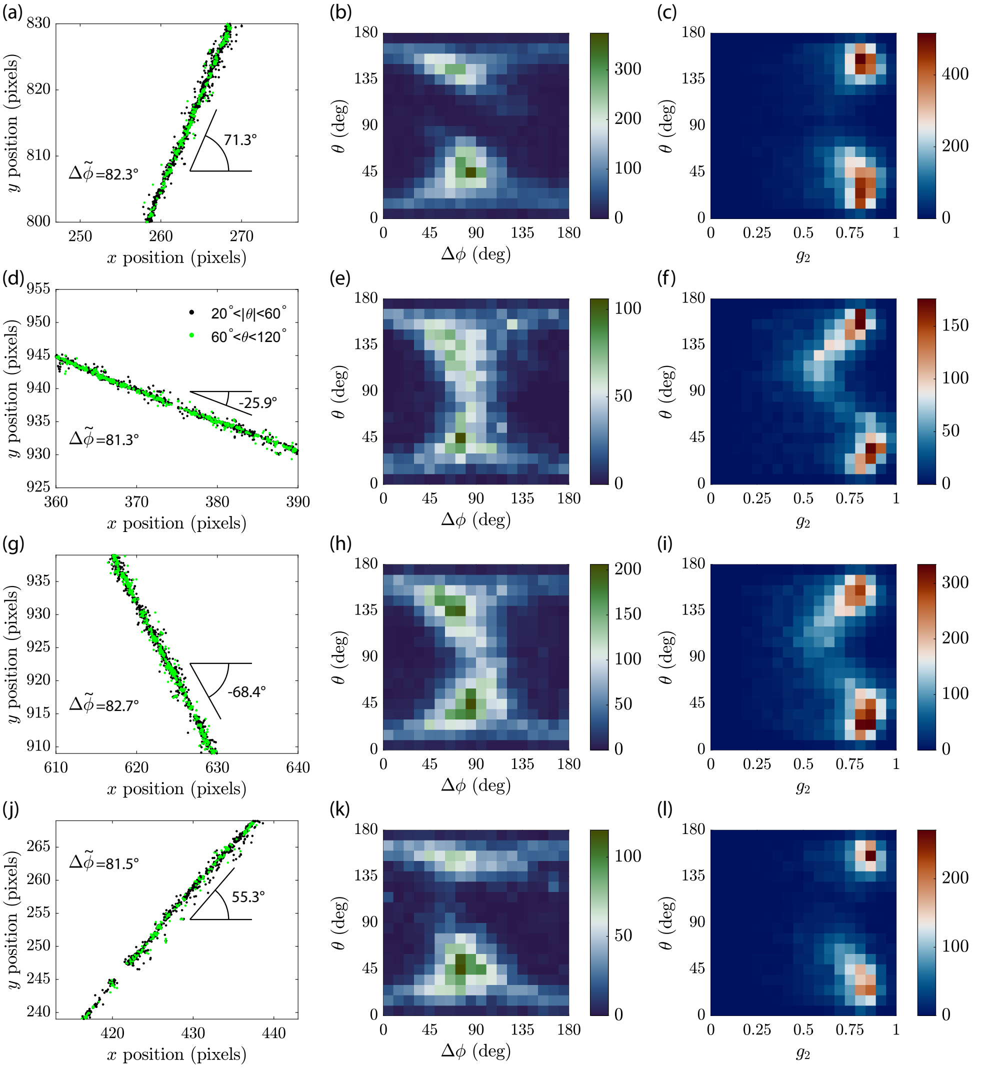

Supplementary Figure 5.11: Distributions of various differently oriented λ-DNA strands throughout the FOV of Figure 4(a), illuminated in TIRF conditions with the QWP. **(a,d,g,j)** Localizations of two different subsets from 4 different strands, in-plane orientations ($60^\circ < \theta < 120^\circ$) in green and out-of-plane orientations ($20^\circ < |\theta| < 60^\circ$) in black. The average DNA orientation and average relative in-plane orientation ($\Delta\tilde{\phi}$) is indicated with each λ-DNA strand. **(b,e,h,k)** 2D histogram of the relative in-plane orientation $\Delta\phi$ and the polar angle θ of the respective λ-DNA strands displayed to the left. These histograms show that the orientational parameter distributions are largely independent of the DNA orientation. The variations around $\theta = 90^\circ$ are caused by in-plane orientations that are excited less efficiently as they are perpendicular to the primary polarization direction. **(c,f,i,l)** 2D histogram of g_2 and θ for the respective λ-DNA strands displayed to the left.

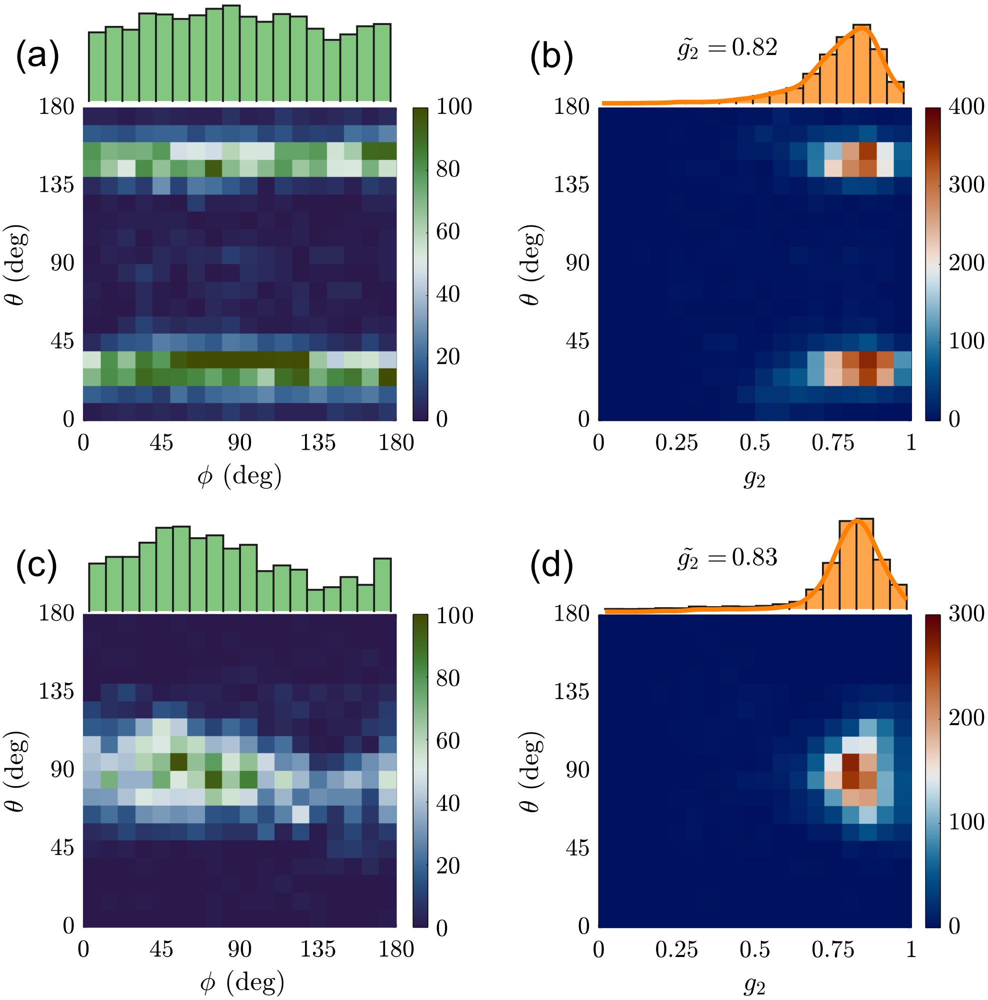

Supplementary Figure 5.12: Estimation of orientational parameters on fixed molecules. **(a)** Bivariate histogram of the azimuth angle (ϕ) versus polar angle (θ) and **(b)** degree of orientational constraint (g_2) versus polar angle as estimated on single molecules directly spin-coated onto a cover slip under TIRF illumination. The marginal histograms show the ϕ and g_2 distribution, respectively, with the median g_2 coefficient specified in the plot. **(c-d)** The same as in (a) and (b), but estimated on single molecules embedded in a thin layer of PMMA under non-TIRF epi-illumination. In both these experimental cases with different orientation distributions, there appears to be no correlation between the estimated parameters. The number of single molecules analyzed is 7042 in (a-b) and 4034 in (c-d) with sample preparation and imaging conditions as further specified in the Methods (5.4).

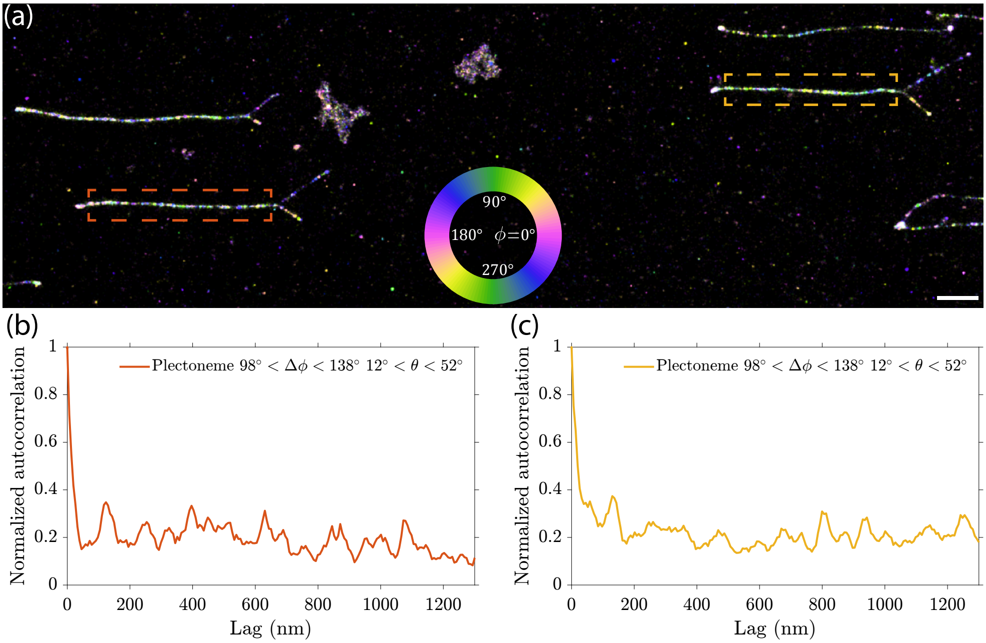

Supplementary Figure 5.13: Orientation and spatial correlation of angular subsets in plectonemes. **(a)** Azimuthal orientation of supercoiled DNA molecules (rotated 90 degrees clockwise to fit figure, scale bar 1 μm). **(b)** Autocorrelation of localizations along the plectoneme highlighted in orange indicating a periodicity of ~ 122 nm. **(c)** Autocorrelation of localizations along the plectoneme highlighted in yellow indicating a periodicity of ~ 130 nm. The autocorrelations are calculated along the x axis with localizations binned in 6.5 nm intervals.

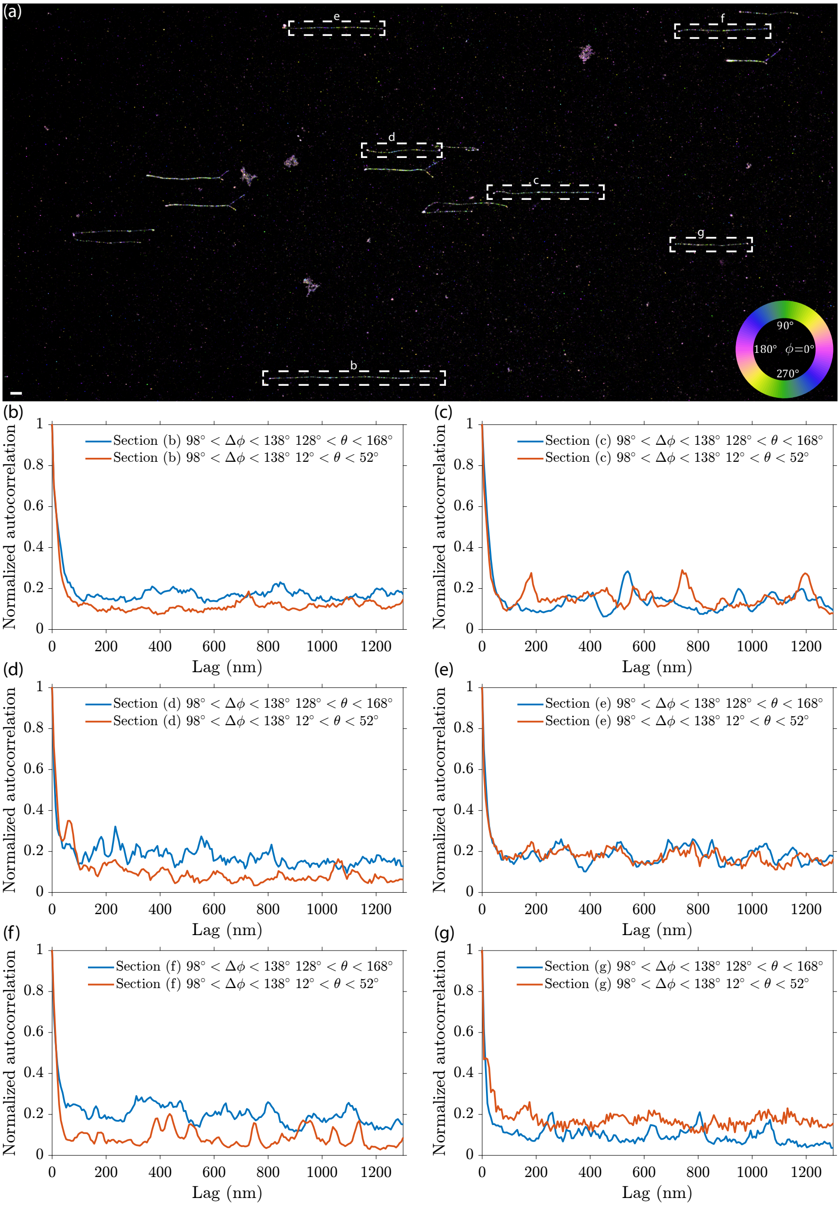

Supplementary Figure 5.14: Spatial autocorrelation of sections from torsionally relaxed DNA molecules made in the supercoiled sample preparation, showing that the periodic spatial correlation found on plectonemes is not present on most straight individual strands. This is because these DNA molecules were attached to the coverslip at only one end and hence internal torsion could not be maintained. **(a)** Average azimuthal orientation (ϕ) of the supercoiled dataset (rotated 90 degrees clockwise to fit figure, scale bar 1 μm). **(b-g)** Autocorrelation of localizations within respective orientation ranges along the DNA axis in 6.5 nm bins from the strands highlighted in (a). Most data show various peaks in the auto correlation but these peaks are not periodic.

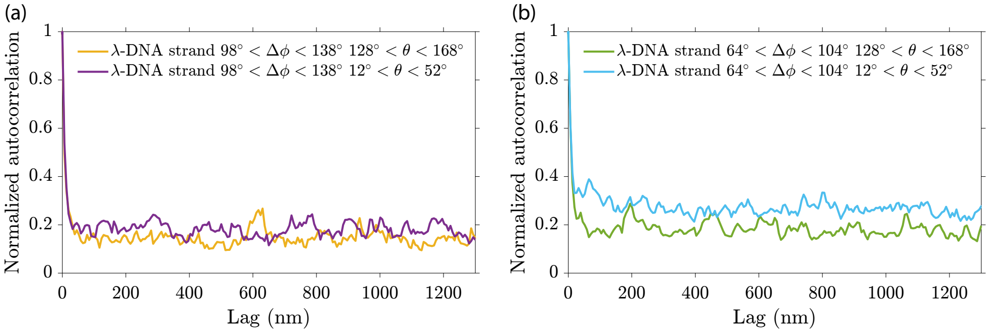

Supplementary Figure 5.15: Spatial autocorrelation of the λ-DNA strand highlighted in Figure 4(a), indicating no periodic spatial correlation in the λ-DNA dataset. **(a)** Autocorrelation of localizations from the λ-DNA strand within respective orientation ranges found from the supercoiled data along the DNA axis in 6.5 nm bins. **(b)** Autocorrelation of localizations within primary orientation ranges found from the λ-DNA data along the DNA axis in 6.5 nm bins.

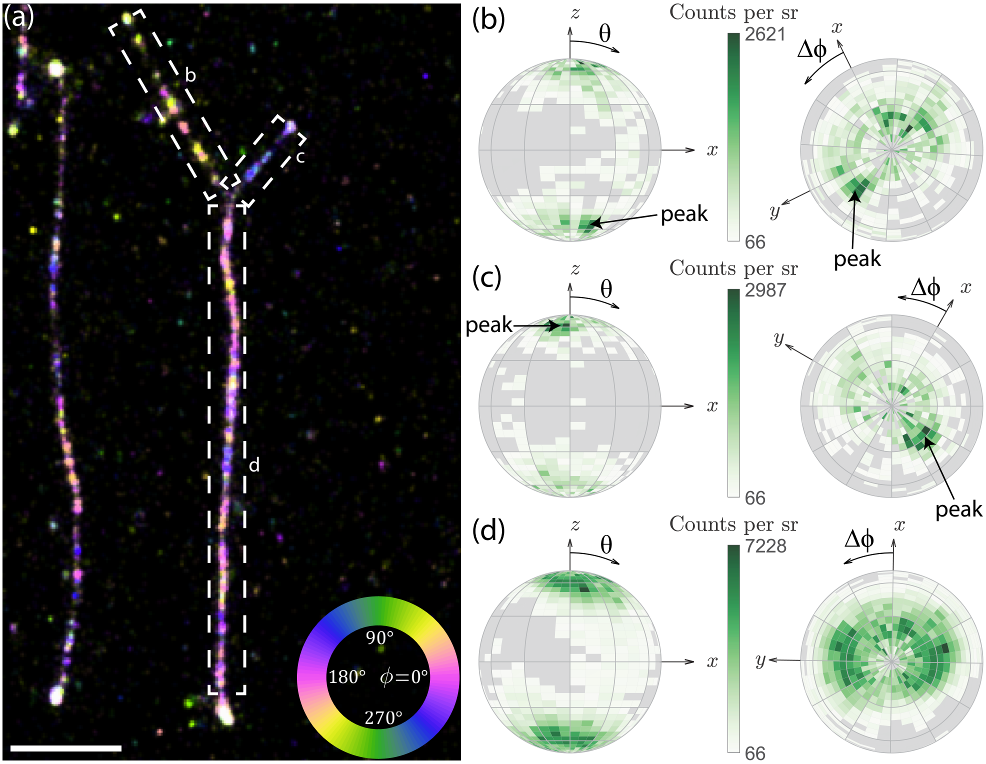

Supplementary Figure 5.16: Orientation distribution of the supercoiled sections before and on the plectoneme. **(a)** Average azimuthal orientation (ϕ) of one of the plectonemes (scale bar 1 μm). **(b)** Orientation distribution of the top-left supercoiled section before overlap highlighted in (a), with the DNA axis aligned in the x direction. On the left the view is aligned along the y axis, on the right is a top view aligned in the negative z direction. The average orientation around the peak value is $\Delta\phi = 111°$ $\theta = 36°$. **(c)** Orientation distribution of the top-right supercoiled section before overlap highlighted in (a), with the DNA axis aligned in the x direction. The average orientation around the peak value is $\Delta\phi = -102°$ and $\theta = 29°$. **(d)** Orientation distribution of the plectoneme with the DNA axis aligned in the x direction highlighted in (a), which appears to show a superposition of the two individual distributions from before the strands intertwined. Each bin spans $5°$ in the polar direction and $10°$ in the azimuthal direction, additionally there is a $30°$ coarse grid.

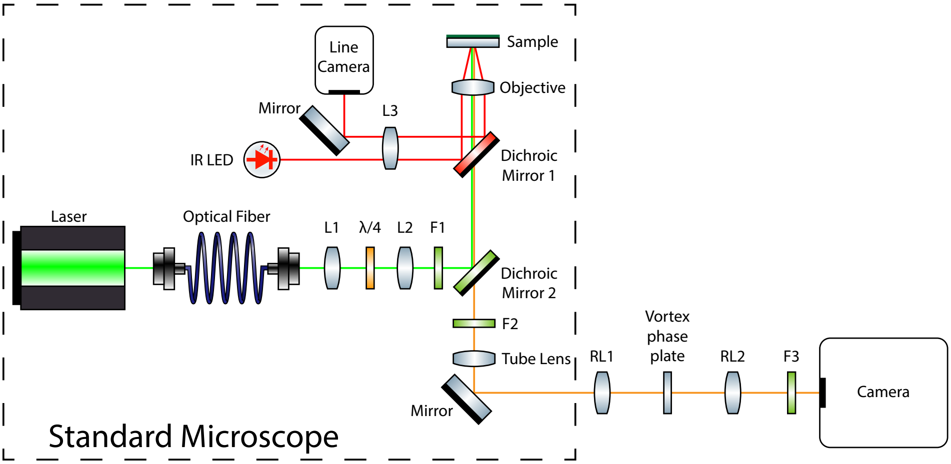

Supplementary Figure 5.17: The optical setup, built around a standard fluorescence microscope (Ti-E, Nikon). Lenses RL1 (AC508-100-A-ML, Thorlabs) and RL2 (AC508-100-A-ML, Thorlabs) relay the original image plane to the camera (Zyla 4.2 PLUS, Andor) with no additional magnification resulting in a pixel size of 65 nm in object (sample) space. The vortex phase plate (V-593-10-1, Vortex Photonics) is placed in the Fourier plane between these two lenses. The standard TIRF microscope has a focus lock consisting of an infrared light emitting-diode, offset lens L3, Dichroic Mirror 1 and a line camera (any unspecified components are part of the Nikon Ti-E or its accessories). The excitation laser (Sapphire 561-150 CW, Coherent) is coupled into a fiber and collimated by lens L1 and thereafter focused onto the back focal plane of the objective (CFI Apochromat TIRF 100XC Oil, Nikon) with lens L2. By translating the fiber face the excitation beam angle coming out of the objective can be adjusted to total internal reflection conditions in the sample. The $\lambda/4$ waveplate converts the linearly polarized laser beam to circular polarization, and the excitation spectrum is filtered by F1 (ZET405/488/561/640x, Chroma). Dichroic Mirror 2 (ZT405/488/561/640rpc, Chroma) splits the excitation and emission path and the emission spectrum is further filtered by F2 (ZET405/488/561/640m-TRF, Chroma) and F3 (FF01-609/57-25, Semrock). The tube lens focuses the image from the sample to the front focal plane of lens RL1.

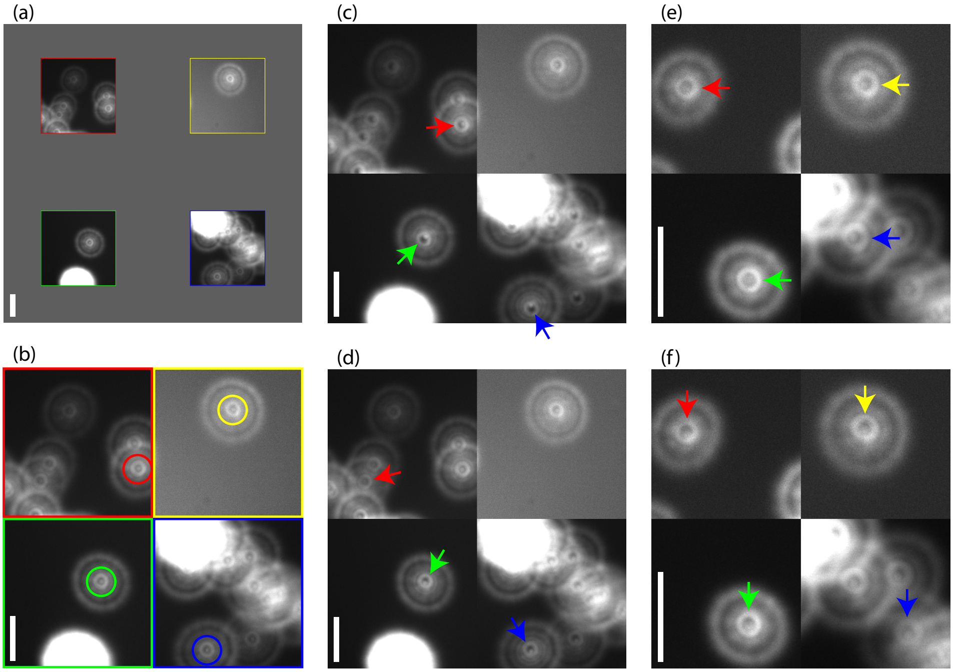

Supplementary Figure 5.18: Vortex phase plate alignment. **(a)** Selected imaged regions of defocused beads on the camera. **(b)** Zoom in on the four selected regions. The circles highlight the central region where a central peak is surrounded by a bright ring. The bright ring moves as the vortex phase plate is moved, in this image the center of the rings and the peaks coincide and thus the phase plate is properly aligned. **(c)** The vortex phase plate is too close to the microscope as the rings created by the vortex phase plate are too far radially outward. The arrows indicate the direction in which the rings should be moved. **(d)** The vortex phase plate is too close to the camera when the rings are too far radially inward. **(e)** When the vortex phase plate is aligned along the optical axis all spots should look the same throughout the FOV. The position can then be fine-tuned by shifting horizontally. **(f)** Vortex phase plate slightly misaligned vertically. Scale bars are 10 μm.

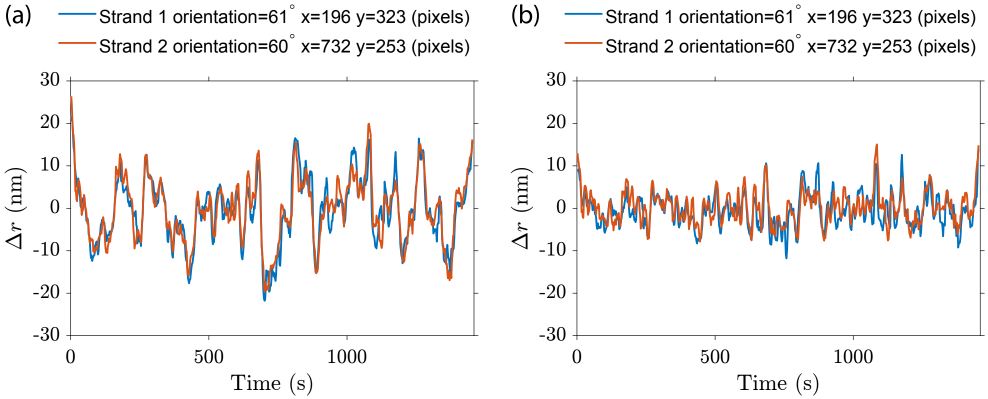

Supplementary Figure 5.19: Fine drift correction using straight λ-DNA strands illustrated on two similarly oriented λ-DNA strands at distant positions in the FOV (35 μm apart). **(a)** Mean deviations from the spline fit to the two DNA strands over time after coarse drift correction. Each data point is the average relative position over 100 frames (10.5 seconds) and shifted in 20 frame steps. The coarse drift correction has corrected ~ 100 nm of slow time scale drift. There is however still a sizeable amount of residual drift as evident by the correlation between the deviations of the two considered λ-DNA strands. The deviations of these two strands have a standard deviation of 7.6 nm over time. The average width of the distribution of localizations around the spline fits of these two λ-DNA strands is 24.5 nm FWHM after coarse drift correction. **(b)** Mean deviations in 100 frame bins after fine drift correction (as described in data analysis in the Methods section (5.4)) shows a reduction in the drift amplitude giving a residual standard deviation of 3.7 nm. The fine drift correction reduces the mean width of localizations on these two λ-DNA strands to 18.3 nm FWHM.

References

[1] E. Betzig, G. H. Patterson, R. Sougrat, O. W. Lindwasser, S. Olenych, J. S. Bonifacino, M. W. Davidson, J. Lippincott-Schwartz, and H. F. Hess, *Imaging intracellular fluorescent proteins at nanometer resolution,* Science **313**, 1642 (2006).

[2] S. T. Hess, T. P. Girirajan, and M. D. Mason, *Ultra-high resolution imaging by fluorescence photoactivation localization microscopy,* Biophysical Journal **91**, 4258 (2006).

[3] M. J. Rust, M. Bates, and X. Zhuang, *Sub-diffraction-limit imaging by stochastic optical reconstruction microscopy (STORM),* Nature Methods **3**, 793 (2006).

[4] M. Heilemann, S. Van De Linde, M. Schüttpelz, R. Kasper, B. Seefeldt, A. Mukherjee, P. Tinnefeld, and M. Sauer, *Subdiffraction-resolution fluorescence imaging with conventional fluorescent probes,* Angewandte Chemie - International Edition **47**, 6172 (2008).

[5] A. Sharonov and R. M. Hochstrasser, *Wide-field subdiffraction imaging by accumulated binding of diffusing probes,* Proceedings of the National Academy of Sciences of the United States of America **103**, 18911 (2006).

[6] R. Jungmann, C. Steinhauer, M. Scheible, A. Kuzyk, P. Tinnefeld, and F. C. Simmel, *Single-molecule kinetics and super-resolution microscopy by fluorescence imaging of transient binding on DNA origami,* Nano Letters **10**, 4756 (2010).

[7] T. J. Gould, M. S. Gunewardene, M. V. Gudheti, V. V. Verkhusha, S. R. Yin, J. A. Gosse, and S. T. Hess, *Nanoscale imaging of molecular positions and anisotropies,* Nature Methods **5**, 1027 (2008).

[8] H. A. Shaban, C. A. Valades-Cruz, J. Savatier, and S. Brasselet, *Polarized super-resolution structural imaging inside amyloid fibrils using Thioflavine T,* Scientific Reports **7**, 1 (2017).

[9] E. J. Peterman, H. Sosa, L. S. Goldstein, and W. E. Moerner, *Polarized fluorescence microscopy of individual and many kinesin motors bound to axonemal microtubules,* Biophysical Journal **81**, 2851 (2001).

[10] E. Toprak, J. Enderlein, S. Syed, S. A. McKinney, R. G. Petschek, T. Ha, Y. E. Goldman, and P. R. Selvin, *Defocused orientation and position imaging (DOPI) of myosin V,* Proceedings of the National Academy of Sciences of the United States of America **103**, 6495 (2006).

[11] M. Wang, J. M. Marr, M. Davanco, J. W. Gilman, and J. A. Liddle, *Nanoscale deformation in polymers revealed by single-molecule super-resolution localization-orientation microscopy,* Materials Horizons **6**, 817 (2019).

[12] E. Betzig and R. J. Chichester, *Single molecules observed by near-field scanning optical microscopy,* Science **262**, 1422 (1993).

[13] R. M. Dickson, D. J. Norris, and W. E. Moerner, *Simultaneous imaging of individual molecules aligned both parallel and perpendicular to the optic axis,* Physical Review Letters **81**, 5322 (1998).

[14] J. Enderlein, E. Toprak, and P. R. Selvin, *Polarization effect on position accuracy of fluorophore localization,* Optics Express **14**, 8111 (2006).

[15] S. Stallinga and B. Rieger, *Accuracy of the Gaussian point spread function model in 2D localization microscopy,* Optics Express **18**, 24461 (2010).

[16] J. Engelhardt, J. Keller, P. Hoyer, M. Reuss, T. Staudt, and S. W. Hell, *Molecular orientation affects localization accuracy in superresolution far-field fluorescence microscopy,* Nano Letters **11**, 209 (2011).

[17] M. D. Lew, M. P. Backlund, and W. E. Moerner, *Rotational mobility of single molecules affects localization accuracy in super-resolution fluorescence microscopy,* Nano Letters **13**, 3967 (2013).

[18] M. D. Lew and W. E. Moerner, *Azimuthal polarization filtering for accurate, precise, and robust single-molecule localization microscopy,* Nano Letters **14**, 6407 (2014).

[19] M. P. Backlund, A. Arbabi, P. N. Petrov, E. Arbabi, S. Saurabh, A. Faraon, and W. E. Moerner, *Removing orientation-induced localization biases in single-molecule microscopy using a broadband metasurface mask,* Nature Photonics **10**, 459 (2016).

[20] O. Nevskyi, R. Tsukanov, I. Gregor, N. Karedla, and J. Enderlein, *Fluorescence polarization filtering for accurate single molecule localization,* APL Photonics **5**, 061302 (2020).

[21] T. Ding, T. Wu, H. Mazidi, O. Zhang, and M. D. Lew, *Single-molecule orientation localization microscopy for resolving structural heterogeneities between amyloid fibrils,* Optica **7**, 602 (2020).

[22] A. P. Bartko and R. M. Dickson, *Imaging three-dimensional single molecule orientations,* Journal of Physical Chemistry B **103**, 11237 (1999).

[23] M. Böhmer and J. Enderlein, *Orientation imaging of single molecules by wide-field epifluorescence microscopy,* Journal of the Optical Society of America B **20**, 554 (2003).

[24] D. Patra, I. Gregor, and J. Enderlein, *Image analysis of defocused single-molecule images for three-dimensional molecule orientation studies,* Journal of Physical Chemistry A **108**, 6836 (2004).

[25] K. I. Mortensen, L. S. Churchman, J. A. Spudich, and H. Flyvbjerg, *Optimized localization analysis for single-molecule tracking and super-resolution microscopy,* Nature Methods **7**, 377 (2010).

[26] K. I. Mortensen, J. Sung, H. Flyvbjerg, and J. A. Spudich, *Optimized measurements of separations and angles between intra-molecular fluorescent markers,* Nature Communications **6**, 8621 (2015).

[27] M. P. Backlund, M. D. Lew, A. S. Backer, S. J. Sahl, G. Grover, A. Agrawal, R. Piestun, and W. E. Moerner, *Simultaneous, accurate measurement of the 3D position and orientation of single molecules,* Proceedings of the National Academy of Sciences of the United States of America **109**, 19087 (2012).

[28] A. S. Backer, M. P. Backlund, M. D. Lew, and W. E. Moerner, *Single-molecule orientation measurements with a quadrated pupil,* Optics Letters **38**, 1521 (2013).

[29] A. S. Backer, M. P. Backlund, A. R. von Diezmann, S. J. Sahl, and W. E. Moerner, *A bisected pupil for studying single-molecule orientational dynamics and its application to three-dimensional super-resolution microscopy,* Applied Physics Letters **104**, 193701 (2014).

[30] O. Zhang, J. Lu, T. Ding, and M. D. Lew, *Imaging the three-dimensional orientation and rotational mobility of fluorescent emitters using the Tri-spot point spread function,* Applied Physics Letters **113**, 031103 (2018).

[31] S. Stallinga and B. Rieger, *Position and orientation estimation of fixed dipole emitters using an effective Hermite point spread function model,* Optics Express **20**, 5896 (2012).

[32] B. Rieger and S. Stallinga, *The lateral and axial localization uncertainty in super-resolution light microscopy,* ChemPhysChem **15**, 664 (2014).

[33] V. Curcio, L. A. Alemán-Castañeda, T. G. Brown, S. Brasselet, and M. A. Alonso, *Birefringent Fourier filtering for single molecule coordinate and height super-resolution imaging with dithering and orientation,* Nature Communications **11**, 5307 (2020).

[34] C. Flors, C. N. Ravarani, and D. T. Dryden, *Super-resolution imaging of DNA labelled with intercalating dyes,* ChemPhysChem **10**, 2201 (2009).

[35] I. Schoen, J. Ries, E. Klotzsch, H. Ewers, and V. Vogel, *Binding-activated localization microscopy of DNA structures,* Nano Letters **11**, 4008 (2011).

[36] S. Stallinga, *Effect of rotational diffusion in an orientational potential well on the point spread function of electric dipole emitters,* Journal of the Optical Society of America A **32**, 213 (2015).

[37] K. I. Willig, S. O. Rizzoli, V. Westphal, R. Jahn, and S. W. Hell, *STED microscopy reveals that synaptotagmin remains clustered after synaptic vesicle exocytosis,* Nature **440**, 935 (2006).

[38] R. V. Shack and K. Thompson, *Influence of alignment errors of a telescope system on its aberration field,* in *Optical Alignment I*, Vol. 0251, International Society for Optics and Photonics (SPIE, 1980) pp. 146–153.

[39] A. S. Backer, M. Y. Lee, and W. E. Moerner, *Enhanced DNA imaging using super-resolution microscopy and simultaneous single-molecule orientation measurements,* Optica **3**, 659 (2016).

[40] C. A. V. Cruz, H. A. Shaban, A. Kress, N. Bertaux, S. Monneret, M. Mavrakis, J. Savatier, and S. Brasselet, *Quantitative nanoscale imaging of orientational order in biological filaments by polarized superresolution microscopy,* Proceedings of the National Academy of Sciences of the United States of America **113**, E820 (2016).

[41] A. S. Biebricher, I. Heller, R. F. H. Roijmans, T. P. Hoekstra, E. J. G. Peterman, and G. J. L. Wuite, *The impact of DNA intercalators on DNA and DNA-processing enzymes elucidated through force-dependent binding kinetics,* Nature Communications **6**, 7304 (2015).

[42] A. S. Backer, A. S. Biebricher, G. A. King, G. J. L. Wuite, I. Heller, and E. J. G. Peterman, *Single-molecule polarization microscopy of DNA intercalators sheds light on the structure of S-DNA,* Science Advances **5**, eaav1083 (2019).

[43] H. Mazidi, E. S. King, O. Zhang, A. Nehorai, and M. D. Lew, *Dense super-resolution imaging of molecular orientation via joint sparse basis deconvolution and spatial pooling,* in *2019 IEEE 16th International Symposium on Biomedical Imaging (ISBI 2019)* (IEEE, 2019) pp. 325–329.

[44] X. Yan, R. C. Habbersett, J. M. Cordek, J. P. Nolan, T. M. Yoshida, J. H. Jett, and B. L. Marrone, *Development of a mechanism-based, DNA staining protocol using SYTOX orange nucleic acid stain and DNA fragment sizing flow cytometry,* Analytical Biochemistry **286**, 138 (2000).

[45] A. Bensimon, A. Simon, A. Chiffaudel, V. Croquette, F. Heslot, and D. Bensimon, *Alignment and sensitive detection of DNA by a moving interface,* Science **265**, 2096 (1994).

[46] X. Michalet, R. Ekong, F. Fougerousse, S. Rousseaux, C. Schurra, N. Hornigold, M. Van Slegtenhorst, J. Wolfe, S. Povey, J. S. Beckmann, and A. Bensimon, *Dynamic molecular combing: Stretching the whole human genome for high-resolution studies,* Science **277**, 1518 (1997).

[47] J. F. Allemand, D. Bensimon, L. Jullien, A. Bensimon, and V. Croquette, *pH-dependent specific binding and combing of DNA,* Biophysical Journal **73**, 2064 (1997).

[48] S. H. Kim, M. Ganji, E. Kim, J. van der Torre, E. Abbondanzieri, and C. Dekker, *DNA sequence encodes the position of DNA supercoils,* eLife **7**, e36557 (2018).

[49] K. Rippe, N. Mücke, and J. Langowski, *Superhelix dimensions of a 1868 base pair plasmid determined by scanning force microscopy in air and in aqueous solution,* Nucleic Acids Research **25**, 1736 (1997).

[50] O. Zhang and M. D. Lew, *Fundamental limits on measuring the rotational constraint of single molecules using fluorescence microscopy,* Physical Review Letters **122**, 198301 (2019).

[51] O. Zhang and M. D. Lew, *Quantum limits for precisely estimating the orientation and wobble of dipole emitters,* Physical Review Research **2**, 33114 (2020).

[52] Y. Li, M. Mund, P. Hoess, J. Deschamps, U. Matti, B. Nijmeijer, V. J. Sabinina, J. Ellenberg, I. Schoen, and J. Ries, *Real-time 3D single-molecule localization using experimental point spread functions,* Nature Methods **15**, 367 (2018).

[53] C. Smith, M. Huisman, M. Siemons, D. Grünwald, and S. Stallinga, *Simultaneous measurement of emission color and 3D position of single molecules,* Optics Express **24**, 4996 (2016).

[54] M. Siemons, C. N. Hulleman, R. Ø. Thorsen, C. S. Smith, and S. Stallinga, *High precision wavefront control in point spread function engineering for single emitter localization,* Optics Express **26**, 8397 (2018).

[55] R. Ø. Thorsen, C. N. Hulleman, M. Hammer, D. Grünwald, S. Stallinga, and B. Rieger, *Impact of optical aberrations on axial position determination by photometry,* Nature Methods **15**, 989 (2018).

[56] A. S. Backer and W. E. Moerner, *Determining the rotational mobility of a single molecule from a single image: a numerical study,* Optics Express **23**, 4255 (2015).

[57] T. Chandler, H. Shroff, R. Oldenbourg, and P. La Rivière, *Spatio-angular fluorescence microscopy I Basic theory,* Journal of the Optical Society of America A **36**, 1334 (2019).

[58] T. Chandler, H. Shroff, R. Oldenbourg, and P. La Rivière, *Spatio-angular fluorescence microscopy III Constrained angular diffusion, polarized excitation, and high-NA imaging,* Journal of the Optical Society of America A **37**, 1465 (2020).

[59] T. Ruckstuhl and D. Verdes, *Supercritical angle fluorescence (SAF) microscopy,* Optics Express **12**, 4246 (2004).

[60] J. Enderlein, I. Gregor, and T. Ruckstuhl, *Imaging properties of supercritical angle fluorescence optics,* Optics Express **19**, 8011 (2011).

[61] T. Yan, C. J. Richardson, M. Zhang, and A. Gahlmann, *Computational correction of spatially variant optical aberrations in 3D single-molecule localization microscopy,* Optics Express **27**, 12582 (2019).

[62] K. Thompson, *Description of the third-order optical aberrations of near-circular pupil optical systems without symmetry,* Journal of the Optical Society of America A **22**, 1389 (2005).

[63] T. Schmid, J. P. Rolland, A. Rakich, and K. P. Thompson, *Separation of the effects of astigmatic figure error from misalignments using Nodal Aberration Theory (NAT),* Optics Express **18**, 17433 (2010).

[64] T. Schmid, K. P. Thompson, and J. P. Rolland, *Misalignment-induced nodal aberration fields in two-mirror astronomical telescopes,* Applied Optics **49**, D131 (2010).

[65] E. Kim, A. M. Gonzalez, B. Pradhan, J. van der Torre, and C. Dekker, *Condensin-driven loop extrusion on supercoiled DNA,* bioRxiv , 2021.05.15.444164 (2021).

[66] A. Japaridze, G. Muskhelishvili, F. Benedetti, A. F. Gavriilidou, R. Zenobi, P. De Los Rios, G. Longo, and G. Dietler, *Hyperplectonemes: A Higher Order Compact and Dynamic DNA Self-Organization,* Nano Letters **17**, 1938 (2017).

[67] M. Ganji, S. H. Kim, J. Van Der Torre, E. Abbondanzieri, and C. Dekker, *Intercalation-based single-molecule fluorescence assay to study DNA supercoil dynamics,* Nano Letters **16**, 4699 (2016).

[68] H. P. Spielmann, D. E. Wemmer, and J. P. Jacobsen, *Solution structure of a DNA complex with the fluorescent bis-intercalator TOTO determined by NMR spectroscopy,* Biochemistry **34**, 8542 (1995).

[69] F. Johansen and J. P. Jacobsen, *1H NMR studies of the bis-intercalation of a homodimeric oxazole yellow dye in DNA oligonucleotides,* Journal of Biomolecular Structure and Dynamics **16**, 205 (1998).

[70] A. Fürstenberg, M. D. Julliard, T. G. Deligeorgiev, N. I. Gadjev, A. A. Vasilev, and E. Vauthey, *Ultrafast excited-state dynamics of DNA fluorescent intercalators: New insight into the fluorescence enhancement mechanism,* Journal of the American Chemical Society **128**, 7661 (2006).

[71] F. Balzarotti, Y. Eilers, K. C. Gwosch, A. H. Gynnå, V. Westphal, F. D. Stefani, J. Elf, and S. W. Hell, *Nanometer resolution imaging and tracking of fluorescent molecules with minimal photon fluxes,* Science **355**, 606 (2017).

[72] C. Roider, A. Jesacher, S. Bernet, and M. Ritsch-Marte, *Axial super-localisation using rotating point spread functions shaped by polarisation-dependent phase modulation,* Optics Express **22**, 4029 (2014).

[73] M. Baranek and Z. Bouchal, *Rotating vortex imaging implemented by a quantized spiral phase modulation,* Journal of the European Optical Society: Rapid Publications **8**, 13017 (2013).

[74] L. J. van Vliet, D. Sudar, and I. T. Young, *Digital fluorescence imaging using cooled charge-coupled device array cameras,* in *Cell Biology*, Vol. III, edited by J. Celis (Academic Press, New York, 1998) 2nd ed., pp. 109–120.

[75] J. Schnitzbauer, M. T. Strauss, T. Schlichthaerle, F. Schueder, and R. Jungmann, *Super-resolution microscopy with DNA-PAINT,* Nature Protocols **12**, 1198 (2017).

[76] F. Xu, D. Ma, K. P. MacPherson, S. Liu, Y. Bu, Y. Wang, Y. Tang, C. Bi, T. Kwok, A. A. Chubykin, P. Yin, S. Calve, G. E. Landreth, and F. Huang, *Three-dimensional nanoscopy of whole cells and tissues with in situ point spread function retrieval,* Nature Methods **17**, 531 (2020).

[77] M. Siemons, B. M. C. Cloin, D. M. Salas, W. Nijenhuis, E. A. Katrukha, and L. C. Kapitein, *Comparing strategies for deep astigmatism-based single-molecule localization microscopy,* Biomedical Optics Express **11**, 735 (2020).

[78] R. Tessieres, *Analysis for alignment of optical systems*, M.sc. thesis, The University of Arizona (2003).

6

Photon efficient orientation estimation using polarization modulation in single-molecule localization microscopy

The precision of single-molecule localization microscopy can be improved by illumination with shifting excitation patterns. We analyze the extension of this idea towards modulation of the illumination polarization to enhance the precision of orientation estimation of fixed emitters. Two modes are analyzed: i) normally incident excitation with three polarization steps to retrieve the in-plane angle of the emitters and ii) obliquely incident excitation with p-polarization with five different azimuthal angles of incidence to retrieve the full orientation. We present a theoretical study of the Cramér-Rao precision bound for these modes. For the oblique incidence mode we find a favourable isotropic orientation precision for all molecular orientations if the polar angle of incidence is equal to $\arccos\sqrt{2/3} \approx 35$ *degrees. A simulation study is performed to assess the performance for low signal-to-background and inaccurate illumination polarization angles. We show that a precision, at the Cramér-Rao bound (CRB), of just* 2.4 *and* 1.6 *degrees in the azimuthal and polar angles could be achieved with only 1000 detected signal photons and 10 background photons per pixel. These precision values indicate that modulation of the excitation polarization can enable single molecule orientation imaging at low light levels. A proof-of-principle experiment is carried out, demonstrating an experimental in-plane precision close to the CRB for signal photon counts ranging from 400 to 10,000.*

Parts of this chapter have been submitted for publication as: R.Ø. Thorsen, **C.N. Hulleman**, B. Rieger, and S. Stallinga, *Photon efficient orientation estimation using polarization modulation in single-molecule localization microscopy*.

6.1. Introduction

Single-Molecule Localization Microscopy (SMLM) is an established super-resolution microscopy technique, taking image resolution from the ~ 200 nm diffraction limit down to the 20 nm regime with many imaging modalities such as (f)PALM [1, 2], STORM [3] and PAINT [4]. SMLM uses emitters that can switch between off- and on-states such that only a sparse subset of all emitters is active in each image frame of a time series. This temporal modulation allows the active emitters to be localized with a precision an order of magnitude below the diffraction limit. Localizations in different time frames accumulate to a list of emitter positions rather than pixel-based images, which means that the image is constituted by a list of single molecule data. New SMLM image modalities can be created by extending this list beyond the x and y coordinates of the molecules [5]. In this chapter we focus on the extension with molecular orientation parameters [6]. Typically the emitters are assumed to rotate freely during the emission states. However, cases exist where the emitters have a fixed pose and therefore experience little rotational diffusion, e.g., when rigidly bound to a target [7–9] or immobilized at a surface [10, 11]. The emitter orientation provides insight into the linking properties and must otherwise be taken into account explicitly as it affects the localization precision [12, 13].

The Point Spread Function (PSF) of conventional widefield fluorescence microscopy is poorly suited for orientation estimation because of inherent symmetries such as the symmetry between positions above and below the nominal focus plane. Therefore the imaging system must be altered for extracting this additional information. A first effort was based on defocused imaging for increasing the variance of the PSF shape with molecular orientation [8]. A major drawback is that the defocus spreads the limited number of signal photons across more pixels, which degrades the localization precision. Long exposures are therefore needed to overcome this photon dilution, making these methods less ideal for localization microscopy. An alternative way to increase the orientation information has been with proposed engineered PSFs [14–16], which can be realized experimentally by adding a phase-shaping element in the optical pathway before the camera. These PSFs vary in shape and performance, yet they commonly increase the PSF size and thereby hinder optimum detection at low signal-to-background ratios (SBRs).

The polarization of the fluorescence excitation and emission is directly coupled to the molecular orientation and therefore offers a direct way to probe orientation. The use of the polarization of the emitted light usually involves placing a polarizing beam splitter in the detection light path to separately collect different polarization components on the camera. The intensity in these sub-images is used as a parametric indicator of molecular orientation [17–19], which can also be combined with PSF engineering approaches [20–23]. Application of excitation polarization modulation has been studied in simulations [24, 25], with notable demonstrations on single fluorophores [26] and biomolecules [27]. It has, however, rarely been applied in the context of SMLM until Backer, Lee, and Moerner used a sequence of images generated with a normally incident illumination beam with linear polarization that toggles between three different directions [28]. In this technique, three sequential images are used to estimate the in-plane orientation of single molecules. The key advantage of using excitation polarization over emission polarization fitting is that the signal photons are not spread out over an area on the camera larger than that of a diffraction-limited spot. This implies that extracting orientational information can be expected to be more efficient for excitation polarization schemes at low photon counts, i.e. if the SBR is unfavorable.

In this chapter we build on the polarization modulation scheme of ref. [28] by a Cramér-Rao Bound (CRB) analysis of the best possible achievable precision, and by a simulation study of the impact of signal photon count, SBR, and polarization purity on precision. The analysis uses a comprehensive Maximum Likelihood Estimation (MLE) method for simultaneous estimation of position and orientation, improving the routine used by Backer, Lee, and Moerner that neglects spot shape [29]. In a next step, we describe a method to overcome a major drawback of the method presented in ref. [28], namely the inability to estimate the out-of-plane, polar angle of the emission dipole of the molecules. This is achieved by changing the illumination from normal incidence to oblique incidence. In the case of oblique incidence the illumination polarization can have a sizeable component along the optical axis, which is used to extract the full orientation (both polar and azimuthal angle). Our re-examination of polarization modulation was inspired by the recent development of modulation-enhanced localization. A series of such estimators have emerged initiated by the work on MINFLUX [30], later followed by SIMFLUX [31] and related proposals [32, 33]. In these concepts a spatially shifting non-uniform illumination pattern is used to improve localization precision, e.g. a standing wave pattern leads to a twofold improvement [31].

The outline of this chapter is as follows. We first expand the imaging model by incorporating the excitation efficiency in the signal strength (photon count) by the conventional square of the cosine of the angle between polarization and dipole orientation. We describe a general framework that incorporates both normal and oblique incidence, even for large angles of incidence that may give rise to evanescent wave illumination in Total Internal Reflection Fluorescence (TIRF) imaging [34]. Next, we set up the MLE framework that underlies the CRB analysis. We use this framework for a general theoretical analysis and in our simulation study, in conjunction with a proper vectorial PSF model. Thereafter, we describe the optical microscope setup and necessary calibration steps to achieve the desired polarization states. This setup is used for a proof-of-principle experiment for the MLE framework with vectorial PSF model, which enables a demonstration of experimental precision of the in-plane orientation of immobilized fluorophores at the level of the CRB. The chapter is concluded with a discussion of the results and an outlook on next steps.

6.2. Theory

6.2.1. Fluorescence excitation model

Figure 6.1 shows our concept of polarization modulation and spot shape detection. We start by assuming that a single common absorption and emission dipole axis completely describes the emitter's orientation [35]. This orientation is parametrised by the space angle $\Omega = (\phi, \theta)$, a shorthand notation for the combination of azimuthal

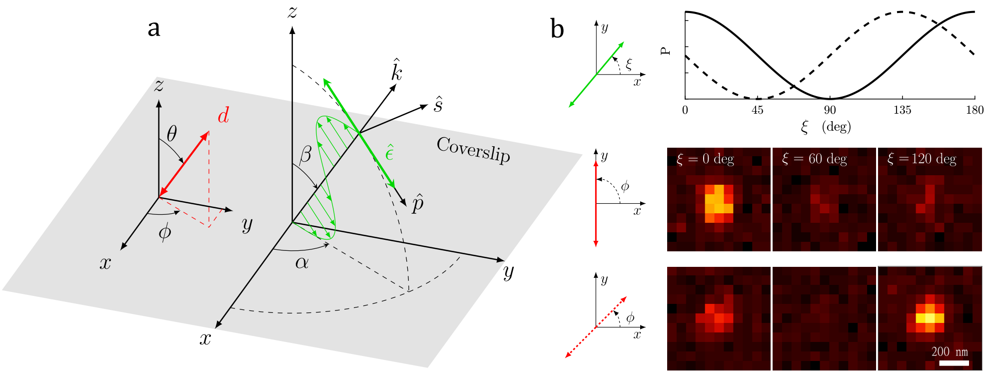

Figure 6.1: Polarization modulation and spot shape detection. **(a)** A constrained dipole is characterized by its azimuthal angle ϕ and a polar angle θ, or equivalently its dipole moment orientation $\hat{d}$. The dipole is excited by a plane wave with a direction along the wavevector $\hat{k}$ with incidence angles α and β, and a polarization state $\hat{\epsilon}$ that lies in the plane perpendicular to the wave vector with components $\hat{p}$ and $\hat{s}$. **(b)** Example of combined estimation for normal ($\alpha = \beta = 0$) excitation with polarization rotation angle ξ. A total of three images are recorded with shifted polarization states at $\xi = [0°, 60°, 120°]$ for two dipole emitters with in-plane angles $\phi = 90°$ and $\phi = 45°$. Combining the shape information of the three frames with the photon count in relation to the polarization shift improves the precision.

angle $0 \leq \phi \leq 2\pi$ and polar angle $0 \leq \theta \leq \pi$, or equivalently by its dipole moment along the unit vector $\hat{d} = (\sin\theta\cos\phi, \sin\theta\sin\phi, \cos\theta)$ (Fig. 6.1(a)). This assumption is usually true as most fluorescent molecules are well-approximated as electric dipoles [36].

The fluorescence excitation efficiency depends on the orientation of this transition moment with respect to the electric field vector of the excitation light:

$$\vec{E} = E\hat{\epsilon}\exp(-i\omega t) \tag{6.1}$$

with E the magnitude, ω the radial frequency, and t time. The complex vector $\hat{\epsilon}$ fully describes the polarization state and this vector satisfies $|\hat{\epsilon}| = 1$. For a propagating plane wave, the polarization ellipse described by $\hat{\epsilon}$ is perpendicular to the unit vector along the direction of propagation given by the wavevector $\hat{k} = (\sin\beta\cos\alpha, \sin\beta\sin\alpha, \cos\beta)$, where α $[0, 2\pi)$ and β $[0, \pi/2]$ defines the azimuthal and polar angle of incidence. In the plane perpendicular to this unit vector, the polarization ellipse can be parametrised by an amplitude ratio $\tan\nu$ and a phase delay 2δ leading to:

$$\hat{\epsilon} = \cos\nu\, e^{-i\delta}\hat{p} + \sin\nu\, e^{i\delta}\hat{s}, \tag{6.2}$$

with the components $\hat{p} = (\cos\beta\cos\alpha, \cos\beta\sin\alpha, -\sin\beta)$ and $\hat{s} = (-\sin\alpha, \cos\alpha, 0)$. In Fig. 6.2(a) the ellipticity angle τ $(-\pi/4, \pi/4]$ and long axis orientation of the polarization ellipse ξ are related to the parameters ν $[0, \pi/2]$ and δ $[0, 2\pi)$ via the

Stokes-vector components:

$$
\begin{aligned}
S_1 &= \cos(2\nu) = \cos(2\tau)\cos(2\xi), && \text{(6.3a)}\\
S_2 &= \sin(2\nu)\cos(2\delta) = \cos(2\tau)\sin(2\xi), && \text{(6.3b)}\\
S_3 &= \sin(2\nu)\sin(2\delta) = \sin(2\tau), && \text{(6.3c)}
\end{aligned}
$$

that satisfy $S_1^2 + S_2^2 + S_3^2 = 1$, i.e., Poincaré-sphere coordinates as shown in Fig. 6.2(b) [37]. The ellipticity angle $|\tau| \leq \pi/4$ has limiting cases $\tau = 0$ and $|\tau| = \pi/4$ for linearly and circularly polarized excitation, respectively.

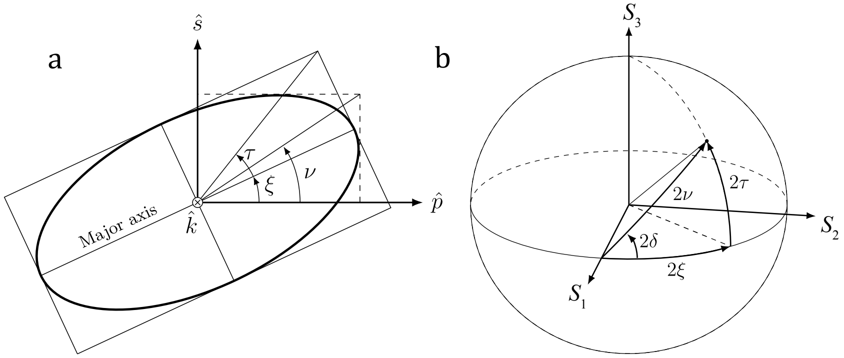

Figure 6.2: Polarization angles. **(a)** Polarization ellipse characterized by its major axis angle ξ and ellipticity angle τ or an amplitude angle ν together with the phase delay δ. **(b)** Poincaré representation of the state of polarization.

If the molecule is effectively stationary during the measurement time, according to the dipole approximation, the measured intensity is proportional to the square of the projection of the transition dipole moment onto the polarization state's direction. Then a fluorophore contributes to the fluorescence signal over a sequence of $m = 1, 2, \ldots, M$ camera frames with changing polarization excitation state $\hat{\epsilon}_m$:

$$
\begin{aligned}
Q_m(\Omega) &= \left|\hat{d} \cdot \hat{\epsilon}_m\right|^2 \\
&= \frac{1}{2}\left[\left|\hat{d} \cdot \hat{p}\right|^2 + \left|\hat{d} \cdot \hat{s}\right|^2\right] + \frac{1}{2}\left[\left|\hat{d} \cdot \hat{p}\right|^2 - \left|\hat{d} \cdot \hat{s}\right|^2\right] S_1 \\
&+ \operatorname{Re}\left\{\left(\hat{d} \cdot \hat{p}\right)\left(\hat{d} \cdot \hat{s}\right)^*\right\} S_2 + \operatorname{Im}\left\{\left(\hat{d} \cdot \hat{p}\right)\left(\hat{d} \cdot \hat{s}\right)^*\right\} S_3. \qquad (6.4)
\end{aligned}
$$

From this we define the modulation function :

$$
P_m(\Omega) = \frac{Q_m(\Omega)}{Q_{\text{norm}}} \qquad (6.5)
$$

where Q_{norm} is a normalization condition that depends on the excitation mode such that:

$$
\sum_{m=1}^{M} P_m(\Omega) = 1. \qquad (6.6)
$$

This modulation function $P_m(\Omega)$ serves as the expectation function in the estimation process and may often be reduced to a relatively simple expression depending on the excitation mode.

6.2.2. Dipole imaging model

The expected photon count (μ_{nm}) at pixel $n = 1, \dots, N_{\text{pix}}$ is modulated with the function $P_m(\Omega)$ (Eq. 6.5) over a sequence of $m = 1, \dots, M$ frames with different excitation polarization states. This expected count depends on the emitter position $\vec{r}_0 = (x_0, y_0)$, the total signal photon count N and background photons per pixel b, and the dipole orientation Ω, given a total of 6 parameters to be estimated. The expected photon count is given by:

$$\mu_{nm} = N P_m(\Omega) H_n(\vec{r}_0, \Omega) + \frac{b}{a^2 M} \tag{6.7}$$

where a is the pixel size and $H_n(\vec{r}_0, \Omega)$ is the expected fluorescence intensity distribution of pixel n for a fluorophore at position $\vec{r}_0$ and with orientation Ω, normalized such that:

$$\sum_n H_n(\vec{r}_0, \Omega) = 1. \tag{6.8}$$

The normalized fluorescence intensity is computed using the vectorial PSF model described elsewhere [38, 39]. For the sake of completeness, the details are presented in appendix 6.9.1. We use standard Maximum Likelihood Estimation (MLE) methods based on the Poissonian noise distribution to find the 6 parameters $(x_0, y_0, N, b, \theta, \phi)$ that best fit the observed single molecule images [40].

6.3. Evaluation of Fisher-information and Cramér-Rao bounds

The expected precision for estimating the different parameters can be assessed by developing an approximation to the Fisher-matrix and the Cramér-Rao bound (CRB). Here we focus on the modulated parameters Ω as the unmodulated ones behave as in standard SMLM, which have been investigated extensively previously [38, 41]. The starting point to retrieve the Fisher-information matrix is the log-likelihood function, where its derivatives with respect to the parameters give rise to the Fisher-information elements [40]. These can be expressed in closed-form if we ignore the finite pixel size, neglect the region of interest's (ROI) finite support, and assume zero background. Following the approach in [31] with the imaging model given by Eq. 6.7, the relevant Fisher-matrix elements involving the modulated parameters become:

$$F_{\Omega\Omega} = N \sum_{n=1}^{N_{\text{pix}}} \frac{1}{H_n(\vec{r}_0, \Omega)} \left(\frac{\partial H_n(\vec{r}_0, \Omega)}{\partial \Omega} \right)^2 + N \sum_{m=1}^{M} \frac{1}{P_m(\Omega)} \left(\frac{\partial P_m(\Omega)}{\partial \Omega} \right)^2 \tag{6.9}$$

where the first term arises from orientation-induced information in the shape of the PSF, the same as for conventional SMLM, and where the second term originates from the polarization modulation. This second term implies that modulation makes these diagonal Fisher-matrix elements larger and hence the associated CRB smaller due to the inversion relation $\mathrm{CRB}_{\Omega} = [F_{\Omega\Omega}]^{-1}$ (the off-diagonal mixing between the orientational parameters Ω and the other parameters is zero).

A simplified approach to assess the impact of modulation is to evaluate Eq. 6.9 under the assumption that the contribution to the Fisher-information from modulation is much larger than the contribution from the PSF shape variations, i.e., the orientation dependency of the PSF is neglected (e.g., for a 2D Gaussian model). This assumption is, however, not used for the actual numerical parameter estimation in simulation later.

6.3.1. Normal incidence

For normally incident light ($\alpha = \beta = 0$) the polarization vector is restricted to the xy imaging plane ($\epsilon_z = 0$). The non-zero components of the polarization vector are $\epsilon_x = \cos\xi\cos\tau - i\sin\xi\sin\tau$ and $\epsilon_y = \sin\xi\cos\tau + i\cos\xi\sin\tau$, with ξ the in-plane orientation of the polarization ellipse and with τ the ellipticity angle (Fig. 6.2). The polarization modulation is implemented by rotating the long axis of the polarization ellipse with equidistant angles $\xi_m = \pi(m-1)/M + \xi_0$, $s = 1, 2, \ldots, M$. The angles are taken relative to the x axis with offset ξ_0, and the number of polarization steps must be $M \geq 3$ to ensure the uniqueness of the solution. Note that the scan range of the equidistant phases is over the π phase range, which is enough to span the polarization plane due to the head-tail symmetry of the dipole axis. Now Eq. 6.5 gives a modulation function that only depends on the azimuthal dipole angle ϕ:

$$P_m(\phi) = \frac{1}{M}\left[1 + \cos(2\tau)\cos\left(2\phi - 2\xi_m\right)\right]. \tag{6.10}$$

It is seen that the modulation contrast is degraded by the ellipticity factor $\cos(2\tau)$, where $\tau = 0$ results in the often-used cosine squared scaling factor $\cos^2(\phi - \xi_m)$, whereas in the case $|\tau| = \pi/4$ no modulation occurs. This modulation factor results in a CRB with a slight dependence on the dipole azimuthal angle ϕ, making the precision somewhat anisotropic. Figure 6.3(a) shows this dependence indicating a strong response on τ close to $\tau \approx 0$ for dipole orientations aligned perpendicular to the applied polarizations. These sharp peaks are mitigated in practice due to non-zero background, as indicated with the grey line in Fig. 6.3(a).

The modulation only approximation to the Fisher-information can be deduced by substituting Eq. 6.10 in the second term of Eq. 6.9 and computing the sum over the different excitation polarizations:

$$F_{\phi\phi} = \frac{4N}{M}\sum_{m=1}^{M}\frac{\cos^2(2\tau)\sin^2(2\phi - 2\xi_m)}{1 + \cos(2\tau)\cos(2\phi - 2\xi_m)}. \tag{6.11}$$

The average Fisher-information over all the molecule orientations follows as:

$$\tilde{F}_{\phi\phi} = \frac{1}{2\pi}\int_0^{2\pi} \mathrm{d}\phi\, F_{\phi\phi} = 4N(1 - 2\cos\tau\,|\sin\tau|) \tag{6.12}$$

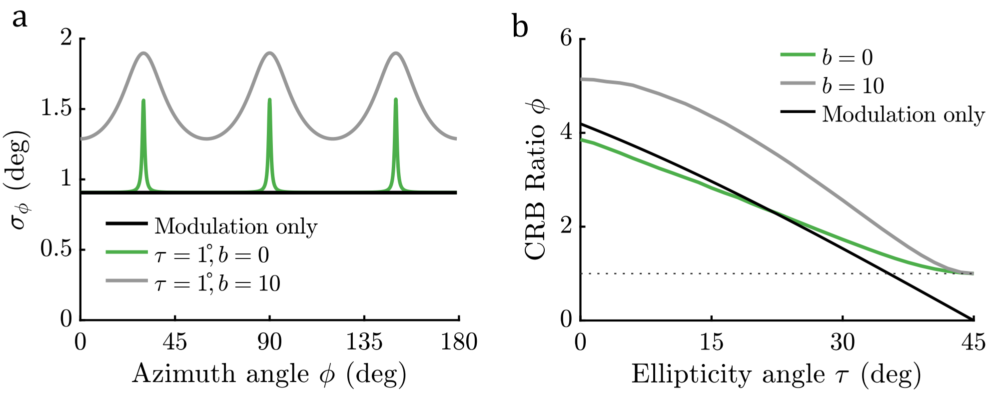

Figure 6.3: CRB performance for normally incident polarization. **(a)** The azimuth angle precision σ_ϕ as a function of the dipole azimuth angle ϕ with polar angle $\theta = \pi/2$ using $M = 3$ polarization steps $\xi_m = [0^\circ, 60^\circ, 120^\circ]$. The precision is computed using Eq. 6.13 with different ellipticity angles τ and numerically with background photons per pixel b. **(b)** The CRB ratio is computed as the average CRB from the polarization modulation relative to the standard (non-modulated) PSF and is shown as a function of the ellipticity angle. The modulation only curve is calculated from Eq. 6.13 and is relative to the standard (non-modulated) PSF. The black dashed line indicates no improvement, i.e., a CRB ratio of 1. All plots are computed with a photon count of $N = 1000$ and the dipole simulations assume matched imaging conditions $n = 1.518$.

where the integral over ϕ can be evaluated using contour integration in the complex plane (substitute $z = \tan\phi$) or by using a computer algebra system. This result in the average precision bound:

$$\tilde{\sigma}_\phi \geq \frac{1}{2\sqrt{N}} \frac{1}{\sqrt{1 - 2\cos\tau |\sin\tau|}} \tag{6.13}$$

independent of the angle offset ξ_0 and referred to here as the modulation only precision. The scaling with $1/\left(2\sqrt{N}\right)$ for linear polarization is a factor $\sqrt{2}$ better than the scaling found for polarimetric detection schemes [20, 42].

This modulation only CRB is plotted relative to the CRB of the standard (non-modulated, $M = 1$) PSF in Fig. 6.3(b) as a function of the ellipticity angle τ. The CRB of the PSF shape is computed numerically from simulated dipole images. The comparison supports the assumption that the modulation term dominates the Fisher-information, at least for the regime $\tau < 30^\circ$. It is likewise seen that the effects of finite support of the fitting Region Of Interest (ROI) and finite pixel size are negligible. The CRB ratio indicates that the precision improves up to four-fold ($\tau = 0$) by the polarization modulation. The CRB ratio in the presence of background ($b = 10$ counts/pixel) is also numerically computed, where the CRB ratio is found to increase to around five. This indicates that the polarization modulation precision scales better with background than the precision based on PSF shape alone. The average precision for $N = 1000$ with zero background ($b = 0$) is $\sigma_\phi = 0.99^\circ$ ($\sigma_\phi = 3.8^\circ$ for $\tau = \pi/4$), whereas for $b = 10$ it is $\sigma_\phi = 1.5^\circ$ ($\sigma_\phi = 7.7^\circ$ for $\tau = \pi/4$). These optimum azimuthal precision levels are better than for example the recent Vortex PSF based method [16], and also better than the experimental results of the original polarization modulation method of ref. [28]. There, an experimentally obtained precision of $\sigma_\phi = 233.9/\sqrt{N = 1000} \approx 7.4^\circ$ for molecules in PMMA (Polymethyl methacrylate) with 50 background counts per pixel per frame is reported. For the same photon counts, we assess the CRB to be around 3.0°. This difference could be due to experimental inaccuracies or to the non-MLE based estimation method [29].

6.3.2. Oblique excitation

Favourable precision levels can be achieved for both the azimuthal and polar angle of the molecule if we generalize the previous scheme to obliquely incident light. This approach to polarization modulation uses the polarization component along the optical axis to probe the polar angle. For the sake of simplicity, we ignore ellipticity now and consider only linearly polarized light along the $\hat{p}$ direction, i.e., $\xi = \tau = 0$. Modulation of polarization is achieved by rotating the direction of incidence around the z-axis, i.e., we take the tilt angle β constant and use azimuthal angles of incidence with equidistant steps $\alpha_m = 2\pi(m-1)/M$. We now find that:

$$Q_m(\phi,\theta) = (\sin\theta\cos\beta\cos(\phi-\alpha_m) - \cos\theta\sin\beta)^2 \tag{6.14}$$

giving rise to a normalization factor:

$$Q_{\text{norm}} = \frac{M}{2} f(\theta) \tag{6.15}$$

with angular dependence:

$$f(\theta) = \cos^2\beta - (3\cos^2\beta - 2)\cos^2\theta. \tag{6.16}$$

The relevant angular derivatives of the expectation function $P_m(\theta,\phi)$ are:

$$\frac{\partial P_m(\theta,\phi)}{\partial\phi} = -\frac{4}{Mf(\theta)}\sqrt{Q_m}\sin\theta\cos\beta\sin(\phi-\alpha_m) \tag{6.17a}$$

$$\begin{aligned}\frac{\partial P_m(\theta,\phi)}{\partial\theta} = \frac{4}{Mf(\theta)}\Big[&\sqrt{Q_m}\,(\cos\theta\cos\beta\cos(\phi-\alpha_m) + \sin\theta\sin\beta) \\ &- \frac{Q_m}{f(\theta)}\left(3\cos^2\beta - 2\right)\cos\theta\sin\theta\Big]\end{aligned} \tag{6.17b}$$

where $Q_m = Q_m(\phi,\theta)$ (Eq. 6.14). These derivatives leads to the modulation-only diagonal Fisher-matrix elements:

$$F_{\phi\phi} = \frac{8N\sin^2\theta\cos^2\beta}{Mf(\theta)}\sum_{m=1}^{M}\sin^2(\phi-\alpha_m) = \frac{4N\sin^2\theta\cos^2\beta}{f(\theta)} \tag{6.18a}$$

$$\begin{aligned}F_{\theta\theta} = \frac{8N\cos^2\beta\sin^2\beta}{f^3(\theta)}\Bigg[&f(\theta) + \frac{c_1}{M}\sum_{m=1}^{M}\cos(2\phi-2\alpha_m) + \\ &\frac{c_2}{M}\sum_{m=1}^{M}\cos(\phi-\alpha_m)\Bigg] = \frac{8N\cos^2\beta\sin^2\beta}{f^2(\theta)}\end{aligned} \tag{6.18b}$$

where $c_1 = 2\cos^2\theta\sin^2\beta$ and $c_2 = \sin(2\theta)\sin(2\beta)$. The off-diagonal Fisher-matrix element $F_{\phi\theta}$ is zero, implying that the precision bounds are:

$$\sigma_\phi \geq \frac{\sqrt{f(\theta)}}{2\sin\theta\cos\beta\sqrt{N}} \tag{6.19a}$$

$$\sigma_\theta \geq \frac{\sqrt{2}f(\theta)}{4\sin\beta\cos\beta\sqrt{N}}. \tag{6.19b}$$

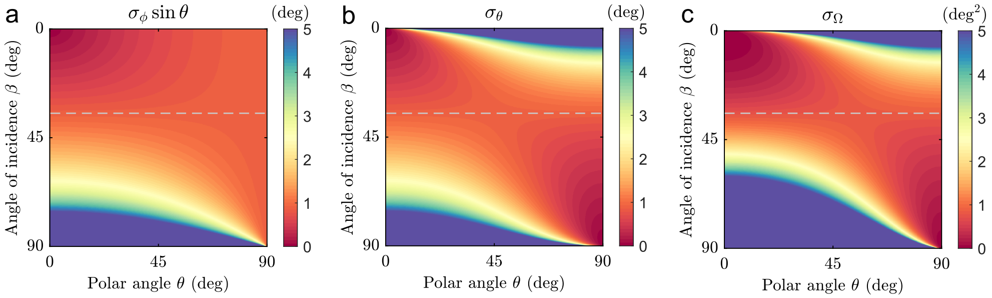

Figure 6.4: Impact of the angle of incidence on the CRB. **(a)** The precision of the dipole azimuth angle σ_ϕ scaled by a factor $\sin\theta$, **(b)** polar angle precision σ_θ, and **(c)** solid angle orientation precision σ_Ω as a function of the dipole polar angle θ and angle of incidence β using Eq. 6.19. The grey dashed line is used to guide the eye for $\beta = \arccos(\sqrt{2/3}) \approx 35^\circ$. All plots are computed with $N = 1000$.

Figure 6.4 shows these precision bounds as calculated for the azimuthal, polar, and combined (solid angle) precision $\sigma_\Omega = \sin\theta\sigma_\theta\sigma_\phi$ as a function of the angle of incidence β and the polar dipole angle θ. It appears that for $\beta < \arccos(\sqrt{2/3}) \approx 35^\circ$ the precision improves with decreasing polar angle θ, whereas for $\beta > \arccos(\sqrt{2/3})$ the precision improves with increasing polar angle θ. In general there is no a priori information on the distribution of polar dipole angles, implying that the choice $\beta = \arccos(\sqrt{2/3})$ is ideal as it generates an isotropic precision. This angle of incidence leads to the simplified precision bounds:

$$\sigma_\phi \geq \frac{1}{2\sin\theta\sqrt{N}} \tag{6.20a}$$

$$\sigma_\theta \geq \frac{1}{2\sqrt{N}} \tag{6.20b}$$

where we used $\cos\beta = \sqrt{2/3}$ and $\sin\beta = \sqrt{1/3}$ to simplify the results. The combined precision in terms of solid angle for this angle of incidence is now $\sigma_\Omega = 1/(4N)$, uniform over the unit sphere representing all dipole orientations. These bounds match the quantum limits for orientation estimation [43].

The modulation only precision, shown in Fig. 6.5 is compared to the numerical simulations with varying ellipticity angle and background levels. The CRB precision over the entire sphere of dipole orientations is displayed in Fig. 6.5(a,d) with an

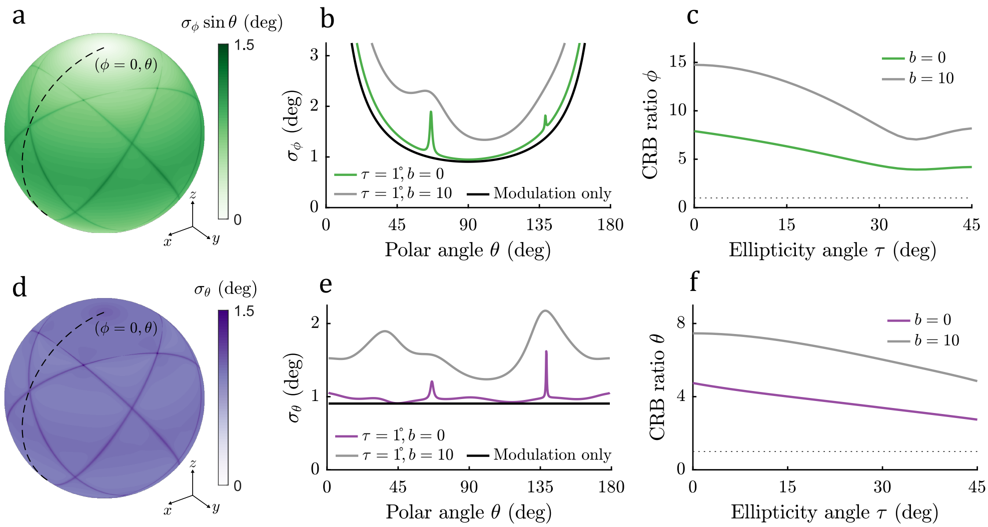

Figure 6.5: CRB performance for oblique polarization. **(a)** The azimuth angle precision σ_ϕ scaled by $\sin\theta$ over the sphere of orientations for five oblique polarization steps at $\beta = \arccos(\sqrt{2/3})$ and ellipticity $\tau = 1^\circ$. **(b)** The azimuth angle precision as a function of the dipole angle (θ) along the black dashed line in (a) ($\phi = 0$). The precision for modulation only is calculated from Eq. 6.20 and computed numerically with $\tau = 1^\circ$ and different background counts per pixel b otherwise. **(c)** The azimuth CRB ratio, which is the CRB from the polarization modulation relative to the CRB of the standard (non-modulated, $M = 1$) PSF as a function of the ellipticity angle. The black dashed line indicates no improvement, i.e., a CRB ratio of 1. **(d, e, f)** Same as above with the polar angle precision. All plots are computed with $N = 1000$ photons and dipole simulations assume matched imaging conditions $n = 1.518$.

ellipticity angle of 1°, where the peaks of deteriorated precision are now relative to the five polarization planes. Fig. 6.5(b,e) shows the azimuth and polar angle precision dependency along the molecules polar angle with constant $\phi = 0$ for different polarization ellipticity and background photon counts. The obtained CRB is plotted relative to the CRB of the standard (non-modulated, $M = 1$) PSF in Fig. 6.5(c,f) as a function of the polarization ellipticity angle τ. The CRB ratio indicates that the modulation improves the orientation precision by a factor of 7.6 and 4.7 for the azimuth and polar angle in the case of zero background and scales up to a factor of 14.4 and 7.8 in the case of 10 background photons per pixel.

6.4. Numerical investigation of estimator performance

We have tested the performance of the combined position and orientation estimator through simulations. We have focused on the impact of the SBR and tolerances for the required set of excitation polarization states at the sample. The latter provides a guideline on how well the microscope must be calibrated.

6.4.1. Simulation setup

The numerical studies were performed with ground truth dipole images calculated with the vectorial imaging theory (see appendix 6.9.1) as input to the developed MLE. We used an image plane grid corresponding to a region of interest (ROI) of 11×11 pixels. The optical settings were taken to match our imaging system (section 6.5.1) with a numerical aperture (NA) of 1.49 and a pixel size of 65 nm in the object space. We assume imaging conditions with refractive indices of 1.33, 1.523, and 1.518 for the imaging medium, cover slip, and immersion medium. Unless stated otherwise, we take 1000 detected photon counts on the camera and 10 background counts per pixel. We neglect readout noise but added Poisson noise to each image with the PSF as the Poisson rate.

The angle of incidence is either $\beta = 0$ (normal incidence) with $M = 3$ or $\beta = \arccos(\sqrt{2/3})$ (oblique incidence) with $M = 5$, where M is the number of different excitation polarizations as outlined in the theory section. Five azimuthal steps were chosen in the case of oblique incidence in order to guarantee the stability of the optimization, even though the theoretical CRB was independent of M. In particular, we found that the sensitivity to the initial values of the parameters in the MLE optimization was unfavourable for three polarization steps, thereby compromising robustness. This behaviour is not unreasonable, as now an additional parameter (the polar angle) must be estimated.

The statistical errors were evaluated from 10,000 random instances with dipole positions taken from a uniform distribution over 1 pixel and dipole orientations uniformly distributed over the unit sphere, i.e., $\phi = \pi u$ and $\theta = \arccos(1-2u)$ where u is a uniform random number from the distribution $U[0,1]$.

6.4.2. Signal-to-background ratio (SBR)

First we quantify the range of photon counts over which the parameters are expected to be estimated reliably. Figure 6.6 shows the performance as a function of the signal-to-background ratio (SBR = N/b) in the dipole images. For an SBR = $1000/10$, the normal incidence polarization mode (averaged over in-plane molecular orientations) gives a localization precision $\sigma_{xy} = 3.6$ nm, and an azimuth precision $\sigma_{\phi} = 1.5^{\circ}$. The signal count and background photon count precision are $\sigma_N = 42$ photons and $\sigma_b = 0.34$ photon per pixel (Fig. 6.6a). For the oblique incidence case (averaged uniformly over the unit sphere) the lateral localization precision is $\sigma_{xy} = 4.6$ nm, azimuth and polar angle precision are $\sigma_{\phi} = 2.4^{\circ}$, $\sigma_{\theta} = 1.6^{\circ}$, and signal and background photon count precision are 49 photons and 0.35 photons per pixel (Fig. 6.6b).

Figure 6.6(c-d) show the estimator efficiency given by the ratio CRB/σ^2. Our estimator performs at the precision bound over a broad range of photon counts. At very low SBR values, however, this is no longer the case. We find that the estimator efficiencies drop below 95% for SBR < 30 and SBR < 50 for the normal incidence and oblique incidence modes, respectively.

Figure 6.6(e-f) show the estimator bias Δ relative to the precision σ. A bias arises at low photon counts SBR $< 10^2$ where the estimator tends to overestimate the signal photon count and underestimate the background photon count by a few percentage points of the precision. This mismatch is much smaller than the conventional

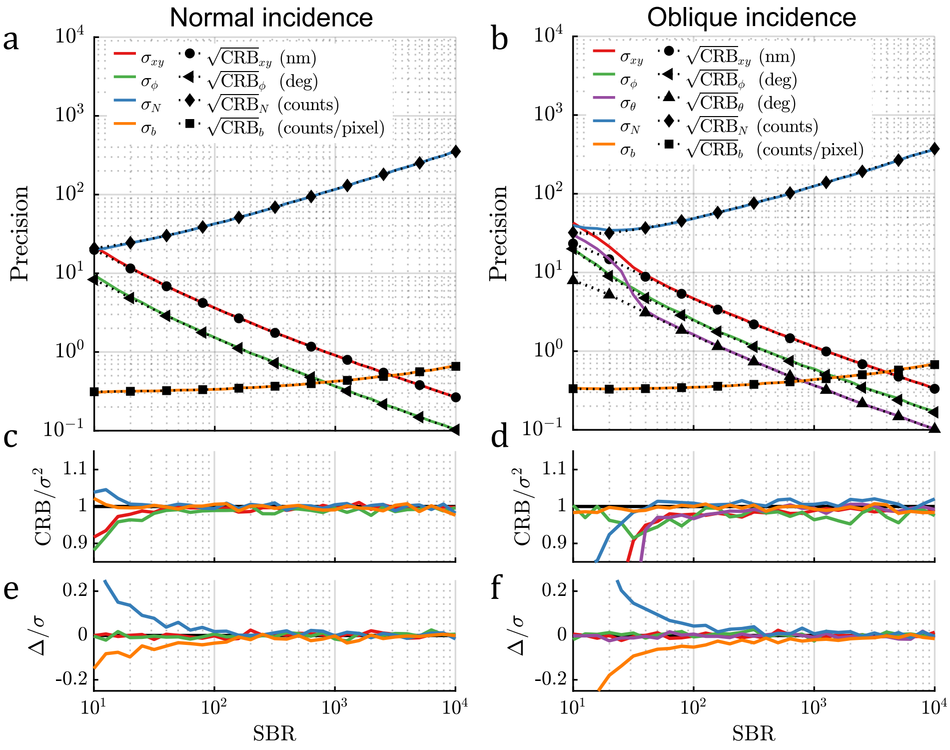

Figure 6.6: Simulation study of signal-to-background ratio (SBR $= N/b, b = 10$). **(a)** The precision for the estimated parameters (coloured lines) as a function of the SBR compared to the CRB (black lines) for the in-plane and **(b)** oblique polarization mode. **(c-d)** The estimator efficiency (CRB/σ^2) for the in-plane polarization and oblique polarization mode. **(e-f)** The estimator bias (Δ/σ) for the in-plane polarization and oblique polarization mode.

Gaussian model, where up to 30% photon count underestimation commonly occurs [44, 45]. We also observe that our MLE with a vectorial PSF model achieves the CRB at very high photon counts SBR $> 10^3$, which is not the case for modulation enhanced SMLM when using a Gaussian model due to large photon count errors [31].

6.4.3. Estimation performance dependence on polarization quality

Normal incidence Simulations were performed to obtain insight into the required accuracy for the illumination polarization parameters. Figure 6.7 shows the results of this analysis for the normal incidence case with a relatively low signal count SBR $= 1000/10$. A significant drawback of this excitation mode is that only the azimuthal angle is modulated. When the molecules are tilted away from the polarization plane, i.e. if θ is less than $90°$ the performance worsens due to model mismatch (Fig. 6.7(a,c)). This mismatch is apparent as the photon count bias accumulates up to $\pm 1\sigma$ if θ deviates from the nominal $90°$ by $18°$. This appears to be the same deviation beyond which the efficiency of the estimator is compromised. Therefore attention must be taken if these tilted molecules are included in the estimation process as their contribution limits the overall localization precision.

The CRB performance as a function of the ellipticity angle τ, or equivalently the (amplitude) extinction ratio $\kappa = \cot \tau$, was shown in Fig. 6.3. There, the assumption was that the polarization parameters are correctly calibrated, which is not always the case in practice. Figure 6.7(b,d) shows the results when the estimator assumes perfect linearly polarized excitation, whereas the ground-truth extinction ratio is varied. It is seen that the assumption of perfect linear polarization is valid for ground-truth extinction ratios above ~20. When the ground-truth extinction ratio is too low, the estimator no longer reaches the lower bound as the imperfect polarization induces photon count biases. Intensity extinction ratios down to 12:1 have been reported in the literature for similar methods [28], and in these cases, it becomes essential to modify the estimator to take calibrated, non-perfect, excitation polarization states into account. These imperfect extinction ratios, in combination with considering molecules with out-of-plane tilt in the analysis, may be contributing factors why the reported precision in [28] falls short of the CRB derived in this chapter.

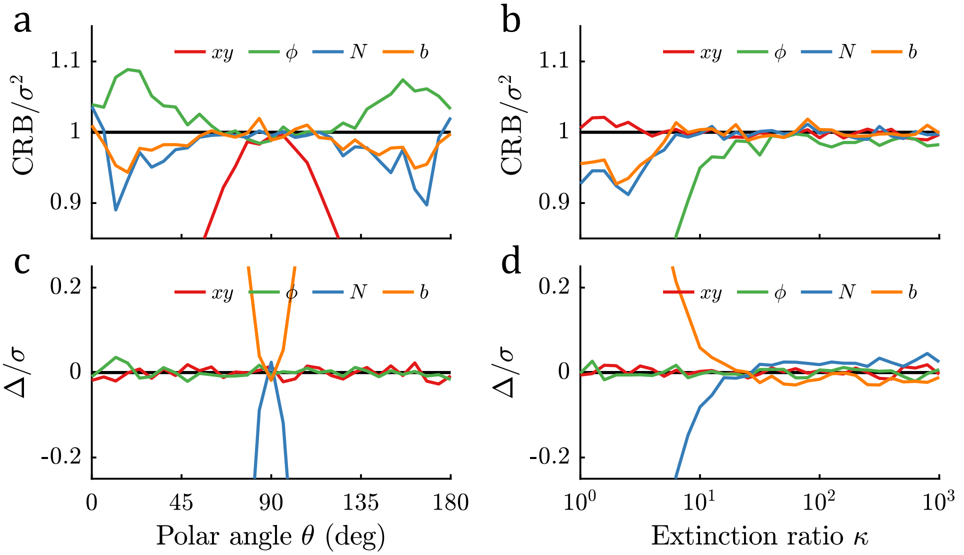

Figure 6.7: Sensitivity analysis of in-plane polarization parameters (SBR = N/b = 1000/10). **(a, c)** The estimator efficiency (CRB/σ^2) and bias (Δ/σ) as a function of dipole polar angle. **(b, d)** The estimator efficiency and bias as a function of a ground-truth extinction ratio where the estimation assumes perfect linearly polarized excitation.

Oblique incidence In the oblique incidence mode the full orientation is estimated, and no deterioration of performance by dipoles tilted from the image plane occurs. On the downside now the angle of incidence β must be calibrated as well. Figure 6.8 shows the results of the sensitivity analysis for the oblique incidence case. The lower limit for the extinction ratio remains about the same, i.e. for values below approximately 20 an experimentally determined value must be used in the estimator (Fig. 6.8(a,c)). It is seen that orientation parameters are the first to drop in estimator efficiency when the extinction ratio is lowered.

The oblique incidence mode requires the calibration of the different directions of incidence of the polarized excitation beams. The estimator maintains an efficiency above 95% for errors $< 1^\circ$ in the angle of incidence (Fig. 6.8(b)). It appears that there is a bias that depends on the ground truth dipole orientation. When averaged over all orientations, however, this bias averages out to zero and instead contributes to the degradation of precision (Fig. 6.8(b,d)).

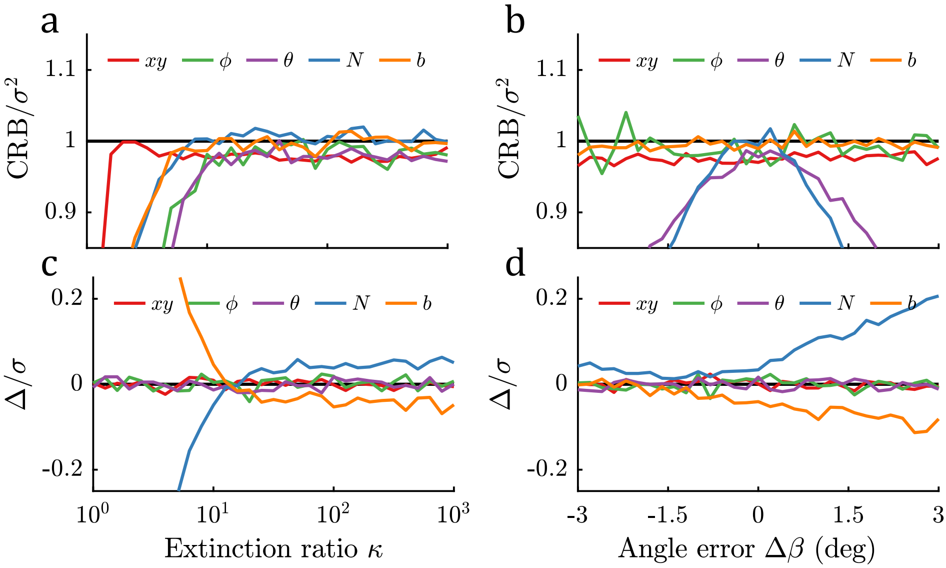

Figure 6.8: Sensitivity analysis of polarization parameters (SBR = $N/b = 1000/10$). **(a, c)** The estimator efficiency (CRB/σ^2) and bias (Δ/σ) as a function of extinction ratio, **(b, d)** as a function of a constant angle error $\Delta\beta$ between the estimation and the ground-truth polarization steps.

6.5. Experimental setup

We have developed a microscope setup with accurate control of the excitation polarization in order to demonstrate the proposed high-precision orientation estimation principles. The key idea is to combine rotation of linear polarization with 2D galvo mirrors to quickly reposition the excitation beam to different positions in the back focal plane of the microscope, resulting in fast switching of the direction of incidence of the excitation beam. The desired level of control of the polarization state and direction of incidence requires an intricate alignment procedure and calibration steps described in detail in the following.

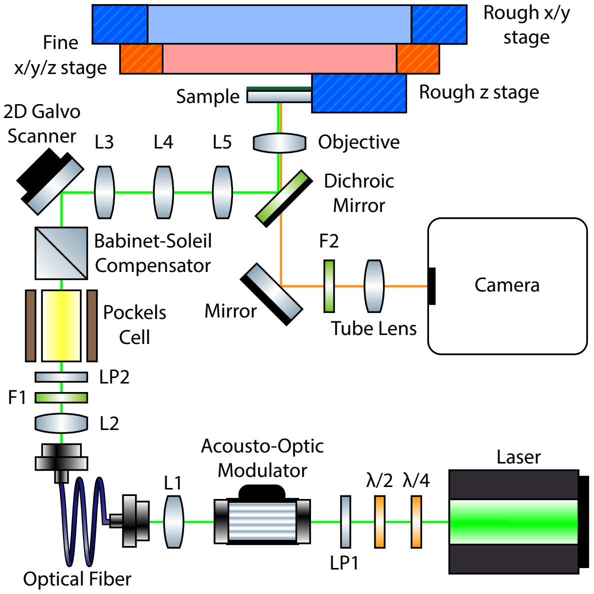

Figure 6.9: Schematic of the optical layout of the widefield microscope with polarization control and beam angle steering in the excitation path.

6.5.1. Layout

Figure 6.9 shows the layout of our optical system with polarization control and consists of the following components. The polarization of the laser (FKL532.100.CWA.L, Omicron) is cleaned up by linear polarizer LP1 (GTH5-A, Thorlabs), the throughput of linearly polarized light is optimized with a $\lambda/4$ waveplate (AQWP05M-600, Thorlabs) and $\lambda/2$ waveplate (WPH05ME-532, Thorlabs). The Acousto-Optic Modulator (AOM) (TEM-85-2, Brimrose) modulates the amount of light coupled into a polarization maintaining fibre (P3-488PM-FC-2, Thorlabs) by lens L1 (C230TMD-A, Thorlabs). Lens L2 (N PLAN L 20x/0.35, Leica) collimates the light from the fibre output, by coupling through the polarization maintaining fibre the beam is spatially filtered and results in a Gaussian beam-profile. After the fibre and the excitation laser spectrum is cleaned up by filter F1 (FF01-532/18, Semrock) and the polarization by LP2 (GTH5-A, Thorlabs). Hereafter the fast axis of the Pockels cell (EM508-2T-F-AR532, Leysop) is oriented 45 degrees to the vertical transmission axis of LP2 and the fast axis of the Babinet-Soleil compensator (SBC-VIS, Thorlabs) is perpendicular to the transmission axis of LP2. The plane in-between the 2D galvo mirrors (GVS002, Thorlabs) is relayed via the lenses L3 (AC254-080-A-ML, Thorlabs), L4 (AC254-300-A-ML, Thorlabs), L5 (AC254-150-A-ML, Thorlabs) and the objective lens (CFI Apo TIRF 100XC Oil, Nikon) to the sample plane. The sample is mounted through a collection of stages, (M-111.1DG with C-863, PI) for the rough z positioning, (P-517.3CL with E-710.4CL, PI) for the fine xyz translation and (H117N2IX, Prior) for rough xy translation. The dichroic mirror (Di03-R405/488/532/635-t1, Semrock) splits the excitation and emission path. After an elliptical mirror (BBE1-E02, Thorlabs) and emission filter F2 (FF01-582/64, Semrock) the emitted fluorescence is focused onto the camera (ORCA-Flash4.0 V2, Hamamatsu) by a tube lens (ITL200, Thorlabs). The exposure output of the camera triggers a data acquisition card (PXIe-6363, NI) to switch between illumination states and sends corresponding signals to the Pockels cell amplifier (M5000, Leysop), AOM RF driver (FFA-85-B1-F1, Brimrose) and the galvo mirrors.

6.5.2. Alignment

To achieve a high extinction ratio of linearly polarized light in the sample plane the polarization optics needs to be properly aligned. The polarization rotation is done with a Pockels cell, Babinet-Soleil compensator and a dichroic mirror. To rotate the polarization whilst maintaining a linear polarization it is necessary to have a $\lambda/4$ waveplate after the Pockels cell, with the fast axis aligned perpendicular to the transmission axis of LP2. The dichroic mirror can induce phase differences between s and p polarized light and thus a diagonally polarized incident beam will no longer be linearly polarized after reflection [46]. To compensate for this effect the Babinet-Soleil compensator can be aligned to either the s or p axis of the dichroic mirror to compensate for any induced phase differences. However, to avoid the use of another $\lambda/4$ waveplate, the Babinet-Soleil compensator is adjusted such that, combined with the dichroic mirror, it has a net $\lambda/4$ wave retardance, aligned perpendicular with respect to LP2. For initial alignment two temporary polarizers are placed after LP2, the first one is cross-polarized with LP2, the second is placed in between and aligned 45° to LP2 such that it maximizes the transmission. Thereafter the crossed polarizer is removed and the light entering the Babinet-Soleil compensator is polarized 45° with respect to LP2. The Babinet-Soleil compensator is then adjusted such that the light after the dichroic mirror is circularly polarized, which is achieved by minimizing the intensity variation (<1.5%) measured with a continuously rotating linear polarizer (LPVISC100-MP2, Thorlabs) in an automatic rotation mount (8MPR16-1, Standa) on a power meter (PM100D and S121C, Thorlabs). Thereafter the temporary polarizer is removed giving the polarization in the sample plane the desired linear polarization.

The modulation of the excitation polarization is achieved with the Pockels cell. To get the best performance, the Pockels cell needs to be rotationally aligned. The tip and tilt can be optimized by placing the Pockels cell between crossed polarizers, then a Maltese cross pattern can be visualized by diffusing the beam with a lens tissue. The tip and tilt is adjusted such that the Maltese cross is centred on the main beam. The roll is adjusted with a voltage applied to the Pockels cell so that the transmission through crossed polarizers is maximized, making the fast axis at 45° to LP2. With the crossed polarizer removed the extinction ratio is measured with the rotating polarizer for varying Pockels cell voltages. The Babinet-Soleil compensator is slightly adjusted to get the purest linear polarization over the full Pockels cell range.

The galvo mirrors are a single unit containing two separate galvo mirrors, one for each axis and spaced 10 mm apart. This unit is positioned such that a reversely propagating beam from an alignment laser (CPS532, Thorlabs) pointed down from the objective in Fig. 6.9 is focused in between the two galvo mirrors. Due to the distance between these two mirrors the plane of tipping and tilting for the forward propagating beam does not coincide.

6.5.3. Calibration

The first calibration step is to relate the applied polarizations to the camera frame of reference. This is done in two steps, firstly connecting the positions in the back focal plane of the objective lens that are addressed with the galvo mirrors with respect to the camera plane. To that end we scan each individual galvo mirror in a defocused liquid ATTO 565 sample inducing a shift in the illumination pattern that is visible on the camera. Tracking this shift gives an angle of $0.005^\circ \pm 0.005^\circ$ for the x galvo mirror and an angle of $88.86^\circ \pm 0.05^\circ$ for the y galvo mirror, close to the desired 0° and 90° (compare Fig. 6.10(a)).

Secondly, the Pockels cell control voltage is calibrated to align the s and p-polarization orientations to the direction of incidence set by the galvo mirrors. Figure 6.10(b) shows the modulation of fluorescence of beads on the cover slip for x and y galvo settings that result in directions of incidence a few degrees beyond the critical angle. A maximum is obtained for a Pockels cell control voltage of -0.0351 V for the x galvo, implying that at this voltage the polarization is p-polarized [47]. Similarly for the y galvo axis there is a minimum at a Pockels cell control voltage of -0.0350 V implying the light is s-polarized. This gives voltage references that calibrate the excitation polarizations to the directions of incidence, which are itself calibrated to the camera xy coordinate frame. In this way the applied polarization states are known in the camera xy coordinate frame, with the advantage that this does not require challenging manual co-alignment of optical components [28], but instead derives fully from fluorescence data.

In a next calibration step to determine the rotation response of the Pockels cell, the change of the polarization angle ξ_{LP} is measured as a function of the Pockels cell control voltage. This is done using a rotating linear polarizer and rotation mount (mentioned in section 6.5.2), combined with a photodiode (DET100A/M, Thorlabs), the angle ξ_{LP} is defined with respect to the zero point of the rotation mount. Figure 6.10(c) shows that there is a rotation of $28.53\ ^\circ/V$ and that the response is linear between ± 2 V. By combining this angle-voltage response with the previous s and p polarization calibration it is now possible to determine ξ, the polarization orientation angle with respect to the camera coordinate frame, as a function of the Pockels cell control voltage.

A final polarization calibration step involves equalization of amplitude differences between the s and p-polarized components, that can arise from differences in reflectivity of the dichroic mirror with polarization. This effect can be compensated by adjusting the AOM that controls the laser power. Figure 6.10(d) shows 3% variation in laser power as the polarization is rotated with the Pockels cell, compensating with the AOM the variation can be reduced to 0.16% (standard deviation of the mean value). Lastly, the intensity extinction ratio is measured using the rotating linear polarizer, lock-in amplifier (SR830, SRS) and optical chopper (MC2000-EC, Thorlabs), and is found to be larger than 211:1 for all polarization orientation angles ξ and 851:1 on average (Fig. 6.10(e)). The extinction ratio still peaks at $\xi = 0^\circ$ and $\xi = \pm 90^\circ$

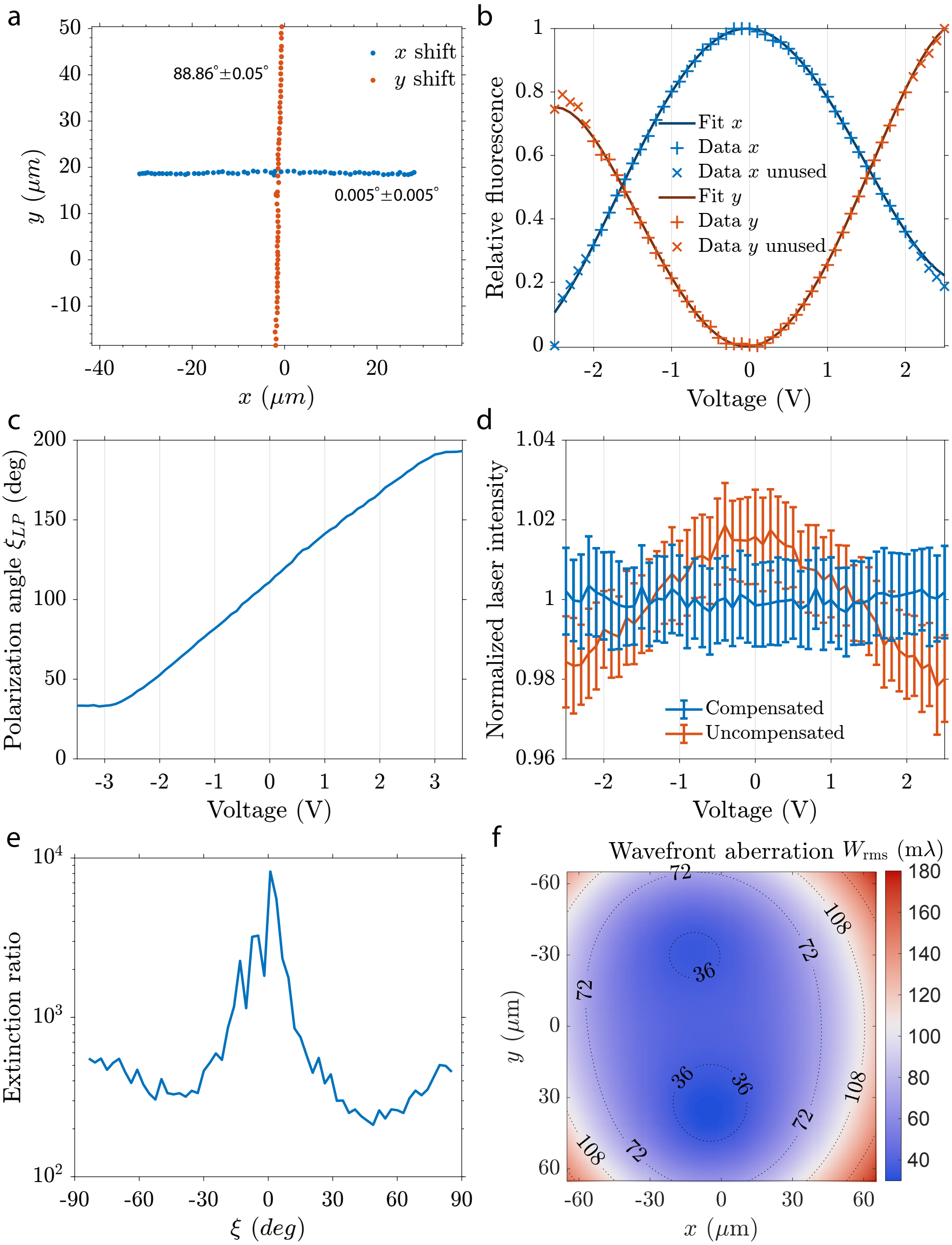

Figure 6.10: Polarization and aberration calibration. **(a)** Illumination scan orientations for each respective galvo mirror axis. **(b)** Fluorescence modulation of beads with illumination just beyond the critical angle with varying polarization states. **(c)** Polarization angle as a function of the Pockels cell control voltage. **(d)** Intensity variation of s and p-polarized light in the sample plane, compensated by varying the incident power with the AOM. **(e)** Extinction ratio (intensity) for different polarization orientation angles. **(f)** Total measured wavefront aberration level in the imaged field for the microscope setup. The dotted contour lines show the aberration level in relation to Maréchal's diffraction limit (<72 mλ).

as the light incident on the dichroic mirror is pure s or p-polarized and deteriorates slightly towards $\xi = \pm 45^\circ$.

In the MLE fitting procedure we have used experimentally obtained optical aberration values as a function of the position in the imaged Field Of View (FOV), generated from a calibration measurement on a sparse bead sample. This aberration calibration procedure [16] guarantees knowledge of the optical aberrations with an accuracy well below < 36 mλ [45], which is needed to minimize non-uniform biases in the localization and orientation estimation. Figure 6.10(f) shows the measured aberration levels across the FOV indicating sizeable aberrations throughout, even beyond the diffraction limit at the edges of the FOV.

6.6. Experimental results

6.6.1. Polarization modulation fitting

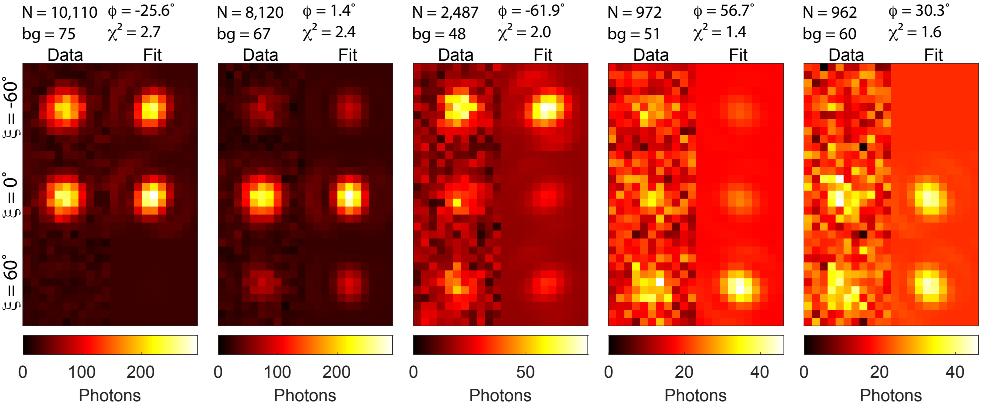

Figure 6.11: Experimental polarization modulation of individual fluorophores and corresponding fit. Each row is illuminated with a different in-plane polarization (ξ). Each column shows a single fluorophore with the data on the left and fit on the right. The estimated parameters (N, b and ϕ) per set of frames are displayed at the top, along with the quality of fit (χ^2).

As a proof of principle, we imaged single fluorophores (ATTO 565) embedded in polymethyl methacrylate (PMMA). These single emitters are rotationally constrained in the PMMA resin (details on the sample preparation are in appendix 6.9.2). The sample was sequentially illuminated with 3 polarization states each shifted by $\Delta\xi = 60^\circ$ at normal incidence. Every individual frame had an exposure time of 300 ms and a laser intensity of 100 W/cm^2. We estimated the position and in-plane orientation of several isolated single molecules from the sequence of images with different polarization states (Fig. 6.11). There is a good agreement between the data on the left and the fit on the right (mean $\chi^2 = 1.7$). For relatively high photon counts the shape change of the PSF can be observed. An elongation of the PSF shape can be seen (diagonally to the bottom left for the first molecule and vertically for the second molecule). The PSF shape is not clearly perceivable at lower photon counts but still needs to be taken into account to make the best possible estimate of position and orientation.

6.6.2. Experimental precision with normal incidence

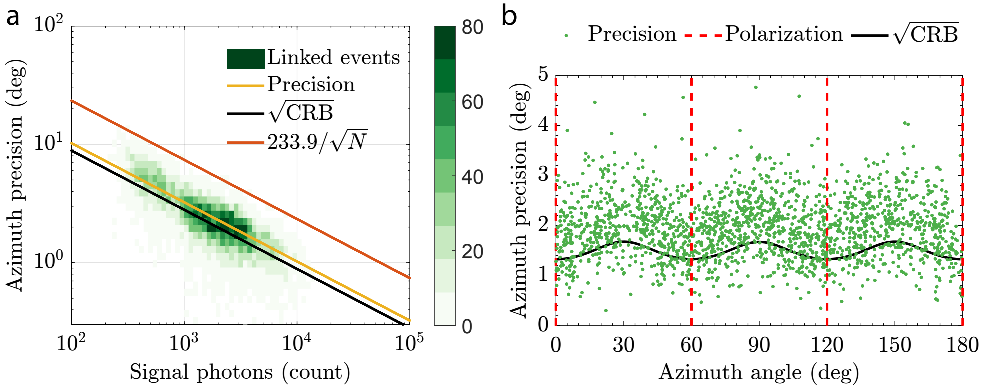

Figure 6.12: Assessment of experimental precision. **(a)** Azimuthal precision from linked localizations ($t_{on} \geq 15$) compared to the estimated photon count (green histogram indicating the number of measurements). The average experimental precision (yellow), theoretical $\sqrt{\mathrm{CRB}}$ (black), and current state-of-the-art [28] precision (red) are also indicated. The photon count range is expanded by combining 8 experiments with varying laser intensities and camera exposure. **(b)** Azimuthal precision compared to the azimuthal angle for photon counts one standard deviation around the average. The applied polarizations are indicated (dashed red), as well as the $\sqrt{\mathrm{CRB}}$ (black), which is calculated from the median photon count ($\tilde{N} = 2696$) and background ($\tilde{b} = 68$).

Next, we continued imaging ATTO 565 molecules embedded in PMMA. In this case 50 cycles of 3 polarization states are acquired at various laser powers and camera exposure times (appendix 6.9.3). This expands the distribution of photon counts such that the angular estimation precision can be analyzed over a wide range of photon counts. To analyze the experimental precision multiple localizations of the same single-molecules are linked (appendix 6.9.3) and analyzed if they are on for more than 4 cycles. On average we obtained 8.3 estimates for each molecule from which we calculated the orientation estimation precision as the standard deviation of the orientation estimates (Fig. 6.12(a)). The average precision σ_ϕ and $\sqrt{\mathrm{CRB}_\phi}$ are obtained from least squares fits of a line with slope proportional to $1/\sqrt{N}$. The information content of the photons on the camera is efficiently used as is evident from the fit between the experimental precision and the CRB, with the experimental precision only 16% above the CRB on average. This experimental azimuthal precision is a factor of about 2.3 better than the previously achieved experimental precision [28]. We furthermore confirm the theoretical prediction that there is a slight variation in precision with the molecular orientation in relation to the three excitation polarization directions (Fig. 6.12(b)).

We attempted the estimation of both the in-plane and out-of-plane angle of the molecules according to the oblique incidence method. Unfortunately, this did not result in reliable fit outcomes, as we found a bias in the polar angle towards the in-plane orientation. One experimental difficulty we encountered relates to a shift of the Gaussian excitation profile across the FOV upon changing the direction of incidence of the illumination beam with the 2D galvo system. This resulted in undesired intensity variations for each molecule that are not coupled to the polarization modulation. This could be compensated for with an additional calibration step, but may not work completely satisfactorily. The use of a single 2D scanning mirror (e.g. a piezo or MEMS mirror) could potentially solve this problem.

6.7. Discussion

6.7.1. Rotational diffusion

The main limitation of the current image formation model is the assumption that the emitter is stationary (section 6.2), i.e., that it has a completely fixed pose in space with negligible rotational diffusion. This assumption could be correct in applications where the rotational mobility of the molecule can be regarded as completely restricted at typical frame rates of milliseconds [10]. The label molecules in a biological sample, however, undergo rotational diffusion and wobble around an average orientation [48]. For instance, common intercalators (e.g., SYTOX orange) as used in the λ-DNA experiments in chapter 5 show a rotational diffusion within a cone with a semi-cone angle on the order of $20^\circ - 30^\circ$ [16, 28, 49]. If not taken into account, this would inadvertently affect the estimated photon counts and thereby worsen the quality of the orientation estimation. An interesting extension to the work presented in this chapter is therefore to parametrize the rotational diffusion and jointly estimate these parameters together with the molecule's position and preferential orientation. Here a PSF model that is a weighted sum of the fully free and fully fixed dipole PSFs, which is appropriate for fast rotational diffusion, seems like the best starting point [16, 50].

6.7.2. Additional parameters

The CRB performance with respect to the orientation estimation or any other parameters could be improved by the use of PSFs engineered towards the specific problems at hand in combination with modulation of the excitation polarization. For example, such PSF designs could be designed to estimate axial position information, which would enable the generalization to the case of 3D SMLM. This could, however, come at the cost of reduced lateral localization precision and a limited axial working range because axial localization usually entails a decrease of the signal-to-background ratio. An interesting question to investigate regarding the combination of PSF engineering and polarization modulation would be the quantification of possible differences between the absorption and emission dipole moment [35, 51].

6.7.3. Multiphoton excitation

Multiphoton excitation induces a non-linear dependence of the fluorescence excitation efficiency on dipole orientation that can be used to enhance the estimation precision. For example, for two-photon excitation, the intensity of fluorescence is proportional to the fourth power of the excitation amplitude $|\hat{d} \cdot \hat{\epsilon}|^4$ [52]. This fourth power dependence improves the polarization contrast, and therefore the CRB precision can, in principle, be reduced. For example, in the case of normal incidence described in section 6.3, the modulation function now takes the following form assuming that $\tau = 0$:

$$P_m(\phi) = \frac{8}{3M} \cos^4(\phi - \xi_m). \tag{6.21}$$

The Fisher-information element can be determined by substituting Eq. 6.21 in the second term of Eq. 6.9:

$$F_{\phi\phi} = \frac{16N}{3M} \sum_{m=1}^{M} [1 - \cos(4\phi - 4\xi_m)] = \frac{16N}{3} \tag{6.22}$$

which yields the precision limit:

$$\sigma_\phi = \frac{\sqrt{3}}{4\sqrt{N}}. \tag{6.23}$$

It is seen that the uncertainty is smaller by a factor of $\sqrt{3}/2 \approx 0.87$ as compared to the precision in section 6.3.

6.7.4. Oblique illumination at the critical angle

A particularly interesting case for polarization modulation at oblique incidence is the case of illumination exactly at the critical angle. In that case the wavevector in the sample medium $\vec{k}_t$ is fully in the sample (xy) plane, and as a consequence the p-polarization vector is then along the optical (z) axis, where as the s-polarization vector is in the sample plane orthogonal to $\vec{k}_t$. Furthermore, the phase shifts for the p and s-polarized components are both zero, as opposed to the case of an angle of incidence beyond the critical angle [47, 53]. This would instead induce an elliptical polarization in the sample when rotating to an incident linear polarization intermediate to the p and s-polarization. This can be avoided at the critical angle, enabling continuous rotation of linearly polarized light with an arbitrary orientation. A difference between the amplitude of transmission for the p and s-polarization components does remain, which would introduce a rotation of the linear polarization inside the sample relative to the incidence polarization, which would have to be taken into account. In order to avoid the TIRF induced polarization phase differences and achieve an amplitude extinction ratio $\kappa \geq 20$, the incident angle needs to be within a challenging 0.06° of the critical angle.

6.8. Conclusion

In conclusion, we proposed a concept to estimate molecular orientation that is compatible with localization microscopy by using polarized excitation. The theoretical performance limits were quantified using a Cramér-Rao bound analysis in terms of the excitation polarization parameters. To this end, analytic expressions for the CRB for cases of normal and oblique incidence were derived. Numerical simulations were performed to evaluate the performance of the polarization modulation method as a function of SBR and to assess the required accuracy of the excitation polarization states in experiments. We showed that a precision below 2.5° can be achieved in principle for both the azimuthal and polar angle with only 1000 photons in the presence of 10 background photons per pixel. The method is considered beneficial for orientation measurements where standard SMLM resolution is desired, particularly for cases where only dim fluorophores are available. We have built a microscope setup for testing the proposed polarization modulation methods, detailing the necessary calibration protocols. The setup enables polarization modulation with a linear polarization purity characterized with an average (intensity) extinction ratio of 851:1. In a proof-of-principle experiment on single molecules embedded in PMMA we achieved an experimental in-plane orientation precision only 16% above the CRB, and a factor 2.3 better than previously reported results [28]. In future work we strive for an experimental demonstration of the in-plane and out-of-plane orientation precision for the oblique illumination scheme. Other future steps worth investigating are the incorporation of a rotational diffusion model, and the combination of polarization modulation with a PSF engineering method.

6.9. Appendix

6.9.1. Dipole image formation model

The expected photon count for pixel n for a fixed dipole emitter at position $\vec{r}_0$ and with orientation Ω is found by integrating the PSF over the pixel area A with size $a \times a$:

$$H_n(\vec{r}_0, \Omega) = \int_A \mathrm{d}x\mathrm{d}y\, H(\vec{r} - \vec{r}_0, \Omega). \tag{6.24}$$

The fixed dipole PSF is proportional to the modulus squared of the electric field in the image plane:

$$H(\vec{r}, \Omega) = \sum_{j=x,y} \left|E_j(\vec{r}, \Omega)\right|^2, \tag{6.25}$$

where the electric field in the imaging plane can be written as:

$$E_j(\vec{r}, \Omega) = \sum_{k=x,y,z} w_{jk}(\vec{r}) d_k(\Omega) \tag{6.26}$$

with components $j = x, y$ taken proportional to the emission dipole component d_k and where the $w_{jk}(\vec{r})$ can be computed by integrating over normalized pupil coordinates $\vec{\rho}$:

$$w_{jk}(\vec{r}) = \frac{1}{\pi} \int \mathrm{d}^2\rho\, A(\vec{\rho}) \exp\left(\frac{2\pi i W(\vec{\rho})}{\lambda}\right) q_{jk}(\vec{\rho}) \exp(-i\vec{k}(\vec{\rho}) \cdot \vec{r}). \tag{6.27}$$

Here the wavevector $\vec{k}(\vec{\rho})$ is given by:

$$\vec{k}(\vec{\rho}) = \frac{2\pi}{\lambda}\left(\mathrm{NA}\rho_x, \mathrm{NA}\rho_y, \sqrt{n_{\mathrm{med}}^2 - \mathrm{NA}^2\vec{\rho}^2}\right) \tag{6.28}$$

with n_{med} the refractive index of the imaging medium. The angular representation of the wavevector is:

$$\vec{k}(\vec{\rho}) = \frac{2\pi n_{\text{med}}}{\lambda} \left(\sin\eta\cos\psi, \sin\eta\sin\psi, \cos\eta\right). \tag{6.29}$$

Other quantities appearing in the integral expression for the $w_{jk}(\vec{r})$ are the aplanatic amplitude correction factor $A(\vec{\rho})$ [54, 55], the phase (aberrations) $W(\vec{\rho})$, and the polarization vector components $q_{xk}(\vec{\rho})$ and $q_{yk}(\vec{\rho})$ which depend on the p and s basis vectors and on the Fresnel coefficients for the different interfaces [39]:

$$\begin{aligned} q_{xk} &= \cos\psi T_{\text{p}} p_k - \sin\psi T_{\text{s}} s_k, & (6.30)\\ q_{yk} &= \sin\psi T_{\text{p}} p_k + \cos\psi T_{\text{s}} s_k, & (6.31)\end{aligned}$$

where the p and s basis polarization vectors in the dipole image formation model are $\vec{p} = (\cos\eta\cos\psi, \cos\eta\sin\psi, -\sin\eta)$ and $\vec{s} = (-\sin\psi, \cos\psi, 0)$ and where the Fresnel coefficients are:

$$T_{\text{a}} = T_{\text{a,med-cov}} T_{\text{a,cov-imm}}, \tag{6.32}$$

for $a = p, s$. Here the Fresnel coefficients for the two contributing interfaces are defined by:

$$T_{\text{a},1-2} = \frac{2c_{a,1}}{c_{a,1} + c_{a,2}}, \tag{6.33}$$

for $a = p, s$ and with $c_{p,l} = n_l / \cos\eta_l$ and $c_{s,l} = n_l \cos\eta_l$ for $l = \text{med}, \text{cov}, \text{imm}$, where the polar angles of incidence are related by Snell's law.

The imaging model's partial derivatives to the parameters are needed for the MLE optimization routine. These are straightforward to evaluate for the signal photon count N and number of background photons per pixel b, as these appear linear in the imaging model. The derivatives with respect to the position parameters $\vec{r}_0$ are the same as in refs. [56, 57]:

$$\frac{\partial \mu_{nm}}{\partial \vec{r}_0} = N P_m(\Omega) \sum_{j=x,y} \int_A \text{d}x\text{d}y \; 2\text{Re}\left\{ E_j^*(\vec{r}-\vec{r}_0,\Omega) \frac{\partial E_j(\vec{r}-\vec{r}_0,\Omega)}{\partial \vec{r}_0} \right\}. \tag{6.34}$$

The derivatives with respect to the orientation parameters become:

$$\frac{\partial \mu_{nm}}{\partial \Omega} = N P_m(\Omega) \sum_{j=x,y} \int_A \text{d}x\text{d}y \; 2\text{Re}\left\{ E_j^*(\vec{r}-\vec{r}_0,\Omega) \frac{\partial E_j(\vec{r}-\vec{r}_0,\Omega)}{\partial \Omega} \right\} + N \frac{\partial P_m(\Omega)}{\partial \Omega} H_n(\vec{r}_0,\Omega) \tag{6.35}$$

where the second term originates purely from the polarization modulation. This involves the electric field derivatives:

$$\frac{\partial E_j(\vec{r}-\vec{r}_0,\Omega)}{\partial \vec{r}_0} = \sum_{k=x,y,z} \frac{\partial w_{jk}(\vec{r}-\vec{r}_0)}{\partial \vec{r}_0} d_k(\Omega), \tag{6.36}$$

with:

$$\frac{\partial w_{jk}(\vec{r}-\vec{r}_0)}{\partial \vec{r}_0} = \frac{i}{\pi}\int \mathrm{d}^2\rho\, A(\vec{\rho})\exp\left(\frac{2\pi i W(\vec{\rho})}{\lambda}\right) q_{jk}(\vec{\rho})\vec{k}(\vec{\rho})\exp(-i\vec{k}(\vec{\rho})\cdot(\vec{r}-\vec{r}_0)). \tag{6.37}$$

The orientational derivatives of the modulation function $P_s(\Omega)$ are simple trigonometric functions, the orientational derivatives of the electric field are:

$$\frac{\partial E_j(\vec{r}-\vec{r}_0,\Omega)}{\partial \Omega} = \sum_{k=x,y,z} w_{jk}(\vec{r}-\vec{r}_0)\frac{\partial d_k(\Omega)}{\partial \Omega}, \tag{6.38}$$

where the orientational derivatives of the dipole vector $d_k(\Omega)$ are again simple trigonometric functions.

6.9.2. Sample preparation

All samples are made on cleaned coverslips (22x22 mm No. 1.5, Marienfeld-Superior) and microscope slides (Microscope slides, Menzel Gläser Thermo Scientific). They are cleaned by sequential sonication in isopropyl alcohol, acetone and isopropyl alcohol again. The coverslips are joined to the microscope slide with double-sided tape (Permanent Double Sided Tape, Scotch) spaced ~ 1 cm apart.

For alignment with respect to the galvo mirrors a liquid sample of ATTO 565 (ATTO 565, Sigma-Aldrich) is used. The ATTO 565 is diluted to 10^{-6} M in Milli-Q (MQ) water. After joining the coverslip to the microscope slide 25 μL of this diluted fluorophore is pipetted in between.

Single-molecule samples in polymethyl methacrylate (PMMA) are prepared by spin-coating fluorophores diluted in PMMA. The PMMA (182265, Sigma-Aldrich) is dissolved in toluene (244511, Sigma-Aldrich) with a 1/100 w/w ratio in a fume hood. Thereafter ATTO 565 prediluted to 10^{-6} M in MQ water is diluted in the PMMA/toluene solution to a final concentration of 10^{-12} M. 20 μL of this mixture is spin-coated at 3000 RPM with an acceleration of 1000 RPM/s for 60 seconds in a fume hood.

For the aberration maps 180 nm orange fluorescent beads (PS-Speck Microscope Point Source Kit, ThermoFisher) are diluted 100 time in MQ water and are dropcast. 9-10 tiny droplets with a total volume of 10 μL are pipetted onto the coverslip and naturally dry over 2-3 hours. Thereafter the coverslip is attached to the microscope slide and just before the experiment a droplet of immersion oil is inserted in between via capillary action for refractive index matching.

6.9.3. Image acquisition and data analysis

The DAQ is triggered when the camera exposure starts and unblocks the laser with the currently set polarization. The level of transmission by the AOM is set to compensate for the polarization varying transmission to the sample. At the end of the camera exposure the DAQ switches states to block the beam with the AOM and shift to the next polarization. This is repeated for the 3 different polarization states and continues for numerous cycles. For the experiments with normal incidence we use 3 polarization states with a varying exposure time and laser power (100 ms with 25 W/cm^2

and 50 W/cm^2 and then 100 W/cm^2 with 100 ms, 150 ms, 200 ms, 300 ms, 500 ms and 1000 ms). This allows us to acquire data with a wide range of photon counts.

For the aberration calibration measurements an exposure time of 200 ms and a laser power of 10 W/cm^2 is used. The sample is moved through focus in fifty 100 nm steps in 8 different locations. The data is fitted with a fully vectorial PSF model [16], from these bead fits the aberrations are determined in 436 discrete locations throughout the FOV. Using the Nodal Aberration Theory (NAT) polynomial surfaces can be fitted to these aberration measurements to generate a continuous aberration prediction throughout the FOV.

The raw images are converted to photon counts by removing the offset and adjusting for the camera sensitivity (0.49 e^-/ADU and 103.1 ADU offset) [58]. To generate an initial estimate of the in-plane angle (ϕ) a lock-in amplification calculation is used which results in a reliable estimate with a low computational cost. The fit results are filtered based on χ^2 where the value can be no more than 2 standard deviations away from the mean. Molecules that have the same position and angle between frames with a deviation of less than 3 times the precision ($\sqrt{\mathrm{CRB}}$) are linked. This linking constraint is applied to the orientation to avoid the inclusion in the precision assessment of molecules that are wobbling or reorienting during the acquisition.

References

[1] S. T. Hess, T. P. Girirajan, and M. D. Mason, *Ultra-high resolution imaging by fluorescence photoactivation localization microscopy,* Biophysical Journal **91**, 4258 (2006).

[2] E. Betzig, G. H. Patterson, R. Sougrat, O. W. Lindwasser, S. Olenych, J. S. Bonifacino, M. W. Davidson, J. Lippincott-Schwartz, and H. F. Hess, *Imaging intracellular fluorescent proteins at nanometer resolution,* Science **313**, 1642 (2006).

[3] M. J. Rust, M. Bates, and X. Zhuang, *Sub-diffraction-limit imaging by stochastic optical reconstruction microscopy (STORM),* Nature Methods **3**, 793 (2006).

[4] A. Sharonov and R. M. Hochstrasser, *Wide-field subdiffraction imaging by accumulated binding of diffusing probes,* Proceedings of the National Academy of Sciences of the United States of America **103**, 18911 (2006).

[5] B. Huang, W. Wang, M. Bates, and X. Zhuang, *Three-dimensional super-resolution imaging by stochastic optical reconstruction microscopy,* Science **319**, 810 (2008).

[6] M. P. Backlund, M. D. Lew, A. S. Backer, S. J. Sahl, and W. E. Moerner, *The Role of Molecular Dipole Orientation in Single-Molecule Fluorescence Microscopy and Implications for Super-Resolution Imaging,* ChemPhysChem **15**, 587 (2014).

[7] E. J. Peterman, H. Sosa, L. S. Goldstein, and W. E. Moerner, *Polarized fluorescence microscopy of individual and many kinesin motors bound to axonemal microtubules,* Biophysical Journal **81**, 2851 (2001).

[8] E. Toprak, J. Enderlein, S. Syed, S. A. McKinney, R. G. Petschek, T. Ha, Y. E. Goldman, and P. R. Selvin, *Defocused orientation and position imaging (DOPI) of myosin V,* Proceedings of the National Academy of Sciences of the United States of America **103**, 6495 (2006).

[9] H. A. Shaban, C. A. Valades-Cruz, J. Savatier, and S. Brasselet, *Polarized super-resolution structural imaging inside amyloid fibrils using Thioflavine T,* Scientific Reports **7**, 1 (2017).

[10] M. Wang, J. M. Marr, M. Davanco, J. W. Gilman, and J. A. Liddle, *Nanoscale deformation in polymers revealed by single-molecule super-resolution localization-orientation microscopy,* Materials Horizons **6**, 817 (2019).

[11] J. Lu, H. Mazidi, T. Ding, O. Zhang, and M. D. Lew, *Single-Molecule 3D Orientation Imaging Reveals Nanoscale Compositional Heterogeneity in Lipid Membranes,* Angewandte Chemie **132**, 17725 (2020).

[12] J. Engelhardt, J. Keller, P. Hoyer, M. Reuss, T. Staudt, and S. W. Hell, *Molecular orientation affects localization accuracy in superresolution far-field fluorescence microscopy,* Nano Letters **11**, 209 (2011).

[13] M. D. Lew, M. P. Backlund, and W. E. Moerner, *Rotational mobility of single molecules affects localization accuracy in super-resolution fluorescence microscopy,* Nano Letters **13**, 3967 (2013).

[14] M. P. Backlund, M. D. Lew, A. S. Backer, S. J. Sahl, G. Grover, A. Agrawal, R. Piestun, and W. E. Moerner, *The double-helix point spread function enables precise and accurate measurement of 3D single-molecule localization and orientation,* in *Single Molecule Spectroscopy and Superresolution Imaging VI*, Vol. 8590 (SPIE, 2013) p. 85900L.

[15] A. S. Backer, M. P. Backlund, M. D. Lew, and W. E. Moerner, *Single-molecule orientation measurements with a quadrated pupil,* Optics Letters **38**, 1521 (2013).

[16] C. N. Hulleman, R. Ø. Thorsen, E. Kim, C. Dekker, S. Stallinga, and B. Rieger, *Simultaneous orientation and 3D localization microscopy with a Vortex point spread function,* Nature Communications **12**, 5934 (2021).

[17] T. J. Gould, M. S. Gunewardene, M. V. Gudheti, V. V. Verkhusha, S. R. Yin, J. A. Gosse, and S. T. Hess, *Nanoscale imaging of molecular positions and anisotropies,* Nature Methods **5**, 1027 (2008).

[18] S. R. P. Pavani, J. G. DeLuca, and R. Piestun, *Polarization sensitive, three-dimensional, single-molecule imaging of cells with a double-helix system,* Optics Express **17**, 19644 (2009).

[19] C. A. V. Cruz, H. A. Shaban, A. Kress, N. Bertaux, S. Monneret, M. Mavrakis, J. Savatier, and S. Brasselet, *Quantitative nanoscale imaging of orientational*

order in biological filaments by polarized superresolution microscopy, Proceedings of the National Academy of Sciences of the United States of America **113**, E820 (2016).

[20] S. Stallinga and B. Rieger, *Position and orientation estimation of fixed dipole emitters using an effective Hermite point spread function model,* Optics Express **20**, 5896 (2012).

[21] A. S. Backer, M. P. Backlund, A. R. Von Diezmann, S. J. Sahl, and W. E. Moerner, *A bisected pupil for studying single-molecule orientational dynamics and its application to three-dimensional super-resolution microscopy,* Applied Physics Letters **104**, 1 (2014).

[22] O. Zhang, J. Lu, T. Ding, and M. D. Lew, *Imaging the three-dimensional orientation and rotational mobility of fluorescent emitters using the Tri-spot point spread function,* Applied Physics Letters **113**, 031103 (2018).

[23] V. Curcio, L. A. Alemán-Castañeda, T. G. Brown, S. Brasselet, and M. A. Alonso, *Birefringent Fourier filtering for single molecule coordinate and height super-resolution imaging with dithering and orientation,* Nature Communications **11**, 5307 (2020).

[24] T. Chandler, S. Mehta, H. Shroff, R. Oldenbourg, and P. J. La Rivière, *Single-fluorophore orientation determination with multiview polarized illumination: modeling and microscope design,* Optics Express **25**, 31309 (2017).

[25] A. T. Blanchard, J. M. Brockman, K. Salaita, and A. L. Mattheyses, *Variable incidence angle linear dichroism (VALiD): a technique for unique 3D orientation measurement of fluorescent ensembles,* Optics Express **28**, 10039 (2020).

[26] M. Prummer, B. Sick, B. Hecht, and U. P. Wild, *Three-dimensional optical polarization tomography of single molecules,* Journal of Chemical Physics **118**, 9824 (2003).

[27] J. N. Forkey, M. E. Quinlan, M. A. Shaw, J. E. Corrie, and Y. E. Goldman, *Three-dimensional structural dynamics of myosin V by single-molecule fluorescence polarization,* Nature **422**, 399 (2003).

[28] A. S. Backer, M. Y. Lee, and W. E. Moerner, *Enhanced DNA imaging using super-resolution microscopy and simultaneous single-molecule orientation measurements,* Optica **3**, 659 (2016).

[29] R. Henriques, M. Lelek, E. F. Fornasiero, F. Valtorta, C. Zimmer, and M. M. Mhlanga, *QuickPALM: 3D real-time photoactivation nanoscopy image processing in ImageJ,* Nature Methods **7**, 339 (2010).

[30] F. Balzarotti, Y. Eilers, K. C. Gwosch, A. H. Gynnå, V. Westphal, F. D. Stefani, J. Elf, and S. W. Hell, *Nanometer resolution imaging and tracking of fluorescent molecules with minimal photon fluxes,* Science **355**, 606 (2017).

[31] J. Cnossen, T. Hinsdale, R. Ø. Thorsen, M. Siemons, F. Schueder, R. Jungmann, C. S. Smith, B. Rieger, and S. Stallinga, *Localization microscopy at doubled precision with patterned illumination,* Nature Methods **17**, 59 (2020).

[32] L. Gu, Y. Li, S. Zhang, Y. Xue, W. Li, D. Li, T. Xu, and W. Ji, *Molecular resolution imaging by repetitive optical selective exposure,* Nature Methods **16**, 1114 (2019).

[33] P. Jouchet, C. Cabriel, N. Bourg, M. Bardou, C. Poüs, E. Fort, and S. Lévêque-Fort, *Nanometric axial localization of single fluorescent molecules with modulated excitation,* Nature Photonics **15**, 297 (2021).

[34] D. Axelrod, *Cell-substrate contacts illuminated by total internal reflection fluorescence.* Journal of Cell Biology **89**, 141 (1981).

[35] N. Karedla, S. C. Stein, D. Hähnel, I. Gregor, A. Chizhik, and J. Enderlein, *Simultaneous measurement of the three-dimensional orientation of excitation and emission dipoles,* Physical Review Letters **115**, 1 (2015).

[36] B. R. Lentz, *Use of fluorescent probes to monitor molecular order and motions within liposome bilayers,* Chemistry and Physics of Lipids **64**, 99 (1993).

[37] M. Born, E. Wolf, A. B. Bhatia, P. C. Clemmow, D. Gabor, A. R. Stokes, A. M. Taylor, P. A. Wayman, and W. L. Wilcock, *Principles of Optics* (Cambridge University Press, 1999).

[38] K. I. Mortensen, L. S. Churchman, J. A. Spudich, and H. Flyvbjerg, *Optimized localization analysis for single-molecule tracking and super-resolution microscopy,* Nature Methods **7**, 377 (2010).

[39] S. Stallinga and B. Rieger, *Accuracy of the Gaussian Point Spread Function model in 2D localization microscopy,* Optics Express **18**, 24461 (2010).

[40] J. Chao, E. Sally Ward, and R. J. Ober, *Fisher information theory for parameter estimation in single molecule microscopy: tutorial,* Journal of the Optical Society of America A **33**, B36 (2016).

[41] B. Rieger and S. Stallinga, *The lateral and axial localization uncertainty in super-resolution light microscopy,* ChemPhysChem **15**, 664 (2014).

[42] M. R. Foreman and P. Török, *Fundamental limits in single-molecule orientation measurements,* New Journal of Physics **13**, 093013 (2011).

[43] O. Zhang and M. D. Lew, *Quantum limits for precisely estimating the orientation and wobble of dipole emitters,* Physical Review Research **2**, 33114 (2020).

[44] C. Franke, M. Sauer, and S. V. De Linde, *Photometry unlocks 3D information from 2D localization microscopy data,* Nature Methods **14**, 41 (2016).

[45] R. Ø. Thorsen, C. N. Hulleman, M. Hammer, D. Grünwald, S. Stallinga, and B. Rieger, *Impact of optical aberrations on axial position determination by photometry,* Nature Methods **15**, 989 (2018).

[46] C. N. Hulleman, M. Huisman, R. J. Moerland, D. Grünwald, S. Stallinga, and B. Rieger, *Fluorescence Polarization Control for On-Off Switching of Single Molecules at Cryogenic Temperatures,* Small Methods **2**, 1700323 (2018).

[47] D. Axelrod, T. P. Burghardt, and N. L. Thompson, *Total Internal Reflection Fluorescence,* Annual Review of Biophysics and Bioengineering **13**, 247 (1984).

[48] I. Munro, I. Pecht, and L. Stryer, *Subnanosecond motions of tryptophan residues in proteins.* Proceedings of the National Academy of Sciences of the United States of America **76**, 56 (1979).

[49] A. S. Backer, A. S. Biebricher, G. A. King, G. J. Wuite, I. Heller, and E. J. Peterman, *Single-molecule polarization microscopy of DNA intercalators sheds light on the structure of S-DNA,* Science Advances **5**, eaav1083 (2019).

[50] S. Stallinga, *Single emitter localization analysis in the presence of background,* in *Optical Systems Design 2015: Computational Optics*, Vol. 9630, edited by D. G. Smith, F. Wyrowski, and A. Erdmann (SPIE, 2015) p. 96300V.

[51] T. Ha, T. A. Laurence, D. S. Chemla, and S. Weiss, *Polarization spectroscopy of single fluorescent molecules,* Journal of Physical Chemistry B **103**, 6839 (1999).

[52] W. L. Peticolas, J. P. Goldsborough, and K. E. Rieckhoff, *Double photon excitation in organic crystals,* Physical Review Letters **10**, 43 (1963).

[53] M. L. Martin-Fernandez, C. J. Tynan, and S. E. Webb, *A 'pocket guide' to total internal reflection fluorescence,* Journal of Microscopy **252**, 16 (2013).

[54] P. Török, P. D. Higdon, and T. Wilson, *Theory for confocal and conventional microscopes imaging small dielectric scatterers,* Journal of Modern Optics **45**, 1681 (1998).

[55] T. Wilson, R. Juškaitis, and P. Higdon, *The imaging of dielectric point scatterers in conventional and confocal polarisation microscopes,* Optics Communications **141**, 298 (1997).

[56] C. Smith, M. Huisman, M. Siemons, D. Grünwald, and S. Stallinga, *Simultaneous measurement of emission color and 3D position of single molecules,* Optics Express **24**, 4996 (2016).

[57] M. Siemons, C. N. Hulleman, R. Ø. Thorsen, C. S. Smith, and S. Stallinga, *High precision wavefront control in point spread function engineering for single emitter localization,* Optics Express **26**, 8397 (2018).

[58] L. J. van Vliet, D. Sudar, and I. T. Young, *Digital fluorescence imaging using cooled charge-coupled device array cameras,* in *Cell Biology*, Vol. III, edited by J. Celis (Academic Press, New York, 1998) 2nd ed., pp. 109–120.

7

Conclusion and outlook

7.1. Conclusion

In this section we highlight the results and conclusions of each respective chapter and elaborate on the implications that these finding could have for future research.

7.1.1. Photon yield enhancement of red fluorophores at cryogenic temperatures

In **chapter 2** we have measured the photon yield of various red organic dyes at cryogenic temperatures. Compared to room temperature there is a more than 100 times increase in the number of photons emitted from each single fluorophore. On average $\sim 5 \times 10^6$ photons are detected from each single molecule corresponding to a mean localization precision around 0.1 nm. This chapter demonstrated the strength of localization microscopy at cryogenic temperatures, the enhanced localization precision. At the same time it also highlights the challenge in localization microscopy at cryogenic temperatures which is switching fluorescent molecules between an on and an off state. The fluorescent molecules did not show significant blinking at cryogenic temperatures and none of the tested photoactivatable dyes could be activated at cryogenic temperatures. Without switching between states it is not possible to create sparsity to perform localization microscopy on dense biological samples.

7.1.2. Fluorescence polarization control for on–off switching of single molecules at cryogenic temperatures

To induce sparsity at cryogenic temperatures we proposed to use polarized STED in **chapter 3**. This relies on the fact that all molecules are frozen in place at cryogenic temperatures and thus the orientation of the fluorescent dipole moment is also fixed. By varying the in-plane polarization orientation of excitation and depletion beams with mutually orthogonal linear polarization the set of angles for which a molecule fluoresces can be reduced. Generating linearly polarized light with an arbitrary polarization orientation angle in a fluorescence microscope is not trivial. The dichroic mirrors used to separate excitation and depletion wavelengths from the emission wavelength, induce phase differences between s and p polarized light. We have optimized our optical design to be able to account for these phase differences. In this chapter we have measured the polarization propagation though our microscope and have optimized the polarization state in the sample plane to have an average extinction ratio of 819:1. The effectiveness of the optimized polarization states has been demonstrated on single fluorescent molecules fixed in a resin at room temperature. With our optimized polarization states diagonally oriented molecules with respect to the dichroic mirror (equally s and p polarized) can now be effectively modulated and the fluorescence minimum reduced to the background levels.

7.1.3. Polarized Stimulated-Emission Depletion and dark-state lifetime at cryogenic temperatures

Chapter 4 applies the optimized polarization states with both polarized excitation and depletion to single molecules at cryogenic temperatures. Rotating linearly polarized excitation generates a very good modulation contrast irrespective of the orientation of frozen single-molecules at cryogenic temperatures. With the addition of a depletion beam with an orthogonal polarization to the excitation beam, we show that it is indeed possible to narrow the set of fluorescing molecules at cryogenic temperatures using polarized STED. The narrowing achieved in practice was limited to 54°, this only generates a sparsity of $3.3 : 1$ which is insufficient for localization microscopy of biological samples. The photon yield with polarized STED was $< 10^5$ which is a lot less than the millions of photons routinely achieved earlier in chapter 2. With the use of intermittent illumination we determined that there was a build up of a dark-state of fluorophores in vacuum and at cryogenic temperatures. This dark-state with a recovery lifetime of $\tau = 38$ ms is much longer than in ambient conditions. Potentially this could be one of the reasons that the photon yield of polarized STED at cryogenic conditions is limited.

7.1.4. Simultaneous orientation and 3D localization microscopy with a Vortex point spread function

With the Vortex PSF in **chapter 5** we have developed a PSF that enables orientation estimation and 3D localization microscopy of constrained emitters with a compact PSF spot size. This might be less applicable to low-NA cryogenic systems, but with a small modification to standard oil-immersion microscopes can reveal a lot of information about the sample. The experimental precision in both proof-of-principle and biological samples is within 30% of the CRLB. With 4000 photons the precision in lateral localization is 5.6 nm, 27 nm in axial localization, 5.5° for the in-plane orientation, 3.1° out-of-plane orientation and 0.08 in the rotational constraint parameter. Initially we verified expected results on linearly combed λ-DNA, finding a relative fluorescence dipole moment orientation of $\Delta\phi = 82^\circ$ with respect to the DNA axis. Thereafter we investigated the binding behaviour of supercoiled DNA structures. Here we identified differences in dipole orientations between the torsionally-relaxed λ-DNA and supercoiled DNA constructs. Furthermore, in the supercoiled DNA structure we could identify a spatial periodicity of $122 - 150$ nm in orientational subsets.

7.1.5. Photon efficient orientation estimation using polarization modulation in single-molecule localization microscopy

In **chapter 6** we have primarily probed the absorption dipole moment rather than the emission dipole moment as done previously in chapter 5 with the Vortex PSF. Linear excitation polarization states are varied in the sample over 3-5 frames and a maximum-likelihood estimation is performed on the set of images to extract the position and orientation of fixed single-molecules. As the orientations of the applied polarization is known, a better precision can be achieved with less photons. With only 1000 photons and 10 background photons an in-plane precision of 2.4° and out-of-plane precision of 1.6° can be achieved. With this setup it is possible to do full orientation estimation by varying polarization states in all directions instead of only rotating in-plane polarization states, this can be achieved by changing the propagation direction and polarization of the incident beam. Alternatively the polarization could be manipulated in TIRF as the evanescent electric fields can be used to generate linearly polarized light in any direction. It is crucial that the beam is incident at exactly the critical angle to reliably control the polarization and generate a pure axial polarization in the evanescent field. As multiple frames need to be captured, the reconstruction frame-rate is similar to PSF fitting but much lower photon counts can be tolerated. This method is ideal for dim fluorophores with stable emission.

7.2. Outlook

In this outlook, suggestions are made for possible developments and long-term research directions.

7.2.1. Cryogenic Oxygen Activated Localization (COAL)

Essential to localization microscopy at cryogenic temperatures is to find a way to switch fluorescent molecules between a fluorescent and non-fluorescent state. So far, inducing sparsity at cryogenic temperatures with organic dyes has not been too successful. Therefore the full potential of localization microscopy at cryogenic temperatures is not utilized. The solution should be sought on the interface between chemistry and physics. A key question here is why dyes behave differently in the absence of oxygen, for example when using oxygen scavengers in aqueous media. Many of the current state-of-the-art organic dyes have been developed for optimal performance in aqueous media as this is the natural state for biological samples. This is a significantly different condition compared to amorphous ice in vacuum or a nitrogen saturated environment as is the case in most cryogenic fluorescence microscopes.

Interestingly a portion of fluorescent molecules like Alexa 488 and ATTO 488 enter a non-fluorescent state when pumped to vacuum [1]. I have found similar behaviour with Alexa 633 (data not shown). Most of these molecules return to a fluorescent state when the chamber is vented and returned to atmospheric pressure. This could either be attributed to the change in pressure or lack of certain gasses in the vacuum environment. It seems likely that the main difference here is the amount of oxygen present, typically involved in triplet state transitions [2, 3]. However counter-intuitive it might sound, the local addition of oxygen in vacuum could be the key to inducing sparsity at cryogenic temperatures.

Such a protocol would initially either localize or bleach all fluorescent molecules depending on the concentration. Thereafter oxygen gas can be applied in a similar manner to electron beam induced deposition (EBID) [4], where a flow of gas through a needle locally increases the gas concentration in a region of only a few hundred microns within a vacuum environment. After a sparse fraction of molecules are switched from a non-fluorescent state to a fluorescent state the gas flow can be stopped and the concentration of oxygen will decrease rapidly in the vacuum environment. Thereafter the switched molecules can be localized and the process repeated. A continuous flow of oxygen at a very low concentration might also work but could reduce the photon yield due to increased photobleaching.

For an initial proof-of-principle, an experiment can be carried out on a integrated correlative light and electron microscope. As these are typically not suitable for single-molecule detection, the concentration can be raised to have one molecule every $10-50$ nm. When pumping to vacuum $\sim 90\%$ of the molecules should transition to a dark state. By adding oxygen (or other individual gasses present in the atmosphere) with an EBID needle any changes in the fluorescence level can be detected. Measuring the change of fluorescence as a function of the chamber pressure will be difficult as it effects both the amount of molecules in the on-state and the overall rate of fluorescence emission. Without measuring single-molecules continuously in focus it will be challenging to disentangle the two effects. If there is a measurable change in fluorescence when a particular gas is added the next step would be to test if single molecules in resin (PVA, PMMA etc.) can be activated. This would demonstrate whether this process works deeper inside samples or if it is only effective on the surface between the sample and vacuum. In parallel it could be investigated if this also works on sparse single-molecules at cryogenic temperatures. This could be done by integrating a needle gas supply to either the large cryotank used in chapter 4 or the cryo-TIRF setup [5]. The cold temperature could, however, hinder the state transition to get these molecules back to a fluorescent state. If any individual step of this proposed process is successful it can have a large impact on correlating high-precision localization microscopy with electron microscopy.

One drawback to this proposed method is that the oxygen would struggle to diffuse through the frozen sample at cryogenic temperatures. A remedy to this would be to image layer by layer, which is common in state of the art cryogenic correlative microscopy [6] and FIB-SEM imaging. This could be implemented by removing a layer of the sample after numerous localization cycles with a focused ion beam. Integrating this into the cryo-lamella workflow for cryo-EM could combine high localization precision and specificity of cryogenic localization microscopy with cryo-EM.

7.2.2. Cryogenic 4-pi microscopy

The resolution in the axial direction can be improved by implementing a 4π microscope [7] at cryogenic temperatures. This is beneficial as most current cryogenic microscopes are not capable of doing 3D localization or they generate 3D reconstructions from multiple cryo-sections. Additionally the collection efficiency is doubled as light is captured from two sides. To enhance the resolution further the 4π microscope is an ideal basis to implement patterned illumination similar to SIMFLUX [8] but along the axial direction [9]. However, from an engineering perspective the development of a 4π microscope at cryogenic temperatures is very challenging as the optical path length difference needs to be very stable between the two arms. If a successful way of inducing sparsity with organic dyes at cryogenic temperatures is not found it will still be beneficial to use fluorescent proteins that are known to work for localization microscopy at cryogenic temperatures [10], albeit at lower photon yields. Performing 3D localization microscopy in correlation with cryo-EM will make a significant impact in this rapidly developing field.

7.2.3. MINFLUX and orientation probing

In recent years iterative triangulation methods for localization microscopy have pushed the localization precision to 1 nm with for example MINFLUX [11] and MINSTED [12]. At this size-scale it does not add much value for biological applications to improve the precision further as it is already on a similar size-scale to linker lengths and small biomolecules, like proteins. In this case it would be great to supplement these high resolution images with information about the orientation of constrained emitters.

In MINFLUX a circularly polarized doughnut beam is used which minimizes the bias from constrained emitters. Once a desired localization precision is achieved the acquisition procedure can be changed to estimate the orientation of constrained emitters instead. This can be done by probing with a radially polarized doughnut beam [13, 14]. Instead of scanning this beam over the single-molecule to create an image, the orientation of the single-molecule can be probed by placing this beam at specific locations such that the constrained molecule is excited by a distinct set of polarizations. From this limited set of point measurements both the in-plane and out-of-plane orientation can be deduced. In a similar iterative fashion the orientation precision can then be improved by applying excitation polarization states that reveal the most information about the molecule's orientation with minimal photon fluxes. Alternatively, a simultaneous acquisition scheme to combine iterative localization and in-plane orientation estimation could be devised with an azimuthally polarized beam.

7.2.4. Accurate PSF models in localization microscopy

With the initial introduction of localization microscopy individual emitters were fitted with a Gaussian function which is a convenient approximation for non-aberrated PSFs. This simplified model made fitting quicker, less computationally intensive and resulted in super-resolution reconstructions with a resolution smaller than the diffraction limit. However, all microscopes have some degree of optical aberrations which makes the PSF asymmetric and the Gaussian model inaccurate [15]. Even for non-aberrated PSFs with high-NA objectives the Gaussian model is inaccurate [15]. Using the Gaussian model creates a misestimate of the photon count of emitters, primarily because the diffraction rings around the central peak are not taken into account [16]. This also means that the information available in the images is not fully utilized in the localization process.

With the ever increasing computational power available, this oversimplification of the PSF model is not necessary. The use of a vectorial PSF model [15, 17] or spline based PSF model [18] should be the standard applied today. The only downside is that typically the PSF of the microscope would need to be calibrated in advance to have an accurate PSF model for fitting. However, even this problem can be overcome as the PSF model can be generated from 3D localization images themselves [19], which is particularly useful for samples where the refractive index of the sample medium changes with position.

In chapter 5 we have shown that the amount of aberrations varies substantially across the field of view. This implies that a single PSF model for the microscope is also inaccurate, as the PSF is different depending on the location in the FOV. The variation of these aberrations is smooth and well described by the Nodal Aberration Theory (NAT) [20]. Using NAT to generate field dependent PSF models should be applied to localization microscopy in a much wider context. Not only in combination with PSF engineering methods like 3D localization with astigmatism [21], a double-helix [22] or tetra-pod [23], but also for standard localization microscopy of freely rotating molecules. The usable FOV is usually limited by illumination power and a non-flat Gaussian profile, making switching and localization at the edge of the FOV difficult. However, even in these adverse conditions with low photon counts and aberrations, localization with a vectorial PSF model using the NAT aberration map yields high-quality data at the edge of the FOV. As the local PSF and model match, localization microscopy can be performed with good precision and accuracy independent of the location in the FOV. This allows the full sensor of current sCMOS cameras to be used for localization microscopy even if the aberrations at the edge of the FOV are no longer diffraction limited. With the introduction of back-illuminated sCMOS cameras that typically have even larger chip sizes, the use of a field dependent PSF becomes increasingly important to perform localization microscopy over larger fields of view.

7.2.5. Accuracy and precision

Pushing the localization precision towards 1 nm means that drift becomes increasingly important. For slow large amplitude drift an image based redundant cross correlation drift correction is sufficient to reduce residual drift to a peak-to-peak value of $20 - 30$ nm. For these slow large amplitude drifts and a precision limit in the same range, this makes sense. However, when trying to push the resolution to single digit nanometres this is not sufficient. The precision of the applied drift correction needs to be on the same size scale as the localization precision to avoid degrading the final reconstruction. To achieve this it is necessary to use either fiducial markers [24] like beads which can be localized with a higher precision or an optimization based on visible structures like lines [25] or DNA-rulers [26]. Importantly when dealing with fast nanometre scale drift, it is no longer appropriate to use a smoothing spline. In this regime drift traces will look noisy but can be a true representation of the actual drift if acquired with a high precision from many localizations.

Quantifying the precision of newly developed techniques has become increasingly common in the field, for example using the CRLB to caluclate the precision of an unbiased estimator. A question that often seems neglected is; am I using an unbiased estimator and is my method generally unbiased? The desire to demonstrate precision seems to outshadow the perhaps more important point, to demonstrate that the method is also accurate. If any bias is not constant throughout the FOV or varies as a function of emitter properties then it is very difficult to correct for. For example, the addition of an otherwise unexplained quarter-waveplate suggests that ModLoc [27] has a polarization dependent PSF and would be biased by constrained emitters. Similarly, using SIMPLER [28] to estimate the distance of fluorophores to a coverslip in TIRF, based purely on intensity values is prone to bias.

It should become standard to also investigate parameters that could influence the accuracy. In simulations the influence of primary aberrations like astigmatism and coma, the influence of defocus and the influence of non freely rotating emitters can easily be quantified. There may be many sources of inaccuracies, however, at least the most likely to occur should be investigated. To quantify the accuracy in experiments special samples with known parameters need to be produced. With modern cleanroom facilities it is easy to produce samples with spatially varying refractive indices or to create a high resolution staircase of different heights throughout the FOV. This could be used to quantify the influence of refractive index and z position.

To manipulate the orientation of fluorescence dipole moments is far more challenging. The average fluorophore orientation can be aligned in sheared PMMA structures [29], or perhaps fluorophores could be aligned within crystalline structures. Potentially a bottom-up biological construct similar to DNA-origami is more appropriate. Intercalators in DNA make a good verification for dipole orientation estimation but the base pair spacing is so small that it is difficult to verify the localization accuracy. A construct with which both the spacing and orientation could be manipulated is far more useful. FlAsH and ReAsH bind to proteins and have two binding sites making these molecules constrained fluorophores [30]. By engineering or choosing specific proteins to image it would be possible to make very small test samples with fixed orientation and spacing between binding sites. The spacing and orientation can be tweaked by changing the order of amino acids in the protein and these parameters can be calculated from well established protein models and verified with TEM or X-ray crystallography.

7.2.6. TIRF based z localization

With the setup built for polarization control in high-NA and TIRF microscopes in chapter 6 the angle of incidence and polarization state can be fully controlled. Using this a much more accurate TIRF based z-localization method than SIMPLER [28] can be developed. By measuring with 2 or 3 different incident angles consecutively a z position estimate can be made from the ratio of intensities. In this way it is no longer dependent on a prior measurement of molecules on the coverslip. In addition these molecules can even be constrained or fixed molecules instead of freely rotating molecules, which would have influenced such a calibration measurement. The excitation intensity is an exponential function of the distance to the coverslip. With varying angles of incidence the penetration depth varies but the ratio between the intensity at two angles of incidence is again an exponential function of the distance to the coverslip. This means that in a certain range there is a steep variation in this ratio and thus a good z precision can be achieved. The minimal required amount of different angles of incidence is two, however, a third measurement at yet another incident angle will help guarantee accuracy, as a curve can always be made to fit nicely through only two points. This z estimation can either be complemented with polarization control and orientation estimation or the polarization control can be used to vary the polarization rapidly such that there is no sensitivity to the orientation of constrained emitters.

7.2.7. Processing time

A common point of discussion in SMLM is the processing times of data [31, 32] where a trade-off is typically made between accuracy and speed. Current advances in technology make it relatively easy to perform localization processing in parallel on GPUs, instead of in series. This allows for an increase in processing speed of a few orders of magnitude. The vectorial PSF fitting code should be converted such that it will run effectively on GPUs, making processing localization data faster and potentially making the code more widely used.

One commonly overlooked aspect, whether processing in series or in parallel, is a good initial estimate. Using a good initial estimate could cut the number of iterations down by a factor of 2 or more. For 2D localization an initial estimate is not difficult to generate. However, for 3D localization or estimation of additional parameters like the wavelength of emission for a simultaneous multicolour acquisition or orientation of the fluorophores, a good initial estimate is much more challenging to generate. Because of the multidimensional parameter space a good initial estimate is even more beneficial. This is an important aspect into which time and effort needs to be devoted when transitioning from proof-of-principle to a widely applied method. If no image based metric can be found to generate a reliable initial estimate it is possible to train a neural network using results previously obtained with a MLE procedure. In this way neural networks can be utilized to speed up the process without replacing the entire procedure with an ambiguous black-box.

7.2.8. Multi-frame estimation

In SIMFLUX [8] and chapter 6 an estimator is used that processes multiple frames with different states, either shifted illumination patterns or varying polarization states. After segmentation a lock-in detection algorithm can be used to generate initial estimates of the estimation parameters. These estimators then process a full set of n unique states of a single molecule. However, if this molecule is in an on-state for more than a full cycle but less than a second cycle then not all the frames will be utilized. Therefore after a fit is performed on a full set of states, the previous and subsequent frames should be compared to the expected value. If the measurements are close to the expected value then the set of simultaneously processed frames should be expanded to all the frames that are close the expected value. To reduce the amount of rejected data because fluorescent molecule are not in an on-state during all n unique states, it is also worth considering scaling the amount of processed frames from 1 up to the amount of on-frames for a molecule. If the molecule is only on for one frame, standard PSF fitting can be used with the corresponding CRLB precision. Only successfully measuring, for example, 2 out of 3 unique states would lead to multiple possible solutions, however, with sufficient photons the PSF shape can eliminate this ambiguity and converge to the correct solution with a precision that is still better than only using PSF fitting.

For cryogenic localization with polarization modulation a multi-frame multi-emitter fitter could be developed that uses the varying contributions of each emitter that varies as the polarization is modulated. As the fluorescent molecules are very stable at cryogenic temperatures when only varying the excitation polarization, many cycles can be acquired. To do this rapidly with stable polarization states, the polarization control as implemented in chapter 6 should be used as it is faster and less sensitive to temperature fluctuations compared to the waveplates in rotation stages used in chapters 3 and 4. Gradually the molecules will bleach until there is only 1 molecule remaining. The variation of intensity over time will reveal more information about the amount of emitters and their orientation. The fitter would then fit all the frames in reverse chronological order starting with the frames with only 1 molecule [33]. In this way more photons are utilized, instead of only fitting single molecules when the time trace indicates that a single flourophore is in the on-state within a diffraction limited spot [34].

7.2.9. More than just localization

Localization microscopy can effectively reveal the 3D structure of specifically labelled biomolecules. The shape or 3D arrangement of biomolecules only reveals a small part of a much larger biological puzzle. To unravel these bigger problems it is necessary to collate as much information as possible. An interesting inroad might be to supplement localization data with multi-modal correlative approaches. Different techniques reveal different properties of the sample, for example the atomic structure can be revealed with transmission electron microscopy or the flexibility measured with atomic force microscopy. There could also be great unexplored potential in the fluorescence signal, to enhance the data beyond just localizations.

As illustrated in this thesis the orientation of constrained fluorescent dipoles can reveal a great deal about the underlying nanoscale arrangement of biomolecules. Exploring other biological structures with the combination of 3D localization, dipole orientation estimation and rotational diffusion estimation can reveal interesting properties of biomolecules rarely investigated in this way. The Vortex PSF can be expanded to include polarization splitting, which in combination with an asymmetric rotational diffusion model will help to investigate the binding modes and interactions between fluorophores and biomolecules in greater detail. This can supplement fine atomic structure from transmission electron microscopy with rotational dynamics.

Bis-intercalators commonly used to label nucleic acid like TOTO and YOYO, are fluorescent molecules that consist of two linked fluorophores. Each fluorescence dipole moment intercalates DNA a few base pairs apart. Without very fast time-gating it is equally likely for a photon to be emitted from either of the fluorescence dipole moments, therefore it is very difficult to optically probe them separately. By developing a double-dipole fitting model with the Vortex PSF it might be possible to identify the mutual orientation of each fluorescence dipole moment. This could function as a reporter for nanometre scale deformations in DNA.

By better understanding the interaction between fluorophores and biomolecules it is feasible to extract parameters influencing these types of interactions. A good example of this is how the orientation and rotational stability of Nile red in lipid membranes varies as a function of cholesterol levels, so that the fluorescence dipole orientation becomes a direct reporter for the local concentration [35]. These types of interactions can be further explored to functionalize fluorophore-biomolecule interactions. Similarly, proteins are known to perform conformational changes when their local environment like the pH level changes [36]. In this way proteins with attached organic dyes in a FRET range or fluorescent proteins could be functionalized to serve as reporters for local environments.

References

[1] W. Li, *Single Molecule Cryo-Fluorescence Microscopy*, Ph.D. thesis, Georg-August-Universität Göttingen (2016).

[2] S. Van De Linde, I. Krstić, T. Prisner, S. Doose, M. Heilemann, and M. Sauer, *Photoinduced formation of reversible dye radicals and their impact on super-resolution imaging,* Photochemical and Photobiological Sciences **10**, 499 (2011).

[3] B. Kozankiewicz and M. Orrit, *Single-molecule photophysics, from cryogenic to ambient conditions,* Chemical Society Reviews **43**, 1029 (2014).

[4] W. F. van Dorp and C. W. Hagen, *A critical literature review of focused electron beam induced deposition,* Journal of Applied Physics **104**, 081301 (2008).

[5] Q. Li, C. N. Hulleman, R. J. Moerland, E. Mailvaganam, S. Ganapathy, D. Brinks, S. Stallinga, and B. Rieger, *Waveguide-based total internal reflection fluorescence microscope enabling cellular imaging under cryogenic conditions,* Optics Express **29**, 34097 (2021).

[6] D. P. Hoffman, G. Shtengel, C. S. Xu, K. R. Campbell, M. Freeman, L. Wang, D. E. Milkie, H. A. Pasolli, N. Iyer, J. A. Bogovic, D. R. Stabley, A. Shirinifard, S. Pang, D. Peale, K. Schaefer, W. Pomp, C. L. Chang, J. Lippincott-Schwartz, T. Kirchhausen, D. J. Solecki, E. Betzig, and H. F. Hess, *Correlative three-dimensional super-resolution and block-face electron microscopy of whole vitreously frozen cells,* Science **367**, 265 (2020).

[7] S. Hell and E. H. K. Stelzer, *Properties of a 4Pi confocal fluorescence microscope,* Journal of the Optical Society of America A **9**, 2159 (1992).

[8] J. Cnossen, T. Hinsdale, R. Ø. Thorsen, M. Siemons, F. Schueder, R. Jungmann, C. S. Smith, B. Rieger, and S. Stallinga, *Localization microscopy at doubled precision with patterned illumination,* Nature Methods **17**, 59 (2020).

[9] L. Gu, Y. Li, S. Zhang, M. Zhou, Y. Xue, W. Li, T. Xu, and W. Ji, *Molecular-scale axial localization by repetitive optical selective exposure,* Nature Methods **18**, 369 (2021).

[10] P. D. Dahlberg, A. M. Sartor, J. Wang, S. Saurabh, L. Shapiro, and W. E. Moerner, *Identification of PAmKate as a Red Photoactivatable Fluorescent Protein for Cryogenic Super-Resolution Imaging,* Journal of the American Chemical Society **140**, 12310 (2018).

[11] F. Balzarotti, Y. Eilers, K. C. Gwosch, A. H. Gynnå, V. Westphal, F. D. Stefani, J. Elf, and S. W. Hell, *With Minimal Photon Fluxes,* Science **355**, 606 (2017).

[12] M. Weber, M. Leutenegger, S. Stoldt, S. Jakobs, T. S. Mihaila, A. N. Butkevich, and S. W. Hell, *MINSTED fluorescence localization and nanoscopy,* Nature Photonics **15**, 361 (2021).

[13] A. I. Chizhik, A. M. Chizhik, A. Huss, R. Jäger, and A. J. Meixner, *Nanoscale probing of dielectric interfaces with single-molecule excitation patterns and radially polarized illumination,* Journal of Physical Chemistry Letters **2**, 2152 (2011).

[14] N. Karedla, S. C. Stein, D. Hähnel, I. Gregor, A. Chizhik, and J. Enderlein, *Simultaneous measurement of the three-dimensional orientation of excitation and emission dipoles,* Physical Review Letters **115**, 1 (2015).

[15] S. Stallinga and B. Rieger, *Accuracy of the Gaussian point spread function model in 2D localization microscopy,* Optics Express **18**, 24461 (2010).

[16] R. Ø. Thorsen, C. N. Hulleman, M. Hammer, D. Grünwald, S. Stallinga, and B. Rieger, *Impact of optical aberrations on axial position determination by photometry,* Nature Methods **15**, 989 (2018).

[17] K. I. Mortensen, L. S. Churchman, J. A. Spudich, and H. Flyvbjerg, *Optimized localization analysis for single-molecule tracking and super-resolution microscopy,* Nature Methods **7**, 377 (2010).

[18] Y. Li, M. Mund, P. Hoess, J. Deschamps, U. Matti, B. Nijmeijer, V. J. Sabinina, J. Ellenberg, I. Schoen, and J. Ries, *Real-time 3D single-molecule localization using experimental point spread functions,* Nature Methods **15**, 367 (2018).

[19] F. Xu, D. Ma, K. P. MacPherson, S. Liu, Y. Bu, Y. Wang, Y. Tang, C. Bi, T. Kwok, A. A. Chubykin, P. Yin, S. Calve, G. E. Landreth, and F. Huang, *Three-dimensional nanoscopy of whole cells and tissues with in situ point spread function retrieval,* Nature Methods **17**, 531 (2020).

[20] R. V. Shack and K. Thompson, *Influence of alignment errors of a telescope system on its aberration field,* in *Optical Alignment I*, Vol. 0251, International Society for Optics and Photonics (SPIE, 1980) pp. 146–153.

[21] B. Huang, W. Wang, M. Bates, and X. Zhuang, *Three-Dimensional Super-Resolution Reconstruction Microscopy,* Science **319**, 810 (2008).

[22] S. R. P. Pavani, M. A. Thompson, J. S. Biteen, S. J. Lord, N. Liu, R. J. Twieg, R. Piestun, and W. E. Moerner, *Three-dimensional, single-molecule fluorescence imaging beyond the diffraction limit by using a double-helix point spread function,* Proceedings of the National Academy of Sciences of the United States of America **106**, 2995 (2009).

[23] Y. Shechtman, L. E. Weiss, A. S. Backer, S. J. Sahl, and W. E. Moerner, *Precise Three-Dimensional Scan-Free Multiple-Particle Tracking over Large Axial Ranges with Tetrapod Point Spread Functions,* Nano Letters **15**, 4194 (2015).

[24] A. Balinovic, D. Albrecht, and U. Endesfelder, *Spectrally red-shifted fluorescent fiducial markers for optimal drift correction in localization microscopy,* Journal of Physics D: Applied Physics **52**, 204002 (2019).

[25] C. N. Hulleman, R. Ø. Thorsen, E. Kim, C. Dekker, S. Stallinga, and B. Rieger, *Simultaneous orientation and 3D localization microscopy with a Vortex point spread function,* Nature Communications **12**, 5934 (2021).

[26] M. Dai, R. Jungmann, and P. Yin, *Optical imaging of individual biomolecules in densely packed clusters,* Nature Nanotechnology **11**, 798 (2016).

[27] P. Jouchet, C. Cabriel, N. Bourg, M. Bardou, C. Poüs, E. Fort, and S. Lévêque-Fort, *Nanometric axial localization of single fluorescent molecules with modulated excitation,* Nature Photonics **15**, 297 (2021).

[28] A. M. Szalai, B. Siarry, J. Lukin, D. J. Williamson, N. Unsain, A. Cáceres, M. Pilo-Pais, G. Acuna, D. Refojo, D. M. Owen, S. Simoncelli, and F. D. Stefani, *Three-dimensional total-internal reflection fluorescence nanoscopy with nanometric axial resolution by photometric localization of single molecules,* Nature Communications **12**, 517 (2021).

[29] M. Wang, J. M. Marr, M. Davanco, J. W. Gilman, and J. A. Liddle, *Nanoscale deformation in polymers revealed by single-molecule super-resolution localization-orientation microscopy,* Materials Horizons **6**, 817 (2019).

[30] S. R. Adams, R. E. Campbell, L. A. Gross, B. R. Martin, G. K. Walkup, Y. Yao, J. Llopis, and R. Y. Tsien, *New biarsenical ligands and tetracysteine motifs for protein labeling in vitro and in vivo: Synthesis and biological applications,* Journal of the American Chemical Society **124**, 6063 (2002).

[31] D. Sage, H. Kirshner, T. Pengo, N. Stuurman, J. Min, S. Manley, and M. Unser, *Quantitative evaluation of software packages for single-molecule localization microscopy,* Nature Methods **12**, 717 (2015).

[32] D. Sage, T. A. Pham, H. Babcock, T. Lukes, T. Pengo, J. Chao, R. Velmurugan, A. Herbert, A. Agrawal, S. Colabrese, A. Wheeler, A. Archetti, B. Rieger, R. Ober, G. M. Hagen, J. B. Sibarita, J. Ries, R. Henriques, M. Unser, and S. Holden, *Super-resolution fight club: assessment of 2D and 3D single-molecule localization microscopy software,* Nature Methods **16**, 387 (2019).

[33] M. P. Gordon, T. Ha, and P. R. Selvin, *Single-molecule high-resolution imaging with photobleaching,* Proceedings of the National Academy of Sciences **101**, 6462 (2004).

[34] S. Weisenburger, D. Boening, B. Schomburg, K. Giller, S. Becker, C. Griesinger, and V. Sandoghdar, *Cryogenic optical localization provides 3D protein structure data with Angstrom resolution,* Nature Methods **14**, 141 (2017).

[35] J. Lu, H. Mazidi, T. Ding, O. Zhang, and M. D. Lew, *Single-Molecule 3D Orientation Imaging Reveals Nanoscale Compositional Heterogeneity in Lipid Membranes,* Angewandte Chemie - International Edition **59**, 17572 (2020).

[36] S. Burgstaller, H. Bischof, T. Gensch, S. Stryeck, B. Gottschalk, J. Ramadani-Muja, E. Eroglu, R. Rost, S. Balfanz, A. Baumann, M. Waldeck-Weiermair, J. C. Hay, T. Madl, W. F. Graier, and R. Malli, *pH-Lemon, a Fluorescent Protein-Based pH Reporter for Acidic Compartments,* ACS Sensors **4**, 883 (2019).

Acknowledgements

I would like to thank: Bernd[1] and Sjoerd[1]for the great supervision, approachability, quick feedback and giving space to develop my own ideas. As per usual, their contribution to my success is genuinely equal. Sjoerd pushed me to develop more on the theoretical aspect of my work and trust my own ideas and findings. Bernd always has a keen sense for picking up on nonsense and conjecture, and helped me keep my research grounded and focused.

Robert for his persuasion in enabling me to start my PhD, being a great supervisor, colleague and paranymph. Also his never ending pursuit of improving my Dutch language is much appreciated and I hope one day his effort will pay off.

Jamie for always pushing me to do the best, through high-school, university and a PhD degree. Both of us pursuing a PhD in parallel was challenging but also an eye opener to how different the process and experience can be. We both struggled with various aspects and maybe one of us enjoyed it more than the other but in the end we (presumably) both made it. I look forward to the next phases of our lives together!

My parents and sister, Rene, Hellen and Meylin for putting up with me and supporting me all these years. From living on the other side of the world to each other, to living together again in the Hague, all the support is much appreciated.

Taylor for being a great lab-mate, friend, brainstorming about crazy new microscopes, and spending all ”our” money. Together we kept the labs running when nobody else was around, kept each other sane or dug a hole together.

Ron for producing our elaborate mechanical designs and always being in for a discussion, especially about good music.

Rasmus for the great collaborative work we have performed over the last years.

All my office-mates, Jelle, Jelle, Lena, Elras and Kote for all the great discussions and help with everything.

The great collaborations with Max, David, Jörg, Ingo, Eugene and Cees allowing me to understand our work from a different point of view.

Jelmer, Daniel and Carlas for the great social(-distanced) gatherings on Fridays and good times during conferences.

Qingru for her commitment, positivity and great teamwork.

Ronald for bringing an infinite amount of positivity to the group.

All my colleagues with a large variety of expertise and interests: Boling, Gyllion, Mohammad, Jeroen, Pierre, Hamid, Yan, Leon, Joor, Willem, Tian, Robiel, Juan Pedro, Richard, Nadia, Tom, Martijn, Jos, Jos, Peter, Awoke, Wenxiu, Anna, Arnica, Marten, Ted, Jeroen, Frans, Jaap, Eric, Lucas, Leo and Jack.

---

[1] These promotors contributed equally

Ellen, Marijn, Maarten, Sten and Alois for the good times as masters students in the group.

Joost, Elil and Gijs for their collaborative effort and appreciation for (unofficially) guiding them.

Mathijs, Yoram and Aditi for discussions about PhD life in another group and a good collaboration.

Wilco, Dustin, Martin and Carel for the great times at the TPKV.

Annelies and Angela for organizing everything, especially the fantastic yearly trips. They were all great and I cannot pick a favourite one, though knocking your promotors over in bubble-football is an unforgettable experience.

Ruud for designing many components together and giving me a better understanding of manufacturability and mechanical design.

I would like to thank everybody in Göttingen for making my time there very enjoyable, in particular: Jan, Simon, Bart, Daniel, Arindam, Anna, Alexey, Soheil, Narain, Roman, Shun, Sebastian, Steffen and Daja.

Kees, Pieter, Jacob, Yan, Gerward, Jan, Sangeetha and Marijke for my great time at the charged particle optics group and my first introduction to the world of research.

Jim, Sjoerd, Thera, Max and Jules for the fantastic times and support during my studies.

All my family and friends for supporting me and enabling me to achieve this milestone, especially my grandparents and Sue, Anton and Albert.

All the influential people during my time in Taiwan: Aad, Li-chao, David, Guy, Stewart, Shyamal, Erin, Gavin and all the other great teachers.

My current colleagues at Lumicks for the great new work environment, especially Siegfried and Raphaël though this list is growing so rapidly it is hard to keep up.

If I forgot to mention you and you feel like you made a significant contribution to this milestone then you already know that your support was greatly appreciated. Lastly, I would like to thank you all for reading my thesis and not skipping straight to the acknowledgements section.

Curriculum Vitæ

Christiaan Nick HULLEMAN

29-10-1990	Born in Spijkenisse, the Netherlands.

Education

1996–2003	Primary School Hill House School, Doncaster, England (1996–2000) OBS De Ammers, Groot Ammers, the Netherlands (2000–2003)
2003–2009	Secondary and High School Taipei European School, Taipei, Taiwan
2009–2015	Bachelors Applied Physics Delft University of Technology, Delft, the Netherlands *Thesis:* Detection system of the secondary electron imaging in the multi-beam scanning electron microscope
2015–2017	Masters Applied Physics Delft University of Technology, Delft, the Netherlands *Thesis:* Polarisation control for cryogenic nanometre resolution nanoscopy
2017–2021	PhD Delft University of Technology, Delft, the Netherlands *Thesis:* Localization microscopy of constrained fluorescent molecules: Pushing towards Ångström-scale resolution through cryogenics *Promotor:* Prof.dr. B. Rieger *Promotor:* Prof.dr. S. Stallinga

Experience

2011-2013	DUT Racing (Formula Student Team), Delft, the Netherlands.

List of Publications

8. R.Ø. Thorsen, **C.N. Hulleman**, B. Rieger, and S. Stallinga, *Photon efficient orientation estimation using polarization modulation in single-molecule localization microscopy*, submitted for publication.
7. **C.N. Hulleman**, R.J. Moerland, S. Stallinga, and B. Rieger, *Polarized Stimulated-Emission Depletion and Dark-State Lifetime at Vacuum and Cryogenic Temperature conditions*, accepted for publication in Physical Review A.
6. **C.N. Hulleman**, R.Ø. Thorsen, E. Kim, C. Dekker, S. Stallinga, and B. Rieger, *Simultaneous orientation and 3D localization microscopy with a Vortex point spread function*, Nature Communications **12**, 5934 (2021).
5. Q. Li, **C.N. Hulleman**, R.J. Moerland, E. Mailvaganam, S. Ganapathy, D. Brinks, S. Stallinga, and B. Rieger, *Waveguide-based total internal reflection fluorescence microscope enabling cellular imaging under cryogenic conditions*, Optics Express **29**, 34097-34108 (2021).
4. R.Ø. Thorsen, **C.N. Hulleman**, M. Hammer, D. Grünwald, S. Stallinga, and B. Rieger, *Impact of optical aberrations on axial position determination by photometry*, Nature Methods **15**, 989–990 (2018).
3. **C.N. Hulleman**, M. Huisman, R.J. Moerland, D. Grünwald, S. Stallinga, and B. Rieger, *Fluorescence Polarization Control for On–Off Switching of Single Molecules at Cryogenic Temperatures*, Small Methods **2**, 1700323 (2018).
2. **C.N. Hulleman**, W. Li, I. Gregor, B. Rieger, and J. Enderlein, *Photon Yield Enhancement of Red Fluorophores at Cryogenic Temperatures*, ChemPhysChem **19**, 1774-1780 (2018).
1. M. Siemons, **C.N. Hulleman**, R.Ø. Thorsen, C.S. Smith, and S. Stallinga, *High precision wavefront control in point spread function engineering for single emitter localization*, Optics Express **26**, 8397-8416 (2018).